Transactions of the ASME, Journal of Heat Transfer (ISSN 0022-1481) is published monthly by The American Society of Mechanical Engineers, Three Park Avenue, New York, NY 10016. Periodicals postage paid at New York, NY and additional mailing offices. POSTMASTER: Send address changes to Transactions of the ASME, Journal of Heat Transfer, c/o THE AMERICAN SOCIETY OF MECHANICAL ENGINEERS, 22 Law Drive, Box 2300, Fairfield, NJ 07007-2300. **CHANGES OF ADDRESS** must be received at Society headquarters seven weeks before they are to be effective. Please send old label and new address.

Journal of Heat Transfer

Published Monthly by ASME

VOLUME 129 • NUMBER 5 • MAY 2007(pp.609-683)

RESEARCH PAPERS

Combustion

609 **Computational Fluid Dynamics Study of Heat Transfer in a Spark-Ignition Engine Combustion Chamber**
A. R. Noori and M. Rashidi

Micro/Nanoscale Heat Transfer

617 **Effects of Various Parameters on Nanofluid Thermal Conductivity**
Seok Pil Jang and Stephen U. S. Choi

Radiative Heat Transfer

624 **Radiative Properties of MoO_3 and Al Nanopowders From Light-Scattering Measurements**
S. M. Begley and M. Q. Brewster

634 **The DRESOR Method for a Collimated Irradiation on an Isotropically Scattering Layer**
Qiang Cheng and Huai-Chun Zhou

Forced Convection

646 **Numerical Study of Laminar Forced Convection Fluid Flow and Heat Transfer From a Triangular Cylinder Placed in a Channel**
Arnab Kumar De and Amaresh Dalal

657 **Effect of Hydraulic Jump on Hydrodynamics and Heat Transfer in a Thin Liquid Film Flowing Over a Rotating Disk Analyzed by Integral Method**
S. Basu and B. M. Cetegen

Bubbles, Particles and Droplets

664 **Transfer From a Droplet at High Peclet Numbers With Heat Generation: Interior Problem**
Adham Souccar and Douglas L. Oliver

TECHNICAL BRIEFS

669 **Least-Squares Radial Point Interpolation Collocation Meshless Method for Radiative Heat Transfer**
J. Y. Tan, L. H. Liu, and B. X. Li

674 **Optimally Staggered Finned Circular and Elliptic Tubes in Turbulent Forced Convection**
R. L. S. Mainardes, R. S. Matos, J. V. C. Vargas, and J. C. Ordonez

679 **Boundary Condition Dependent Natural Convection in a Rectangular Pool With Internal Heat Sources**
Seung Dong Lee, Jong Kuk Lee, and Kune Y. Suh

(Contents continued on inside back cover)

This journal is printed on acid-free paper, which exceeds the ANSI Z39.48-1992 specification for permanence of paper and library materials. ♾™
♻ 85% recycled content, including 10% post-consumer fibers.

Journal of Heat Transfer Volume 129, Number 5 MAY 2007

ERRATUM

683 Publisher's Note: "Phase-Change Heat Transfer in Microsystems" [Journal of Heat Transfer, 2007, 129(2), pp. 101–107]
Ping Cheng, Hui-Ying Wu, and Fang-Jun Hong

The ASME Journal of Heat Transfer is abstracted and indexed in the following:

Applied Science and Technology Index, Chemical Abstracts, Chemical Engineering and Biotechnology Abstracts (Electronic equivalent of Process and Chemical Engineering), Civil Engineering Abstracts, Compendex (The electronic equivalent of Engineering Index), Corrosion Abstracts, Current Contents, E & P Health, Safety, and Environment, Ei EncompassLit, Engineered Materials Abstracts, Engineering Index, Enviroline (The electronic equivalent of Environment Abstracts), Environment Abstracts, Environmental Engineering Abstracts, Environmental Science and Pollution Management, Fluidex, Fuel and Energy Abstracts, Index to Scientific Reviews, INSPEC, International Building Services Abstracts, Mechanical & Transportation Engineering Abstracts, Mechanical Engineering Abstracts, METADEX (The electronic equivalent of Metals Abstracts and Alloys Index), Petroleum Abstracts, Process and Chemical Engineering, Referativnyi Zhurnal, Science Citation Index, SciSearch (The electronic equivalent of Science Citation Index), Theoretical Chemical Engineering

Computational Fluid Dynamics Study of Heat Transfer in a Spark-Ignition Engine Combustion Chamber

A. R. Noori
e-mail: a_noori@ip-co.com
Combustion and Heat Transfer Department,
Iran-Khodro Powertrain Company (IPCO),
Tehran, Iran

M. Rashidi
e-mail: rashidi@shirazu.ac.ir
Mechanical Engineering Department,
Engineering College,
Shiraz University,
Shiraz, Iran

The objective of this study is the thermal investigation of a typical spark-ignition (SI) engine combustion chamber with particular focus in determination of the locations where the heat flux and heat transfer coefficient are highest. This subject is an important key for some design purposes especially thermal loading of the piston and cylinder head. To this end, CFD simulation using the KIVA-3V CFD code on a PC platform for flow, combustion, and heat transfer in a typical SI engine has been performed. Some results including the temporal variation of the area-averaged heat flux and heat transfer coefficient on the piston, combustion chamber, and cylinder wall are presented. Moreover, the temporal variation of the local heat transfer coefficient and heat flux along a centerline on the piston as well as a few locations on the combustion chamber wall are shown. The investigation reveals that during the combustion period, the heat flux and heat transfer coefficient vary substantially in space and time due to the transient nature of the flame propagation. For example, during the early stages of the flame impingement on the wall, the heat flux undergoes a rapid increase by as much as around 10 times the preimpingement level. In other words, the initial rise of the heat flux at any location is related to the time of the flame arrival at that location. [DOI: 10.1115/1.2712474]

Keywords: combustion chamber, heat flux, heat transfer coefficient, spark ignition engine

Introduction

Characterization of thermal energy transport, rate of heat transfer, and rate of heat release has become a key focus in recent years because these factors affect engine performance, fuel economy, and exhaust emission as well as the life of the components such as piston, rings, and valves. It should be noted that the heat flux varies substantially with location. The regions of the combustion chamber that are contacted by rapidly moving high temperature burned gases generally experience the highest heat flux that can reach as high as 10 MW/m^2 during the combustion period [1]. Accurate prediction of the wall heat transfer is not only needed for calculating heat release rate and flame propagation from in-cylinder pressure data, but is also necessary for improving the overall accuracy of the engine combustion simulation. Numerous engine heat transfer measurements and studies have been conducted on SI engine cylinder head, combustion chamber, and piston [2–8]. A concise review of the engine heat transfer characteristics has been given by Heywood [1].

Overbye et al. [9] measured the heat flux at several positions on the cylinder head of a CFR engine. Tests were performed at near stoichiometric air fuel ratio and an engine speed of 830 rpm. The effects of intake manifold pressure, turbulence and wall deposits on the heat flux were investigated. Oguri [10] measured the instantaneous heat flux at one position on the cylinder head of a spark ignition engine. He proposed an empirical correlation similar to that of Elser's [11] that showed agreement with his experimental results. Alkidas [12] measured the transient heat flux at four positions on the cylinder head of a four stroke single cylinder SI engine. Tests were performed for both firing and motoring operation of the engine. He showed that the heat flux varies considerably with the position of the measurement. He also showed that at the firing conditions, the initial rise of heat flux at each position agrees with the time of the flame arrival at that position. Alkidas [13] followed his studies by investigating the influence of air fuel ratio and load on heat transfer within the combustion chamber. He showed that the heat flux is highest at near stoichiometric composition. Also an increase in load from 40 to 60% resulted in an increase in peak heat flux of about 30%.

In the area of computational methods, Jennings and Morel [14] performed a CFD simulation to demonstrate the effect of the wall temperature on the temperature gradient in the vicinity of the wall. Moreover, Popp and Baum [15] investigated in detail the effect of the wall temperature on the surface heat flux in a SI engine. They showed that the wall heat flux falls as the wall temperature decreases because of the flame quenching near the wall. Kleemann et al. [16] using a CFD package predicted the wall heat transfer in reciprocating engines with particular reference to diesel engines working at high peak pressures where accurate predictions of thermal and pressure loading of the metal components were required.

It should be noted that there are a number of commercial CFD packages; however, the most widely used for engine simulation is the KIVA family of programs originally developed at Los Alamos National Laboratory. The basic features of the code have been well documented [17–19].

In this study the KIVA-3V CFD code for engine simulation has been used. KIVA-3V is a three-dimensional, multicomponent model capable of simulating multiphase flow under steady state and transient conditions. The code solves the unsteady three-dimensional compressible average Navier-Stokes equations coupled to a k-ε turbulence model. The k-ε model uses the wall

Contributed by the Heat Transfer Division of ASME for publication in the JOURNAL OF HEAT TRANSFER. Manuscript received January 12, 2005; final manuscript received August 21, 2006. Review conducted by Louis C. Burmeister. Paper presented at the ASME Summer Heat Transfer Conference (HT2003), July 21–23, 2003, Las Vegas, NV.

Fig. 1 Combustion chamber, piston, and cylinder head of the PAYKAN engine. Photographs have been taken using a digital camera at the Iran-Khodro Powertrain Company (IPCO).

function that is an analytic solution to simplified turbulence equations to infer wall shear stress and heat loss to bridge the viscous sublayer region.

Engine Geometry

In this study, a specific engine called PAYKAN with a flat roof combustion chamber including two valves, circular runners, and a dish piston crown has been simulated. Figure 1 shows the combustion chamber, piston, and cylinder head of this engine. Moreover, a cross section of the inlet and outlet ports has been illustrated in Fig. 2. More information about the engine specifications has been shown in Table 1.

Fig. 2 A cross section of inlet port (*a*) and outlet port (*b*)

Table 1 Engine specifications

Bore	87 mm
Stroke	67 mm
Connecting rod length	126 mm
Compression ratio	7.8
Intake valve diameter	32 mm
Maximum intake valve lift	9.6 mm at 106 deg ATDC
Intake valve opening	44 deg BTDC
Intake valve closing	84 deg ABDC
Exhaust valve diameter	26 mm
Maximum exhaust valve lift	9.6 mm at 62 deg ABDC
Exhaust valve opening	66 deg BBDC
Exhaust valve closing	18 deg ATDC

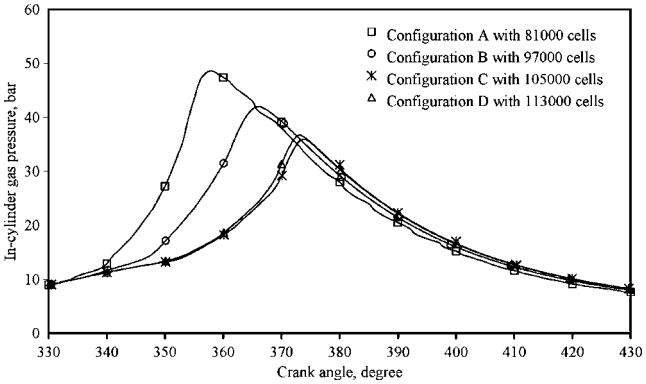

Fig. 3 Variation of in-cylinder pressure with crank angle based on operating conditions shown in Table 2 for four different mesh sizes

Mesh Generation and Grid Independence

The KIVA-3V preprocessor has been used for computational mesh generation. Successive runs with mesh refinement were performed in order to check grid independence of the results. Results were compared until no difference was seen for at least two successive mesh sizes. Figures 3 and 4 4 show the variation of in-cylinder pressure and temperature with crank angle (CA) based on operating conditions shown in Table 2 for four different configurations. It is seen that there is no significant difference between configurations C and D. Therefore, we should choose configuration C with 105,000 cells at bottom dead center (BDC) as a final computational mesh. Figure 5 shows the computational mesh, with 105,000 cells at BDC, created for the CFD simulation of the PAYKAN engine.

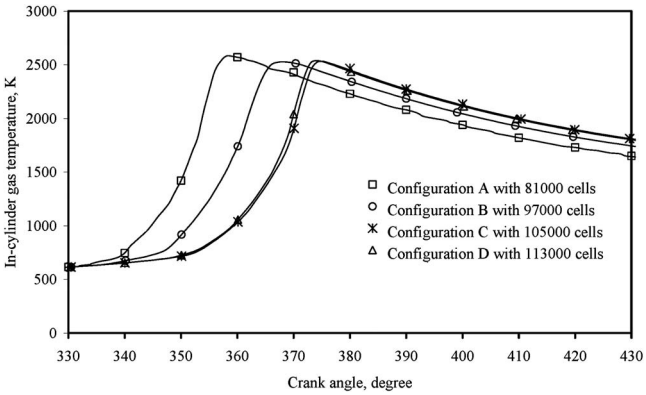

Fig. 4 Variation of in-cylinder temperature with crank angle based on operating conditions shown in Table 2 for four different mesh sizes

Table 2 Operating conditions

Cylinder head temperature	450 K
Piston temperature	450 K
Cylinder wall temperature	400 K
Intake valve temperature	450 K
Exhaust valve temperature	550 K
Intake charge temperature	300 K
Intake charge pressure	0.7 bar
Spark timing	30 BTDC
Engine speed	2500 rpm

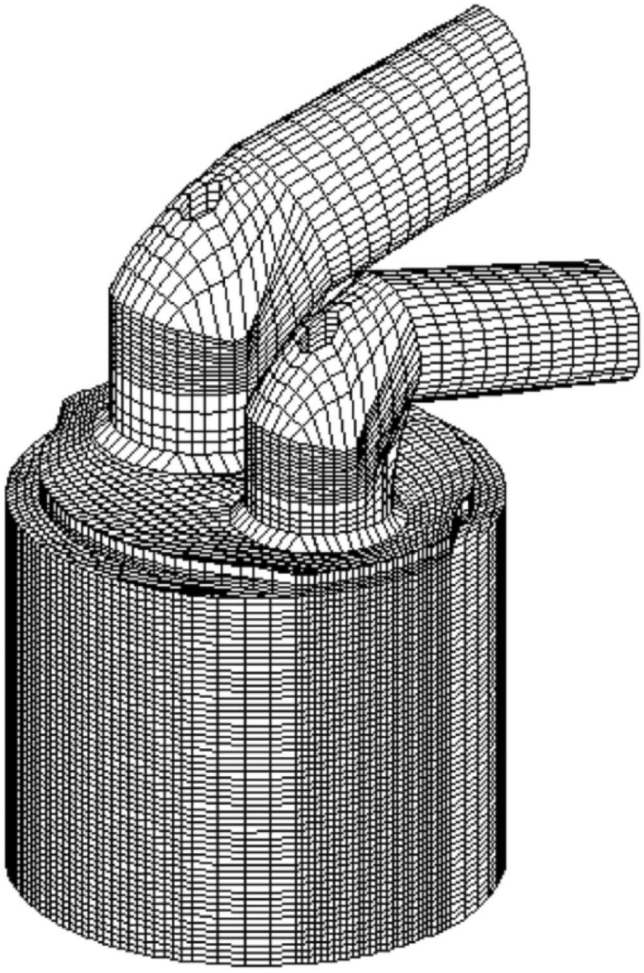

Fig. 5 Computational mesh with 105,000 cells at the BDC created for the CFD simulation of the PAYKAN engine

Combustion Model

The combustion model used is Spalding's [20] eddy breakup model. This model relates the local and instantaneous turbulent combustion rate to the fuel mass fraction and the characteristic time scale of turbulence. The successful application of this model for trend and sensitivity analysis requires a preliminary adjustment of a specific coefficient and spark timing in order to match the experimental combustion rate with the computational combustion rate. The joint application of this combustion model and the present k-ε turbulence model has been successfully applied to reciprocating engines for both motoring and firing operation [21,22].

Heat Transfer Model

Flow within the engine cylinder is turbulent and boundary layer thickness is thin relative to the practical computational grid size; therefore in order to determine shear stress and heat transfer in the vicinity of the wall, application of the velocity and temperature wall functions is necessary in the boundary layers on the solid surfaces. In this study, the logarithmic law-of-the-wall is used for both velocity and temperature profiles in the near-wall regions. The following are some assumptions used to create wall functions in the engine applications [17]:

1. The flow is quasisteady.
2. The fluid velocity is parallel to the wall and varies only in the normal direction to the wall.
3. There are no streamwise pressure gradients.

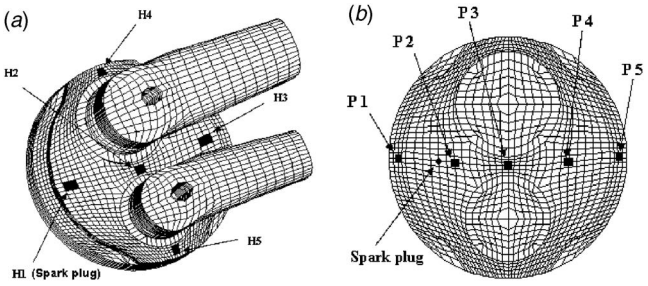

Fig. 6 A few locations on the combustion chamber surface (*a*) and piston (*b*) where the thermal characteristics are considered

4. There are no chemical reactions on the walls.
5. The dimensionless wall heat loss (ζ) is small compared to unity.
6. Reynolds numbers are large (i.e., $\mu \gg \mu_l$).
7. Mach numbers are small, so that dissipation of turbulent kinetic energy is a negligible source relative to the internal energy.

With the above assumptions, in the near-wall regions where the Reynolds number is low, the wall heat flux J_w, is computed by Eq. (1) and in the logarithmic regions where the Reynolds number is higher, J_w is given by Eq. (2),

$$J_w = \frac{\rho u^* c_P (T - T_w)}{\left(\mathrm{Pr}_l \dfrac{u}{u^*}\right)} \tag{1}$$

$$J_w = \frac{\rho u^* c_P (T - T_w)}{\left\{\mathrm{Pr}\left[\dfrac{u}{u^*} + \left(\dfrac{\mathrm{Pr}_l}{\mathrm{Pr}} - 1\right) R_c^{1/2}\right]\right\}} \tag{2}$$

where Pr_l is 0.74. It should be noted that T is referred to the gas temperature at the nearest node in the vicinity of the wall.

Initial and Boundary Conditions

The in-cylinder pressure and temperature, species concentration, turbulent kinetic energy, and turbulence length scale are assumed to be uniform at the time of the intake valve opening when the calculations are started. Initial conditions for pressure, temperature, and species concentration were created using a preliminary cycle simulation. The initial value of turbulent kinetic energy k, was assumed to be 10% of the total kinetic energy based on mean piston speed and the initial value of dissipation rate ε, was

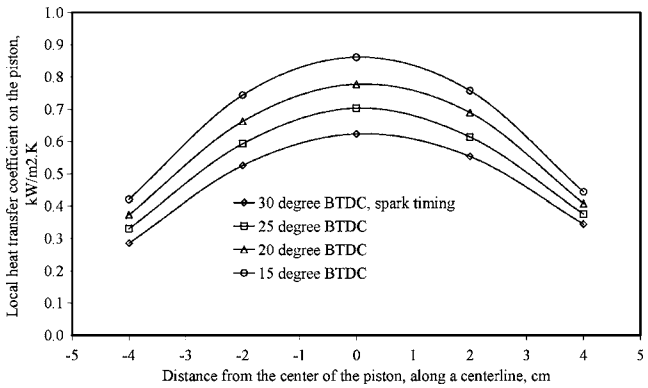

Fig. 7 Spatial and temporal variation of heat transfer coefficient during the compression stroke and before flame initiation for the locations shown in Fig. 6(*b*)

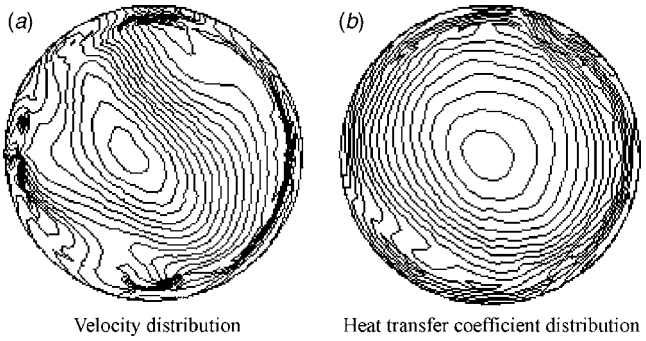

Fig. 8 Distribution of the velocity and heat transfer coefficient in the vicinity of the piston at 30 deg BTDC, before flame initiation

calculated using the procedures in the code [23]. At the solid surfaces, a constant wall temperature was assumed throughout the computation [23].

Boundary conditions for intake charge pressure and temperature were kept constant. Moreover, local turbulent kinetic energy at the intake was assumed to be 10% of the kinetic energy based on the mean flow velocity at the intake boundary. The length scale during induction is a constant equal to half the maximum intake valve lift. A similar approach was considered for boundary conditions at the exhaust [23].

Results and Discussion

Figure 6 shows a few locations on the combustion chamber surface within the cylinder head (a) and also some locations along a centerline on the piston surface (b) where the heat flux, heat transfer coefficient and other thermal characteristics are considered. H and P refer to the locations on the cylinder head and piston respectively and H1 is about where the spark plug is located.

In general, within the engine cylinder, the local heat transfer coefficient is affected by both the local gas velocity and density. During the compression stroke and before flame initiation as the piston moves toward the top dead center (TDC), the gas density through the cylinder uniformly increases. Therefore, the heat transfer coefficient anywhere in the combustion chamber also increases and its local distribution is only affected by the local distribution of the velocity within the cylinder. Figure 7 shows the spatial and temporal variation of heat transfer coefficient during the compression stroke and before flame initiation. It is seen that the heat transfer coefficient near the center of the piston is maximum as a result of the high gas velocity in this region. Distribution of the velocity and heat transfer coefficient over the piston illustrated in Fig. 8 confirms the above statement.

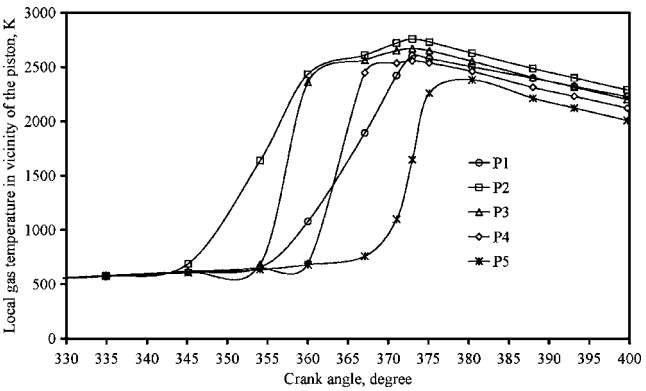

Fig. 9 Temporal variation of the gas temperature in the vicinity of the piston for the locations shown in Fig. 6(*b*)

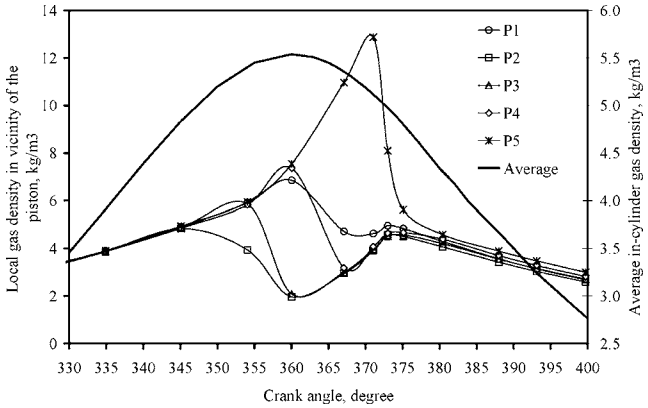

Fig. 10 Temporal variation of the average in-cylinder gas density as well as the local gas density in the vicinity of the piston for the locations shown in Fig. 6(*b*)

After flame initiation and during the flame propagation, gas density distribution in the cylinder is not only uneven but also highly affected by the in-cylinder temperature gradient created by the flame propagation or heat release. This is because the in-cylinder pressure during the combustion uniformly increases and there is not any pressure gradient in the combustion chamber. Moreover, density and temperature of the gas at any location are merely related by the ideal gas equation of state.

Figures 9 and 10 show the effect of the flame propagation on the gas temperature and density in the vicinity of the piston. It is seen that as the flame arrives at any location, the gas temperature rapidly increases and as a result the gas density falls rapidly. After that, as the flame progresses and leaves the specific location, the gas density at that location can be increased providing the rate of in-cylinder pressure rise due to heat release is more than the rate of temperature rise.

Moreover, Fig. 9 shows that the gas temperature at location P2 is higher than the other locations during the flame propagation because P2 (near the spark plug) is where the flame arrives at the early stages of the flame propagation. Figure 10 shows that the average in-cylinder gas density has its maximum value at TDC where the cylinder volume is lowest; whereas the gas density at location P5 has the highest value at about the time of peak cylinder pressure. This is because the flame arrives at location P5 when the cylinder pressure is highest.

Figure 11 shows the variation of heat transfer coefficient with crank angle on the piston during the flame propagation. A comparison between Fig. 7 and Fig. 11 shows that during the flame

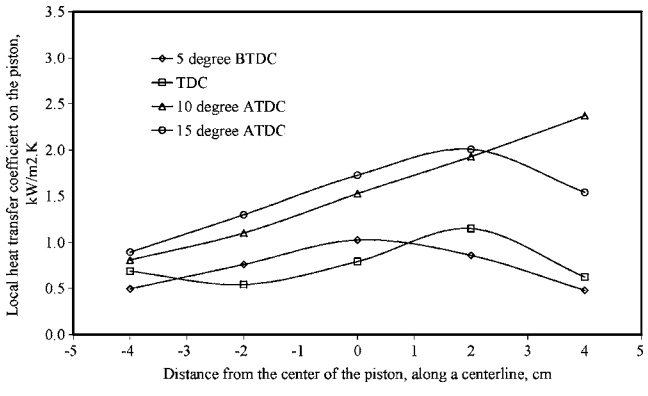

Fig. 11 Spatial and temporal variation of heat transfer coefficient during the flame propagation for the locations shown in Fig. 6(*b*)

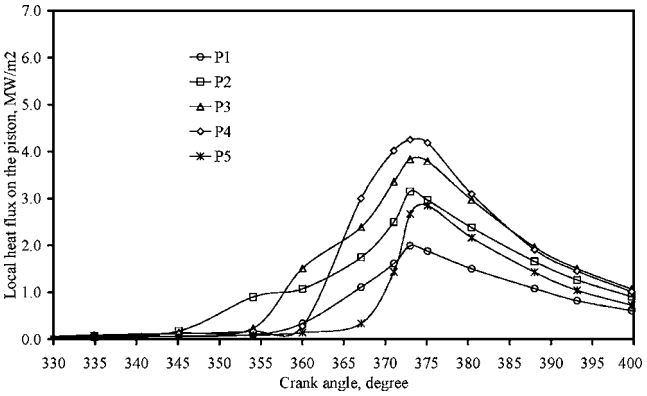

Fig. 12 Variation of heat flux with crank angle for the locations shown in Fig. 6(*b*)

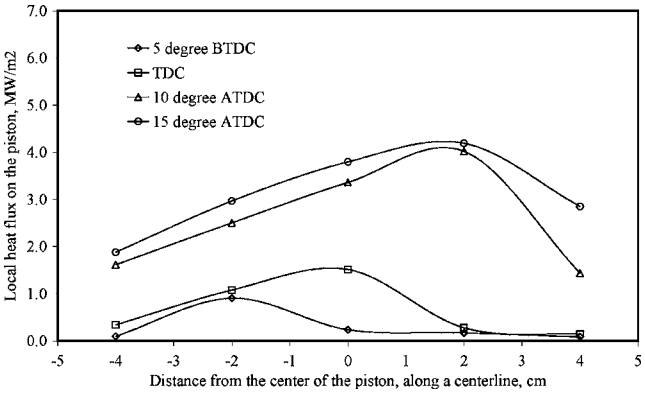

Fig. 14 Spatial and temporal variation of heat flux during the flame propagation for the locations shown in Fig. 6(*b*)

propagation, distribution of the heat transfer coefficient is more affected by the gas density distribution than the velocity distribution.

Figure 12 shows the variation of heat flux with crank angle for the locations shown in Fig. 6(*b*). It is seen that, at any location the heat flux rises rapidly when the flame arrives at that location and has its maximum value at about the time of peak cylinder pressure and temperature. After that, heat flux at the specific location decays to relatively low levels as the piston moves away from TDC and the expansion cools the in-cylinder burned gases. The maximum heat flux on the piston occurs where both temperature gradient and heat transfer coefficient on the wall are highest; but the effect of temperature gradient is more dominant because the gas temperature within the cylinder during the combustion period is of the order of 1000 K, whereas the heat transfer coefficient is of the order of 10 $kW/m^2 K$. For example, Fig. 13 shows that the heat transfer coefficient at location P4 is relatively lower than the one at location P5 around the 10 deg crank angle ATDC; whereas, as has been illustrated in Fig. 12, the heat flux at the same time at location P4 is much higher than the value of the heat flux at location P5. This is because the gas temperature and as a result the temperature gradient on the wall at location P4 is much more than the temperature gradient at location P5.

There are some locations in the combustion chamber that experience the highest heat flux. These locations are where the flame arrives at the time of peak cylinder pressure. Figure 14 shows that the location P4, about 2 cm from the center of the piston, has the above situation so that it experiences the highest heat flux around the 15 deg crank angle ATDC.

Some information about the distribution of the gas temperature and heat flux on the piston during the flame propagation has been illustrated in Figs. 15 and 16. It can be seen that the heat flux distribution on the piston is extremely affected by the gas temperature distribution in the vicinity of the piston.

During the combustion, in the flame front or reaction zone, air-fuel mixture expands as a result of heat release. Therefore, the burned and unburned gases, respectively, behind and in front of the flame escape from the flame front or reaction zone. This phenomenon increases the local gas motion and also heat transfer coefficient in this region. For example, the flame front is schematically distinguished by distribution of the gas velocity vectors shown in Fig. 17.

Figures 18–20 illustrate some information about thermal characteristics of the locations shown in Fig. 6(*a*). In this regard all previous descriptions about the similar figures are valid.

Figures 21 and 22 show the temporal variation of the area-averaged heat flux and heat transfer coefficient on the piston, cylinder head, cylinder wall, and total combustion chamber. It is seen that the heat flux and heat transfer coefficient increases rapidly once the combustion starts, reaches a maximum at the time of peak cylinder pressure, and decays to a low value by 40–60 deg crank angle ATDC.

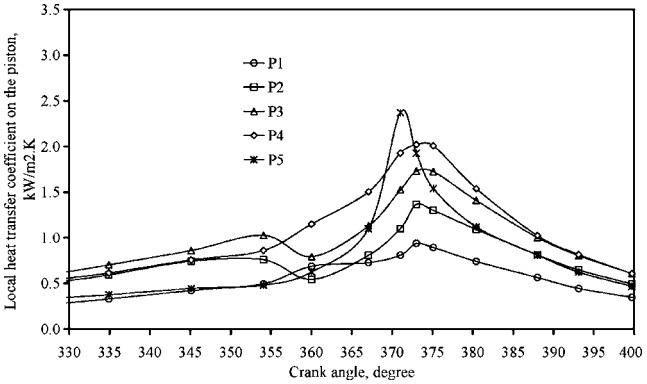

Fig. 13 Variation of heat transfer coefficient with crank angle for the locations shown in Fig. 6(*b*)

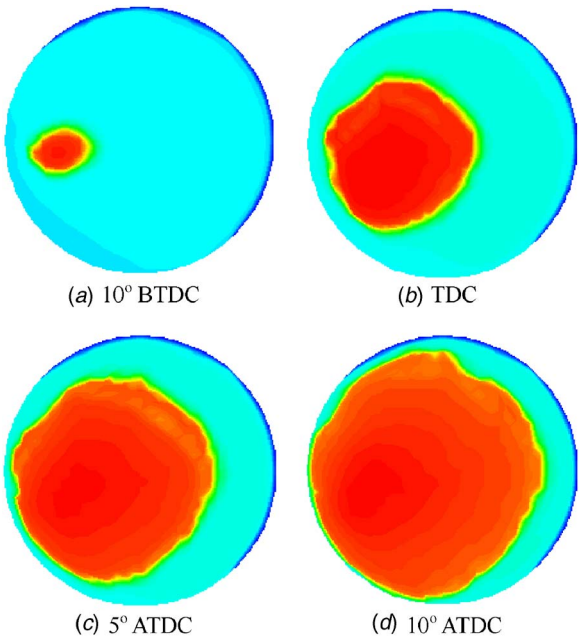

Fig. 15 Distribution of the gas temperature in the vicinity of the piston during the flame propagation

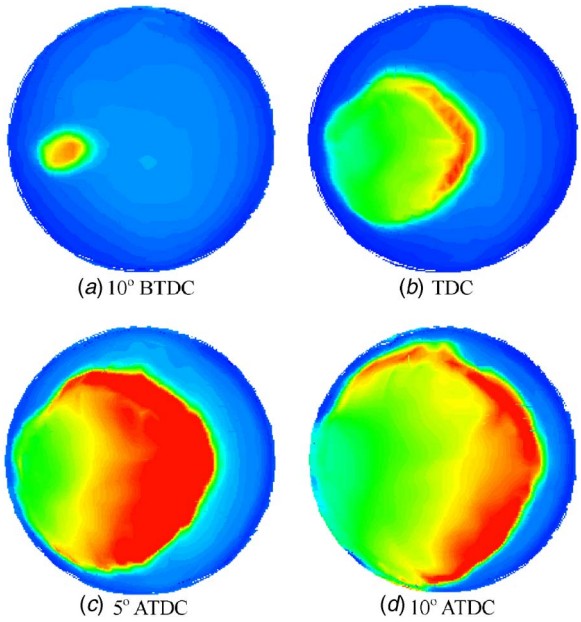

Fig. 16 Distribution of heat flux on the piston during the flame propagation

The heat flux on the cylinder head is usually higher than the heat flux on the piston and cylinder wall. This would be expected since the cylinder head is where most of the combustion takes place and gas velocities are higher. Moreover, the area-averaged heat flux on the cylinder wall is much lower than the other places. Again this would be expected since the combustion gases do not contact the cylinder wall until later in the expansion stroke when their temperature is much below the peak value.

Figure 23 shows a comparison between the area-averaged heat flux calculated using CFD simulation and Woschni's correlation. In general, the heat flux obtained using Woschni's correlation

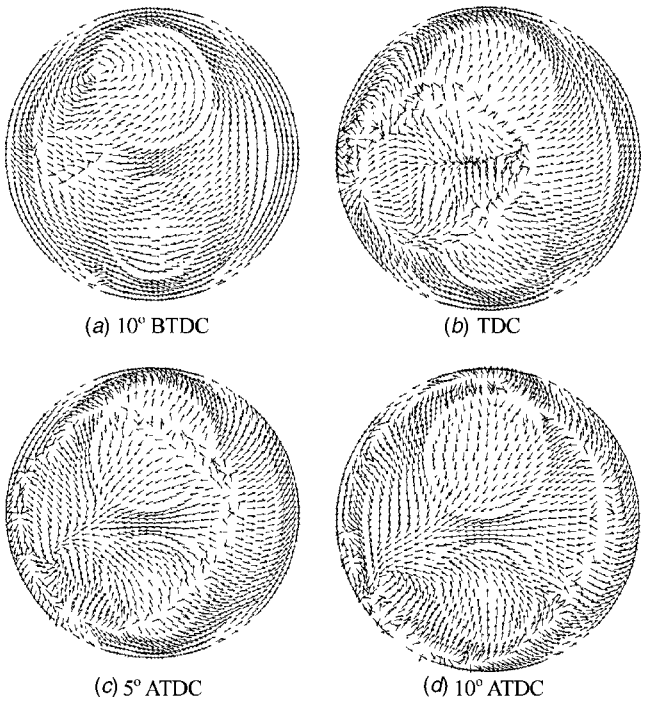

Fig. 17 Distribution of the gas velocity vectors in the vicinity of the piston during the flame propagation

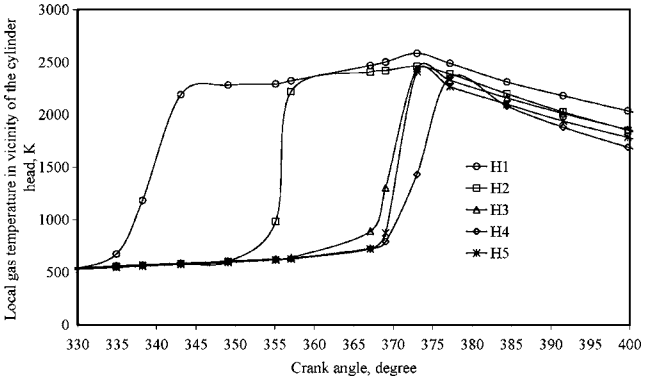

Fig. 18 Temporal variation of the gas temperature in the vicinity of the cylinder head for the locations shown in Fig. 6(*a*)

based on bulk gas temperature is lower than the corresponding heat flux calculated using CFD simulation. This is especially true during the combustion period. Moreover, Fig. 24 illustrates a comparison between the local heat flux calculated using CFD simulation and area-averaged heat flux predicted by Woschni's correlation. It should be noted that the heat flux value predicted using both calculating methods just before and after combustion period approximately are the same.

Conclusions

- Before flame initiation the gas density distribution through the cylinder is uniform, whereas, during the combustion, gas density distribution in the cylinder is not only uneven but

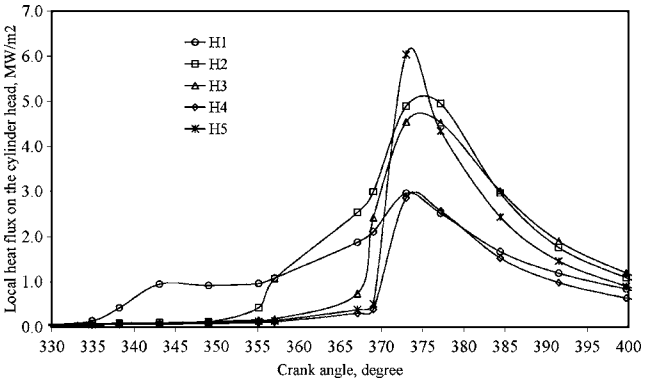

Fig. 19 Variation of heat flux with crank angle for the locations shown in Fig. 6(*a*)

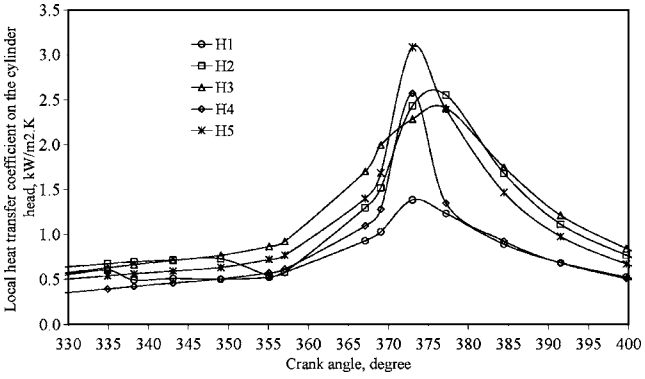

Fig. 20 Variation of heat transfer coefficient with crank angle for the locations shown in Fig. 6(*a*)

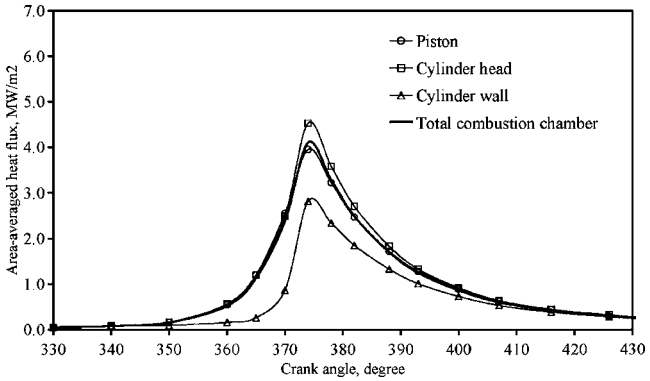

Fig. 21 Temporal variation of the area-averaged heat flux on the piston, cylinder head, cylinder wall, and total combustion chamber

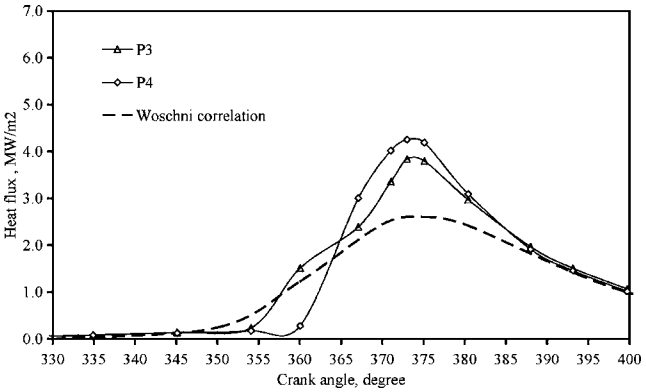

Fig. 24 Comparison of the local heat flux calculated using CFD simulation at locations P3 and P4 with the area-averaged heat flux calculated using Woschni's correlation

also highly affected by the in-cylinder temperature gradient created by the flame propagation or heat release.

- During the compression stroke heat transfer coefficient distribution on the walls is only affected by the gas velocity distribution; whereas, during the combustion it is affected by both the local gas velocity and density but the effect of the density is more dominant.
- At any location the heat flux rises rapidly when the flame arrives at that location and has its maximum value at about the time of peak cylinder pressure and temperature.
- The locations where the flame arrives at the time of peak cylinder pressure, experience the highest heat fluxes.

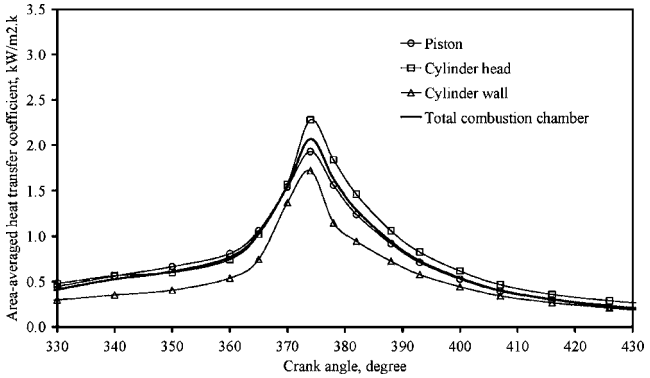

Fig. 22 Temporal variation of the area-averaged heat transfer coefficient on the piston, cylinder head, cylinder wall, and total combustion chamber

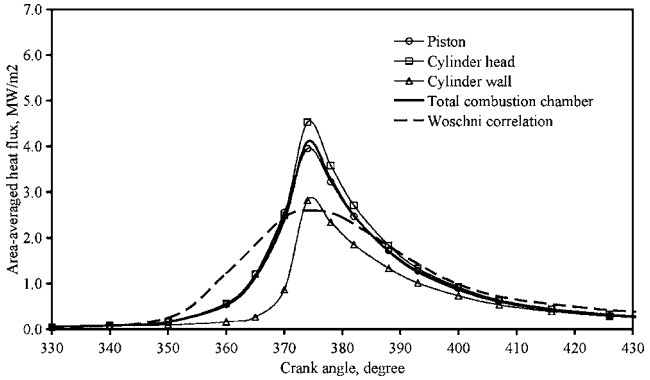

Fig. 23 Comparison of the area-averaged heat flux variations predicted by CFD simulation and Woschni's correlation

- The locations where the flame arrives at the early stages of the flame propagation, experience the highest gas temperature through the combustion.
- The area-averaged heat flux and heat transfer coefficient on the cylinder head are the highest and on the cylinder wall are the lowest.

Acknowledgment

This work was supported and carried out at Iran-Khodro Powertrain Company (IPCO), Tehran, Iran. Financial contribution of the board of directors is gratefully acknowledged. I would like to also express my gratitude to all reviewers of this paper for their comments and suggestions.

Nomenclature

ATDC = after top dead center
BDC = bottom dead center
BTDC = before top dead center
c_P = specific heat capacity
J_w = heat flux on the wall, Eqs. (1) and (2)
k = turbulent kinetic energy
Pr = Prandtl number
Pr_l = laminar Prandtl number
R_c = critical Reynolds number
T = gas temperature near the wall
TDC = top dead center
T_w = wall temperature
u = magnitude of the gas velocity relative to the wall
u^* = friction velocity ($\sqrt{\tau_w/\rho}$)
ε = dissipation rate of turbulent kinetic energy
μ = dynamic viscosity
μ_l = laminar dynamic viscosity
ρ = gas density near the wall
τ_w = wall shear stress
ζ = dimensionless wall heat loss ($J_w/\rho u^* c_P(T - T_w)$)

References

[1] Heywood, J. B., 1987, *Internal Combustion Engine Fundamentals*, McGraw-Hill, New York.
[2] Eichelberg, G., 1939, "Some New Investigations on Old Combustion Engine Problems," Engineering (London), **148**, pp. 463–547.
[3] Annand, W. J. D., 1963, "Heat Transfer in the Cylinders of Reciprocating Internal Combustion Engines," Proc. Inst. Mech. Eng., **177**(36), pp. 973–990.
[4] Woschni, G., 1967, "A Universally Applicable Equation for the Instantaneous Heat Transfer Coefficient in the Internal Combustion Engine," SAE Trans., **76**, pp. 3065–3083.
[5] LeFeuvre, T., Myers, P. S., and Uyehara, O. A., 1969, "Experimental Instan-

taneous Heat Fluxes in a Diesel Engine and Their Correlation," SAE Paper No. 690464.
[6] Whitehouse, N. D., 1970–1971, "Heat Transfer in a Quiescent Chamber Diesel Engine," Proc. Inst. Mech. Eng., **185**, pp. 963–975.
[7] Flynn, P., Mizusawa, M., Uyehara, O. A., and Myers, P. S., 1972, "An Experimental Determination of the Instantaneous Potential Radiant Heat Transfer Within an Operating Diesel Engine," SAE Paper No. 720022.
[8] Dent, J. C., and Suliaman, S. L., 1977, "Convective and Radiative Heat Transfer in a High Swirl Direct Injection Diesel Engine," SAE Paper No. 770407.
[9] Overbye, V. D., Bennethum, J. E., Uyehara, O. A., and Myers, P. S., 1961, "Unsteady Heat Transfer in Engines," SAE Trans., **69**, pp. 461–494.
[10] Oguri, T., 1960, "On the Coefficient of Heat Transfer Between Gases and Cylinder Walls of the Spark-Ignition Engine," Bull. JSME, **3**(11), pp. 363–374.
[11] Elser, K., 1954, "Der Instationare Warmeubergang in Dieselmotoren," Mitt Inst. Thermodyn., Zurich, No. 15.
[12] Alkidas, A. C., 1980, "Heat Transfer Characteristics of a Spark-Ignition Engine," ASME J. Heat Transfer, **102**(2), pp. 189–193.
[13] Alkidas, A. C., and Myers, J. P., 1982, "Transient Heat-Flux Measurements in the Combustion Chamber of a Spark-Ignition Engine," ASME J. Heat Transfer, **104**, pp. 62–67.
[14] Jennings, M. J., and Morel T., 1990, "An Improved Near Wall Heat Transfer Model for Multidimensional Engine Flow Calculations," SAE Paper No. 900251.
[15] Popp, P., and Baum, M., 1995, "Heat Transfer and Pollutant Formation Mechanisms in Insulated Combustion Chambers," SAE Paper No. 952387.
[16] Kleemann, A. P., Gosman, A. D., and Binder, K. B., 2001, "Heat Transfer in Diesel Engines: A CFD Evaluation Study," *The 5th International COMODIA Symposium on Diagnostics and Modeling of Combustion in Internal Combustion Engines*.
[17] Amsden, A. A., O'Rourke, P. J., and Butler, T. D., 1989, "Kiva-II: A Computer Program for Chemically Reactive Flows With Sprays," L. A. Report No. 111560-MS.
[18] Amsden, A. A., Ramshaw, J. D., O'Rourke, P. J., and Dukowicz, J. K., "KIVA: A Computer Program for Two- and Three-Dimensional Fluid Flows With Chemical Reactions and Fuel Sprays," Los Alamos National Laboratory Report No. LA-10245-MS.
[19] Amsden, A. A., Butler, T. D., O'Rourke, P. J., and Ramshaw, J. D., 1985, "KIVA: A Comprehensive Model for 2D and 3D Engine Simulations," SAE Paper No. 850554.
[20] Spalding, D. B., 1976, "Development of the Eddy-Breakup Model of Turbulent Combustion," in *Proceedings of the 16th International Symposium on Combustion*, Pittsburgh, PA, pp. 1657–1663.
[21] Gosman, A. D., 1985, "Computer Modeling of Flow and Heat Transfer in Engines, Progress and Prospect," in *Proceedings of the COMODIA Symposium, JSME, SAE, and MESJ*, Tokyo, Japan.
[22] Diwakar, R., 1984, "Assessment of the Ability of a Multidimensional Computer Code to Model Combustion in a Homogeneous Charge Engine," SAE Paper No. 840230.
[23] Das, S., and Dent, J. C., 1995, "Simulation of the Mean Flow in the Cylinder of a Motored 4-Valved Spark Ignition Engine," SAE Paper No. 952384.

Effects of Various Parameters on Nanofluid Thermal Conductivity

Seok Pil Jang
School of Aerospace and Mechanical Engineering,
Hankuk Aviation University,
Goyang, Gyeonggi-do, 412-791, Korea
Energy Systems Division,
Argonne National Laboratory,
Argonne, IL 60439

Stephen U. S. Choi[1]
Energy Systems Division,
Argonne National Laboratory,
Argonne, IL 60439

The addition of a small amount of nanoparticles in heat transfer fluids results in the new thermal phenomena of nanofluids (nanoparticle-fluid suspensions) reported in many investigations. However, traditional conductivity theories such as the Maxwell or other macroscale approaches cannot explain the thermal behavior of nanofluids. Recently, Jang and Choi proposed and modeled for the first time the Brownian-motion-induced nanoconvection as a key nanoscale mechanism governing the thermal behavior of nanofluids, but did not clearly explain this and other new concepts used in the model. This paper explains in detail the new concepts and simplifying assumptions and reports the effects of various parameters such as the ratio of the thermal conductivity of nanoparticles to that of a base fluid, volume fraction, nanoparticle size, and temperature on the effective thermal conductivity of nanofluids. Comparison of model predictions with published experimental data shows good agreement for nanofluids containing oxide, metallic, and carbon nanotubes. [DOI: 10.1115/1.2712475]

Keywords: nanofluids, thermal conductivity, Brownian motion, Brownian-motion-induced nanoconvection

1 Introduction

Most ideas for enhancing the heat transfer coefficient of fluids have focused on two strategies. The first is to increase the Nusselt number, which is dependent on the Reynolds number, the Prandtl number and geometry. Many investigators [1–3] have been interested in finding the optimal geometry to improve the heat transfer coefficient because the Nusselt number depends on geometry under fully developed laminar flow. The second is to decrease a characteristic length that is inversely proportional to not only the heat transfer coefficient as shown in Eq. (1) but also the surface area per unit volume,

$$h = \frac{\mathrm{Nu}\, k_f}{D_C} \tag{1}$$

where h, D_C, Nu, and k_f are the heat transfer coefficient, characteristic length, Nusselt number, and fluid thermal conductivity, respectively. Based on the second strategy, microchannel heat sinks have been developed as cooling devices, which can be applied to compact electronic devices with high heat flux [4–6].

Lee et al. discovered that nanofluids (see Fig. 1), fluids with unprecedented stability of suspended nanoparticles despite huge differences in the density of nanoparticles and fluid, have thermal conductivity enhancement much better than predicted [7]. These materials hold great promise for developing next-generation cooling devices. Subsequently, researchers [7–13] have investigated the thermal characteristics of nanofluids containing various nanoparticles such as copper oxide, aluminum oxide, copper, and carbon nanotubes. Dispersion of a very small amount of nanotubes produces a remarkable change in the effective thermal conductivity of the base fluid, an increase by up to a factor of 2.5 at 1 vol% nanotubes [10]. In addition, nanofluids possess two new thermal phenomena compared to fluid containing particles with millimeter or micrometer size [14] and solid thin films with nanoscale thickness [15]. One is that the effective thermal conductivity of nanofluids increases with decreasing size of the nanoparticles suspended in base fluid. The other is that the effective thermal conductivity of nanofluids increases with temperature [12]. This temperature-dependent property implies that nanofluids are "smart" fluids, "sensing" their thermal environment and adjusting their thermal conductivity accordingly.

Even though the thermal phenomena for nanofluids are experimentally confirmed, nanofluids still offer theoretical challenges because the phenomena cannot be explained by previous traditional models [16–19]. Keblinski et al. [20] proposed four potential mechanisms for the anomalous increase in nanofluid heat transfer: Brownian motion of nanoparticles, ballistic phonon transport inside nanoparticles, interface layering of liquid molecules, and nanoparticle clustering. Yu and Choi [21] used the assumption that the solid-like nanolayer of liquid molecules would lead to a higher thermal conductivity than that of the bulk liquid and predicted the effective thermal conductivity of nanofluids with a modified Maxwell model. However, the thickness and thermal conductivity of the nanolayer are not known even though liquid molecules close to a solid surface are known to form layer structures [22]. Xuan et al. [23] developed a theoretical model to predict the thermal conductivity of nanofluids taking into account the effect of nanoparticle aggregation due to the collision among suspended Brownian nanoparticles. Recently, Jang and Choi [14] theoretically found that the Brownian motion of nanoparticles at the molecular and nanoscale level is the key mechanism governing the thermal behavior of nanofluids. Kumar et al. [24] presented another dynamic model for heat conduction in nanofluids, using the assumption that the thermal conductivity of nanoparticles is directly proportional to the mean velocity of nanoparticles given by

$$k_p = C \cdot \bar{u}_P \tag{2}$$

where k_p, C, and $\bar{u}_p$ are the thermal conductivity of nanoparticles, constant coefficient, and mean velocity of nanoparticles, respectively. With Eq. (2), they derived the effective thermal conductivity of nanofluids. Koo and Kleinstreuer [25] and Prasher et al. [26] also developed dynamic models based on the idea that Brownian-motion of nanoparticles is important in enhancing the thermal conductivity of nanofluids. Most recently, Evans et al. [27], with the assumptions that the entire volume of the fluid diffuses together with the nanoparticles and that the velocity of the fluid is the same as the velocity of the particles, developed a nanoscale

[1]Corresponding author. Current address: High Efficiency Energy Research Department, Korea Institute of Energy Research, Yuseong-gu, Daejeon, 305-343, Korea. e-mail: suschoi@kier.re.kr

Contributed by the Heat Transfer Division of ASME for publication in the JOURNAL OF HEAT TRANSFER. Manuscript received April 30, 2005; final manuscript received August 2, 2006. Review conducted by Costas Grigoropoulos.

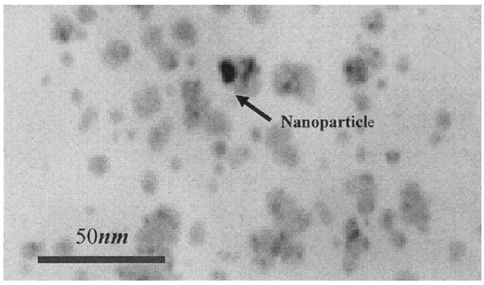

Fig. 1 Bright-field transmission electron micrograph of copper nanoparticles produced by a single-step process into ethylene glycol. Nanofluids containing these small (<10 nm) nanoparticles with little agglomeration can conduct heat one order-of-magnitude faster than scientists had predicted to be possible.

convection model to show that the hydrodynamics effects associated with Brownian motion have only a minor effect on the enhancement of the effective thermal conductivity of the nanofluid. However, the views on how nanoconvection contributes to the enhanced thermal conductivity of nanofluids are quite different among these studies [14,23–27]. This shows that the scientific basis for the mechanisms of enhanced thermal conductivity of nanofluids is not yet completely understood.

Although Jang and Choi were the first to propose the Brownian-motion-induced nanoconvection as a key nanoscale mechanism governing the thermal behavior of nanofluids [14], they did not clearly explain the new ideas used in their model and did not consider the effects of various parameters on the thermal conductivity of nanofluids. Therefore, the objectives of this paper are to explain in detail the new concepts and simplifying assumptions we used in order to develop our model [14] and to investigate the effects of various parameters such as the ratio of the thermal conductivity of nanoparticles to that of a base fluid, volume fraction, nanoparticle size, and temperature on the effective thermal conductivity of nanofluids.

2 Model of Nanofluid Thermal Conductivity

Thermal conduction involves energy transfer from more to less energetic particles of a substance due to interactions between the particles. For example, the energy can be transported by lattice waves in a solid nonconductor and by the translational motion of the free elections in a solid conductor [28]. In the gas and liquid case, net energy is transported by collisions of molecules in random motion as a diffusion of energy [29]. Based on the kinetic theory we can derive the thermal conductivity of gas or liquid as follows. The molecules travel freely only over the mean free path after which they collide [29]. Net flux across a plane at z is given by

$$J_U = [\rho_U(z) - \rho_U(z+l)]\bar{C} = -l\hat{C}_V\bar{C}\frac{dT}{dz} \tag{3}$$

where J_U, $\bar{C}$, $\hat{C}_V$, l, T, and ρ_U are the flux of energy, mean speed of molecules, heat capacity per unit volume, mean free path, temperature, and energy density, respectively. The spatial average of $l\bar{C}$ is $\frac{1}{3}l\bar{C}$ [29]. So, the thermal conductivity is given by

$$k = \tfrac{1}{3}l\bar{C}\hat{C}_V \tag{4}$$

The mean speed of molecules can be calculated by [29]

$$\bar{C} = \int_0^\infty uP(u)du = \left(\frac{8k_bT}{\pi M}\right)^{1/2} \tag{5a}$$

and

$$P(u) = 4\pi\left(\frac{M}{2\pi k_bT}\right)^{3/2} u^2 e^{-Mu^2/2k_bT} \tag{5b}$$

where $k_b = 1.3807 \times 10^{-23}$ J/K is Boltzmann's constant, and M, T, and u are the molecular weight, absolute temperature, and velocity of molecules, respectively.

Based on Eq. (3), we can derive the effective thermal conductivity of nanofluids, including four modes that contribute to the energy transfer.

First Mode: Base Fluid Molecules. The first mode is collision of base fluid molecules with each other, which physically indicates the heat transfer by the thermal conductivity of the base fluid, as given by

$$J_U = -\frac{1}{3}l_{\mathrm{BF}}\hat{C}_{V,\mathrm{BF}}\bar{C}_{\mathrm{BF}}(1-f)\frac{dT}{dZ} = -k_{\mathrm{BF}}(1-f)\frac{dT}{dZ} \tag{6}$$

where f, k_{BF}, and subscript BF are the volume fraction, thermal conductivity of base fluid molecules, and base fluid, respectively.

Second Mode: Nanoparticles. The second mode is thermal diffusion in nanoparticles in fluids which physically indicates the heat transfer by the thermal conductivity of nanoparticles as given by

$$J_U = -\frac{1}{3}l_{\mathrm{nano}}\hat{C}_{V,\mathrm{nano}}\bar{v}f\frac{dT}{dZ} = -k_{\mathrm{nano}}\frac{dT}{dZ}f \tag{7}$$

where k_{nano}, l_{nano}, and $\bar{v}$ are the effective thermal conductivity of a nanoparticle, mean free path of heat carriers in nanoparticles, and mean speed of free electron or lattice wave in nanoparticles, respectively. We consider the effect of size of nanoparticles to calculate their thermal conductivity by using Chen's correlation [15] and the Kapitza resistance [30]. Chen [15] investigated thermal conductivity of a single particle whose size is smaller than the mean free path of the energy carrier and predicted the effective thermal conductivity as

$$k_{\mathrm{particle}} = k_{\mathrm{bulk}}\frac{0.75\dfrac{d_{\mathrm{nano}}}{l_{\mathrm{nano}}}}{0.75\dfrac{d_{\mathrm{nano}}}{l_{\mathrm{nano}}}+1} \tag{8}$$

where k_{particle}, d_{nano}, and k_{bulk} are the thermal conductivity of nanoparticles, characteristic length of nanoparticles, and thermal conductivity of bulk material, respectively. In addition, we consider the Kapitza resistance per unit area [30] which can be calculated as

$$R_k = (\tfrac{1}{4}\hat{C}_V\bar{v}\alpha)^{-1} \tag{9}$$

where R_k and α are the Kapitza resistance per unit area and averaged transmission probability, respectively. The latter is given by

$$\alpha = \frac{4Z_1Z_2}{(Z_1+Z_2)^2} \sim O(10^{-1}) \quad Z = \rho\bar{v} \tag{10}$$

where ρ is the density. By using Eqs. (9) and (10), we estimate the order of R_k as

$$R_K \sim O(10^{-7}) \tag{11}$$

This value of the Kapitza resistance per unit area is very small. However, we need to consider the Kapitza resistance per unit area between nanoparticles and base fluid to determine the effective thermal conductivity of nanoparticles suspended in fluid, because the thermal resistance per unit area of the nanoparticle given by Eq. (12) is smaller than the Kapitza resistance per unit area when the characteristic length of the nanoparticle is at the nanoscale,

$$R_{\mathrm{nanoparticle}} = \frac{d_{\mathrm{nano}}}{k_{\mathrm{particle}}} \tag{12}$$

By using the series model of the thermal resistance,

$$R_K + \frac{d_{\text{nano}}}{k_{\text{particle}}} = \frac{d_{\text{nano}}}{k_{\text{nano}}} \tag{13}$$

we can obtain the effective thermal conductivity of nanoparticles

$$\frac{k_{\text{nano}}}{k_{\text{particle}}} = \frac{d_{\text{nano}}}{d_{\text{nano}} + k_{\text{particle}} R_k} = \beta \sim O(10^{-2}) \tag{14}$$

Based on Eq. (14), Eq. (7) can be expressed as

$$J_U = -\beta k_{\text{particle}} \frac{dT}{dZ} f \quad \beta = 0.01 \tag{15}$$

where β is a constant for considering the Kapitza resistance per unit area. Huxtable et al. have experimentally confirmed the results for interfacial resistance between nanoparticles and base fluid [31].

Third Mode: Collision of Nanoparticles With Each Other. The third mode is the collision of nanoparticles with each other by translational motion due to the Brownian motion with long wavelength. The flux of energy by collision of nanoparticles with each other is given by

$$J_U = -\frac{1}{3} \Lambda_{\text{nano}} \hat{C}_{V,\text{nano}} \bar{C}_T f \frac{dT}{dZ} \tag{16}$$

where $\bar{C}_T$ and Λ_{nano} are the translational speed of a nanoparticle and mean collision length of nanoparticles, respectively. From kinetic theory, the translational speed of a nanoparticle can be calculated by

$$\frac{1}{2} m \bar{C}_T^2 = \frac{3}{2} k_b T \rightarrow \bar{C}_T = \sqrt{\frac{18 k_b T}{\rho \pi d_{\text{nano}}^3}} \tag{17}$$

By the order-of-magnitude analysis of Eq. (17), we have found that the third mode is much smaller than the other modes and is given by

$$\tfrac{1}{3} \Lambda_{\text{nano}} \hat{C}_{V,\text{nano}} \bar{C}_T f \sim O(10^{-5}) \tag{18}$$

Fourth Mode: Nanoconvection. The last mode is the Brownian motion of nanoparticles with short wavelength which results from collisions between base fluid molecules and nanoparticles by thermally induced fluctuations. So, the thermally induced fluctuations would cause a particle suspended in base fluid to vary in direction many millions of times per second [32]. Even though the random motion of nanoparticles by collisions with base fluid molecules is zero if the Brownian motion with short wavelength is averaged by time [33], the thermal interaction between nanoparticles and base fluid molecules is nonzero. Following Bejan's scaling analysis [34], the temperature gradient in the thermal boundary layer $(T_{\text{nano}} - T_{\text{BF}})/\delta_T$ can be simplified as the fluid temperature gradient dT/dZ. This substitution can be justified further because the thickness of the thermal boundary layer is on the order of 1 nm. The assumption of a linear temperature profile in the thermal boundary layer greatly simplifies our model development without negating the idea of convection because both h and δ_T in Eq. (19) maintain the effect of convection. So, the heat flux due to the last mode, called Brownian-motion-induced nanoconvection [14], is defined by

$$J_U = h(T_{\text{nano}} - T_{\text{BF}}) f = h \delta_T f \frac{(T_{\text{nano}} - T_{\text{BF}})}{\delta_T} \sim -h \delta_T f \frac{dT}{dZ} \tag{19}$$

where h and δ_T are the heat transfer coefficient for flow past nanoparticles and thermal boundary layer, respectively.

By using order-of-magnitude analysis, we confirmed that the third mode is much smaller than the other modes [14,20]. So, the third mode can be neglected and the effective thermal conductivity of nanofluids, k_{eff} can be derived from Eqs. (6), (15), (19),

$$k_{\text{eff}} = k_{\text{BF}}(1 - f) + \beta k_{\text{particle}} f + f h \delta_T \tag{20}$$

For a uniform cross flow past a sphere the Nusselt number is given by [35]

$$\text{Nu} = 2.0 + 0.5\ \text{Re}\ \text{Pr} + O(\text{Re}^2\ \text{Pr}^2) \tag{21}$$

Instead of the more conventional situation in which the convective heat transfer from a large sphere takes place in a uniform cross flow and the last term in Eq. (21) is ignored, we assume that Peclet number (Re Pr) dependence would be more prominent in nanofluids. In other words, we assume that, in nanofluids, the last term becomes dominant compared with the first two terms and the heat transfer coefficient is calculated from the correlation of the Nusselt number which can be expressed by

$$\text{Nu} \sim \text{Re}^2\ \text{Pr}^2 \tag{22}$$

A physical explanation for this unconventional choice is based on the physical meaning of the Peclet number and the difference between uniform flow and rapidly fluctuating flow past a sphere. The Peclet number is a measure of eddy scale convection compared to conduction. In nanofluids the Brownian motion causes nanoparticles to rapidly vary in direction [32] and liquid molecules impinge on the nanoparticle surface. Therefore, nanoscale convection from a nanometer-sized particle in a randomly, rapidly fluctuating and impinging flow is more strongly dependent on the eddy scale convection than the more typical situation in a uniform cross flow. It is interesting to note that, when we use the expression $\text{Nu} = \text{Re}^m\ \text{Pr}^n$ in our model and determine the values of m and n by fitting the model to experimental data [7,9,10,36], the values of m and n are nearly identical to 2. However, since no experimental studies have been carried out on the convective heat transfer in a randomly fluctuating flow past a single nanoparticle, it requires challenging, single nanoparticle experiments to confirm this nonconventional Eq. (22).

Based on Eq. (22), the heat transfer coefficient for flow past nanoparticles is defined by

$$h \sim \frac{k_{\text{BF}}}{d_{\text{nano}}} \text{Re}_{d_{\text{nano}}}^2\ \text{Pr}^2 \tag{23}$$

The nanoscale thermal boundary layer, δ_T, is deduced from the physical meaning of the Prandtl number

$$\delta_T \sim \frac{\delta}{\text{Pr}} \tag{24}$$

where δ is the hydrodynamic boundary layer. Generally, the hydrodynamic boundary layer is inversely proportional to the Reynolds number [37]. However, Yu et al. [22] have experimentally shown that liquid molecules close to a solid surface form layer structures. However, little is known about the connection between this nanostructure at the solid liquid interface and the hydrodynamic boundary layer over a moving nanoparticle. It was very challenging to find this connection because the issue of how to relate the new nanostructure to flow structure at the nanoscale is not covered in textbooks or published papers. Therefore we made a simplifying assumption that the hydrodynamic boundary layer is proportional to the thickness of the liquid layer at the surface of a nanoparticle suspended in fluid. This assumption is based on the fact that the boundary layer remains well attached to nanoparticle surface and the velocity in the boundary layer is much lower than outside of the boundary layer and that base fluid molecules remain well fixed at the interface between the solid and fluid and have much lower velocity than that of free molecules in fluid. So, the hydrodynamic boundary layer can be defined as follows:

$$\delta \sim d_{\text{BF}} \tag{25}$$

From Eqs. (20) and (23)–(25), the effective thermal conductivity of nanofluids is defined by

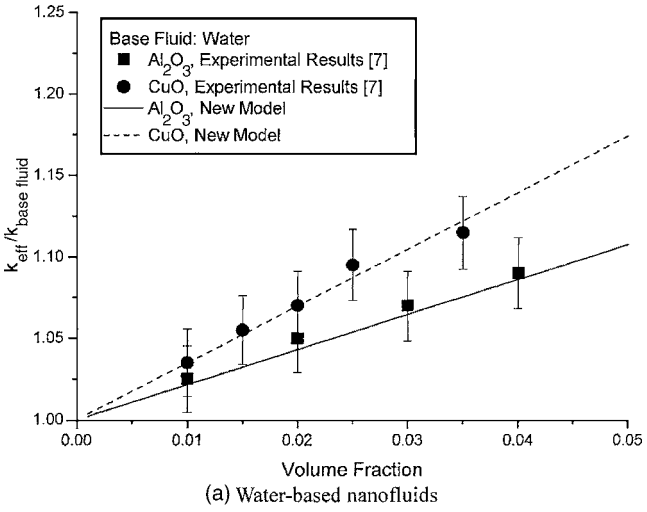

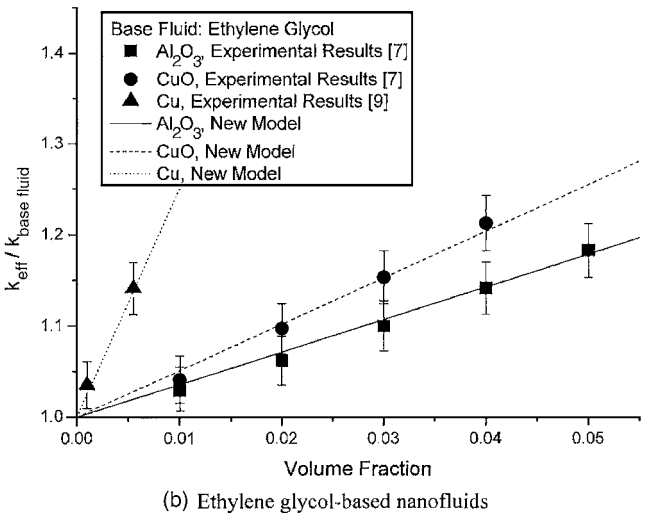

Fig. 2 Experimental data for nanofluids containing oxide and metallic nanoparticles and predictions from Eq. (26): (*a*) water-based nanofluids and (*b*) ethylene glycol-based nanofluids

$$k_{\text{eff}} = k_{\text{BF}}(1-f) + \beta k_{\text{particle}} f + C_1 \frac{d_{\text{BF}}}{d_{\text{nano}}} k_{\text{BF}} \text{Re}_{d_{\text{nano}}}^2 \text{Pr} f \quad (26)$$

where $C_1 = 18 \times 10^6$ is a proportional constant, and the Reynolds number is defined by

$$\text{Re}_{d_{\text{nano}}} = \frac{\bar{C}_{\text{R.M.}} d_{\text{nano}}}{v} \quad (27)$$

where $\bar{C}_{\text{R.M.}}$ and v are the random motion velocity of a nanoparticle and kinematic viscosity of base fluid, respectively.

Nanoparticles, when suspended in a liquid, move about in an irregular, rapid fashion. We are interested in this random, instantaneous velocity of a nanoparticle. To relate the macroscopic diffusion coefficient D_o with this random motion velocity of a nanoparticle $\bar{C}_{\text{R.M.}}$, we assume that a nanoparticle freely moves over a distance of the mean-free path of a base fluid, l_{BF}. $\bar{C}_{\text{R.M.}}$ can thus be defined by

$$\bar{C}_{\text{R.M.}} = \frac{D_0}{l_{\text{BF}}} \quad (28)$$

where D_o is given by Einstein [32] as

Table 1 Material properties of fluids and nanoparticles (T = 300 K)

	Water	Cu	Al_2O_3	CuO	$C_2H_6O_2$(EG)
Conductivity (W/m k)	0.613	401	42.34	18	0.252
Density (m^3/kg) (300 K)	997	8933	3880	6510	1114
Specific heat (J/kg k)	4170	385	729	540	2415
Mean free path (nm)	0.738	42–43	35	27	0.875
Viscosity (N s/m^2)	0.855×10^{-3}				1.57×10^{-2}
Equivalent diameter (nm)	0.384	6–10	24.4	18	0.561

$$D_o = \frac{k_b T}{3\pi\mu d_{\text{nano}}} \quad (29)$$

In this way we get the instantaneous velocity of a nanoparticle on the order of 0.1 m/s. This is consistent with the numerical simulation of Min [33]. However, the random motion velocity of a single nanoparticle should be measured to confirm the fundamental concept that the combination of the diffusion coefficient D_o and the liquid mean free path l_{BF} gives the random motion velocity of a nanoparticle $\bar{C}_{\text{R.M}}$.

3 Validation of a Modified Model

To validate modified model for the effective thermal conductivity of nanofluids, we compared experimental data with predictions obtained from Eq. (26). The experimental results are thermal conductivities of Al_2O_3+water, Al_2O_3+EG (ethylene glycol), CuO +water, CuO+EG, and Cu+EG [7,9]. The experimental results match well with results obtained from our modified model as shown in Fig. 2. The material properties such as the mean free path, heat capacity per unit volume, and the equivalent diameter of a base fluid molecule are summarized in Table 1. The equivalent diameter of a base fluid molecule d_{BF} is calculated from

$$M/n = \frac{4}{3}\pi\left(\frac{d_{\text{BF}}}{2}\right)^3 \rho \quad (30)$$

where M and n are the molecular weight and Avogadro number. The mean free path of a base fluid [29] is calculated by

$$l = \frac{3k_f}{\rho \bar{C} C_v} \quad (31)$$

In nonmetals such as CuO, Al_2O_3 the mean free path of phonon is estimated by the simplest theory due to Debye [38] as given by

$$l = \frac{10aT_m}{\gamma T} \quad (32)$$

where $a \cong 0.5$ is the lattice constant, $\gamma \cong 1$ is the Gruneisen, and T_m is the melting point. In metals such as Cu the mean free path of electron can be obtained by

$$l = v_{\text{av}} \tau \quad (33)$$

where v_{av} is the average speed of the electron and τ is the mean time.

In Fig. 3, we compare model predictions with experimental data for the nanotube-in-oil case [10]. In this case, the geometry of high-aspect-ratio nanotubes is very different from other spherical nanoparticles. As a result, the nanotube suspension in oil does not have Brownian motion because the characteristic length of the

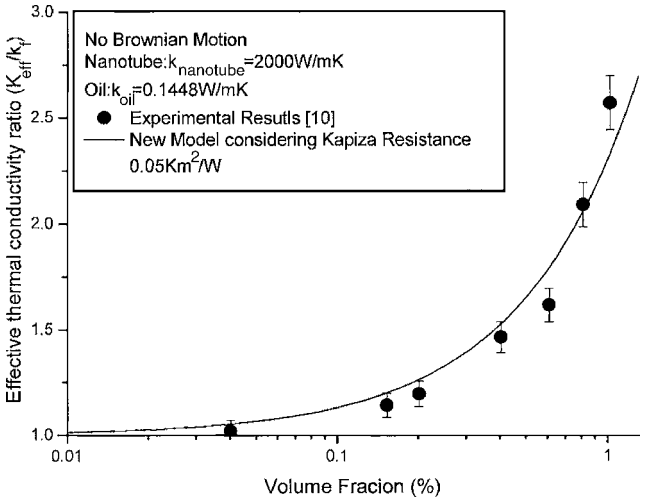

Fig. 3 Experimental data for nanofluids containing carbon nanotubes and predictions from Eq. (26)

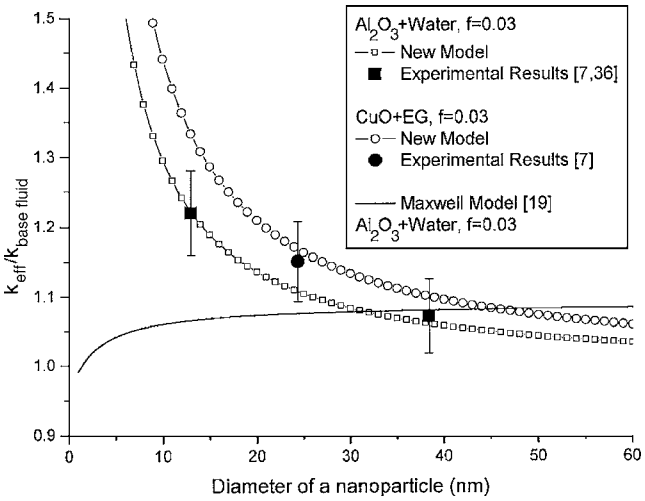

Fig. 5 Effect of diameter of nanoparticle on thermal conductivity of nanofluids

nanotube is near the microscale. Therefore, without the fourth mode we can accurately predict the effective thermal conductivity of the nanotube-in-oil case as shown in Fig. 3.

It should be noted that there are several authors who have made some experimental observations supporting our model. For example, Chon et al. [39], following the previously proposed conjecture from the theoretical point-of-view [14], have experimentally validated that the Brownian motion of nanoparticles constitutes a key mechanism of the thermal conductivity enhancement with increasing temperature and decreasing particle size. Krishnamurthy et al. [40] have visualized dye diffusion in nanofluids and observed an enhancement in the effective mass diffusivity of nanofluids. Because mass transfer and convection are similar processes, their observations lend some support to our model.

4 Effects of Various Parameters on Effective Thermal Conductivity

Ratio of Thermal Conductivity of Nanoparticles to That of Base Fluid. Figure 4 shows the effect of the ratio of the thermal conductivity of nanoparticles to that of the base fluid on the effective thermal conductivity of nanofluids. These results are calculated for $d_{nano}=10$, 20, and 30 nm from the model developed in this paper. As shown in Fig. 4, the thermal conductivity of nanofluids slowly increases with the ratio of the thermal conductivity of nanoparticles to that of the base fluid. We conclude from these results that the thermal conductivity of nanoparticles is not a major factor in the enhancement of the thermal conductivity of nanofluids. This effect is negligible because the second term on the right-hand side of Eq. (26) is very small owning to the Kapitza resistance [30], which is consistent with experimental findings by Huxtable et al. [31].

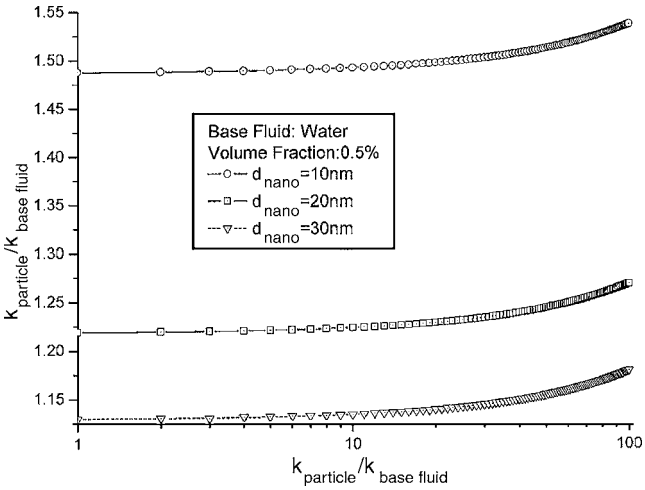

Fig. 4 Effect of ratio of thermal conductivity of nanoparticles to that of base fluid on the thermal conductivity of nanofluids

Volume Fraction. As we discussed and have shown in Fig. 2, the effective thermal conductivity of nanofluids increases with the volume fraction of nanoparticles. However, as the volume fraction is increased, the assumption that nanoparticles are suspended in base fluid becomes invalid. Therefore, the new thermal phenomena of nanofluids are only observed in a low volume fraction range [7,9,11,12].

Nanoparticle Size. Figure 5 shows the nanoparticle size dependency of the nanofluid conductivity. There has not yet been a systematic experimental investigation of this effect. However, the few available data [7,36] fall on the predicted curves. Figure 5 shows that, as the nanoparticle diameter is reduced, the effective thermal conductivity of nanofluids becomes larger. This size-dependent conductivity cannot be explained by previous models such as the Maxwell model [19] and modified approaches [16–18]. However, our model predicts the new phenomenon, as shown in Fig. 5. As the particle size decreases, the Brownian motion of nanoparticles is greater and then nanoconvection becomes dominant. As a result, the effective thermal conductivity of nanofluids becomes larger. However, when the Maxwell model [19] is used to calculate the thermal conductivity of nanofluids and the size effect on nanoparticle thermal conductivity is taken into account by the Chen correlation [15], the thermal conductivity of nanofluids decreases with decreasing nanoparticle size as shown in Fig. 5. Therefore, the Maxwell model, which does not take into account Brownian motion of nanoparticles, cannot predict the effective thermal conductivity of nanofluids at all. Figure 6 shows the effective thermal conductivity of nanofluids as a function of particle diameter when the volume fraction of Cu in EG is 0.5%, 1%, and 3%. Smaller nanoparticles (<5 nm) can significantly enhance the thermal conductivity of nanofluids. However, if the particles approach to micrometer size, they do not remain suspended in the base fluid. Thus, large microparticles do not have Brownian motion any more, and there is no enhancement of the effective thermal conductivity by nanoconvection.

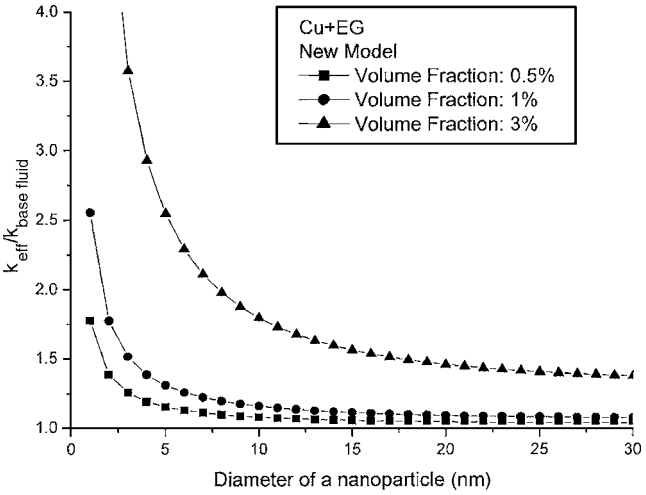

Fig. 6 Effect of diameter of nanoparticle on thermal conductivity of ethylene glycol-based nanofluids containing copper

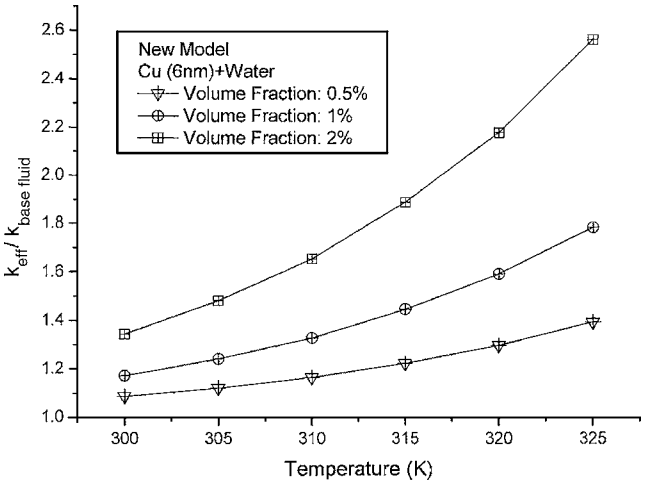

Fig. 8 Temperature versus thermal conductivity enhancement predicted by Eq. (26) for water-based nanofluids containing 6 nm copper

Temperature. The effect of temperature on the effective thermal conductivity of nanofluids is shown in Fig. 7. Recently, Das et al. [12] experimentally discovered that the thermal conductivity of nanofluids increases with temperature by up to fourfold over a small temperature range (20–50°C). This phenomenon cannot be explained by classical models such as the Maxwell model [19] as shown in Fig. 7. However, our model calculations show good agreement with experimental data, as also shown in Fig. 7. The thermal effect is due to the fact that as temperature is increased, the dynamic viscosity of a base fluid is decreased, and the Brownian motion of the nanoparticles is increased. Because of these two effects, the nanoconvection term is remarkably increased with temperature. Therefore, the effective thermal conductivity of nanofluids dramatically increases with temperature.

Using the present model we calculated the effective thermal conductivity of nanofluids with 6 nm Cu nanoparticles dispersed in water, which is 20 times more viscous than the water used by Das et al. [12]. Figure 8 shows that the thermal conductivity is enhanced nearly two times that of a base fluid in water-based nanofluids containing 2 vol % of 6 nm Cu at 320 K.

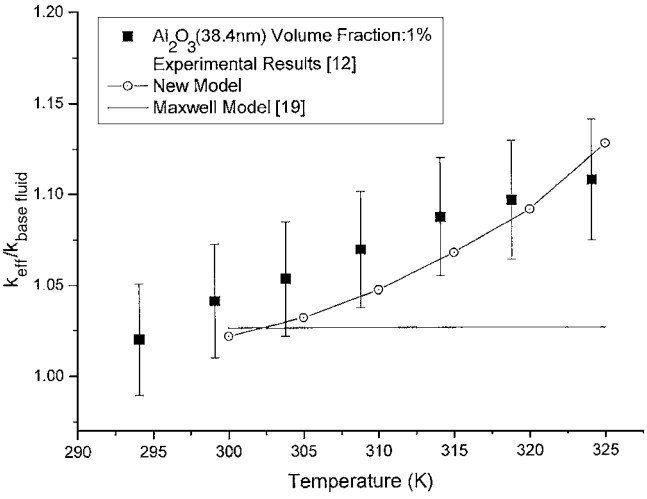

Fig. 7 Experimental data for temperature-dependent conductivity of and predictions from Eq. (26) and the Maxwell model

5 Conclusion

The recently discovered thermal phenomena of nanofluids have been experimentally reported in many investigations. For example, nanofluids have anomalously high thermal conductivities at very low volume fraction and strongly temperature- and size-dependent conductivity. Traditional conductivity theories such as the Maxwell or other macroscale approaches cannot explain why nanofluids have these intriguing features. Recently, Jang and Choi proposed and modeled for the first time the Brownian-motion-induced nanoconvection as a key nanoscale mechanism governing the thermal behavior of nanofluids, but did not explain clearly this and other new concepts used in the model and did not consider the effects of various parameters on the thermal conductivity of nanofluids. Realizing the complexity of the problems related to modeling the Brownian-motion-induced nanoconvection, we started developing a dynamic model with new concepts for submodels and used several simplifying assumptions. In this paper we explained in detail the new concepts and simplifying assumptions. The experimental data for nanofluids containing oxide and metallic nanoparticles and carbon nanotubes were compared with the predictions from this theoretical conductivity model, and a good agreement was found for all three kinds of nanofluids. Model calculations also showed that the volume fraction, temperature, and nanoparticle size have major effects on the nanofluids conductivity. However, the effect of the ratio of the thermal conductivity of nanoparticles to that of the base fluid is minor. With a better understanding of the role of these parameters provided by this new model, it will be possible to design and engineer nanotechnology-based coolants with widespread industrial and biomedical applications in high-heat-flux cooling. Finally, it should be noted that nanofluids are still an emerging field and present a wealth of opportunities and challenges for thermal scientists. For example, new concepts should be confirmed experimentally and more realistic submodels should be developed in the future.

Acknowledgment

This work was supported by the U.S. Department of Energy, Office of Basic Energy Sciences and Office of FreedomCar and Vehicle Technologies, under Contract No. W-31-109-Eng-38, and by the Korean Electric Power Research Institute (KEPRI).

Nomenclature

$\bar{C}$ = mean speed (m/s)

$\bar{C}_{R,M}$ = random motion velocity of nanoparticle (m/s)
$\bar{C}_T$ = translation speed of nanoparticle (m/s)
$\hat{C}_V$ = heat capacity per unit volume (J/m^3 K)
d = equivalent diameter (m)
D_o = Einstein diffusion coefficient (m^2/s)
D_C = characteristic length (m)
f = volume fraction
h = heat transfer coefficient (W/m^2 K)
J_U = heat flux (W/m^2)
k = thermal conductivity (W/mK)
k_b = Boltzmann constant (J/K)
l = mean free path (m)
M = molecular weight (kg)
M_{nano} = weight of nanoparticle (kg)
M_{BF} = molecular weight of base fluid
n = number of base fluid molecules which form three layers on a nanoparticle
Nu = Nusselt number
R_k = Kaptiza resistance per unit area ($K/W/m^2$)
T = temperature (K)
u = velocity of molecules (m/s)
$\bar{\nu}$ = mean speed of free electron or lattice wave

Greek Symbols

α = averaged transmission probability
δ = hydrodynamic boundary layer (m)
δ_T = thermal boundary layer (m)
Λ_{nano} = mean collision length of a nanoparticle (m)
λ = number of layer of liquid molecules on a nanoparticle
ρ = density (kg/m^3)
ρ_U = energy density (J/m^3)

Subscripts

BF = base fluid
eff = nanofluids
f = fluid
nano = nanoparticle with the Kapitza resistance
particle = nanoparticle without the Kapitza resistance

References

[1] Bar-Cohen, A., and Jelinek, M., 1986, "Optimum Arrays of Longitudinal, Rectangular Fins in Convective Heat Transfer," Heat Transfer Eng., **6**, pp. 596–601.
[2] Knight, R. W., Hall, D. J., Gooding, J. S., and Jaeger, R. C., 1992, "Heat Sink Optimization With Application to Microchannels," IEEE Trans. Compon., Hybrids, Manuf. Technol., **15**, pp. 832–842.
[3] Wirtz, R. A., Chen, W., and Zhou, R., 1994, "Effect of Flow Bypass on the Performance of Longitudinal Fin Heat Sinks," ASME J. Electron. Packag., **116**, pp. 206–211.
[4] Tuckerman, D. B., and Pease, R. F. W., 1981, "High-Performance Heat Sinking for VLSI," IEEE Electron Device Lett., **2**, pp. 126–129.
[5] Min, J. Y., Jang, S. P., and Kim, S. J., 2004, "Effect of Tip Clearance on the Cooling Performance of a Microchannel Heat Sink," Int. J. Heat Mass Transfer, **45**, pp. 2823–2327.
[6] Jang, S. P., Kim, S. J., and Paik, K. W., 2003, "Experimental Investigation of Thermal Characteristics for a Microchannel Heat Sink Subject to an Impinging Jet, Using a Micro-thermal Sensor Array," Sens. Actuators, A, **A105**, pp. 211–224.
[7] Lee, S., Choi, S. U. S., Li, S., and Eastman, J. A., 1999, "Measuring Thermal Conductivity of Fluids Containing Oxide Nanoparticles," ASME J. Heat Transfer, **121**, pp. 280–289.
[8] Xuan, Y., and Li, Q., 2000, "Heat Transfer Enhancement of Nanofluids," Int. J. Heat Fluid Flow, **21**, pp. 58–64.
[9] Eastman, J. A., Choi, S. U. S., Li, S., Yu, W., and Thompson, L. J., 2001, "Anomalously Increased Effective Thermal Conductivity of Ethylene Glycol-Based Nanofluids Containing Copper Nanoparticles," Appl. Phys. Lett., **78**, pp. 718–720.
[10] Choi, S. U. S., Zhang, Z. G., Yu, W., Lockwood, F. E., and Grulke, E. A., 2001, "Anomalous Thermal Conductivity Enhancement in Nanotube Suspensions," Appl. Phys. Lett., **79**, pp. 2252–2254.
[11] Patel, H. E., Das, S. K., Sundararajan, T., Nair, A. S., George, B., and Pradeep, T., 2003, "Thermal Conductivities of Naked and Monolayer Protected Metal Nanoparticle Base Nanofluids: Manifestation of Anomalous Enhancement and Chemical Effects," Appl. Phys. Lett., **83**, pp. 2931–2933.
[12] Das, S. K., Putra, N., Thiesen, P., and Roetzel, W., 2003, "Temperature Dependence of Thermal Conductivity Enhancement for Nanofluids," ASME J. Heat Transfer, **125**, pp. 567–574.
[13] Xie, H., Lee, H., Youn, W., and Choi, M., 2003, "Nanofluids Containing Multiwalled Carbon Nanotubes and Their Enhanced Thermal Conductivities," J. Appl. Phys., **94**, pp. 4967–4971.
[14] Jang, S. P., and Choi, S. U. S., 2004, "Role of Brownian Motion in the Enhanced Thermal Conductivity of Nanofluids," Appl. Phys. Lett., **84**, pp. 4316–4318.
[15] Chen, G., 1996, "Nonlocal and Nonequilibrium Heat Conduction in the Vicinity of Nanoparticles," ASME J. Heat Transfer, **118**, pp. 539–545.
[16] Hamilton, R. L., and Crosser, O. K., 1962, "Thermal Conductivity of Heterogeneous Two-component Systems," Indust. & Eng. Chem., **1**, pp. 187–191.
[17] Cheng, S. C., and Vachon, R. I., 1969, "The Prediction of the Thermal Conductivity of Two and Three Phase Solid Heterogeneous Mixtures," Int. J. Heat Mass Transfer, **12**, pp. 249–264.
[18] Jeffrey, D. J., 1973, "Conduction Through a Random Suspension of Spheres," Proc. R. Soc. London, Ser. A, **335**, pp. 355–367.
[19] Maxwell, J. C., 1873, *Electricity and Magnetism*, Clarendon, Oxford, UK.
[20] Keblinski, P., Phillpot, S. R., Choi, S. U. S., and Eastman, J. A., 2002, "Mechanism of Heat Flow in Suspension of Nano-Sized Particles (Nanofluids)," Int. J. Heat Mass Transfer, **45**, pp. 855–863.
[21] Yu, W., and Choi, S. U. S., 2003, "The Role of Interfacial Layers in the Enhancement Thermal Conductivity of Nanofluids: A Renovated Maxwell Model," J. Nanopart. Res., **5**, pp. 167–171.
[22] Yu, C.-J., Richter, A. G., Datta, A., Durbin, M. K., and Dutta, P., 1999, "Observation of Molecular Layering in Thin Liquid Films Using X-Ray Reflectivity," Phys. Rev. Lett., **82**, pp. 2326–2329.
[23] Xuan, Y., Li, Q., and Hu, W., 2003, "Aggregation Structure and Thermal Conductivity of Nanofluids," AIChE J., **49**, pp. 1038–1043.
[24] Kumar, D. H., Patel, H. E., Rajeev Kumar, V. R., Sundararajan, T., Pradeep, T., and Das, S. K., 2004, "Model for Heat Conduction in Nanofluids," Phys. Rev. Lett., **93**, p. 144301-1-4.
[25] Koo, J., and Kleinstreuer, C., 2004, "A New Thermal Conductivity Model for Nanofluids," J. Nanopart. Res., **6**, pp. 577–588.
[26] Prasher, R. S., Bhattacharya, P., and Phelan, P. E., 2005, "Thermal Conductivity of Nanoscale Colloidal Solution," Phys. Rev. Lett., **94**, pp. 025901-1-4.
[27] Evans, W., Fish, J., and Keblinski, P., 2006, "Role of Brownian Motion Hydrodynamics on Nanofluid Thermal Conductivity," Appl. Phys. Lett., **88**, 093116-1-3.
[28] Incropera, F. P., and Dewitt, D. P., 1996, *Fundamentals of Heat and Mass Transfer*, 4th ed., Wiley, New York.
[29] Kittel, C., and Kroemer, H., 1980, *Thermal Physics*, 2nd ed., W.H. Freeman and Company, San Francisco.
[30] Kapitza, P. L., 1941, "The Study of Heat Transfer in Helium II," J. Phys. (Moscow), **4**, p. 181-210.
[31] Huxtable, S. T., et al., 2003, "Interfacial Heat Flow in Carbon Nanotube Suspensions," Nat. Mater., **2**, pp. 731–734.
[32] Einstein, A., 1956, *Investigation on the Theory of Brownian Movement*, Dover, New York.
[33] Min, J. Y., Jang, S. P., and Choi, S. U. S., "Motion of Nanoparticles in Nanofluids under an Electric Field," in *Proceedings of IMECE 2005, 2005 ASME International Mechanical Engineering Congress and Exhibition*, Orlando, Florida, November 5–11, 2005, Paper No. IMECE2005-80139.
[34] Bejan, A., 1995, *Convective Heat Transfer*, 2nd ed., Chap. 2, Wiley, Hoboken, Chap. 2.
[35] Tomitika, S., Aoi, T., and Yosinabu, H., 1953, "On the Force Acting on a Circular Cylinder Set Obliquely in a Uniform Stream at Lower Values of Reynolds Number," Proc. R. Soc. London, Ser. A, **219**, pp. 233–244.
[36] Masuda, H., Ebata, A., Teramae, K., and Hishinuma, N., 1993, "Alternation of Thermal Conductivity and Viscosity of Liquid by Dispersing Ultra-Fine Particles," Netsu Bussei, **4**, pp. 227–233.
[37] Schlichting, H., 1979, *Boundary Layer Theory*, 7th ed., McGraw-Hill, New York.
[38] Geiger, G. H., and Poirier, D. R., 1973, *Transport Phenomena in Metallurgy*, Addision-Wesley, Reading, PA.
[39] Chon, C. H., Kihm, K. D., Lee, S. P., and Choi, S. U. S., 2005, "Empirical Correlation Finding the Role of Temperature and Particle Size for Nanofluid (Al2O3) Thermal Conductivity Enhancement," Appl. Phys. Lett., **87**, p. 153107-1-3.
[40] Krishnamurthy, S., Bhattacharya, P., and Phelan, P. E., 2006, "Enhanced Mass Transport in Nanofluids," Nano Lett., **6**, pp. 419–423.

Radiative Properties of MoO_3 and Al Nanopowders From Light-Scattering Measurements

S. M. Begley

M. Q. Brewster[1]
e-mail: Brewster@uiuc.edu

Mechanical Science and Engineering Department,
University of Illinois at Urbana-Champaign,
Urbana, IL 61801

The combustion behavior of nanometer-scale energetic materials is much different than micron size or larger materials. Burning rates up to 950 m/s have been reported for a thermite composition of nanosized aluminum and molybdenum trioxide. The energy transport mechanisms in the reactive wave are still uncertain. The relative contribution of radiation has not yet been quantified. To do so analytically requires dependent scattering theory, which has not yet been fully developed. Radiative properties for nanoaluminum and nanomolybdenum-trioxide were obtained experimentally by comparing light scattering measurements on a one-dimensional slab of powder with multiple-scattering simulations using Monte Carlo and discrete ordinate methods. The equivalent isotropic-scattering extinction coefficient for close-packed molybdenum trioxide (MoO_3) nanopowder was found to be $5900 \pm 450\ cm^{-1}$; the equivalent isotropic-scattering albedo was 0.97 ± 0.035. Aluminum (Al), which proved to be more difficult to work with, had an albedo of 0.35 and 0.38 from two tests. The radiative conductivity based on the MoO_3 results is two orders of magnitude less than the diffusive thermal conductivity, indicating that radiation is not a dominant heat transfer mode for the reactive wave propagation of nanothermites under optically thick conditions. [DOI: 10.1115/1.2712476]

Keywords: radiation, multiple scattering, nanothermite, metastable-intermolecular-composite, nanoaluminum, molybdenum-trioxide, reactive-wave propagation

1 Introduction

Nanoenergetic materials show great promise in a variety of applications due to their reaction properties differing significantly from those of conventional (micron or larger sized) energetic materials. Nanothermites have drawn interest due to their reaction rates, nontoxic components, and large heat release. These materials generally consist of a metal and a metal-oxide on submicron particle-size scale and have also been called metastable intermolecular composites (MIC). Thermite reactions have the ability to release a large amount of thermal energy with minimal gas generation and have often been used as heat sources for tasks in remote locations [1]. Conventional reactions with micron-sized particles are capable of producing temperatures in excess of 3000°C due to the high reaction enthalpy (–4.69 kJ/g for Al/MoO_3, 12% higher than TNT [2]), but at a slow (5 cm/s) [3] reaction-wave propagation rate. A renewed interest in thermites developed recently after a nanoparticle formulation study led to reaction-wave propagation speeds in excess of 950 m/s [4]. At these reaction rates they can serve as replacements and improvements in many applications that require a high heat-release and reduced gas-generation from a reliable source and at the same time avoid toxic reactants and products [4].

To be most useful and adaptable for the widest variety of applications the reaction rates and properties must be predictable and controllable. However, nanomaterials have a combustion behavior that is quite different from that of bulk materials and the dependence of reactive wave speed on particle size and packing densities does not necessarily correspond to intuitive expectations. This suggests that previously neglected mechanisms such as radiation could play a significant role in the reactive wave propagation. Little is known about this radiative mechanism in nanoenergetic materials since the behavior falls into the category of radiative transfer theory known as dependent scattering. This area is difficult to describe because it includes the effects of close particle packing (shadowing and multiple scattering within neighboring particles) and electromagnetic wave interference from neighboring particles. Work has been done in the independent scattering regime with aluminum and boron particles in a surrounding dielectric oxidizer. These studies have found absorptive cross sections in optically thin tests [5]. However, in order to reliably tailor the reaction rates of loosely packed nanoenergetic materials, similar studies in the dependent optically thick regime must be conducted.

This paper explores the radiative and optical properties of two nanoenergetic materials, molybdenum trioxide (MoO_3) and aluminum (Al). The overall objective of this research is to investigate the reactive wave propagation mechanisms in nanoenergetic materials by determining the relative importance of radiative and conductive energy transport. It is of interest to be able to estimate the radiative contribution to the energy transfer rate during propagation and compare it to other modes, i.e., conduction and gas permeation or convection. Since theoretical descriptions of the dependent scattering regime of radiative transfer are still largely unproven and incomplete, an experimental approach must be taken to characterize the effect of radiation in nanosized materials.

The approach taken here is to make experimental measurements of visible light scattering from test cells of nanoenergetic materials; specifically, directly transmitted laser flux and bidirectional transmission and reflection as a function of polar angle are obtained for 1D slabs of powder confined in or deposited on glass slides. The desired optical properties of the system, the equivalent isotropic extinction coefficient and albedo, are obtained by comparison of measured profiles using the configuration shown in Fig. 1 with computational simulations of systems considered representative of the sample.

[1]Corresponding author.

Contributed by the Heat Transfer Division of ASME for publication in the JOURNAL OF HEAT TRANSFER. Manuscript received June 15, 2005; final manuscript received June 28, 2006. Review conducted by Costas Grigoropoulos.

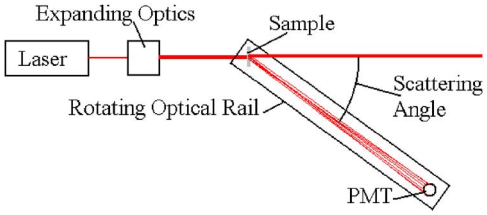

Fig. 1 Overview of experimental setup

2 Light Scattering Measurements

2.1 1D Approximation. In a fully 3D light scattering medium, intensity varies with three spatial coordinates (x,y,z) as well as two directions (θ,ϕ). In an effort to eliminate multidimensional effects and focus on determining unknown optical properties a one-dimensional approximation is employed. This is done by using a system designed to approach a 1D plane-parallel slab subject to a normally incident, infinite plane wave (Figs. 1 and 2). With this configuration, intensity variations occur only in the direction normal to the slab (in the direction of the incident wave propagation). Having chosen this as an ideal system it must be recognized that there are challenges with achieving it in practice. In particular, it is difficult to consistently isolate the intensity emerging from a specific small area of the fully illuminated sample while varying the polar angle of detection. To overcome this difficulty, a reciprocal method can be used in which the incident beam is restricted to a small, finite diameter and the detector views a substantially larger area. In this case the incident beam has a small cross-sectional area defined by an iris and the detection area is arbitrarily large. The same symmetries exist as long as the incident beam is located roughly in the center of the area viewed by the detector.

2.2 Experimental Bidirectional Properties. To describe the directional dependence of scattered energy the spectral bidirectional transmissivity, τ'', and reflectivity, ρ'', are used. These functions are defined by Eq. (1) for wavelength, λ, polar angles, $\theta_{i,r,t}$, azimuthal angles, $\phi_{i,r,t}$, and path length L [6]. The subscripts i, r, and t represent incident, reflected, and transmitted intensities, respectively,

$$\tau''_{\lambda},\rho''_{\lambda}(\lambda,\theta_i,\phi_i,\theta_{t,r},\phi_{t,r},L)=\frac{\pi I_{\lambda_{t,r}}(\theta_{t,r},\phi_{t,r},\lambda)}{\Delta q^{-}_{\lambda}} \tag{1}$$

In the experimental setup the 1D approximation noted above was incorporated (no ϕ-dependence) and all experiments were conducted at room temperature. These simplifications result in

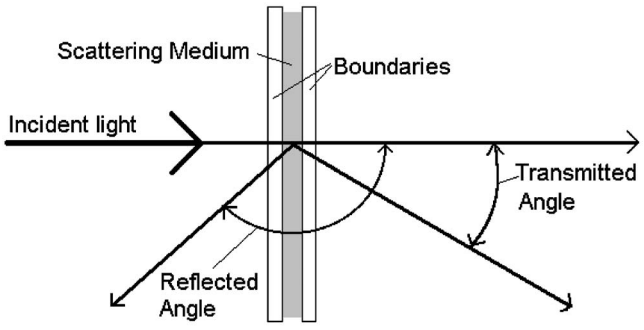

Fig. 2 Sample position and angle measurement

$$\tau''_{\lambda},\rho''_{\lambda}(\lambda,\theta_{t,r},L)=\frac{\pi I_{\lambda_{t,r}}(\theta_{t,r},\lambda)}{\Delta q^{-}_{\lambda}} \tag{2}$$

With normal incidence, the bidirectional transmissivity applies for scattering polar angles between $0\leqslant\theta_t<90$ deg while the reflectivity applies over 90 deg$\leqslant\theta_r<180$ deg (see Figs. 1 and 2). The spectral partial (collimated) incident flux, Δq^{-}_{λ}, is found by taking the power of the incident beam detected by the photomultiplier tube (PMT), Q, and dividing by its area, A_b and the transmitted/reflected intensity, $I_{\lambda_{t,r}}(\theta_{t,r})$, is found using the power measured by the PMT for each angle, the sample area perpendicular to the line of sight, $A_{\perp}$, and the solid angle subtended by detector area viewed from the sample

$$I_{\lambda_{t,r}}(\theta)=\frac{Q(\theta)}{A_{\perp}\Omega_d} \tag{3}$$

2.3 Radiative Parameters. The interaction of light with assemblies of particles can be characterized by several parameters. The scattering and extinction efficiencies, Q_s and Q_e, relate the scattering and extinction cross sections to the geometric projected area of a particle. Their ratio, Q_s/Q_e, is referred to as the single-scattering albedo, ω_0 which gives the fraction of light that upon interaction with a particle is scattered as opposed to absorbed. The volumetric extinction coefficient describes the strength of extinction (=absorption+scattering) within a small elemental volume containing multiple particles. For the case of an assembly of identical, independent, monosized spherical particles the extinction coefficient is

$$K_e=\frac{1.5Q_ef_v}{d(1-f_v)} \tag{4}$$

where the particle volume fraction is f_v, and the particle diameter is d [7].

2.4 Optical Depth. When light encounters a scattering slab of thickness L the light will either be scattered, absorbed, or unaffected. Light that passes through the unaffected medium is referred to as direct transmission. In a slab that is bounded on one or two sides the interfaces will have reflectivities R_{12} and R_{23}. Light passing through the entire system can be referred to as the direct transmission of the system, τ_{system}. When the interface reflectivities at both the front and back surfaces, R_{12} and R_{23}, are considered the relationship between the system transmission and the slab transmission, τ_{slab}, is found to be

$$\tau_{\text{system}}=\frac{q_{\theta=0,t=t_L}}{q_{\text{incident}}}=\frac{(1-R_{12})(1-R_{23})\tau_{\text{slab}}}{1-\tau_{\text{slab}}{}^2R_{12}R_{23}} \tag{5}$$

for normal incidence. This equation can be rearranged to get the slab transmission of the sample in a simple form when the quantity $\tau_{\text{slab}}{}^2R_{12}R_{23}$ is much smaller than one as it is in many cases of interest

$$\tau_{\text{slab}}=\frac{\tau_{\text{system}}}{(1-R_{12})(1-R_{23})} \tag{6}$$

This slab transmission can be readily determined from the measured system transmissivity and theoretical Fresnel interface reflectivities and used to determine the optical depth (OD) of the sample from the following relations:

$$\tau_{\text{slab}}=\frac{I_{\theta=0,x=L}}{I_{\text{incident}}}=e^{-\text{OD}} \tag{7}$$

or

$$\mathrm{OD} = \ln\left(\frac{I_{\theta=0,x=L}}{I_{\text{incident}}}\right) = \ln(\tau_{\text{slab}}) \tag{8}$$

in which emission and in-scattering are neglected. When the extinction coefficient is constant throughout the medium the optical depth can be related to the extinction coefficient.

$$\mathrm{OD} = K_e L \tag{9}$$

The optical depth of a sample can also be obtained semi-theoretically if the scattering particles are characterized well enough that the extinction efficiency, Q_e, is known along with particle size and concentration information. Equations (4) and (9) can be combined to give

$$\mathrm{OD} = \frac{1.5 f_v Q_e}{d(1-f_v)} L \tag{10}$$

which allows the OD to be calculated from the properties of the particles if they are known.

2.5 Experimental Setup. Figures 1 and 2 show diagrams for the equipment used in the experimental scattering measurements. The light source is a 7 mW unpolarized helium-neon laser that produces light at 632.8 nm with a beam diameter of 0.81 mm. The beam is expanded and reduced in intensity by beam expanders and neutral density filters to obtain a uniform beam with a suitable power level. The detector is a Hamamatsu R2949 Photomultiplier Tube (PMT) mounted on an optical rail that pivots around the scattering test cell maintaining the intersection of the beam and the sample in the center of the detector's view. The rail is able to rotate and take measurements spanning 0 deg–135 deg from the forward direction.

Ideally every photon strike on the active area of the cathode produces the same amount of current leaving the anode; therefore, the time averaged voltage, V, across a resistor is proportional to the average power, Q, striking the detector over the measured time period

$$V = CQ \tag{11}$$

All power measurements are used in calculations relative to other (reference) power measurements. Because of this the constant C is not needed and is given the value of one so that Q and V can be used interchangeably as relative measurements.

Any analysis of experimental data depends on the measurements satisfying the approximations and assumptions made in the analysis. Here those assumptions include the slab being uniform and of constant thickness over an area significantly larger than the cross section of the incident laser beam to insure that the 1D geometry assumption is satisfied. Also the sample must be positioned so that the slab and glass substrates are perpendicular to the incident beam of light and the axis of rotation of the optical rail passes through the center of the sample.

Within the 1D approximation the bidirectional scattering properties are obtained from the PMT detector signal as follows. The incident beam is used as a reference signal. This beam and the directly transmitted, unscattered beam are both collimated and have an area defined by an iris. These collimated beams interact with the PMT to produce a voltage. This signal, generated from a narrow, collimated beam, is different from that of the scattered measurements where approximately uniform illumination occurs over the entire detector area similar to that from a diffuse source. The PMT detector's sensitivity is not spatially uniform, which requires a correction factor, C_f, to be employed when comparing the measured power of scattered (diffuse) and collimated light. Reduction of Eq. (2) leads to the following equation for the experimentally measured bidirectional properties.

$$\rho''_\lambda, \tau''_\lambda(\theta) = \frac{\pi I_\lambda(\theta)}{\Delta q^-_\lambda} = \frac{\pi V(\theta) C_f}{V_{\text{inci}} A/S^2 |\cos(\theta)|} \tag{12}$$

The voltages measured for the incident beam, V_{inci}, and at each angle, $V(\theta)$, are used to determine the bidirectional properties along with the area of the detector A and the length from the sample to the detector S. The area in the intensity term is modified by the absolute value of the cosine of the polar angle to obtain the scattering area perpendicular to the detector line of sight.

3 Sample Properties and Preparations

3.1 Latex Suspension. The experimental apparatus was calibrated with a reference suspension of polystyrene latex particles with known optical properties and size. The calibration medium was polystyrene nanospheres made by Duke Scientific. Latex spheres are often used for calibration due to their high degree of sphericity and well characterized optical constants (i.e., applicability of Mie theory). The Duke 5022 particles have a reported mean diameter of 222 nm with a size variation of less than 3% [8]. The optical constants for polystyrene can be given in the form of a Cauchy dispersion relation [9] with values at 632.8 nm of $n=1.58$, $k=5\text{e-}4$ [10].

When independent Mie scattering theory (BHMIE code [15]) is applied at 632.8 nm to the homogeneous 222-nm spherical particles dispersed in water ($n=1.33$) the result is an extinction efficiency of 0.0979 and an albedo of 0.983. This indicates the extinction cross section of these particles at this wavelength is an order of magnitude smaller than their physical cross section and that an individual particle scatters about two orders of magnitude more energy than it absorbs. However, while an albedo of 0.983 seems to be very close to one (pure scattering), in multiple scattering situations it indicates a relatively large amount of absorption for particles that are generally believed to be nonabsorbing. The single-scattering phase function was also calculated, thus allowing the scattering of light by the latex suspension to be modeled computationally for the purpose of calibration.

3.2 Aluminum. The optical properties of Al have been studied extensively and are generally well characterized [6]. Bulk aluminum exhibits classical metallic behavior, dominated by free electrons with bound electron influence exhibited in the near infrared around 800 nm. At a wavelength of 632.8 nm (HeNe laser) optical constants are $n=1.4$ and $k=7.6$. Substituting these values in the Fresnel relation, Eq. (14), and Beer's law, Eq. (13), shows that bulk aluminum is very opaque (mean free photon path, mfp ~ 7 nm)

$$\frac{I(x)}{I(0)} = \exp\left[-\frac{4\pi k x}{\lambda_0}\right]$$

$$\mathrm{mfp} = \frac{\lambda_0}{4\pi k} \tag{13}$$

$$R_n = \frac{(n_2 - n_{\text{surr}})^2 + k_2^2}{(n_2 + n_{\text{surr}})^2 + k_2^2} \tag{14}$$

and very reflective ($R_n=0.91$).

Nanosized aluminum particles have been characterized in the literature with respect to their oxide coating thickness, thermodynamic properties, and size distribution [2,11–13]. Visually the powder appears to be fine with a dark gray appearance indicating more absorption than the bulk properties would suggest. The nominal particle size of powders used here has been reported by the manufacturer to be 34 nm with a narrow size distribution. This includes a crystalline core of aluminum and the aluminum oxide shell that passivates the aluminum with respect to oxygen in the environment. Using SEM and SANS typical oxide shells have been determined to be between 2 and 3 nm thick [14].

The observation of a gray appearance of the nano-Al is consis-

tent with independent particle scattering theory, which shows the possibility that in finely divided particulate form normally shiny particles can exhibit strong absorption characteristics and take on even a black appearance. Based on Mie calculations, a solid Al spherical particle with a diameter of 34 nm and the optical constants given above has an extinction efficiency of 0.0263 and an albedo of 0.094, indicating strong absorption and a dark gray or black appearance. It is important to remember that a passivating oxide layer coats these particles. When this layer is included in the single-scattering calculations for a coated sphere [15], it slightly reduces the extinction efficiency to 0.0191 and the albedo to 0.0925. However, Mie theory results are probably not quantitatively applicable to most nanopowders. This is because close packing of particles and dependent scattering due to the high volume fraction can have significant effects.

3.3 MoO_3. The optical constants of MoO_3 have not been as widely reported as those of Al [16,17]. Molybdenum trioxide, a transition metal oxide, falls in a category that could be termed optically either a weak semiconductor or a lossy dielectric, depending on its structure. Its optical properties have attracted some interest recently because of its chromogenic or electrochromic property—the ability to be switched between optical states, which might be of use for displays. In the visible and near infrared region the refractive index is reported with fair uniformity to range from 1.8 to 2.25 [16–18]. The absorption index, as is usually the case, shows more variability in reported values, mostly due to differences in samples through preparation but also through differences in the technique used. In [16] films of MoO_3 prepared by thermal evaporation are reported as being "nearly transparent" above 450 nm. For wavelengths below 400 nm the absorption index varies from 0.01 to about 0.3 at 300 nm. In the visible/near infrared region between 400 and 800 nm the absorption index is not reported but the implication is given that its value is below 0.01. Oscillations (i.e., apparent absorption peaks) observed in the transmission spectrum in the 400 and 800 nm region were attributed to interference (multiple reflection) effects, absorption effects. In [17] molybdenum was CVD-deposited (from $Mo(CO)_6$) to form polycrystalline films. The films were then annealed in air or oxygen enriched air at temperatures of 500 or 600°C to form transparent MoO_3. The resulting films are reported as having a fairly constant visible/near infrared (400–1000 nm) absorption index of about 0.022–0.04, depending on preparation conditions. The k-value being so constant over such a wide spectral region leads to suspicion that some artifact of the technique is responsible for the unphysical behavior. In [18] thermally evaporated films of MoO_3 are reported as having k values ranging from 0.015 for as-grown films to 0.10 for irradiated (with uv/vis/nir light from a xenon lamp) films at 632.8 nm. However, it appears a factor of 2 error was introduced in converting absorption coefficient to absorption index and these values should actually be 0.007 (nonirradiated) to 0.05 (irradiated 50 min), which would at least make them consistent with the values reported in [17]. Perhaps the samples in [17] naturally experienced some of the coloring or darkening reported in [18] through light exposure. It may also be worth noting that in [18] peaks or oscillations in transmission/absorption spectra were observed in the visible range, similar to [16]; however, whereas in [16] the peaks were attributed to thin-film interference effects (multiple reflection), in [18] they were taken as absorption features (separate interference features were seen in [18] in the reflectance spectra). This leads us to conclude that a re-examination of the techniques and data analysis in [16–18], particularly for the visible region, may be useful. It would seem that there is also a need for further investigation of the optical constants of MoO_3; presently available results are not sufficiently consistent between investigators nor are they sufficiently self-consistent.

Analysis of the molybdenum trioxide sample's interaction with light is more difficult than that of the aluminum. Visually the molybdenum trioxide sample was seen to be light green in color indicating some water content. The color observed shows that the visible red region may be more absorptive than blues and greens and the spectral dependence should be considered. In a previous study, the powder was determined to have sheet-like structures intermixed with aggregates. The thickness of the sheets was determined using small angle scattering measurements of neutrons and x rays to be 15.5 nm [14]. The sheet-like particles of MoO_3 do not conform well to the spherical approximations of Mie theory and are difficult to model by other means.

3.4 Sample Preparation. The experiment used a planar slab of uniform thickness to conform to the 1D approximation of the analysis. A support medium was required to accomplish this for the materials of interest in the density and thickness desired. Consequently, all samples had at least one face that was bounded by a glass plane perpendicular to the light path. The interfaces of air-to-glass or glass-to-sample both cause Fresnel interface reflections due to the differing refractive indices according to Snell's law [6],

$$n_1 \sin(\theta_1) = \tilde{n}_2 \sin(\tilde{\theta}_2) \tag{15}$$

These are effects that had to be accounted for in theoretical simulations in order to accurately model the experimental scattering profile. This was done by including Fresnel interface reflections and refraction in the analysis.

3.4.1 Latex Suspension. The calibration aqueous latex particle suspensions were contained in NSG Precision Cells type-1 cell with optical glass and a 1 or 2 mm path length. These cells were capable of containing the suspension for several hours without leaking and with negligible concentration changes due to evaporation. Calibration began with the 222-nm polystyrene in the "as-received" mass fraction of 0.1. Irregularities were observed in the scattered distribution at this volume fraction suggesting that dependent scattering may be affecting the distribution. References [19–21] provide relations that indicate the dependent scattering effects should be significant for this concentration. Based on these findings the as-received suspension was diluted with distilled water to particle volume fractions of 0.0023 and 0.0032 for calibration.

3.4.2 Al/MoO_3 *Demountable Cells*. The first attempt to produce a uniform slab of the sample medium was to directly place the dry sample in a demountable cell. The NSG Precision Cell type-20 optical glass or IR quartz demountable cells with path lengths ranging from 0.1 to 1 mm were used. Dry powder was placed in this cell in a manner that would produce a uniform slab with constant density. Vibratory methods were used in an attempt to uniformly distribute the powders. Caking, particle attraction to the glass containers, and agglomeration proved to be difficult obstacles to overcome. Results obtained by this method were reasonable for MoO_3, more so for reflectivity than transmissivity. The reason transmissivity was not entirely satisfactory is that the minimum cell path length available resulted in rather large optical thicknesses such that measured transmission signals were quite low; hence, signal/noise was compromised. However good results were obtained for reflectivity as discussed in the Results. Usable samples could not be obtained by this method for aluminum as the properties of aluminum were such as to preclude sufficient uniformity by dry preparation, which prevented even backscattering measurements.

3.4.3 Al/MoO_3 *Liquid Deposition*. As an alternative to working with the dry powders, the aluminum and molybdenum trioxide powders were added at a mass fraction between 0.01 and 0.10 to hexane or isopropyl alcohol and dispersed using a sonic bath. Hexane was found ill-suited to the macroscopic sample processing techniques due to fast settling and was unable to produce useful samples. Isopropyl alcohol worked well to produce samples with no apparent chemical effects. To produce the most test samples,

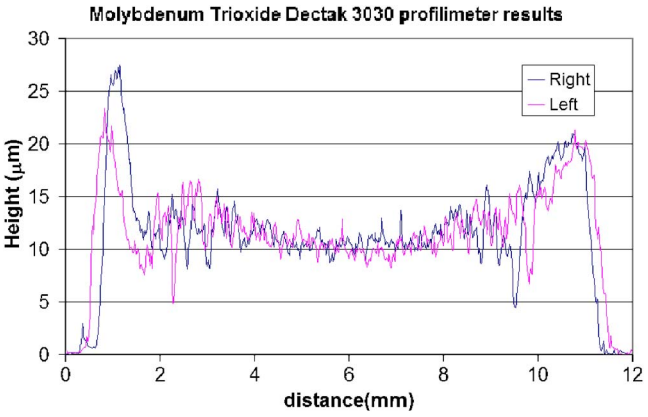

Fig. 3 Profilometer measurement for MoO_3

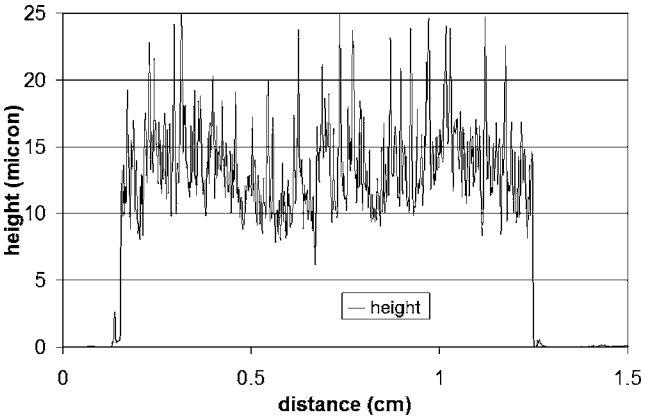

Fig. 4 Profilometer measurement for Al

the end of a short polypropylene tube (1 cm diameter) was abrasively flattened to form a liquid-tight flat circular seal when pressed lightly against a glass slide. Polypropylene was chosen over glass due to its nonwetting properties that result in less curvature of the liquid surface and less deposition on the tube as the liquid evaporated. The tube was used to confine 3–15 drops of suspension on a small area to obtain the desired result of a circular layer of the powdered sample deposited on the glass slide with a uniform thickness and enough adhesion that the slide could be held in the vertical position for testing without sample loss. A number of problems with the current method still exist wherein some samples crack or adhere more to the polypropylene tube than the glass slide.

The uniformity of the produced layer was examined visually for cracks, uneven distribution, and erosion. A thickness measurement of the layer using a Detak 3000 profilometer was then made for use in determining the extinction coefficient as well as observing the surface uniformity. The microscopic characteristics of the powder before and after evaporation-deposition were examined using a scanning electron microscope (SEM). It was found that many sample problems could be reduced or eliminated and the sample thickness controlled by adjusting the suspension's concentration, the volume applied to a slide or the evaporation rate (which was convectively controlled).

The height (layer thickness) profile for a typical molybdenum trioxide test sample is shown in Fig. 3. This information is necessary to determine the slab thickness for use in calculating the extinction coefficient as well as observing the uniformity of the slab. In this figure two paths across the sample are shown, one several millimeters to the left and one several millimeters to the right of center. The characteristics of the profile shown are typical of most samples during testing. The sample typically dried from the center to the edges with the most uniform section existing 1–3 mm from the center. The center of the profiles shown represents this uniform area where the light scattering measurements were made. The height obtained from this profile was 11 μm.

The SEM image of a sample prepared similarly to those tested, but on a silicon wafer instead of a glass slide showed a number of interesting characteristics. Most notably, there were large rectangular particles embedded in the surface with lengths in the 2–10 μm range, much larger than their 15 nm thickness. Similar particles could be seen in images of the powder before deposition, suggesting it is not an agglomeration effect of processing. In both types of images the large particles appear to be accompanied by large numbers of smaller particles. Also seen in the SEM was a crack that developed from contraction. Similar cracks and some more severe were also observed visually in many samples. These were of concern initially because of the possibility that they might allow light to travel though them unattenuated. However, based on observations of the samples during characterization and the ability of MoO_3 to be modeled by reasonable simulations ignoring cracks (as discussed in the Results), this effect was assumed to be negligible in MoO_3.

The height profile for a test sample of Al is shown in Fig. 4. Measurement with the Detak 3000 was found to be much more difficult for Al than for MoO_3. The deposited layer seemed to be much softer and easier to scratch or plow through with the profilometer stylus. Due to the gouging of the surface by the stylus on even the lowest force settings the indicated height profile is likely less accurate with more noise than the profile of the oxide, but it is still believed to give an approximate average thickness. The height obtained from this profile was 13.7 μm. During preparation, the outer edges of the desired circular deposited layer would stick to the confining tube or simply crack and peel away from the glass slide reducing the area available to test significantly. Along with this, the sample may have suffered throughout from cracking as a result of contraction during the drying process.

A SEM image of a sample prepared similarly to those tested, but on a silicon wafer instead of a glass slide was also obtained for Al. This image showed large particle agglomerations 20–100 micron in size (which were also present in the powder as-received) and that these agglomerates had features 34–170 nm in size.

4 Theory

4.1 Slab Scattering. The scattering medium is modeled as a 1D planar slab with boundaries of air or glass. It consists of particles in either an air or water continuum. The radiative transfer equation along a line of sight in a plane-parallel scattering medium is [6]

$$\mu\frac{dI(t,\mu,\phi_s)}{dt} = -I(t,\mu,\phi_s) + (1-\omega_0)I_b(t) + \frac{\omega_0}{4\pi}\int_0^{2\pi}\int_{-1}^{1} I(t,\mu',\phi_s')p(\mu,\phi_s;\mu',\phi_s')d\mu' d\phi' \tag{16}$$

where I is the intensity at optical depth t, cosine of the polar angle μ, and azimuthal angle ϕ. I_b is the blackbody intensity at an optical depth into the slab. Primes denote directions not in the line of sight that are scattered into the line of sight. The scattering phase function $p(\mu,\phi_s;\mu',\phi_s')$ determines how much of the energy scattered from the prime direction propagates in the nonprime direction independent of the optical depth. A number of simplifications including neglecting emission and assuming azimuthal symmetry result in

$$\mu \frac{dI(t,\mu)}{dt} = -I(t,\mu) + \frac{\omega_0}{2}\int_{-1}^{1} I(t,\mu')p(\mu,\mu')d\mu' \quad (17)$$

This equation determines the intensity field throughout the medium given the optical thickness of the slab, albedo, a slab phase function, and appropriate boundary conditions.

4.2 Single Scattering Phase Function. The angular distribution of light scattered by a single particle or an assembly of particles in an optically thin, single-scattering differential volume is described by the single-scattering phase function, $p(\mu_p)$. This phase function is dependent on particle size, shape, composition, the wavelength of light as well as the effects of neighboring particles. The use of an asymmetry parameter simplifies the description of the phase function significantly

$$g = \frac{1}{2}\int_{-1}^{1} p(\mu)\mu d\mu \quad (18)$$

It varies from a value of −1 for entirely backscattering to 1 for forward-scattering particles, giving a relative description of the phase function. Since this work involved scattering in the dependent-scattering regime with nonspherical particles, the asymmetry parameter was utilized to represent the phase function.

To minimize errors associated with the asymmetry parameter simplification, functions must be used that have behavior similar to that of an actual phase function. This includes satisfaction of the conservation of scattered energy, producing the desired asymmetry parameter, and having a shape similar to that of the actual phase function. Functions such as the Heyney-Greenstein function [22],

$$p(\mu) = \frac{(1-g^2)}{(1+g^2-2g\mu)^{3/2}} \quad (19)$$

demonstrate a desirable form as well as meeting the single-scattering phase function conservation of energy requirement. Graaff and co-workers found that the Heyney-Greenstein phase function worked well for asymmetry parameters with absolute values less than 0.8 [22]. In cases involving greater forward scattering, the Heyney-Greenstein phase function is said to peak too strongly in the forward direction in a narrow range of polar angles. Graaff suggests using the Rayleigh-Gans function for a sphere. This function is not a direct function of g, but only varies with the particle size parameter; the asymmetry parameter is calculated after the phase function is computed. Other researchers claim that although the Rayleigh-Gans form does match the Mie phase function in the important forward scattering region, the computational advantages of using this function are very slight when compared with using the full Mie solution [23].

Another useful phase-function concept in a hypothetical/modeling sense is isotropic scattering in which the phase function is unity for all directions. Isotropic scattering is useful for modeling purposes but because it deviates from the actual anisotropic scattering situation, the remaining parameters of albedo and optical thickness must be modified to equivalent isotropic values to obtain accurate solutions of the transfer equation and therefore accurate scattering intensity and bidirectional property distributions.

4.3 Slab. The slab phase function for multiple scattering, $p(\mu,\mu')$, can be constructed from the single particle phase function using several different method. This function describes the phase function for scattering from the μ' cone of directions into the μ cone of directions. An equation based on azimuthal symmetry has been presented to obtain this function directly from the single particle phase function [6]

$$p(\mu,\mu') = \frac{1}{\pi}\int_{\mu_{p_0}}^{\mu_{p_\pi}} \frac{p(\mu_p)d\mu_p}{[(1-\mu^2)(1-\mu'^2)-(\mu_p-\mu\mu')^2]^{1/2}} \quad (20)$$

$$\mu_{p_0} = \mu\mu' + \sqrt{1-\mu^2}\sqrt{1-\mu'^2} \quad (21)$$

$$\mu_{p_\pi} = \mu\mu' - \sqrt{1-\mu^2}\sqrt{1-\mu'^2} \quad (22)$$

An alternative to the integration method is the Legendre polynomial representation. Legendre polynomials, P_i, can be fit to a phase function by obtaining a set of coefficients, a_i, such that

$$p(\mu_p) = \sum_{i=0}^{N_L} a_i P_i(\mu_p) \quad (23)$$

Chu and Churchill give a method of obtaining the coefficients [24]. These coefficients can then be used to produce the slab phase function as a summation of Legendre polynomials [6].

$$p(\mu,\mu') = \sum_{i=0}^{N_L} a_i P_i(\mu)P_i(\mu')$$

4.4 Equivalent Isotropic Albedo and Extinction Coefficient. Isotropic scattering is a useful approximation for modeling radiative heat transfer in scattering media. However, all particles exhibit some degree of anisotropic scattering. It is therefore useful if anisotropic scattering can be converted in a rational way to equivalent isotropic scattering, for example, by modifying the extinction coefficient and albedo. It can be shown that under optically thick conditions for which the diffusion approximation holds, a rational conversion from actual extinction coefficient, K_e (with anisotropic scattering) to an equivalent isotropic extinction coefficient is [6]

$$K_{e,I} = (1-\omega_0 g)K_e \quad (24)$$

Similarly an equivalent isotropic albedo under optically thick conditions can be defined as [25]

$$\omega_{0_I} = \frac{\omega_0(1-g)}{1-\omega_0 g} \quad (25)$$

5 Computational Methods

Two approaches were used to solve the radiative transfer equation, discrete ordinates (DO) and Monte Carlo (MC). In the DO approach the transfer equation was discretized into M spatial locations (optical depths) and N directions to produce $M \times N$ linear equations of form similar to

$$0 = \frac{\mu I_{m-1,n}}{2\Delta t} - \frac{\mu I_{m+1,n}}{2\Delta t} - I_{m,n} + \frac{\omega_0}{2}\sum_{k=1:N} I_{m,k}p(n,k)\Delta\mu \quad (26)$$

with variations occurring at the boundaries due to surface interfaces and step sizes of Δt in optical depth and $\Delta\mu$ in direction cosine. Appropriate boundary conditions were applied depending on whether one or two glass slides were present. These boundary conditions were a necessary account for Fresnel reflection and refraction at interfaces and multiple internal reflections. Inputs to the equations were optical depth of the sample, single-scattering albedo of the particles, and scattering phase function. In order to compare calculated intensities with experimental results, the internal intensities at the boundaries were transformed into intensities outside the sample medium. From these external intensities and the incident flux the bidirectional reflectivities and transmissivities were determined as indicated by Eq. (12). In the MC method the equivalent power of all the photon bundles exiting in each direction is combined with the exit direction spacing and the equivalent incident power to determine the bidirectional reflectivities and transmissivities. Computations by both methods were checked and debugged by comparison with previous results and existing solutions.

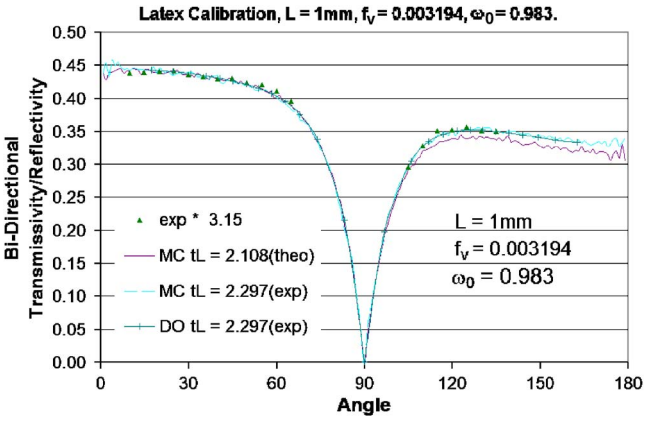

Fig. 5 Latex calibration, L=1 mm, d=222 nm, f_v=0.0032, ω_0 =0.983

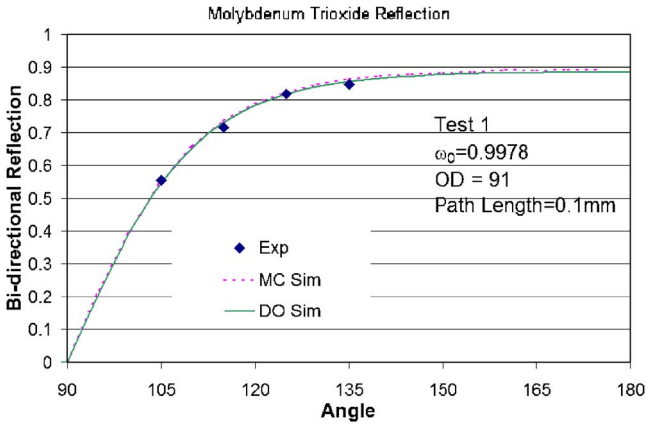

Fig. 7 Bidirectional reflection for MoO_3 powder in 0.1-mm glass cell

6 Light Scattering Results

6.1 Latex. The latex calibration measurements were done in two cells of 1 and 2 mm path lengths, with aqueous suspensions having latex volume fractions of 0.0032 and 0.0023, respectively. Results for the 1 mm cell with latex volume fraction of 0.0032 are shown in Fig. 3. As a calibration factor the experimental data were multiplied by a factor of 3.15 to match the theoretical predictions. This is the method by which the experimental calibration factor was determined for use with the samples (Al and MoO_3) having unknown properties. Optical thickness of the latex suspension t_L could be determined two ways: theoretically using Eq. (10) (theo-value in Fig. 5) and experimentally from the direct (unscattered, unabsorbed) transmission measurements and the incident flux measurements (exp-value in Fig. 5). The difference between the two optical depths is less than 10%. The slightly higher experimental value was used in preference to the theoretical one in the scattering calculations since the theoretical t_L value assumes independent scattering and monosized particle distribution, which assumptions are not perfectly satisfied. Three other tests similar to that of Fig. 3 but with varying latex volume fraction and cell path length were performed and corresponding calibration factors determined. The average calibration factor from these four test conditions was determined to be 3.188. This factor was used to correct the measured scattering results for aluminum and molybdenum trioxide samples. Analysis of the origins of the correction factor pointed to a number of sources including spatial nonlinearity across the PMT detection area and normal uncertainty in the optical density of the neutral density filters. Nevertheless, in spite of these nonideal factors in the measurement system, the agreement between scaled experimental values and simulations shown in Fig. 3 is very good. In both the forward and backward directions, the shapes of the curves match well and the relative forward-to-backward scattering ratio is equivalent for all cases. All four calibration cases showed similar good agreement.

6.2 Molybdenum Trioxide. Experimental bidirectional scattering profiles for molybdenum trioxide are shown in Figs. 6–9. The results from the 100-μm demountable cell are shown in Figs. 6 and 7. The bidirectional transmission values (Fig. 6) were nearly four orders of magnitude smaller than the reflection values (Fig. 7), which approached 0.9 for the normal backward direction (180 deg). Isotropic-scattering simulations resulted in an albedo of 0.9978 and an optical depth of 91. The large difference between forward and backward scattered intensities combined with the difficulty in producing testable samples drove testing towards alternative methods of sample production (as noted above under Sample Preparation) that were capable of producing pathlengths an order of magnitude smaller, i.e., the liquid-suspension deposition/evaporation method.

Samples produced with the suspension-evaporation method produced bidirectional transmission and reflection values of the same order of magnitude, which is conducive to better sensitivity in determining scattering parameters. These results are shown in Figs. 8 and 9 for two sample thicknesses, 5.6 and 11 μm. Several simulation parameter sets were able to provide a reasonable match to a given experimental case, as summarized in the figures and in

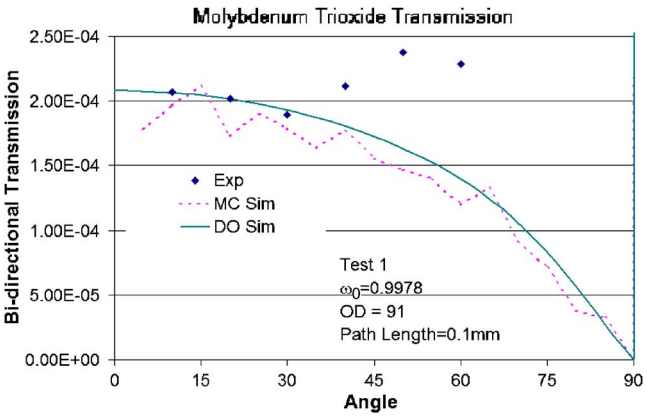

Fig. 6 Bidirectional transmission for MoO_3 powder in 0.1-mm glass cell

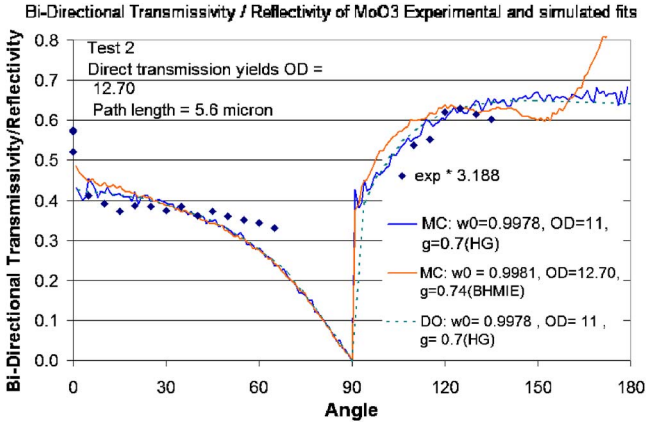

Fig. 8 Bidirectional transmissivity/reflectivity for MoO_3 deposited on glass slide; test 2: path length 5.6 μm

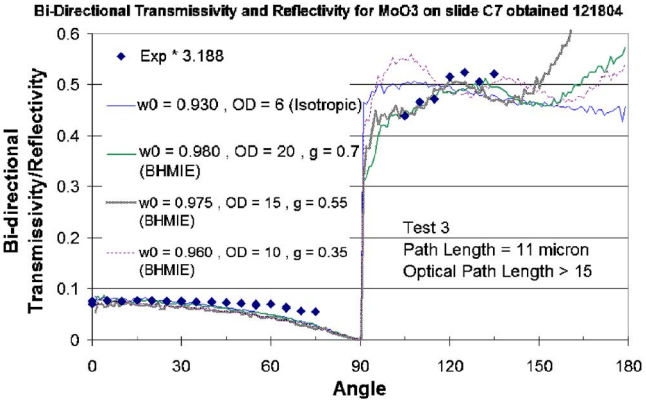

Fig. 9 Bidirectional transmissivity/reflectivity of MoO_3 deposited on glass slide; test 3: path length 11 μm

Table 1; that is, the 3-parameter set was not necessarily unique. In all simulations that appeared to fit the experiments, the transmission profiles had a similar shape with a consistent deviation from the experimental data as the angle approached 90 deg. The reflection profiles had a more varying shape, which can be attributed to the different phase functions being less blurred by multiple scattering than the transmission signal. The exact shape of the distribution was not expected to match because the effects of particle shape and dependent scattering are not accounted for in the representative phase function, which is patterned after independent Mie scattering theory.

The extra information necessary to determine more unique simulated fits for an experimental measurement with the 3-parameter set (albedo, optical thickness, and scattering asymmetry parameter) is the direct, unscattered transmission. The problem with using this information is that it merges with the scattered transmission signal in a way that makes their separation subject to some ambiguity. Furthermore, in samples that are sufficiently optically thick the unscattered transmission is negligibly small and therefore unavailable for use. The 5.6-μm test of Fig. 8 showed a sharp peak in the forward direction. This sharp jump is thought to be an effect of direct transmission. The direction transmission was separated from the scattered transmission by extrapolating the scattered transmission data from the 30–60 deg region to 0 deg. This method is somewhat arbitrary; there is no guarantee that the actual bidirectional transmission data should follow such an extrapolation. However, simulation results show such behavior for most parameters thought to be representative of these conditions, suggesting that such an approach is at least plausible. This method resulted in an optical depth of approximately 12.70. For the 11-μm sample of Fig. 9 the unscattered transmission was undetectable above the scattered signal at 0 deg. This finding indicates that the optical depth for the 11-μm test is greater than 13 and most likely greater than 15; a range consistent with the slab having nearly twice the thickness of the 5.6-μm sample.

The scattering parameters used in the simulations are shown in Figs. 8 and 9 and the results obtained are summarized in Table 1. Examining these results it can be seen that the three scattering parameters vary significantly for the different simulations fit to the data, especially when isotropic results are compared with anisotropic. For a single experiment such as the 11-μm test the optical thickness used in simulations ranged from 6 to 20, all producing scattering profiles that appear to match the experiment. The other two parameters had to be adjusted accordingly, requiring the albedo and asymmetry parameters to have ranges from 0.93 to 0.98 and 0.0 to 0.7, respectively. Even with so much variation in the three scattering parameters, conversion of anisotropic-scattering parameters by Eqs. (24) and (25) to the equivalent isotropic albedo and extinction coefficient values showed that the amount of variation is much less in the latter two parameters and indicates that these two parameters can be obtained reliably and somewhat independently from the bidirectional scattering data as long as the bidirectional profiles reasonably match. The most consistent results come from the anisotropic parameter fits, however; isotropic-scattering simulations are apparently too far from the actual anisotropic-scattering situation to yield equivalent isotropic parameters of any reasonable consistency with those obtained from the anisotropic simulations. The equivalent isotropic extinction coefficients for MoO_3 tests in Table 1 are approximately 5450–6350 1/cm and the equivalent isotropic albedos are 0.935 to 1.0. From these results we suggest that the equivalent isotropic extinction coefficient of MoO_3 nanoparticles under these conditions is 5900 ± 450 cm^{-1} and the equivalent isotropic albedo is 0.97 ± 0.035. These extinction coefficient values are consistent with what would be expected for 100-nm representative spherical particles in high volume fractions if dependent scattering was ignored (independent Mie scattering theory), but the albedo and asymmetry parameters are not. These results point out the inability of independent Mie scattering approximations to model accurately and completely these high volume-fraction, nanometer-sized particle samples. More advanced methods accounting for dependent scattering and non-spherical particles would need to be employed for theoretical calculations to become accurate.

6.3 Aluminum. Experimental bidirectional scattering measurements for aluminum are shown in Figs. 10–12. The profiles feature a very strong peak in the forward direction. The peak appears like those attributed to direct transmission in the molybdenum trioxide measurements but persists out to higher angles, approaching 20 or 30 deg. The simulation methods developed were not able to reproduce this profile with realistic parameters to obtain a match with a similar shape; nevertheless, the source of the peak is of interest. One possibility is that cracks in the samples allowed localized "direct" (or nearly direct) transmission, which gave a signal having the appearance of a strong direct transmission component.

Because the bidirectional transmission curve with the forward peak that could not be matched with simulations an alternative

Table 1 Molybdenum trioxide experimental data and simulations parameters

Test	Length (micron)	Optical length	Albedo	Asym. param.	K_e (1/cm)	$K_{e,I}$ (1/cm)	Albedo E. Iso.	k_r[a] (W/m K)
1	100	91	0.9978	0	9100	9100	0.998	0.00897
2	5.6	1.8	0.991	0	3214.3	3214.3	0.991	0.0254
2	5.6	12.7	0.9981	0.74	22679	5928.3	0.993	0.01377
2	5.6	11	0.9978	0.7	19643	5923.1	0.993	0.01378
3	11	6	0.93	0	5454.5	5454.5	0.930	0.01497
3	11	10	0.96	0.35	9090.9	6036.4	0.940	0.01353
3	11	15	0.975	0.55	13636	6323.9	0.946	0.01291
3	11	20	0.98	0.7	18182	5709.1	0.936	0.0143

[a]Temperature of 3000 K used in calculations.

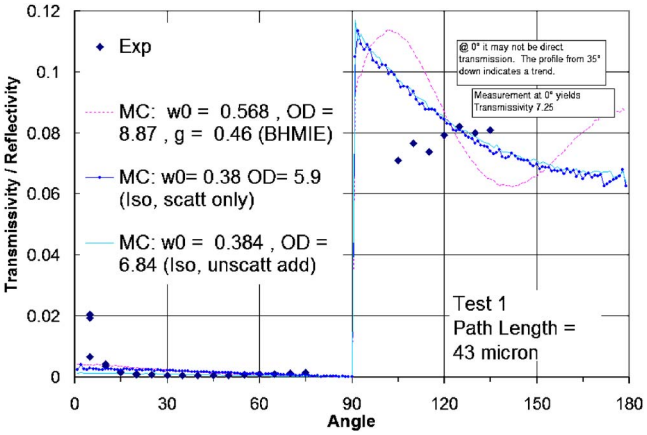

Fig. 10 Experimental bidirectional properties of aluminum, test 1

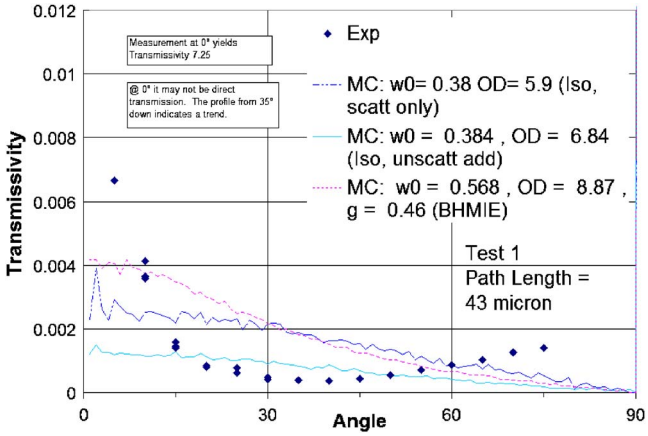

Fig. 11 Experimental bidirectional transmission of aluminum, test 1

approach was used to try to determine volumetric radiative properties; the hemispherical reflectivity and transmissivity were obtained from the simulations and matched to those obtained from integrating a profile based on the experimental measurements. In this manner the hemispherical values could be used to obtain the isotropic matches and the hemispherical values plus the direct transmission could be used to obtain anisotropic matches with an asymmetry parameter. From this the results in Table 2 were obtained.

Along with the broadened forward peak in the aluminum profiles, the relationships between the path lengths and the simulation optical depths leads to further suspicion that the samples are not as uniform as desired. Even though the difference in sample thickness was nearly a factor of 3 between the two experiments the optical depths matched to these experiments were very similar. Due to this, the extinction coefficients showed a great deal of variation that was not corrected when converted to equivalent isotropic form.

The equivalent isotropic albedo could be obtained from the scattering profile using isotropic phase functions. The extra direct transmission through any cracks that existed would have only a negligible effect on the reflection that for semi-infinite slabs is only affected by the albedo. From the two tests the isotropic albedo was found to be 0.35 and 0.38. Equivalent isotropic albedos for the anisotropic simulation fits were noticeably higher, but this is attributed to the problems encountered when attempting to match the forward direction.

The experimental albedos of 0.35 and 0.38 are quadruple that predicted by Mie theory, but agreement was not expected. The optical depth and asymmetry parameters could not be determined due to the lack in confidence of the measured scattered and direct transmission.

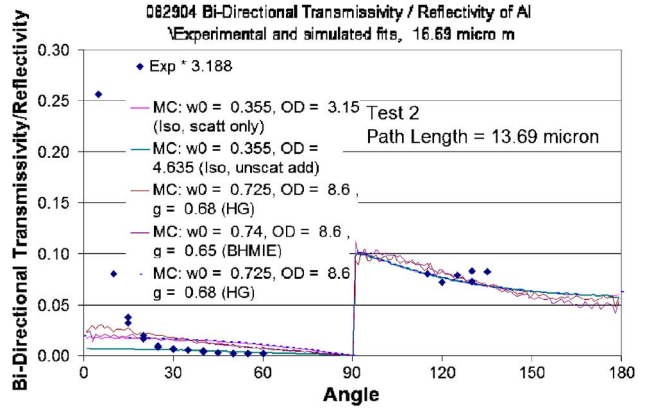

Fig. 12 Experimental bidirectional properties of aluminum, test 2

6.4 Comparison of Energy Transfer Modes. Typically, the radiative component of energy transfer is neglected in combustion waves, but in nanopowders with such small particle sizes and possible dependent scattering, it remains a possibility that must be evaluated. To do this the radiation diffusion approximation was used. For the diffusion approximation to be valid under nanothermite reaction wave conditions, the photon mean free path (mfp=$1/K_{el}$) must be much less than the characteristic length for temperature change in the reaction wave. The latter is related to the induction length scale, which has been estimated by Wilson and Kim [26] as 10 μm. The mfp for MoO_3 as discussed above is 1.7 μm. Thus, invoking the diffusion approximation to estimate radiative flux seems reasonable.

The radiation diffusion approximation can be formulated in terms of a radiative conductivity k_r as follows:

$$q'' = \frac{-4}{3K_{e_R}}\frac{de_b}{dx} = -k_r(T)\frac{dT}{dx}$$

$$k_r(T) = \frac{16\sigma T^3}{3K_{e,R}} \tag{27}$$

Here the Rosseland mean extinction coefficient K_{eR} is the spectrally averaged isotropic extinction coefficient and e_b is the total hemispherical blackbody flux [6]. The Rosseland mean extinction coefficient is approximated as the spectral value of K_{e_l} at 632 nm as determined above. These values for MoO_3 ranged from 5500 to 6500 cm^{-1}, which with an assumed characteristic reaction wave temperature of 3000 K results in a radiative conductivity of 1.4×10^{-2} W/m K. Compared with the diffusive thermal conduc-

Table 2 Aluminum experimental data and simulations parameters

Test	Length (micron)	Optical length	Albedo	Asym. param.	K_e (1/cm)
1	43	5.9	0.38	0	1372.1
1	43	6.84	0.384	0	1590.7
1	43	8.87	0.568	0.4627	2062.8
2	13.69	3.15	0.3545	0	2300.9
2	13.69	4.635	0.3552	0	3385.7
2	13.69	8.6	0.725	0.68	6282
2	13.69	8.6	0.74	0.65	6282

tivity for a typical ceramic material and air at this temperature, which is on the order of 1 W/m K suggests that radiation can be neglected as an energy transfer mode in a nanopowder reactive wave for the tested conditions. Increasing the assumed temperature to 4000 K [26] increases the radiative conductivity to 3.3 $\times 10^{-2}$ W/m K, which is still negligible.

Even if radiation is not an important factor there still remains the often surprising behavior of nanomaterials compared with larger particles or bulk materials such as nonintuitive dependence of reactive wave speed on particle size and packing density. Another energy transfer mode with the possibility of high energy transport rates is that associated with the mass transfer of hot materials from the reaction zone to the cooler regions of unreacted material upstream by advection. Bockmon et al. suggest that such a mechanism may play a dominant role due to the high pressures present during nanothermite testing and they offer a supporting Peclet number analysis [27].

7 Summary

A one-dimensional light scattering technique proved capable of determining radiative properties from a high volume-fraction slab of nanomolybdenum trioxide by matching multiple scattering simulations with experimental distributions. The equivalent isotropic albedo was found to be 0.97 ± 0.035 and the equivalent isotropic extinction coefficient was found to be 5900 ± 450 cm^{-1}. Based on these results, the radiative conductivity of molybdenum trioxide is much less than the diffusive thermal conductivity under optically thick conditions. This suggests that radiation is not a dominant mode of heat transfer in the reactive wave propagation of nanothermites.

Sample preparation was found to be the most challenging and limiting element of this research as made evident by the aluminum samples. The experimental requirements of the 1D slab combined with a moderate optical thickness resulted in more problems with the metallic aluminum than the molybdenum trioxide. The experimental bidirectional profiles for aluminum had a broadened forward peak, possibly due to cracking, that could not be matched in shape with simulations. Improvements in the preparation techniques could allow thinner more uniform layers and produce better scattering results.

Acknowledgment

Research for this publication was carried out in the Center for Microanalysis of Materials, University of Illinois at Urbana-Champaign, which is partially supported by the U.S. Department of Energy under Grant No. DEFG02-91-ER45439. The authors acknowledge the financial support of Los Alamos National Lab and the helpful discussions with Steve Son and Blaine Asay.

References

[1] Fischer, S. H. and Brublich, M. C., 1998, "Theoretical Energy Release of Thermites, Inter-Metallics and Combustible Metals," *24th International Pyrotechnics Seminar*, Monterey, CA.

[2] Aumann, C. E., Skofronick, G. L., Martin, and J. A., 1995, "Oxidation Behavior of Aluminum Nanopowders," J. Vac. Sci. Technol. B, **13**(3), pp. 1178–1183.

[3] Ivanov, G. V., Surcov, V. G., and Viktroenco, A. M., 1979, "Anomalous Dependence of the Combustion Rate of Thermite Mixtures on the Pressure," Combust., Explos. Shock Waves, **15**, pp. 266–268.

[4] Son, S. F., 2003, "Performance and Characterization of Nanoenergetic Materials at Los Alamos," *Materials Research Society Symposium Proceedings*, December 1–4, 2003, Boston, MA, Vol. 800, pp. 161–172.

[5] Yang, Y., Wang, S., Sun, Z., and Dlott, D., 2005, "Near-Infrared and Visible Absorption Spectroscopy of Nanoenergetic Materials Containing Aluminum and Boron," Propellants, Explos., Pyrotech., **30**(3), pp. 171–177.

[6] Brewster, M. Q., 1992, *Thermal Radiative Transfer and Properties*, Wiley, New York.

[7] Brewster, M. Q., 2004, "Volume Scattering of Radiation in Packed Beds of Large, Opaque Spheres," J. Heat Transfer, **126**, pp. 1048—1050.

[8] Duke Scientific, 2004, "Research and Test Particles," Duke Scientific Corporation Bulletin—91N, June 15, 2004.

[9] Duke Scientific, 1996, "Index of Refraction," Duke Scientific Corporation Technical Note—007B, December 1, 1996.

[10] Ma, X., Lu, J. Q., Brock, R. S., Jacobs, K. M., Yang, P., and Hu, X.-H., 2003, "Determination of Complex Refractive Index of Polystyrene Microspheres from 370 to 1610 nm," Phys. Med. Biol., **48**, pp. 4165–4172.

[11] Kwok, Q. S. M., Fouchard, R. C., Turcotte, A. M., Lightfoot, P. D., Bowes, R., and Jones, D. E. G., 2002, "Characterization of Aluminum Nanopowder Compositions," Propellants, Explos., Pyrotech., **27**, pp. 229–240.

[12] Pranda, P., Prandova, K., and Hlavacek, V., 2000, "Particle Size and Reactivity of Aluminum Powders," Combust. Sci. Technol., **156**, pp. 81–96.

[13] Jones, D. E. G., Brousseau, P., Fouchard, R. C., Turcotte, A. M., and Kwok, Q. S. M., 2000, "Thermal Characterization of Passivated Nanometer Size Aluminum Powders," J. Therm Anal. Calorim., **61**, pp. 805–818.

[14] Son, S. F., Busse, J. R., Asay, B. W., Peterson, P. D., Mang, J. T., Bockmon, B., and Pantoya, M. L., 2002, "Propagation Studies of Metastable Intermolecular Composites (MIC)," *in Proceedings of the International Pyrotechnics Society, The Twenty-Ninth International Pyrotechnics Seminar*, Colorado, July 14–19, 2002.

[15] Bohren, C. F., and Huffman, D. R., 1983, *Absorption and Scattering of Light by Small Particles*, Wiley New York.

[16] Khawaja, E. E., Durrani, S. M. A, and Daous, M. A., 1997, "Optical Properties of Thin Films of WO_3, MoO_3 and Mixed Wxides WO_3/MoO_3," J. Phys. Condens. Matter, **9**, pp. 9381–9392.

[17] Abdellaoui, A., Leveque, G., Donnadieu, A., Bath, A., and Bouchikhi, B., 1997, "Iteratively Derived Optical Constants of MoO_3 Polycrystalline Thin Films Prepared by CVD," Thin Solid Films, **304**, pp. 39–44.

[18] Reyes-Betanzo, C., Herrera-Perez, J. L., Cocoletzi, G. H., and Zelaya-Angel, O., 2000, "Refractive Index of Colored Films of Molybdenum Trioxide," J. Appl. Phys., **88**(1), pp. 223–226.

[19] Tien, C. L., and Drolen, B. L., 1987, "Thermal Radiation in Particulate Media with Dependent and Independent Scattering," Annu. Rev. Numer. Fluid Mech. Heat Transfer, **1**, pp. 1–32.

[20] Kumar, S., and Tien, C. L., 1990, "Dependent Absorption and Extinction of Radiation by Small Particles," J. Heat Transfer, **112**, pp. 178–185.

[21] Drolen, B. L., and Tien, C. L., 1987, "Independent and Dependent Scattering in Packed-Sphere Systems," J. Thermophys. Heat Transfer, **1**(1), pp. 63–68.

[22] Graaff, R., Aarnoudse, J. G., de Mul, F. F. M., and Jentink, H. W., 1989, "Light Propagation Parameters for Anisotropically Scattering Media Based on the Rigorous Solution of the Transport Equation," Appl. Opt., **28**(12), pp. 2273–2279.

[23] Brewster, M. Q, and Yamada, Y., 1995, "Optical Properties of Thick Turbid Media from Picosecond Time-Resolved Light Scattering Measurments," Int. J. Heat Mass Transfer **38**(14), pp. 2569–2581.

[24] Chu, C.-M., and Churchill, S. W., 1955, "Representation of the Angular Distribution of Radiation Scattered by a Spherical Particle," J. Opt. Soc. Am., **45**(11), pp. 958–962.

[25] Lee, H., and Buckius, R. O., 1982, "Scaling Anisotropic Scattering in Radiation Heat Transfer for a Planar Medium," J. Heat Transfer, **104**, pp. 68–75.

[26] Wilson, D. E., and Kim, K., 2003 "A Simplified Model for the Combustion of Al/MoO_3 Nanocomposite Thermites," 39th AIAA/ASME/SAE/ASEE Joint Propulsion Conference AIAA 2003–4536, Huntsville, AL, USA, July 20–23, 2003.

[27] Bockmon, B. S., Pantoya, M. L., Son, S. F., Asay, B. W., and Mang, J. T., 2005, "Combustion Velocities and Propagation Mechanisms of Metastable Interstitial Composites," J. Appl. Phys., **98**(6), pp. 064903.

The DRESOR Method for a Collimated Irradiation on an Isotropically Scattering Layer

Qiang Cheng

Huai-Chun Zhou[1]
e-mail: hczhou@mail.hust.edu.cn

State Key Laboratory of Coal Combustion,
Huazhong University of Science and Technology,
Wuhan 430074, P.R.C.

Forward and backward Monte Carlo methods may become inefficient when the radiant source is collimated and radiation onto a small, arbitrary spot and onto a small, arbitrary direction cone is desired. In this paper, the DRESOR method was formulated to study the radiative heat transfer process in an isotropically scattering layer exposed to collimated radiation. As the whole spherical solid angle space was uniformly divided into 13,316 discrete solid angles, the intensity at some point in up to such discrete directions was given. The radiation fluxes incident on a detector inside the layer for varying acceptance angles by a step of 2 deg *were also measured, which agreed well with those in literature. The radiation flux across the top and the bottom boundaries were also provided.* [DOI: 10.1115/1.2712477]

Keywords: radiative transfer equation, collimated irradiation, DRESOR method, Monte Carlo method, isotropically scattering

1 Introduction

When radiation onto a small spot and/or onto a small direction cone is desired, the forward Monte Carlo method can become terribly inefficient, since that for a large amount of energy bundles emitted and tracked until they are absorbed or leave the system, only the results from a small part of the bundles which hit on the spot or enter the cone are effective. For this kind of problem, the backward Monte Carlo method is a much better choice, and a comprehensive formulation for the method was given by Modest [1]. Some other methods were also applied to study radiative transfer problems with collimated irradiation. For example, Lacroix [2] applied the Discrete Ordinates method to analyze the interaction of a laser beam with the plume generated by the laser, Wu [3] used the integral equation method to study radiative transfer in a two-dimensional cylindrical medium exposed to collimated irradiation, and Modest and Tabanfar [4] applied the modified P_l approximation to study collimated irradiation problems.

Though many methods have been devoted to radiative transfer with collimated irradiation, few of them could give the angular distribution of intensity with high directional resolution, which plays a key the role in the most inverse radiative transfer problems [5–7] and radiative image processing in some industrial applications, for example, monitoring of temperature distributions in industrial combustion furnaces [8]. At present, a modernized charge-coupled device (CCD) can give up to 1024×1024 pixels of image data, but unfortunately, it is not easy to analyze the radiation intensity captured by such a CCD with the existing methods of radiative transfer.

A new approach, called the DRESOR method, based on the Monte Carlo method, was developed to calculate the radiative intensity and solve the radiative transfer equation (RTE) for a gray, plane-parallel medium with diffusely or specularly reflecting boundaries, and the results obtained by the DRESOR method were validated by the integral formulation of RTE [9,10]. By this method, the intensity with high directional resolution at any point could be obtained with high precision without the requirement of radiative equilibrium [10].

In this paper, a comprehensive formulation for the DRESOR method was proposed to deal with the purely scattering medium and absorbing and scattering medium with collimated irradiation. The intensities varied with the polar angle, θ, and the azimuthal angle, φ, with high directional resolution at any point can be calculated by the DRESOR method. The method was validated by the data in literature and the energy conservation law for the purely scattering medium by the Monte Carlo method with different scattering coefficients. Then, the DRESOR values, in which the radiation intensity varied with θ and φ, and the radiation flux, were obtained for four cases with various radiative properties. Finally, some concluding remarks were given.

2 Formulas of the DRESOR Method for Collimated Irradiation

2.1 Basic Description of the DRESOR Method. As shown in Fig. 1, collimated irradiation is incident on the surface dA at the location $\mathbf{r}_w$ on a nonreflecting and nonrefracting surface. The equation for radiative transfer in a cold, absorbing and scattering medium under the surface is written as [11]

$$\hat{\mathbf{s}}\cdot\nabla I_\eta(\mathbf{r},\hat{\mathbf{s}}) = -\beta_\eta I_\eta(\mathbf{r},\hat{\mathbf{s}}) + \frac{\sigma_{s\eta}}{4\pi}\int_{4\pi} I_\eta(\mathbf{r},\hat{\mathbf{s}}_i)\Phi_\eta(\hat{\mathbf{s}}_i,\hat{\mathbf{s}})\mathrm{d}\Omega_i \quad (1)$$

The integral solution for Eq. (1) is

$$I_\eta(\mathbf{r},\hat{\mathbf{s}}) = I_{ow}(\mathbf{r}_w,\hat{\mathbf{s}})\exp\left[-\int_0^s \beta_\eta \mathrm{d}s''\right] + \int_0^s S_\eta(\mathbf{r}',\hat{\mathbf{s}})\exp\left[-\int_0^{s'}\beta_\eta \mathrm{d}s''\right]\beta_\eta \mathrm{d}s' \quad (2)$$

where $I_{ow}(\mathbf{r}_w,\hat{s})$ denotes the collimated irradiation intensity at the location $\mathbf{r}_w$,

[1]Corresponding author.

Contributed by the Heat Transfer Division of ASME for publication in the JOURNAL OF HEAT TRANSFER. Manuscript received October 25, 2005; final manuscript received July 5, 2006. Review conducted by Walter W. Yuen.

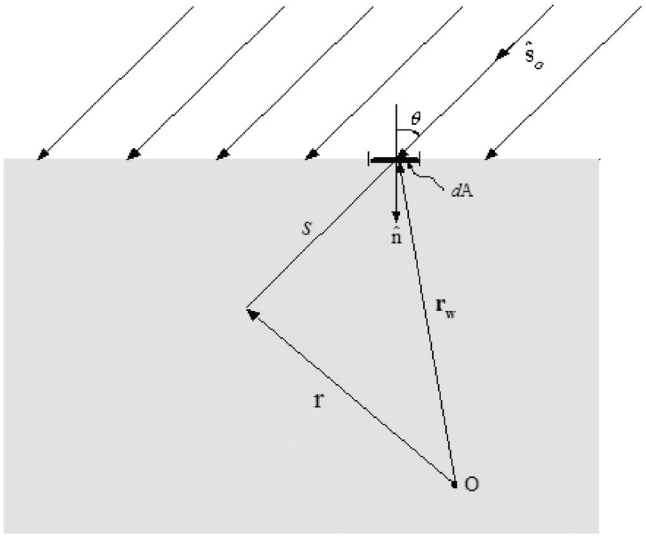

Fig. 1 Collimated irradiation impinging on an arbitrary surface

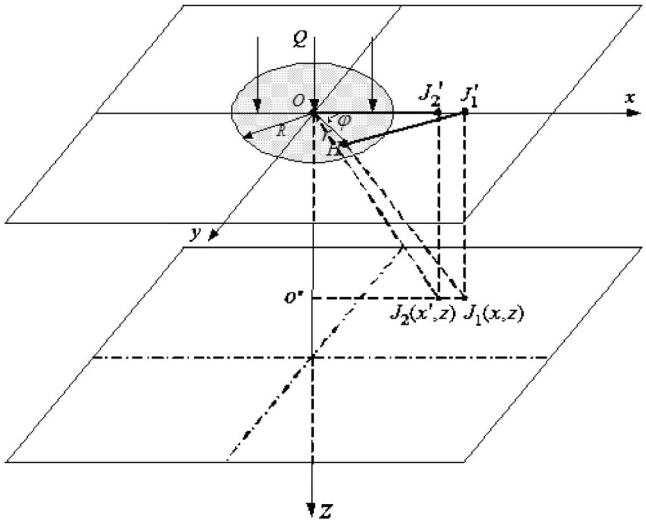

Fig. 2 Geometry of a one-dimensional layer subjected to collimated irradiation (a), and the geometric relation of points, J_1, J_2, in the *x-z* plane to the points, *H*, *O*, in the disk subjected to the collimated irradiation used to derive the DRESOR value $R_d^s(\mathbf{r}_H, \mathbf{r}_{J_1})$ from $R_d^s(\mathbf{r}_o, \mathbf{r}_{J_2})$ (b)

$$I_{ow}(\mathbf{r}_w, \hat{s}) = q_o(\mathbf{r}_w)\,\delta[\hat{s} - \hat{s}_o(\mathbf{r}_w)] \tag{3}$$

where $q_o(\mathbf{r}_w)$ is the flux of the collimated irradiation, δ is the Dirac-delta function, $\hat{s}_o(\mathbf{r}_w)$ is the direction of the collimated irradiation.

The new formula for $S_\eta(\mathbf{r}', \hat{\mathbf{s}})$ in the DRESOR method is

$$S_\eta(\mathbf{r}', \hat{\mathbf{s}}) = \frac{\omega_\eta}{4\pi}\left[\int_{4\pi} I_\eta(\mathbf{r}', \hat{\mathbf{s}}_i)\Phi_\eta(\hat{\mathbf{s}}_i, \hat{\mathbf{s}})\,\mathrm{d}\Omega_i\right] = \frac{1}{4\pi}\left[\int_W q_o(\mathbf{r}_w) R_d^s(\mathbf{r}_w, \mathbf{r}', \hat{\mathbf{s}})\,\mathrm{d}A\right] \tag{4}$$

where, $R_d^s(\mathbf{r}_w, \mathbf{r}', \hat{\mathbf{s}})$, called DRESOR (Distributions of Ratios of Energy Scattered by the medium Or Reflected by the boundary surfaces) values, denotes the ratios of the energy scattered by a unit volume around the point $\mathbf{r}'$ into a unit solid cone around the direction $\hat{\mathbf{s}}$ multiplied by 4π, to the collimated irradiation incident on a unit area around the point $\mathbf{r}_w$ on the surface. The detailed definition of the DRESOR value can be referred to [10].

Substituting Eq. (4) into Eq. (2) gives a new solution formula for the radiative transfer with collimated irradiation by the DRESOR method,

$$I_\eta(\mathbf{r}, \hat{\mathbf{s}}) = q_o(\mathbf{r}_w)\,\delta[\hat{s} - \hat{s}_o(\mathbf{r}_w)]\exp\left[-\int_0^s \beta_\eta \mathrm{d}s''\right] + \frac{1}{4\pi}\int_0^s \int_W q_o(\mathbf{r}_w) R_d^s(\mathbf{r}_w, \mathbf{r}', \hat{\mathbf{s}})\,\mathrm{d}A \times \exp\left[-\int_0^{s'} \beta_\eta \mathrm{d}s''\right]\beta_\eta \mathrm{d}s' \tag{5}$$

From Eqs. (3) and (5) it is obvious that, for a scattering, absorbing and nonemitting medium with given distributions of scattering and absorption coefficients, once all the DRESOR values, $R_d^s(\mathbf{r}_w, \mathbf{r}', \hat{\mathbf{s}})$, are known, $I_\eta(\mathbf{r}, \hat{\mathbf{s}})$, the angular distribution of radiation intensity in any point $\mathbf{r}$, can be expressed as a function of the flux of the collimated irradiation, $q_o(\mathbf{r}_w)$.

In the early development of the DRESOR method [9,10], the DRESOR method was formulated primarily and validated in gray, plane-parallel media. The method was also applied to multidimensional problems to visualize the three-dimensional temperature distribution in a coal-fired furnace [8]. An anisotropic scattering, emitting, absorbing, one-dimensional medium with different boundary conditions was studied in [12] by the DRESOR method. The DRESOR method was also used to deal with the transient radiative transfer problems [13]. In this paper, the DRESOR method was proposed to study the radiative heat transfer process in an isotropically scattering layer exposed to collimated radiation, and most importantly, the radiation intensity with high directional resolution was to be obtained.

2.2 Formulas for a Simple Case. Considering that a collimated irradiation with energy Q is normally incident on a nonreflecting surface, equally distributed over a disk $0 \le r \le R$, labeled as W, as shown in Fig. 2(*a*) [1,11]. The media under the surface is assumed to be gray, homogeneous, and isotropically scattering, and bounded by cold, nonreflecting surfaces (i.e., completely transparent or black). As stated in [10], for the isotropically scattering, $R_d^s(\mathbf{r}_w, \mathbf{r}', \hat{\mathbf{s}})$ reduced to $R_d^s(\mathbf{r}_w, \mathbf{r}')$. The origin of the coordinates, O, is just at the center of the disk W. The DRESOR values are distributed symmetrically due to the homogeneity of the medium and the symmetrically collimated irradiation source. Then, Eqs. (3) and (5) could be simplified, respectively, as

$$I_{ow}(\mathbf{r}_w, \hat{s}) = \frac{Q}{\pi R^2}\,\delta[\hat{s} - \hat{s}_o(\mathbf{r}_w)] \tag{6}$$

$$I(\mathbf{r}, \hat{\mathbf{s}}) = \frac{Q\,\delta[\hat{s} - \hat{s}_o(\mathbf{r}_w)]}{\pi R^2}\exp\left[-\int_0^s \beta \mathrm{d}s''\right] + \frac{1}{4\pi}\frac{Q}{\pi R^2}\int_0^s \int_W R_d^s(\mathbf{r}_w, \mathbf{r}')\mathrm{d}A\,\exp\left[-\int_0^{s'} \beta \mathrm{d}s''\right]\beta \mathrm{d}s' \tag{7}$$

Let us define

$$R_d^s(W, \mathbf{r}') = \frac{1}{\pi R^2}\int_W R_d^s(\mathbf{r}_w, \mathbf{r}')\mathrm{d}A \quad 1/\mathrm{m}^3 \tag{8}$$

Here we could take two ways to calculate $R_d^s(W, \mathbf{r}')$. One way is to emit abundant bundles which are uniformly distributed within the disk W along the same direction of the collimated irradiation, and to simulate the bundles' traveling by the Monte Carlo

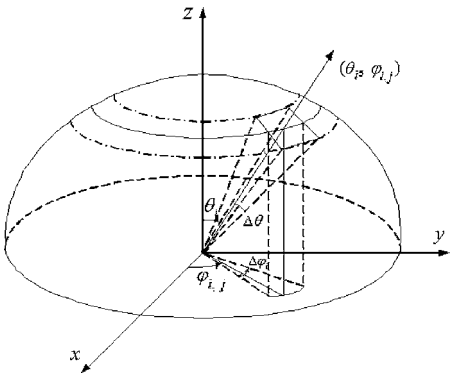

Fig. 3 Discrete angles of θ_i and $\varphi_{i,j}$ and their steps, constant $\Delta\theta$ and variable $\Delta\varphi_i$, in the hemisphere solid angle space

method. In order to obtain statistically averaged results, the number of the bundles should be set as large as, for example in this study, 1,000,000. It is a time-consuming way.

The other way is that, at first, we should only track the traveling of the bundles emitted from the center point of the disk, $\mathbf{r}_o$, and get $R_d^s(\mathbf{r}_o, \mathbf{r}')$. For this purpose, the number of the bundles needed will be much smaller than that for the first method mentioned above, and 100,000 bundles are enough here.

As shown in Fig. 2(*b*), point $H(r,\varphi)$ is located arbitrarily in the collimated irradiation disk, and the DRESOR value for the point $H(r,\varphi)$ to an arbitrary point $J_1(x,z)$, is recorded as $R_d^s(\mathbf{r}_H, \mathbf{r}_{J_1})$. The projection of point $J_1(x,z)$ on the x axis of the top boundary surface is $J_1'(x,0)$. A point $J_2(x',z)$ exists, with $J_2'(x',0)$ as its projection on the x axis, satisfying $HJ_1' = OJ_2'$. Then, $OJ_2' = HJ_1' = \sqrt{r^2+x^2-2xr\cos\varphi}$. Due to the homogeneity of the medium and the symmetrically collimated irradiation source,

$$R_d^s(\mathbf{r}_H, \mathbf{r}_{J_1}) = R_d^s(\mathbf{r}_o, \mathbf{r}_{J_2})$$

So, the integration over the whole disk W by the following equation leads to the DRESOR values of the collimated irradiation for an arbitrary point in the medium,

$$\begin{aligned} R_d^s(W, \mathbf{r}_{J_1}) &= R_d^s[W,(x,z)] \\ &= \frac{1}{\pi R^2}\int_W R_d^s(\mathbf{r}_H, \mathbf{r}_{J_1})\mathrm{d}A \\ &= \frac{1}{\pi R^2}\int_0^{2\pi}\int_0^R R_d^s[\hat{\mathbf{r}}_O, (\sqrt{r^2+x^2-2xr\cos\varphi}, z)]r\mathrm{d}r\mathrm{d}\varphi \end{aligned} \tag{9}$$

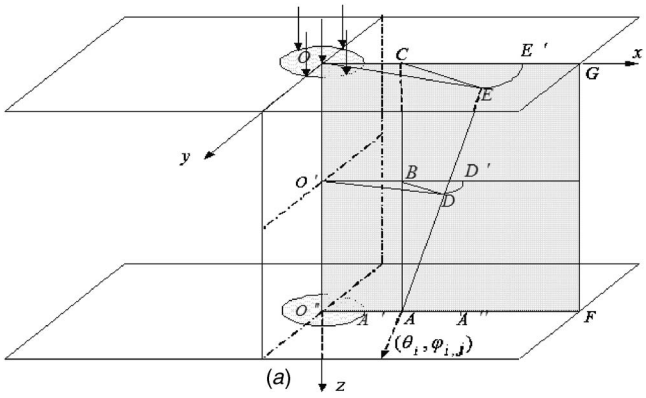

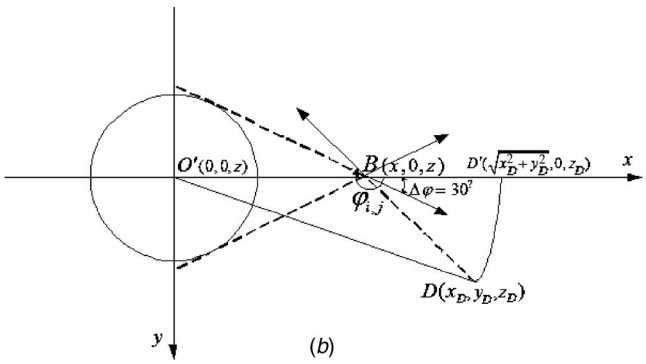

Fig. 4 Geometry of the discrete direction $(\theta_i, \varphi_{i,j})$ traversing the layer in the three-dimensional space (a), and the projection of the horizontal plane at O' on the x-y plane (b)

Substituting Eq. (8) into Eq. (7), the solution for the collimated radiation by the DRESOR method can be obtained as

$$\begin{aligned} I(\mathbf{r},\hat{\mathbf{s}}) = {} & \frac{Q\delta[\hat{s}-\hat{s}_o(\mathbf{r}_w)]}{\pi R^2} \\ & \times\exp\left[-\int_0^s \beta\mathrm{d}s''\right] \\ & + \frac{Q}{4\pi}\int_0^s R_d^s(W,\mathbf{r}')\exp\left[-\int_0^{s'}\beta\mathbf{d}s''\right]\beta\mathrm{d}s' \end{aligned} \tag{10}$$

The first term in the right-hand side of the above equation is denoted as $I_1(\mathbf{r},\hat{\mathbf{s}})$, which is contributed directly by the collimated irradiation, and the second term is denoted as $I_2(\mathbf{r},\hat{\mathbf{s}})$, which is

Table 1 M_i, the number and $\Delta\varphi_i$, the angle step of discrete $\varphi_{i,j}$ for different θ_i

i	θ_i (deg)	$\Delta\varphi_i$ (deg)	M_i	i	θ_i (deg)	$\Delta\varphi_i$ (deg)	M_i	i	θ_i (deg)	$\Delta\varphi_i$ (deg)	M_i
0	0	360.0	1	16	32	2.975	121	32	64	1.748	206
1	2	51.43	7	17	34	2.813	128	33	66	1.722	209
2	4	24.00	15	18	36	2.687	134	34	68	1.698	212
3	6	15.65	23	19	38	2.553	141	35	70	1.674	215
4	8	11.61	31	20	40	2.449	147	36	72	1.659	217
5	10	9.231	39	21	42	2.353	153	37	74	1.636	220
6	12	7.660	47	22	44	2.264	159	38	76	1.622	222
7	14	6.545	55	23	46	2.195	164	39	78	1.607	224
8	16	5.714	63	24	48	2.118	170	40	80	1.600	225
9	18	5.143	70	25	50	2.057	175	41	82	1.593	226
10	20	4.615	78	26	52	2.000	180	42	84	1.586	227
11	22	4.235	85	27	54	1.946	185	43	86	1.579	228
12	24	3.871	93	28	56	1.895	190	44	88	1.572	229
13	26	3.600	100	29	58	1.856	194	45	90	1.572	229
14	28	3.364	107	30	60	1.818	198				
15	30	3.158	114	31	62	1.782	202				

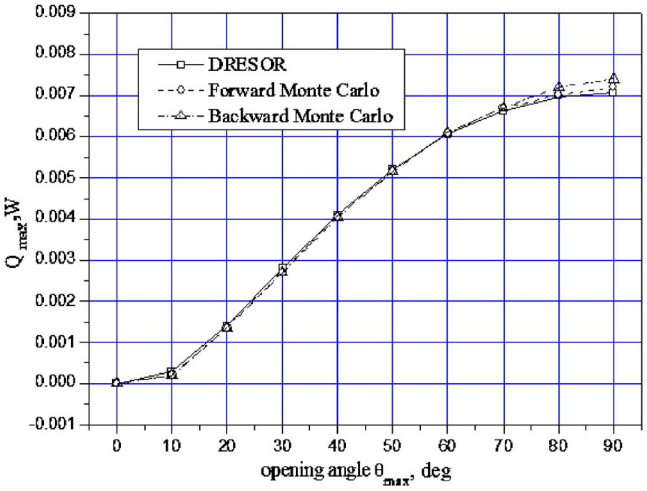

Fig. 5 Comparisons of the fluxes incident on the detector located at point *A* by the DRESOR method and by Modest [1] for varying acceptance angles for case 1

contributed indirectly by the collimated irradiation due to scattering of the medium.

2.3 Calculation of the DRESOR Values. The outline of the method for calculation of the DRESOR values can be found in [9,10] following the general procedure of the READ method [14], a Monte Carlo method. The studies on the radiative transfer problems by the Monte Carlo methods are still active now [15,16]. The treatments for the bundles' traveling in the medium, such as random determination of the emitting direction and position, the length of the traveling path, the attenuation of the energy E_0 due to absorption, and the change of the traveling direction due to scattering, etc., are all as described in [9,10,14]. All the initial DRESOR values are set to zero in the beginning of the calculation. Once ΔR_d^s, an updating for a DRESOR value, is obtained, R_d^s can be renewed by

$$R_{d,\text{new}}^s = R_{d,\text{old}}^s + \Delta R_d^s \tag{11}$$

The updating for $R_d^s(\mathbf{r}_w, \mathbf{r}')$ can be calculated as [10]

$$\Delta R_d^s(\mathbf{r}_w, \mathbf{r}') = C_0 \frac{E_0}{N_0}\{1 - \omega(\mathbf{r}')\exp(-|\Delta\tau(\mathbf{r}')|)\} \tag{12}$$

where $\mathbf{r}_w$ refers to the initial position, $\mathbf{r}'$ is the position being passed, $\Delta\tau$ is the optical distance through which the bundle passes the discrete volume containing $\mathbf{r}'$. For the collimated irradiation studied here, if the discrete volume for the passed position is $\Delta V(\mathbf{r}')$, the factor C_0 is $1/\Delta V(\mathbf{r}')$. Here, $\Delta V(\mathbf{r}') = \Delta V(x_{i'}, z_{j'}) = \pi(x_{i'+1}^2 - x_{i'}^2)\cdot(z_{j'+1} - z_{j'})$, and

$$C_0 = 1/\Delta V(x_{i'}, z_{j'}) = 1/[\pi(x_{i'+1}^2 - x_{i'}^2)\cdot(z_{j'+1} - z_{j'})]$$

where i', j', refer to the discrete x and z coordinates, respectively.

2.4 Determination of Discrete Directions $(\theta_i, \varphi_{i,j})$. The most significant advantage of the DRESOR method is that it can give radiation intensity with high directional resolutions [9,10]. For the collimated irradiation problem studied in this paper, the radiation intensity varies with both positions and directions, and its directional space covers the whole 4π solid angle space. As shown in Fig. 3, taking a hemisphere as an example, the polar angle θ in $[0, \pi]$ is divided uniformly into N parts, and $\Delta\theta = \pi/N$,

$$\theta_i = \Delta\theta \cdot i, \quad i = 0,\ 1,\ \ldots\ N \tag{13}$$

The azimuthal angle φ in $[0, 2\pi]$ is divided into M_i parts for different θ_i, and $\Delta\varphi_i = 2\pi/M_i$,

$$\varphi_{i,j} = \Delta\varphi_i \cdot j, \quad j = 1,\ 2,\ \ldots,\ M_i \tag{14}$$

In principle, every discrete direction $(\theta_i, \varphi_{i,j})$ should have nearly the same small solid angle space, and then M_i, is just determined as below. When $\theta_i = 0 (i = 0)$, or $\theta_i = \pi (i = N)$, the azimuthal angles $\varphi_{0,1}$ and $\varphi_{N,1}$ are only divided into one direction and have arbitrary value in the range $[0, 2\pi]$, that means, $M_0 = M_N = 1$. The solid angle of the cone containing $\theta_i = 0 (i = 0)$ with inclined angle $\Delta\theta$ can be obtained as

$$\Omega_0 \approx \pi[\sin(\Delta\theta/2)]^2 \tag{15}$$

When $\theta_i = \Delta\theta \cdot i (i = 1, 2, \ldots, N)$, all the cones containing the discrete direction $(\theta_i, \varphi_{i,j})$ should have nearly the same solid angle as Ω_0. For θ_i, the solid angle covered by the torus centered in θ_i and with inclined angle $\Delta\theta$ can be obtained as

$$\Omega_i \approx 2\pi \sin\theta_i \Delta\theta \tag{16}$$

So, the division of Ω_i by Ω_0 is just equal nearly to M_i, that is

$$M_i = \text{int}[\Omega_i/\Omega_0] = \text{int}[2\pi \sin\theta_i \Delta\theta/(\pi(\sin(\Delta\theta/2)))^2]$$
$$= \text{int}[2\Delta\theta \sin(\Delta\theta \cdot i)/(\sin(\Delta\theta/2))^2] \tag{17}$$

By the above-mentioned way, when $N = 90$, we have $\Delta\theta = \pi/90$, and the discrete numbers M_i of $\varphi_{i,j}$ for different θ_i are shown in Table 1. For the hemisphere, the total number of the discrete directions of $(\theta_i, \varphi_{i,j})$ is 6658. So, the whole 4π solid angle space is divided into $6658 \times 2 = 13{,}316$ discrete solid cones. It is stated that there are no serious problems in increasing the directional resolution for the intensity in the DRESOR method, such as $N = 180$ $(\Delta\theta = \pi/180)$, $N = 360$ $(\Delta\theta = \pi/360)$, etc.

2.5 Computation of Intensity in the Discrete Positions and Directions. The intensity varies not only with the polar angle θ_i but also with the azimuthal angle $\varphi_{i,j}$. The zones where the line of a discrete direction $(\theta, \varphi_{i,j})$ traverses are in three-dimensional space, but the DRESOR distribution is obtained in the two-

Table 2 Comparison of the results by the DRESOR method and Monte Carlo method

Radiative parameters, m^{-1}	Methods	Q_{absorb}, W	$Q_{\text{out}}^{\text{direct}}$, W	$Q_{\text{out}}^{\text{indirect}}$, W		Q_{out}, W
				$Q_{\text{out}}^{\text{down}}$	$Q_{\text{out}}^{\text{up}}$	
$\sigma_s = 0.1$	MCM	0	90.4328	4.7030	4.7459	99.8817
$k_a = 0.0$	DRESOR	0	90.4837	4.7171	4.6917	99.8925
$\sigma_s = 1.0$	MCM	0	36.6925	29.2582	33.9866	99.9373
$k_a = 0.0$	DRESOR	0	36.7880	29.2955	33.7385	99.8220
$\sigma_s = 10.0$	MCM	0	0.0043	15.4570	84.4595	99.9563
$k_a = 0.0$	DRESOR	0	0.0045	15.4112	84.3890	99.8047

Table 3 Four cases studied with different radiative properties

Radiative parameters, m^{-1}	Case 1	Case 2	Case 3	Case 4
k_a	0.0	0.25	0.5	0.75
σ_s	1.0	0.75	0.5	0.25

dimensional plane in this study. As shown in Fig. 4(*a*), the symmetric characteristics of the medium and the collimated irradiation are utilized again to simplify the calculation, that means, the DRESOR values of those points are equal to those which are with the same z coordinate and the same distance to the z axis in the x-y plane. For example, when the intensity of point A in the direction $(\theta_i, \varphi_{i,j})$ is calculated, the line of integration starting from point A along the inverse direction of $(\theta_i, \varphi_{i,j})$ traverses point D and ends at point E on the top boundary. The DRESOR values in the points $D(x_D, y_D, z_D)$ and $E(x_E, y_E, z_E)$ can be replaced by those in the corresponding points $D'(\sqrt{x_D^2+y_D^2}, 0, z_D)$ and $E'(\sqrt{x_E^2+y_E^2}, 0, z_E)$, due to $\overline{OE'}=\overline{OE}$, $\overline{O'D'}=\overline{O'D}$.

Let us give a computation procedure for intensity at the point $A(x,z)$ in the direction $(\theta_i, \varphi_{i,j})$, $I[(x,z),(\theta_i,\varphi_{i,j})]$. At first, considering $0 \le \theta_i \le \pi/2$. As shown in Fig. 4(*a*), if the point (x,z) is shadowed directly by the collimated irradiation, which means that $0 \le x \le R$, the direct part of $I[(x,z),(\theta_i,\varphi_{i,j})]$, $I_1[(x,z),(\theta_i,\varphi_{i,j})]$, will take a nonzero value as the direction $(\theta_i, \varphi_{i,j})$ coincides with the direction of the collimated irradiation. So,

$$I_1[(x,z),(\theta_i,\varphi_{i,j})] = \frac{Q\,\delta[\hat{s}-\hat{s}_0(\mathbf{r}_w)]}{\pi R^2} \exp\left[-\sum_0^z \beta \Delta z''\right] \quad (18)$$

Along the path of $\overline{AE}$, z' is selected as the calculation variable, which is the same coordinate of points O' and D' in the z axis. As shown in Fig. 4(*b*), $\overline{BD}=(z-z')\tan\theta_i$,

Table 4 $R_{dL}^{s}[\mathbf{r}_o, \mathbf{r}'(x,z)]$ for three columns of discrete zones, 1: $0 \le x \le 1$ cm, 2: 1 cm $< x \le 2$ cm, and 3: 2 cm $< x \le 3$ cm for case 1

	x, cm				x, cm		
z, cm	1	2	3	z, cm	1	2	3
1	3195.497	7.11167	4.01837	51	1950.417	10.43025	5.98583
2	3183.128	12.58396	6.59005	52	1926.156	9.95733	6.38726
3	3152.156	13.59487	7.39208	53	1907.545	9.93871	5.80366
4	3123.311	13.83153	7.6985	54	1886.193	9.52642	6.21423
5	3096.023	14.58036	7.77832	55	1867.168	10.10103	5.92048
6	3061.289	14.89549	8.13111	56	1848.295	10.1004	5.56725
7	3033.414	15.08269	7.82525	57	1830.191	9.80713	5.80119
8	3002.616	13.91701	8.33642	58	1816.273	9.78503	5.68107
9	2970.976	15.41751	8.55688	59	1795.835	9.56754	5.7758
10	2944.901	15.12178	8.79656	60	1778.946	9.62497	5.41335
11	2908.613	15.32945	9.29013	61	1759.698	8.95878	5.41403
12	2885.368	14.08924	9.08186	62	1744.678	9.16837	5.37539
13	2856.332	14.34667	8.80509	63	1724.882	8.47984	5.74533
14	2832.699	14.86504	8.83015	64	1711.324	9.12739	5.701
15	2799.886	14.36487	8.38744	65	1693.753	9.25658	5.90989
16	2774.061	14.59056	8.01294	66	1675.822	8.85745	5.72633
17	2748.544	14.24436	8.38657	67	1661.382	9.82671	5.54641
18	2718.971	14.33763	8.76614	68	1647.826	9.66385	5.257
19	2686.979	14.35183	8.59249	69	1631.843	8.94653	5.39395
20	2663.985	14.02433	8.33981	70	1613.583	8.29755	5.00992
21	2639.84	14.19942	8.74637	71	1595.296	8.75908	4.84422
22	2605.468	13.33262	8.01129	72	1580.509	8.76396	5.39493
23	2582.88	13.68075	8.32501	73	1564.075	7.9286	5.4014
24	2554.53	13.06715	7.85683	74	1548.765	8.24249	5.06383
25	2531.393	12.98293	7.63703	75	1538.416	7.96437	5.08561
26	2505.977	13.14761	7.60326	76	1518.676	7.9898	4.99411
27	2487.994	13.64646	7.8005	77	1505	7.94313	4.59319
28	2459.579	13.4525	7.89855	78	1488.775	7.87532	4.76926
29	2434.682	13.29079	8.09358	79	1474.686	7.5985	5.11416
30	2408.239	12.90552	7.91943	80	1459.856	7.67162	4.83511
31	2386.498	14.21984	7.86714	81	1445.313	7.70942	4.45658
32	2361.878	12.45273	7.65271	82	1428.84	7.50067	4.25459
33	2340.258	12.89162	7.948	83	1415.441	7.67126	4.38255
34	2315.055	12.51401	7.73438	84	1403.41	7.69959	4.41817
35	2291.657	12.65122	7.37025	85	1386.771	7.64852	4.42553
36	2267.476	12.21726	7.87836	86	1374.513	7.69231	4.48428
37	2241.825	11.79945	6.92354	87	1360.938	7.5756	4.36778
38	2220.767	11.25295	6.78168	88	1340.642	7.62021	4.14055
39	2199.112	11.403	6.82586	89	1328.872	7.62339	4.2739
40	2181.224	12.28468	6.84356	90	1316.748	6.95915	3.98434
41	2156.589	11.43014	7.22494	91	1304.81	6.93369	4.06515
42	2133.949	11.15346	7.51728	92	1288.003	6.28855	4.187
43	2112.311	11.55018	7.3795	93	1277.402	6.7879	3.84635
44	2096.101	12.26994	7.00149	94	1265.793	6.48244	3.52893
45	2068.623	11.3463	6.84806	95	1251.881	6.55649	4.12721
46	2046.789	11.0598	6.79055	96	1239.938	6.06304	3.45532
47	2026.352	10.89537	6.64856	97	1227.636	5.98192	3.57969
48	2006.164	10.83355	6.17466	98	1213.096	5.82069	3.51198
49	1989.403	11.17371	6.4645	99	1201.191	5.67236	2.99164
50	1968.898	11.11101	6.76066	100	1188.883	5.01762	2.85189

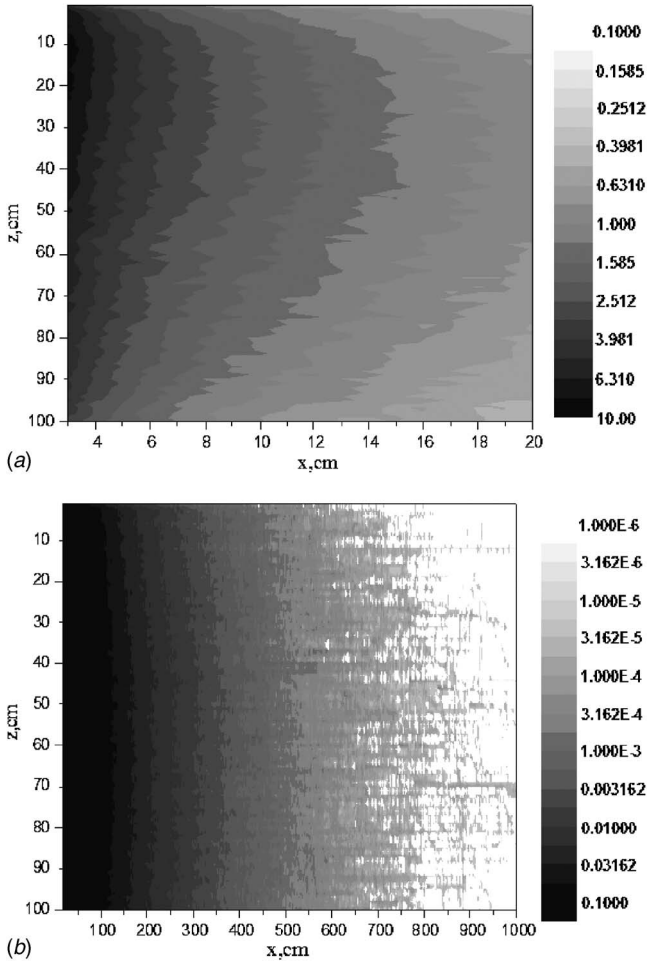

Fig. 6 Two-dimensional distribution of $R_d^s[\mathbf{r}_o, \mathbf{r}'(x,z)]$ for 3 cm $< x \leq 20$ cm (a) and 20 cm $< x \leq 10$ m (b) for case 1

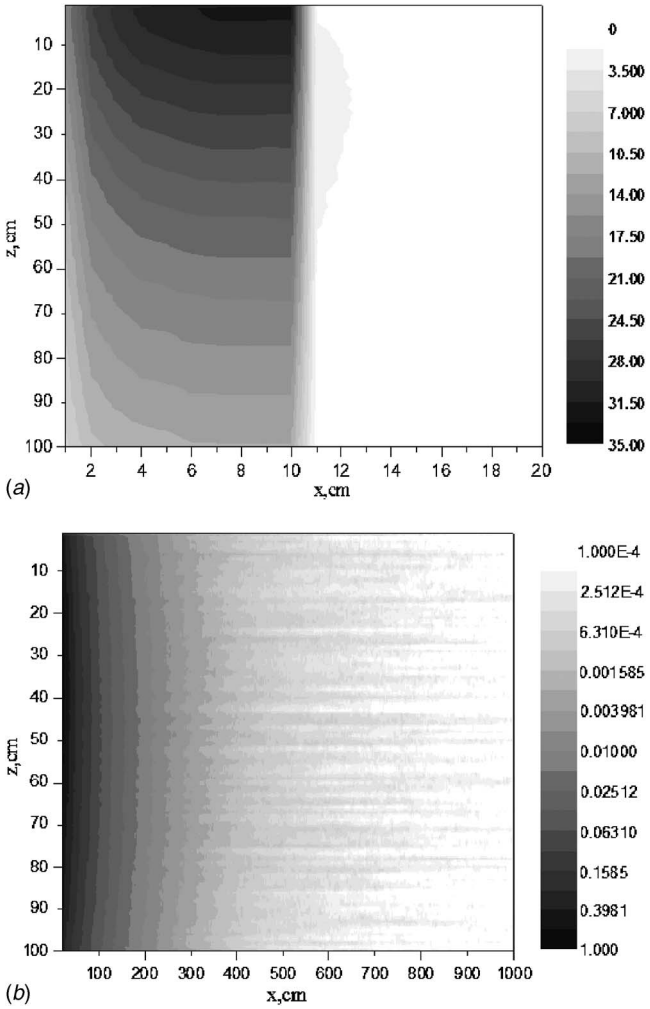

Fig. 7 Two-dimensional distribution of $R_d^s[W, \mathbf{r}'(x,z)]$ for $x \leq 20$ cm (a) and 20 cm $< x \leq 10$ m (b) for case 1

$$\overline{O'D} = \overline{O'D'} = \sqrt{[x + (z - z')\tan\theta_i \cos\varphi_{i,j}]^2 + [(z - z')\tan\theta_i \sin\varphi_{i,j}]^2} \tag{19}$$

then

$$R_d^s(W,D) = R_d^s(W,D') \tag{20}$$

The indirect part of the intensity, $I_2[(x,z),(\theta_i,\varphi_{i,j})]$, can be obtained as

$$I_2[(x,z),(\theta_i,\varphi_{i,j})] = \frac{Q}{4\pi}\sum_0^z \left\{ R_d^s(W,D')\exp\left[-\sum_0^{z'} \beta\Delta z''/\cos\theta_i \right] \times \beta\Delta z'/\cos\theta_i \right\} \tag{21}$$

In a summary, the intensity $I[(x,z),(\theta_i,\varphi_{i,j})]$ with $0 \leq \theta_i \leq \pi/2$ is

$$I[(x,z),(\theta_i,\varphi_{i,j})] = I_1[(x,z),(\theta_i,\varphi_{i,j})] + I_2[(x,z),(\theta_i,\varphi_{i,j})] \tag{22}$$

For $\pi/2 < \theta_i \leq \pi$, $I_1((x,z),(\theta_i,\varphi_{i,j})) = 0$, and

$$I[(x,z),(\theta_i,\varphi_{i,j})] = I_2[(x,z),(\theta_i,\varphi_{i,j})] = \frac{Q}{4\pi}\sum_L^z \left\{ R_d^s[W,(\overline{O'D},z')] \times \exp\left[-\sum_{z'}^{z} \beta\Delta z''/\cos\theta_i \right] \times \beta\Delta z'/\cos\theta_i \right\} \tag{23}$$

Now, we consider a detector with downward normal direction and varying acceptance angles, $\theta_{\max}$, $0 \leq \theta_{\max} \leq \pi/2$. There is $N_{\max}$ so that $N_{\max} = \text{int}[\theta_{\max}/\Delta\theta]$. After the intensity is obtained, the radiation flux incident on the detector can be calculated as

$$q^{\text{down}}_{\theta_{\max}}(x,z) = \sum_{i=0}^{N_{\max}} \sum_{j=0}^{M_i} I[(x,z),(\theta_i,\varphi_{i,j})]\sin\theta_i \cos\theta_i \Delta\theta\Delta\varphi_j \tag{24}$$

If the radiation flux incident on a detector with upward normal direction and varying acceptance angles, $\theta_{\max}$, $\pi/2 \leq \theta_{\max} \leq \pi$, is needed, that is

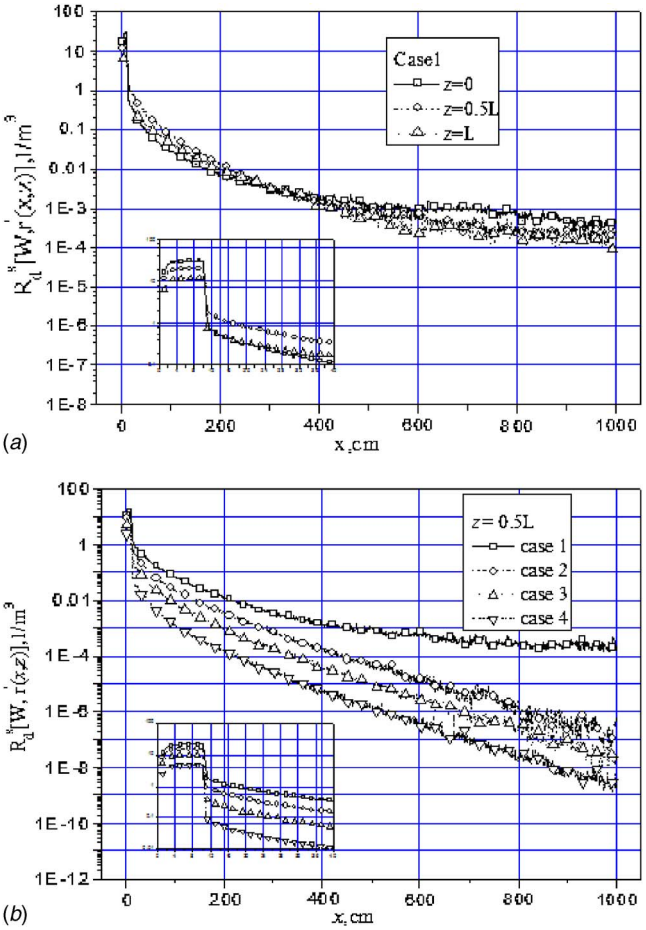

Fig. 8 $R_d^s[W,\mathbf{r}'(x,z)]$ **varied with** x **at** $z=0$, $z=0.5L$, **and** $z=L$ **for case 1 (a), and at** $z=0.5L$ **for the four cases (b)**

$$q^{\mathrm{up}}_{\theta_{\max}}(x,z)=\sum_{i=N}^{N-N_{\max}}\sum_{j=1}^{M_i} I[(x,z),(\theta_i,\varphi_{i,j})]\sin\theta_i|\cos\theta_i|\Delta\theta\Delta\varphi_j \tag{25}$$

and the total radiation flux can be obtained as

$$q(x,z)=q^{\mathrm{down}}_{\theta_{\max}}(x,z)-q^{\mathrm{up}}_{\theta_{\max}}(x,z) \tag{26}$$

3 Computation Accuracy and Efficiency

3.1 Computation Accuracy. A one-dimensional layer $0\le z\le L=1$ m of a gray, purely isotropically scattering medium was considered. On the top boundary surface of the layer, the collimated irradiation of strength $Q=100$ W is normally incident and equally distributed over the disk $0\le r\le R=10$ cm, as shown in Fig. 2. A small detector with 2 cm×2 cm in size and opening angle $\theta_{\max}$ is located on the bottom surface at $x_A=20$ cm, $z_A=L$. It is needed to determine the flux incident on the detector for varying acceptance angle [1,11]. The maximum zone in the x axis for the calculation is taken as $x_{\max}=10$ m, the number of grids is 1000, and so one discrete zone had $\Delta x=1$ cm. 100 grids are used in the z axis direction for the layer, and $\Delta z=1$ cm. In the DRESOR method, the total number of energy bundles incident on the central point O of the disk W from the collimated irradiation was chosen as 100,000.

Validation was made by comparison between the results got by the present method with those of Modest [1], as shown in Fig. 5. The flux incident on the detector for varying acceptance angle calculated by the present method agrees well with that of Modest with high precision.

A further validation was made by the law of energy conservation for the system. The total energy leaving the top and bottom surfaces, Q_{out}, should be equal to the energy of collimated irradiation incident into the purely scattering media, Q, if no absorption occurs, $Q_{\mathrm{absorb}}=0$. A direct part of energy leaving the bottom disk after being attenuated by scattering is $Q_{\mathrm{out}}^{\mathrm{direct}}$, which is just the integration of $I_1[(x,z),(\theta_i,\varphi_{i,j})]$ over the hemispheric space and the bottom surface. The energy leaving the top and bottom surfaces and being scattered at least one time by the medium are $Q_{\mathrm{out}}^{\mathrm{down}}$ and $Q_{\mathrm{out}}^{\mathrm{up}}$, respectively, which are integrations of $I_2[(x,z),(\theta_i,\varphi_{i,j})]$ over the hemispheric space and on the top and bottom surfaces, respectively. Then, $Q_{\mathrm{out}}^{\mathrm{indirect}}=Q_{\mathrm{out}}^{\mathrm{up}}+Q_{\mathrm{out}}^{\mathrm{down}}$.

Comparisons between the results by the DRESOR method and the Monte Carlo method were made with different scattering coefficient σ_s, as shown in Table 2. In the Monte Carlo method, the number of energy bundles for the collimated irradiation uniformly distributed on the whole disk W is 1,000,000. For different σ_s, the total energy leaving the layer, $Q_{\mathrm{out}}=Q_{\mathrm{out}}^{\mathrm{indirect}}+Q_{\mathrm{out}}^{\mathrm{direct}}$, is almost equal to Q (100 W), and the errors are all less than 1%. The comparisons show excellent agreement.

From Table 2 it is seen that, as the scattering coefficient σ_s increases, the energy passing directly through the layer and leaving the bottom surface, $Q_{\mathrm{out}}^{\mathrm{direct}}$, decreases obviously; meanwhile, the energy leaving the two surfaces becomes larger. There are different trends for $Q_{\mathrm{out}}^{\mathrm{down}}$ and $Q_{\mathrm{out}}^{\mathrm{up}}$. As the scattering coefficient σ_s increases, $Q_{\mathrm{out}}^{\mathrm{down}}$ increases at first, and then decreases. It can be easily understood. A larger scattering coefficient makes the effect of scattering more significant; but a scattering coefficient that is too large makes the collimated irradiation difficult to pass through the layer. It is not the case for $Q_{\mathrm{out}}^{\mathrm{up}}$; the larger the scattering coefficient becomes, the larger $Q_{\mathrm{out}}^{\mathrm{up}}$ appears.

3.2 Computation Efficiency. Due to the Monte Carlo characteristic of the method, the DRESOR method is concerned about the computation efficiency. In general, the computational efficiency of the DRESOR method is lower than other methods, such as the DO method, FVM, etc., for some simple objectives, for example, 1D plane-parallel systems, if only integrated quantities, such as radiation flux, incident radiation, are needed. But the intensity with high directional resolutions can only be provided by the DRESOR method, which is the most significant advantage of the method. Compared with the general Monte Carlo method, the DRESOR method can save computational time through only computing the DRESOR values for one time. The comparison for computation efficiency between the MCM and DRESOR method to calculate irradiation onto a detector located on point A from the collimated source was made. The variances of all the data were less than 2%. All the DRESOR values are obtained in 8.2 s by an Intel Celeron 2.4 G with 256 RAM with 100,000 bundles. Then it takes about 1 s to get the radiative intensity in all 13,316 discrete angles and the radiation flux at one position. But for the Monte Carlo method, 1,000,000 bundles and 138.3 s are needed to achieve the same calculation accuracy for the radiation flux at the position.

4 Results and Discussion

In order to show the effect of scattering on the radiative intensity and flux, four cases were studied here, as shown in Table 3. In all four cases, the attenuation coefficient is kept constant as 1.0 m^{-1} with different scattering albedo. At first, the DRESOR value distributions would be given.

4.1 DRESOR Values. The DRESOR value distribution is the key in the DRESOR method. $R_d^s[\mathbf{r}_o,\mathbf{r}'(x,z)]$ refers to the DRESOR value distribution in the x-z plane for the collimated irradiation incident on the central point of the impinging disk, W. The finest zone used in the calculation by the Monte Carlo method

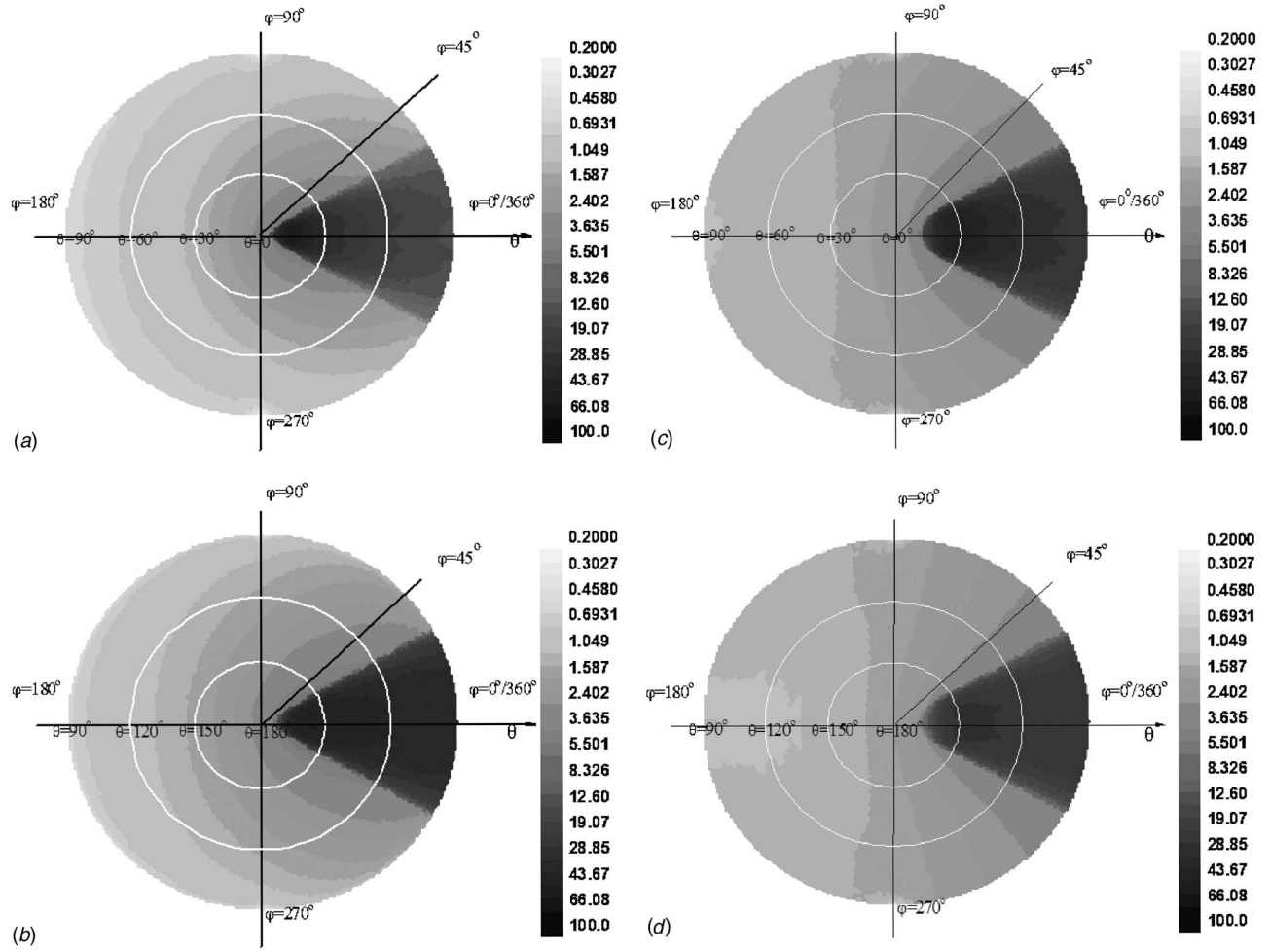

Fig. 9 $I(\theta_i, \varphi_{i,j})$ **at point** ***A*** **as** θ **within [0 deg, 90 deg] (a), at point** ***C*** **as** θ **within (90 deg, 180 deg) (b), at point** ***B*** **as** θ **within [0 deg, 90 deg] (d), and at point** ***B*** **as** θ **within (90 deg, 180 deg) (d) for case 1**

is 1 cm × 1 cm in the x-z plane, which means that all the energy bundles emitted from the origin point O of the x-z plane are propagating along the z axis with $x=0$ cm before they are scattered. Table 4 shows the DRESOR values for the three discrete zones, $0 \le x \le 1$ cm, 1 cm $< x \le 2$ cm, and 2 cm $< x \le 3$ cm, varied with z for case 1.

It can be seen that all the DRESOR values in the discrete zone $0 \le x \le 1$ cm vary from 1000 m^{-3} to 3200 m^{-3}, being significantly larger than those in the other two zones. It is explained as below. The scattering processes occurring in the discrete zone $0 \le x \le 1$ cm mainly appear in the z axis where all the energy bundles are emitted. If the discrete zone becomes finer, the DRESOR values also become larger, because the DRESOR values are normalized in a unit volume, 1 m^{-3}. If the discrete zone becomes zero, the DRESOR values will tend to infinite, because the ratios of the energy scattered within the zone are not zero, but the volume of the zone tends to zero. The DRESOR values for 3 cm $< x \le 20$ cm and 20 cm $< x \le 1000$ cm are shown in Figs. 6(a) and 6(b). All the energy passing through the zones with $x > 1$ cm comes from the scattered energy, and the DRESOR values are less than 20 m^{-3}. As x increases, the DRESOR values decay quickly, and they are about 15 m^{-3}, 2 m^{-3}, 0.1 m^{-3}, and 0.0001 m^{-3} for the zones around 2 cm, 10 cm, 100 cm, and 1000 cm, respectively, caused by the scattering effect.

From Eq. (9), $R_d^s[W, \mathbf{r}'(x,z)]$ can be obtained from $R_d^s[\mathbf{r}_o, \mathbf{r}'(x,z)]$, and its distribution can be found in Figs. 7(a) and 7(b) for 0 cm $< x \le 20$ cm and 20 cm $< x \le 1000$ cm, respectively. It can be seen from Fig. 7(a) that the DRESOR values for the zones under the collimated irradiation region (0 cm $< x \le 10$ cm) are all larger than those in the other regions, but the magnitudes decreased to about 35 m^{-3}. It is explained as below. For a point $\mathbf{r}'(x,z)$ with 0 cm $< x \le 10$ cm, in the total energy scattered in the discrete zone including $\mathbf{r}'(x,z)$, only a small part comes directly from the irradiation on the point $(x,0)$ in the disk W, and all the rest comes indirectly from the irradiation on the disk except the point $(x,0)$ by scattering, which is smaller than that coming directly from the irradiation on the point $(x,0)$, as indicated in Table 4.

Figure 8 shows $R_d^s[W, \mathbf{r}'(x,z)]$ varied with x at $z=0$, $z=0.5L$, and $z=L$ in the medium for the case 1 (a), and at $z=0.5L$ for the four cases (b). It can be seen that, for the zones under the region of collimated irradiation, 0 cm $\le x \le 10$ cm, the DRESOR values decrease as z increases. This is caused by the attenuation of the medium. For the zones out of the region of collimated irradiation, 10 cm $< x \le 10$ m, the DRESOR values decrease as x increases, and do not vary significantly at a fixed x, as shown in Fig. 8(a), when z changes.

$R_d^s[W, \mathbf{r}'(x,0.5L)]$ varied with x at $z=0.5L$ for the four cases with different scattering and absorption coefficients are shown in Fig. 8(b). For case 1 with $\sigma_s = 1.0$ m^{-1} and $k_a = 0.0$ m^{-1}, a purely scattering case, the DRESOR values are all larger than those in the other cases. As k_a increases and σ_s decreases while the attenuation coefficient remains constant, $k_a + \sigma_s = 1.0$ m^{-1}, more energy

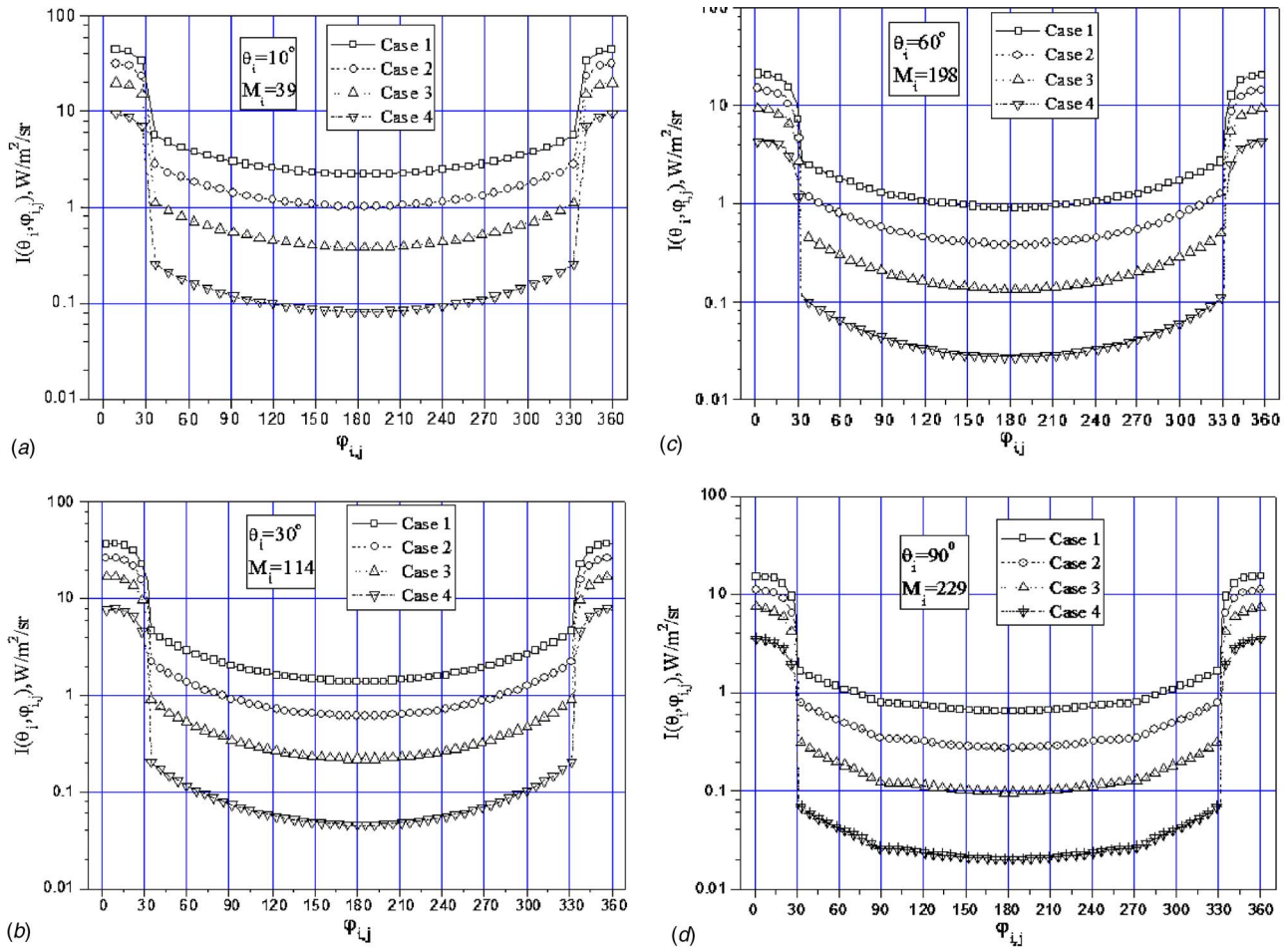

Fig. 10 $I(\theta_i, \varphi_{i,j})$ **in point** A **as** θ_i**=10 deg (a),** θ_i**=30 deg (b),** θ_i**=60 deg (c), and** θ_i**=90 deg (d) for the four cases, respectively**

is absorbed along the propagation of the bundle, and the scattering effect becomes weakened, so the fraction of the scattered energy decreases, resulting in an obvious decrease of the DRESOR values.

4.2 Radiative Intensity. The intensity varied with θ, the polar angle, and φ, the azimuthal angle, with high directional resolution in points A, B, and C for case 1 is shown in Figs. 9(a)–9(d). From all the figures, there is a fan-shaped zone around the direction $\varphi=0$ deg with boundaries of $\varphi=\pm 30$ deg where the intensity is larger than 5 W/(m^2 sr), since the direction lines within this fan-shaped zone inversely traverse the shadowed region of the collimated irradiation, as shown in Fig. 4(b), where the tangents of the disk W passing through the point B or A had $\Delta\varphi = \pm 30$ deg.

The intensity of point A is not zero as θ within [0 deg, 90 deg] and has the maximum value of 64.4 W/(m^2 sr), as shown in Fig. 9(a); for cases 2, 3, and 4, the maximum intensity is 46.1, 29.4, and 14.1 W/(m^2 sr), respectively; it is zero as θ within (90 deg, 180 deg). In contrast, the intensity of point C is not zero as θ within (90 deg, 180 deg) and has the maximum value of 53.8 W/(m^2 sr), as shown in Fig. 9(b); for cases 2, 3, and 4, the maximum intensity is 38.2, 24.2, and 11.5 W/(m^2 sr), respectively; it is zero as θ within [0 deg, 90 deg].

For the point B which is located inside the medium, its intensity is not zero as θ within the whole range of [0 deg, 180 deg], and shown in Fig. 9(c) as θ within [0 deg, 90 deg] with the maximum intensity of 55.9 W/(m^2 sr), and in Fig. 9(d) as θ within (90 deg, 180 deg) with the maximum intensity of 31.7 W/(m^2 sr), respectively. The maximum intensity for θ within [0 deg, 90 deg] is 40.1, 25.8, and 12.4 W/(m^2 sr), and that for θ within (90 deg, 180 deg) is 22.5, 14.3, and 6.8 W/(m^2 sr) for cases 2, 3, and 4, respectively.

The distributions of $I(\theta_i, \varphi_{i,j})$ for the point A for the four cases with different typical θ_i are shown in Figs. 10(a)–10(d). As shown in these figures, when the scattering coefficient decreases and the absorption coefficient increases from cases 1 to 4, the intensity decreases significantly in all directions of (θ, φ). From Figs. 10(a)–10(d), it can also be seen that there are obvious drops for the intensity as $\varphi=30$ deg and $\varphi=330$ deg or -30 deg.

It can be imaged that, using the forward Monte Carlo method, it is almost not possible to give the intensity in so many discrete directions as up to $2\times 6658 = 13{,}316$ ones. Even for the backward Monte Carlo method, it is also not easy to emit many energy bundles from every discrete direction one by one for the total 13,316 discrete directions. In the DRESOR method, it is only needed to repeat calculation by Eqs. (18)–(23), and not necessary to repeat calculation for the DRESOR values.

4.3 Radiative Flux. Consider that the same detectors are located on points O, O', O'' A', A'', B, and C. The fluxes incident on these detectors for varying acceptance angles can be obtained by Eqs. (24) and (25), and the results are shown in Figs. 11(a)–11(c) for case 1. Due to the collimated irradiation incident on the top surface, the DRESOR values for the upper medium are larger than those for the lower medium, so, as shown in Fig. 11(a), the fluxes incident on the detector C are larger than those on detectors B and A. As shown in Fig. 11(b), as θ within [0 deg, 90 deg], the detec-

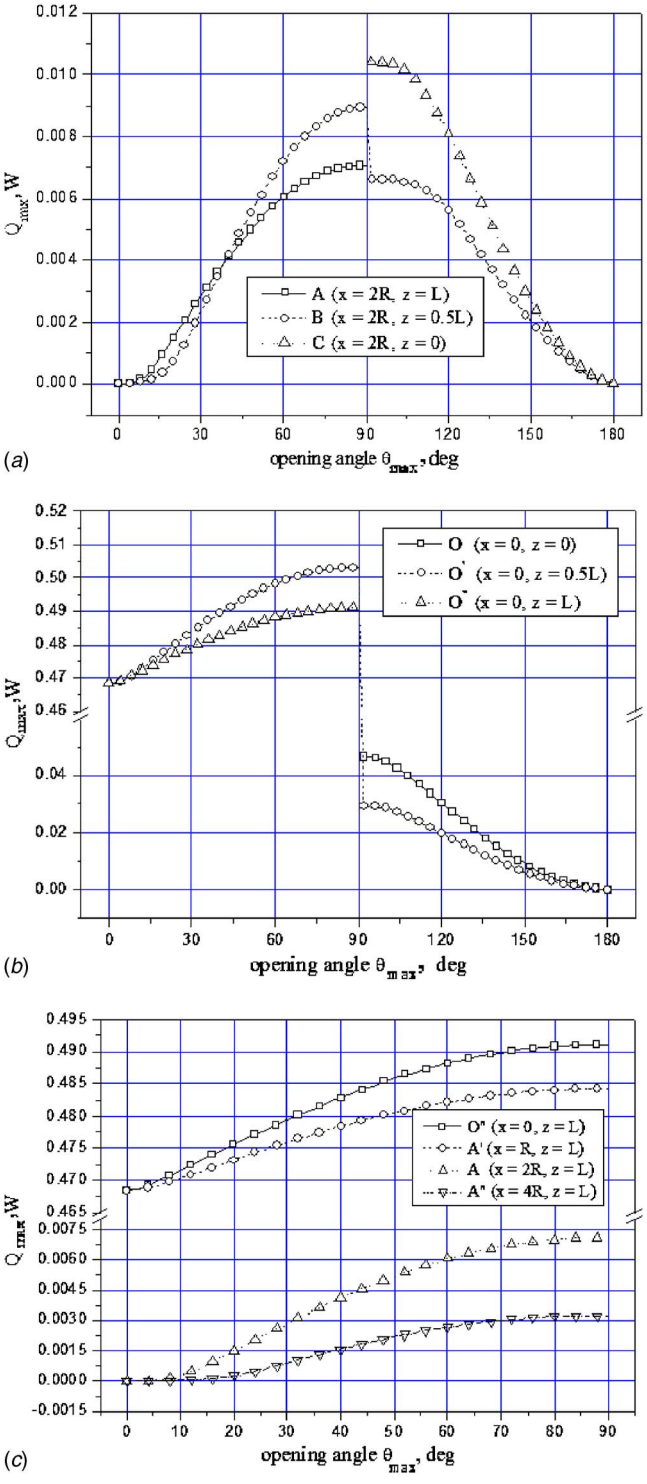

Fig. 11 The flux incident on detectors at points *A*, *B* and *C* (a), at points *O*, *O′*, and *O″* (b), and at points *O″*, *A′*, *A*, and *A″* (c) varied with the opening angle θ_{max} for case 1

tors O' and O'' can receive more energy directly from the collimated irradiation, and the fluxes incident on them as θ within [0 deg,90 deg] are larger than those incident on the detectors O and O' as θ within (90 deg,180 deg) by almost one order in magnitude.

Comparisons are also made for the detectors O'', A', A, and A'' located in the bottom surface. As shown in Fig. 11(*c*), since detectors O'' and A' are located under the disk of collimated irradiation, they can accept more energy, and the fluxes incident on them as θ within [0 deg,90 deg] are larger than those incident on the detectors A and A'' by almost two orders in magnitude.

Some typical radiative fluxes leaving the two surfaces along the x axis for cases 1–4 are given in Table 5. Since there is a direct component energy leaving the bottom surface, the fluxes under the region of the collimated irradiation on the bottom surface as $x \leq 0.1$ m are obviously larger than other regions as $x > 0.1$ m. Table 5 also shows the variation of the radiative fluxes as the optical coefficients change. When the scattering coefficient σ_s decreases and absorption coefficient k_a increases, the energy absorbed by the medium increases, and the energy leaving the top and bottom surfaces decreases, leading to reduced radiative fluxes $q(x,L)$ and $q(x,0)$.

In fact, using the forward Monte Carlo method, it is easy to calculate radiative fluxes such as $q(x,L)$ and $q(x,0)$, but the difficulty is that, if it is necessary to get the flux incident on a point within different opening angles, the number of the energy bundles would increase up to a large level which is hard to be accepted. For the backward Monte Carlo method, it is efficient to get the flux incident on a point within a special opening angle as compared to the forward Monte Carlo method, but if such information is desired in many points and for many directions, the calculation procedure will be repeated again and again, resulting in a low efficiency.

5 Concluding Remarks

The DRESOR method based on the Monte Carlo method was applied to solve the radiative heat transfer process in an isotropically scattering layer exposed to collimated radiation. In the DRESOR method, the fractions of energy scattered by the scattering medium to the energy of collimated irradiation are calculated by the Monte Carlo method, leading to the distribution of DRESOR values inside the two-dimensional medium for different scattering albedo. The DRESOR values are only governed by the radiative properties and the geometry of the space. The flux obtained by the DRESOR method agreed well with that in the literature, and more comparisons were made by the energy conservation law, all showing good accuracy. The comparisons for computation efficiency between the MCM and DRESOR method were made, and the DRESOR method is more efficient than MCM. In order to show the distinguished features of the DRESOR method, the two-dimensional intensity in 13,316 discrete directions varied with the polar and azimuthal angles at some typical points were shown for the first time as we knew, and this is not easy for the existing methods, such as forward and backward Monte Carlo methods. After the intensity varied with the polar and azimuthal angles is obtained, the flux incident on a detector with different opening angles can be easily obtained, as well as the radiation flux across any point inside the medium.

Acknowledgment

The present study has been partially supported by the Teaching and Research Award Program (1999) for Outstanding Young Teachers in Higher Institutions of The Ministry of Education, P. R. China, and the National Natural Science Foundation of China (No. 50546021).

Nomenclature

A = area, m^2
C_0 = compensating factor defined in Eq. (13), m^{-3}
E_0 = relative energy of energy bundles
I = radiation intensity, $W/(m^2\ sr)$
I_1, I_2 = direct and indirect parts of radiation intensity defined in Eqs. (18) and (21), respectively, $W/(m^2\ sr)$
I_{ow} = collimated irradiation intensity, $W/(m^2\ sr)$

Table 5 Distributions of radiative flux across the bottom surface, $q(x,L)$, and the top surface, $q(x,0)$, for all four cases

	$q(x,L)$, W/m^2				$q(x,0)$, W/m^2			
x, m	Case 1	Case 2	Case 3	Case 4	Case 1	Case 2	Case 3	Case 4
0.01	1227.735	1210.718	1199.544	1182.863	116.77	83.897	61.532	26.547
0.02	1227.686	1210.676	1199.462	1182.856	116.73	83.89	61.366	26.467
0.03	1227.831	1210.78	1199.218	1182.893	117.58	83.85	60.831	25.696
0.04	1227.624	1210.62	1198.816	1182.855	117.36	83.703	59.922	25.671
0.05	1226.975	1210.138	1198.242	1182.705	116.03	82.714	58.607	25.37
0.06	1225.878	1209.335	1197.483	1182.455	113.6	80.935	56.872	24.82
0.07	1224.249	1208.122	1196.48	1182.073	109.89	78.215	54.559	23.961
0.08	1222.107	1206.571	1195.265	1181.576	104.92	74.582	51.698	22.81
0.09	1219.166	1204.401	1193.662	1180.887	98.137	69.615	47.995	21.229
0.10	1214.76	1201.169	1191.329	1179.842	88.488	62.522	42.852	18.94
0.20	18.586	11.855	7.4574	3.0647	27.871	18.239	11.704	4.8761
0.30	11.871	7.2081	4.3323	1.723	15.435	9.5677	5.8398	2.3448
0.40	8.3836	4.8813	2.8263	1.0946	9.9439	5.8731	3.4303	1.3352
0.50	6.2138	3.4864	1.9543	0.73979	6.9289	3.9151	2.1974	0.83153
0.60	4.7365	2.5665	1.3945	0.51673	5.0502	2.7372	1.4805	0.54553
0.70	3.6711	1.9203	1.0127	0.36724	3.7992	1.9786	1.0335	0.37115
0.80	2.9072	1.475	0.75776	0.27011	2.9322	1.4714	0.7433	0.26052
0.90	2.3165	1.1396	0.57027	0.19935	2.3085	1.1176	0.54733	0.18745
1.00	1.8688	0.89211	0.43569	0.14956	1.8426	0.86292	0.41001	0.13747
2.00	0.31562	0.1136	0.04476	0.01311	0.30616	0.10636	0.04004	0.01112
3.00	0.081	0.02182	0.00748	0.00199	0.08024	0.02068	0.00669	0.00166
4.00	0.02718	0.00488	0.00142	3.19e-4	0.02813	0.00475	0.00133	2.82e-4
5.00	0.01243	0.00129	3.43e-4	7.57e-5	0.01327	0.00126	3.22e-4	6.63e-5
6.00	0.00712	3.47e-4	8.39e-5	1.69e-5	0.00791	3.58e-4	8.11e-5	1.55e-5
7.00	0.00482	1.03e-4	2.39e-5	4.93e-6	0.0055	1.07e-4	2.24e-5	4.06e-6
8.00	0.0033	3.51e-5	6.00e-6	9.61e-7	0.00385	3.59e-5	6.02e-6	9.30e-7
9.00	0.0024	1.19e-5	1.82e-6	3.02e-7	0.00266	1.18e-5	1.83e-6	2.84e-7
10.0	9.82e-4	2.86e-6	4.52e-7	7.70e-8	0.00112	2.84e-6	4.53e-7	7.02e-8

L = thickness of the one-dimensional layer, m
M_i = numbers of discrete $\varphi_{i,j}$ for different θ_i
N = number of discrete polar angles
N_0 = number of energy bundles used in the Monte Carlo method
$\hat{\mathbf{n}}$ = normal vector of surface
q = radiative flux, W/m^2
q_0 = radiative flux of collimated irradiation, W/m^2
Q = strength of collimated irradiation, W
Q_{absorb} = energy absorbed by the medium, W
Q_{out} = energy leaving the layer, W
$Q_{\text{out}}^{\text{direct}}$ = energy directly leaving the bottom surface, W
$Q_{\text{out}}^{\text{down}}$ = energy leaving the bottom surface by scattering, W
$Q_{\text{out}}^{\text{up}}$ = energy leaving the top surface by scattering, W
R_d^s = DRESOR values
r = radius, m
$\mathbf{r}$ = position vector
$\mathbf{r}_o$ = position vector of the center point of the impinging disk
R = radius of the impinging disk by collimated irradiation, m
S = source function
s = distance, m
$\hat{\mathbf{s}}$ = direction vector
W = impinging disk by collimated irradiation
k_a = absorption coefficient, m^{-1}
σ_s = scattering coefficient, m^{-1}
β = extinction coefficient, m^{-1}
$\theta_{\max}$ = acceptance angle of the detector
θ = polar angle, $[0, \pi]$
φ = azimuthal angle, $[0, 2\pi]$
ω = scattering albedo
τ = optical thickness
Ω = solid angle
Φ = scattering phase function

Superscripts

up = upward direction
down = downward direction

Subscripts

old = old value before updating
new = new value after updating
max = maximum value
O = original point
η = wave number
i,j = discrete direction
i',j' = discrete grid
W = wall surface
x,y,z = rectangular coordinates

References

[1] Modest, M. F., 1992, "Backward Monte Carlo Simulations in Radiative Heat Transfer," ASME J. Heat Transfer, **35**(12), pp. 3323–3333.
[2] Lacrox, D., Jeandel, G., and Boudot, C., 1998, "Solution of the Radiative Transfer Equation in an Absorbing and Scattering Nd:YAG Laser-induced Plume," J. Appl. Phys., **84**, pp. 2443–2449.
[3] Wu, S. C., and Wu, C. Y., 1997, "Radiative Heat Transfer in a Two-dimensional Cylindrical Medium Exposed to Collimated Radiation," Int. Commun. Heat Mass Transfer, **24**(4), pp. 475–484.
[4] Modest, M. F., and Tabanfar, S., 1983, "A Multidimensional Differential Approximation for Absorbing/Emitting Anisotropically Scattering Media with Collimated Irradiation," J. Quant. Spectrosc. Radiat. Transf., **29**, pp. 339–351.
[5] Menguc, M. P., and Manickavasagam, S., 1993, "Inverse Radiation Problem in Axisymmetric Cylindrical Scattering Media," J. Thermophys. Heat Transfer, **7**(3), pp. 479–486.
[6] Siewert, C. E., 1993, "An Inverse Source Problem in Radiative Transfer," J. Quant. Spectrosc. Radiat. Transf., **50**(6), pp. 603–609.
[7] Silva Neto, A. J., and Ozisik, M. N., 1995, "An Inverse Problem of Simultaneous Estimation of Radiation Phase Function, Albedo and Optical Thickness," J. Quant. Spectrosc. Radiat. Transf., **53**, pp. 397–409.
[8] Zhou, H. C., Lou, C., Cheng, Q., Jiang, Z. W., He, J., Huang, B. Y., Pei, Z. L., and Lu, C. X., 2005, "Experimental Investigations on Visualization of Three-dimensional Temperature Distributions in a Large-scale Pulverized-coal-fired Boiler Furnace," Proc. Combust. Inst., **30**(1), pp. 1699–1706.
[9] Zhou, H. C., Chen, D. L., and Cheng, Q., 2004, "A New Way to Calculate Radiative Intensity and Solve Radiative Transfer Equation Through Using the Monte Carlo Method," J. Quant. Spectrosc. Radiat. Transf., **83**, pp. 459–481.

[10] Zhou, H. C., and Cheng, Q., 2004, "The DRESOR Method for the Solution of the Radiative Transfer Equation in Gray Plane-parallel Media," in *Proceedings of the Fourth International Symposium on Radiative Transfer*, Istanbul, Turkey, M. P. Menguc and N. Selcuk, eds., pp. 181–190.
[11] Modest, M. F., 2003, *Radiative Heat Transfer*, 2nd ed., Academic, New York.
[12] Zhou, H. C., Cheng, Q., Huang, Z. F., and He, C., 2006, "The Influence of Anisotropic Scattering on the Radiative Intensity in a Gray, Plane-Parallel Medium Calculated by the DRESOR Method," J. Quant. Spectrosc. Radiat. Transf., **104**(1), pp. 99–115.
[13] Zhou, H. C., and Cheng, Q., 2006, "The DRESOR Method for the Transient Radiative Transfer in an Isotropically Scattering Plane-Parallel Medium," in *Proceedings of the Eurotherm Seminar 78: Computational Thermal Radiation in Participating Media II*, Poitiers, France, D. Lemonnier, N. Selcuk, and P. Lybaert, eds., pp. 105–114.
[14] Yang, W. J., H. Taniguchi, and K. Kudo, 1995, "Radiative Heat Transfer by the Monte Carlo Method," in *Advances in Heat Transfer*, J. P. Hartnett and F. T. Irvines, eds., Academic, San Diego, Vol. 27, pp. 1–215.
[15] Daun, K. J., Morton, D. P., and Howell, J. R., 2005, "Smoothing Monte Carlo Exchange Factors Through Constrained Maximum Likelihood Estimation," ASME J. Heat Transfer, **127**, pp. 1124–1128.
[16] Lu, Xiaodong, and Hsu, Pei-feng, 2004, "Reverse Monte Carlo Method for Transient Radiative Transfer in Participating Media," ASME J. Heat Transfer, **126**, pp. 621–627.

Numerical Study of Laminar Forced Convection Fluid Flow and Heat Transfer From a Triangular Cylinder Placed in a Channel

Arnab Kumar De[1]
e-mail: arkde@iitk.ac.in

Amaresh Dalal
e-mail: amaresh@iitk.ac.in

Department of Mechanical Engineering,
Indina Institute of Technology Kanpur,
Kanpur-208 016, India

Computational study of two-dimensional laminar flow and heat transfer past a triangular cylinder placed in a horizontal channel is presented for the range $80 \leq Re \leq 200$ and blockage ratio $1/12 \leq \beta \leq 1/3$. A second-order accurate finite volume code with nonstaggered arrangement of variables is developed employing momentum interpolation for the pressure-velocity coupling. Global mode of cross-stream velocity oscillations predict the first bifurcation point increases linearly with blockage ratio with no second bifurcation found in the range of Re studied. The Strouhal number and rms of lift coefficient increase significantly with blockage ratio and Reynolds number while overall Nusselt number remains almost unchanged for different blockage ratios. At lower blockage ratios, flow is found to be similar to the unconfined flow and is more prone to wake instability. Instantaneous streak lines provide an excellent means of visualizing the von Kármán vortex street. [DOI: 10.1115/1.2712848]

Keywords: triangular cylinder, blockage, onset, vortex shedding, heat transfer, streak lines

1 Introduction

Flow past bluff bodies has been a topic of intense research in fluid mechanics for a long time. It is of relevance to many practical applications, such as electronic cooling, heat exchanger systems, offshore structures, suspension bridges, chimneys, and acoustic emission. It also embodies a great deal of academic interest due to a range of fluid mechanical issues it presents. In recent years, it has received attention in terms of both numerical and experimental studies as a result of ever increasing computational power and advent of new experimental techniques.

It is understood that above a critical Reynolds number, flow around slender cylindrical bodies, in general, exhibits the well-known time-periodic vortex shedding as a result of the Bénard–von Kármán instability leading to alternate vortical structures known as the von Kármán vortex street. This phenomenon is responsible for fluctuating forces on the body that may cause structural vibrations, acoustic noise emissions, and some times resonance triggering the failure of structures. Thus, it is important from engineering point of view to investigate flow around slender bodies with different shapes.

In the confined cylinder flow, blockage ratio of the channel plays a dominant role. Davis et al. [1] studied the confined flow past a square cylinder for a wide range of Reynolds numbers and two different blockage ratios ($\beta = 1/6$ and $1/4$) both experimentally and numerically. A maximum Strouhal number was observed at $Re = 200-350$, depending on the blockage ratio. In their study, the Reynolds number was based on the maximum velocity of the inflow profile. For higher Reynolds numbers, the Strouhal number decreases and reaches an almost constant level. Mukhopadhyay et al. [2] carried out two-dimensional (2D) numerical simulations of flow past a square cylinder in a channel in the range $90 \leq Re \leq 1200$ at two blockage ratios, $\beta = 1/4$ and $1/8$. Strouhal number was seen to increase with increase in blockage ratio. Suzuki et al. [3] performed simulations for $53.6 \leq Re \leq 225$ and $1/20 \leq \beta \leq 1/5$. They reported that the maximum Strouhal number was found at $Re = 150$ for a blockage ratio of $1/5$. In an another study, Suzuki and Suzuki [4] conducted a numerical as well as experimental study for a heated cylinder placed in a channel at $\beta = 1/10$, $1/5$, and $1/3$. They found that high-vorticity wall layers play an important role on the criss-cross motion of the von Kármán vortices and the augmentation of heat transfer from the channel walls. In their numerical study on vortex shedding from a square cylinder, Hwang and Yao [5] indicated that the presence of the walls had a strong effect on the properties of the generated vortices, which altered the lift and drag coefficients. Sohankar et al. [6] studied confined flow over a square cylinder at incidence to investigate the influence of Re and angle of incidence on Strouhal number, lift, drag, and base suction coefficients. Breuer et al. [7] carried out numerical investigation on 2D flow past a square cylinder inside a channel ($\beta = 1/8$) for $0.5 \leq Re \leq 300$. They compared the accuracy of two numerical techniques, namely, the lattice-Boltzmann automata (LBA) and finite volume method (FVM). Study of critical values of Re predicting transition from steady to periodic flow over a square cylinder for different blockage ratios by Turki et al. [8] reported Re_{cr} to be 62, 85, and 120 for $\beta = 1/8$, $1/6$, and $1/4$, respectively. Sharma and Eswaran [9] performed a numerical investigation on the flow structure and heat transfer characteristics for a square cylinder in cross flow for both unconfined and channel confined ($\beta = 1/10$ to $1/2$ in steps of $1/10$) flows at $Re = 50$, 100, 150 and $Pr = 0.7$. For both uniform heat flux and constant cylinder temperature cases, enhancement of the cylinder Nusselt number due to channel confinement increases with blockage ratios with maximum enhancement obtained at the lowest Reynolds number.

Jackson [10] examined the onset of periodic behavior in two-dimensional laminar flow past bodies of various shapes in freestream. He reported the critical Reynolds number as 34.318 and corresponding Strouhal number as 0.13554 for an isosceles triangle with base 1 and height 0.8. Zielinska and Wesfreid [11] numerically investigated the wake flow behind an equilateral tri-

[1]Corresponding author.

Contributed by the Heat Transfer Division of ASME for publication in the JOURNAL OF HEAT TRANSFER. Manuscript received November 7, 2005; final manuscript received June 30, 2006. Review conducted by Louis C. Burmeister.

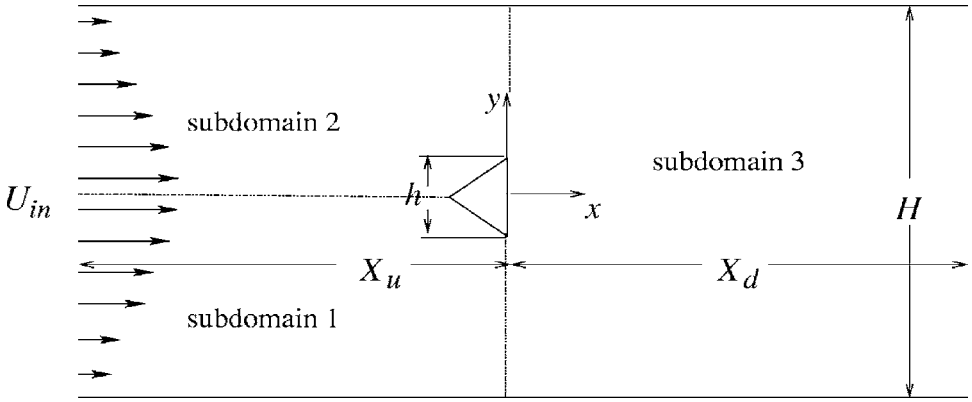

Fig. 1 Flow geometry with dimensions

angular obstacle with a blockage ratio of 1/15. They found a critical Reynolds number of 38.3, which was further confirmed by the experiments of Wesfreid et al. [12]. Abbassi et al. [13] studied the structure of laminar flow and heat transfer from a built-in triangular prism placed in a differentially heated channel. The transition from symmetric to periodic flow was observed at Re=45 for a blockage ratio of 1/4. An augmentation of ~85% in the time-averaged overall Nusselt number was recorded at Re=250 in the presence of a triangular prism compared to that obtained without a prism. Recently, Johansson et al. [14] computed turbulent flow past triangular-shaped flame holders using k-ε model. To the best of our knowledge, there are comparatively fewer laminar flow and heat transfer studies on the channel confined flow around triangular cylinder, which has mainly motivated the present work.

The organization of this paper is as follows. After a brief statement of the problem, governing equations along with boundary conditions are compiled. In Sec. 3, a brief discussion on the numerical method is presented, which is followed by validation and grid refinement test results. In Sec. 4, results for onset of vortex shedding, unsteady flow and heat transfer, integral parameters, Strouhal number, and Nusselt number are reported with relevant discussions followed by information on visualization of wake. The paper ends with the conclusions that summarize the findings.

1.1 Statement of the Problem. The present paper focuses on the laminar unsteady flow and heat transfer of air (Pr=0.71) past an equilateral triangular cylinder of side h placed in a channel of height $H=1/\beta$ in the range $80 \le \mathrm{Re} \le 200$ and $1/12 \le \beta \le 1/3$. Figure 1 shows the geometry in detail where an upstream length $X_u=10h$ and a downstream length $X_d=25h$ has been used.

2 Governing Equations and Boundary Conditions

The set of equations that govern the two-dimensional, laminar, incompressible forced convection fluid flow and heat transfer with constant fluid properties are continuity, momentum, and the energy equations, written in normalized form

$$\frac{\partial u_j}{\partial x_j} = 0 \tag{1}$$

$$\frac{\partial u_j}{\partial t} + \frac{\partial (u_j u_k)}{\partial x_k} = -\frac{\partial p}{\partial x_j} + \frac{1}{\mathrm{Re}} \frac{\partial^2 u_j}{\partial x_k \partial x_k} \tag{2}$$

$$\frac{\partial \theta}{\partial t} + \frac{\partial (u_k \theta)}{\partial x_k} = \frac{1}{\mathrm{RePr}} \frac{\partial^2 \theta}{\partial x_k \partial x_k} \tag{3}$$

The scales used for the normalization are: side of the cylinder h for lengths, maximum velocity at the inlet $U_{\max}$ for velocity, and $(T-T_{\mathrm{in}})/(T_c-T_{\mathrm{in}})$ for temperature. Thus, the Reynolds number is defined as $\mathrm{Re}=U_{\max} h/\nu$.

Boundary conditions applied in the present simulation are as follows:

Inflow plane. A parabolic profile [7] for the streamwise velocity, Neumann condition for pressure, and specified temperature of the incoming air have been employed

$$u = 1 - 4\beta^2 y^2, \quad v = 0, \quad \frac{\partial p}{\partial x} = 0, \quad T = T_{\mathrm{in}} \quad t > 0, \quad x = -X_u,$$

$$-\frac{1}{2\beta} \le y \le \frac{1}{2\beta}$$

Solid boundaries. No-slip condition for velocity, normal gradient condition for pressure, and isothermal condition for temperature are used on the cylinder

$$u = v = 0, \quad \nabla p \cdot \hat{n} = 0$$

where $\hat{n}$ is the normal unit vector and $T=T_c$.

Channel walls. At the channel walls, which are adiabatic, the no-slip condition for velocity and Neumann condition of pressure is applied

$$u = v = 0, \quad \frac{\partial p}{\partial y} = 0, \quad \frac{\partial T}{\partial y} = 0 \quad t > 0$$

$$y = -\frac{1}{2\beta}, \frac{1}{2\beta}, \quad -X_u \le x \le X_d$$

Exit boundary. Flows with unsteady wake or convecting vortices, the boundary condition at the exit not only affects the quality of the solution but also the convergence properties of the numerical method. Convective boundary condition (CBC), which employs the first-order wave equation, facilitates undistorted passage of the flow structures across the domain and puts lesser constraint on the convergence behavior [15]. In the present study CBC has been used for velocity and temperature while pressure has been specified at the exit plane

$$\frac{\partial \phi}{\partial t} + U_{av} \frac{\partial \phi}{\partial x} = 0, \quad \phi = u, v, T; \quad p = 0 \quad t > 0, \quad x = X_d,$$

$$-1/2\beta \le y \le 1/2\beta$$

where U_{av} is the average streamwise velocity at the exit plane.

3 Numerical Details

The governing equations are reduced to systems of simultaneous linear equations by integrating them over finite volumes covering the whole domain. Variables have been arranged in a nonstaggered manner with momentum interpolation, a variant of the classic Rhie Chow scheme [16] applied to unsteady flows, used for the velocity-pressure coupling. For computational conve-

nience, the domain has been divided into three subdomains, as shown in Fig. 1, facilitating the use of structured grids. An implicit Crank-Nicolson scheme has been used for the time integration of the governing equations. Convective terms have been discretized by a QUICK scheme [17] applied to nonuniform grids while the diffusive terms by the central difference scheme.

The integrated form of the continuity, momentum, and the energy equations are

$$\sum_f F_f^{n+1} = 0 \tag{4}$$

$$V_P \frac{u_{iP}^{n+1} - u_{iP}^n}{\Delta t} + \frac{1}{2}\left(\sum_f F_f^{n+1} u_{if}^{n+1} + \sum_f F_f^n u_{if}^n\right) = -\frac{1}{2}\left(\sum_f p_f^{n+1} S_{fi} + \sum_f p_f^n S_{fi}\right) + \frac{1}{2\,\mathrm{Re}}\left(\sum_f F_{df,u_i}^{n+1} + \sum_f F_{df,u_i}^n\right) \tag{5}$$

$$V_P \frac{\theta_P^{n+1} - \theta_P^n}{\Delta t} + \frac{1}{2}\left(\sum_f F_f^{n+1} \theta_f^{n+1} + \sum_f F_f^n \theta_f^n\right) = \frac{1}{2\,\mathrm{Re}\,\mathrm{Pr}}\left(\sum_f F_{df,\theta}^{n+1} + \sum_f F_{df,\theta}^n\right) \tag{6}$$

where P and f denote the cell center and cell faces, respectively, of a finite volume, and the indices $i=1,2$ refer to the streamwise (x) and cross-stream (y) directions, respectively.

3.1 Solution Algorithm. A provisional velocity field is calculated first from the momentum equations excluding the pressure gradient taking mass fluxes from the previous time

$$V_P \frac{u_{iP}^* - u_{iP}^n}{\Delta t} + \frac{1}{2}\left(\sum_f F_f^{n+1,l} u_{if}^* + \sum_f F_f^n u_{if}^n\right) = \frac{1}{2\,\mathrm{Re}}\left(\sum_f F_{df,u_i}^* + \sum_f F_{df,u_i}^n\right) \tag{7}$$

where l denotes counter of the flux loop, which is rotated until mass flux converges for all finite volumes. This velocity is devoid of the pressure gradient, which is then added to it at the finite volume faces to calculate mass flux at the faces

$$F_f = F_f^* - \Delta t (\nabla p)_f \cdot \mathbf{S}_f \tag{8}$$

where F_f^* is the mass flux computed from the volume interpolated provisional velocities at the cell faces

$$F_f^* = \rho \mathcal{L}(\mathbf{u}_P^*, \mathbf{u}_{nb}^*) \cdot \mathbf{S}_f \tag{9}$$

where operator $\mathcal{L}$ denotes volume interpolation

$$\mathcal{L}(\mathbf{u}_P^*, \mathbf{u}_{nb}^*) = \frac{\mathbf{u}_P^* V_{nb} + \mathbf{u}_{nb}^* V_P}{V_P + V_{nb}} \tag{10}$$

The mass flux of Eq. (8) when inserted into the discretized continuity equation, Eq. (4), the following equation for pressure is obtained, which is analogous to the pressure-correction equation of the SIMPLE-like algorithm [18]:

$$\sum_f F_f^{n+1,l+1} = \sum_f F_f^* - \Delta t \sum_f (\nabla p)_f \cdot \mathbf{S}_f = 0 \Rightarrow \sum_f (\nabla p)_f \cdot \mathbf{S}_f = \frac{1}{\Delta t}\sum_f F_f^* \tag{11}$$

This is the Poisson equation for pressure to be solved at each flux loop level. Within a time-step calculation, mass flux and the pressure field at the attainment of flux convergence give the divergence-free field, which is then used to compute the velocity field using Eq. (5) and the temperature using Eq. (6).

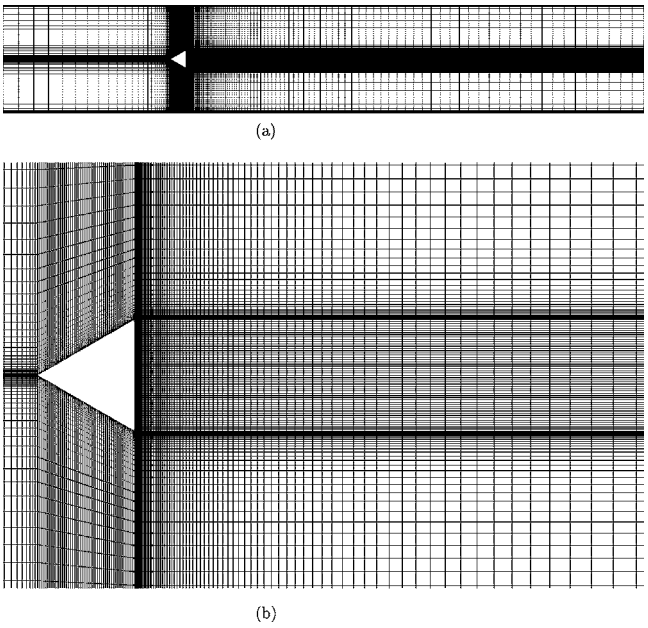

Fig. 2 A typical grid (200×122) used for $\beta=1/6$: (*a*) full view and (*b*) zoomed view

The sequential steps that constitute the solution method are written below.

1. Initialize u, v, p, θ at the solution points and apply boundary condition with mass flux, $F_f^{n+1,l} = F_f^n$
2. Solve Eq. (7) for $\mathbf{u}^*$
3. Compute F_f^* (from Eq. (9)), which is the source term in the pressure equation, Eq. (11)
4. Solve the pressure equation, Eq. (11)
5. Estimate new mass flux from Eq. (8) using new estimates of p obtained from step 4 and set the flux-loop counter $l=l+1$
6. Repeat steps 2–5 till convergence of the fluxes, $|F_f^{n+1,l+1} - F_f^{n+1,l}| < \epsilon$, where the norm is taken separately for all the faces over all the finite volumes
7. Solve Eq. (5) for $\mathbf{u}^{n+1}$ and Eq. (6) for θ using converged mass flux and pressure
8. Set $n=n+1$ and repeat steps 2–7 to march in time

The system of simultaneous linear equations arising from Eqs. (5)–(7) and (11) are solved by the SOR technique. The residue norm (in the root-mean-square sense) of the equations are computed after each complete sweep, and the solution is terminated once the norm goes below 10^{-6}. The flux convergence has been set at 10^{-7}.

A time increment, $\Delta t=0.01$ has been used for all cases studied with an upstream length $X_u=10$ and downstream length $X_d=25$. Three subdomains have been fitted with structured grids with adequate resolution near the solid boundaries and in the near wake region. Figure 2(*a*) shows the full grid and Fig. 2(*b*) the zoomed grid for $\beta=1/6$.

3.2 Computer-Code Validation. Results obtained with the present code have been compared to that of Breuer et al. [7] for flow past a square cylinder placed in a channel with blockage ratio $\beta=1/8$ in the range $50 \le \mathrm{Re} \le 200$ using 210×160 nonuniform grid. The time-averaged drag coefficient C_D and Strouhal number St compare well to values predicted by Breuer et al. [7], which used a finite volume method (FVM) employing 560×340 nonuni-

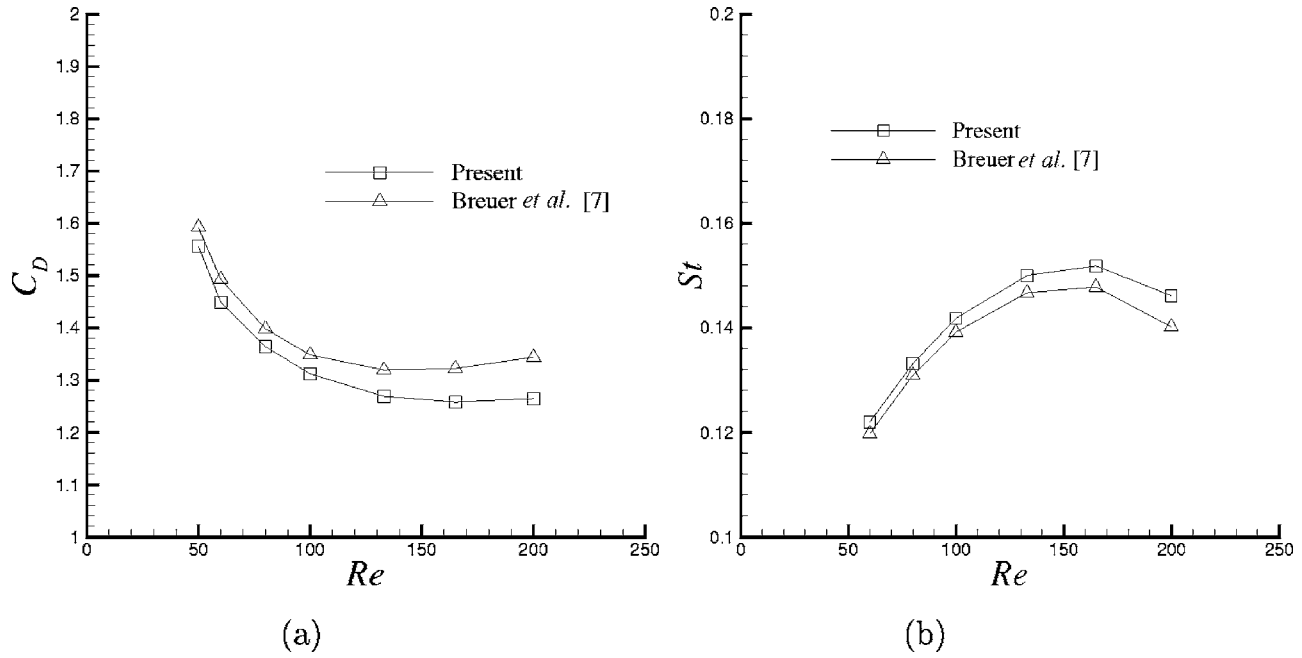

Fig. 3 Comparison with Breuer et al. [7]: (*a*) C_D and (*b*) St

form grid as shown in Figs. 3(*a*) and 3(*b*) respectively. The results are in good agreement with the published literature as C_D differs by at most 5%, whereas it is 4% for St.

3.3 Effect of Grid Refinement. Computations have been carried out for three progressively refined grids, namely, 135×84, 170×112, and 200×140, to reveal the effects of grid size. In these calculations we have limited ourselves to Re=100 at $\beta=1/6$ with $X_u=10$ and $X_d=25$. Number of grid nodes distributed over a side of the cylinder are 50, 60, and 70, respectively, at these three grid levels. During the refinement, the smallest and largest cell size has been maintained approximately at $\delta=0.004$ and $\Delta=0.5$, respectively. The results are summarized in Table 1. When we moved from the coarsest to the intermediate grid level, the variation in C_D and C_{Dp} were found to be ~9% while it was 5% for St and 11% for $C_{L\text{rms}}$. Further refining the grid diminished the variation in C_D,C_{Dp}, $C_{L\text{rms}}$, and St as can be seen from Table 1. The same observations were also made for average Nusselt numbers on the three faces of the cylinder. Thus, moving from the intermediate to the finest grid level leads to a difference below 1% for all the parameters except for St and $C_{L\text{rms}}$, whose variation were around 2% and 3%, respectively. This has lead us to use 200×140 grids for all subsequent calculations for $\beta=1/6$. Basing on the grid used for $\beta=1/6$ grids for other configurations with different blockage ratios have been selected.

Table 1 Results for grid refinement test with Re=100, X_u=10, X_d=25, and β=1/6

Parameter	135×84	170×112	200×140
C_D	1.492	1.625 (8.9)	1.610 (0.92)
C_{Dp}	1.079	1.179 (9.3)	1.168 (0.9)
$C_{L\text{rms}}$	0.1921	0.1728 (11.1)	0.1668 (3.6)
St	0.1859	0.1960 (5.4)	0.1910 (2.55)
Nu_r	2.563	2.745 (7.1)	2.748 (0.1)
Nu_t	6.104	6.470 (6)	6.482 (0.18)
Nu_b	6.117	6.477 (5.9)	6.488 (0.16)

4 Results

4.1 Onset of Vortex Shedding. The first Hopf bifurcation point, which marks the onset of vortex shedding leading to a well-established time-periodic flow, has been determined by considering global modes of velocity oscillations in the wake. In the present study, 29 equispaced axial stations in the wake, which are referred to as the history points, have been created at two different cross-stream locations, namely, $y=0$ and $y=0.5$. The cross-stream velocity has been recorded at these history points after flow attains the saturated state. For any blockage, calculation has been started at a Reynolds number considerably larger than the expected critical value. Computations at lower Reynolds number have been carried out taking the saturated state of the next higher Re as its initial field. At each Re, the code is allowed to run until changes in the peak-to-peak amplitude of velocity oscillations go below 10^{-4}. The maximum amplitude of oscillations of cross-stream velocity at different axial locations for $\beta=1/6$ are shown in Fig. 4(*a*) for $y=0$ and Fig. 4(*b*) for $y=0.5$. The amplitude of oscillations at any Re, as revealed by these Fig. 4, increases as one moves from the cylinder and after attaining a maximum value it decreases in the far wake. The global maximum amplitude increases with Re, and the location of its occurrence moves toward the cylinder. This fact has been observed at both the cross-stream locations, $y=0$ and $y=0.5$. Global maximum amplitude of velocity oscillations ($A_v^2(y=0)$) when plotted against Re, as shown in Fig. 4(*c*), shows a linear growth in the vicinity of critical Re. Extrapolation of the amplitudes to zero gives the Re_{cr}. Figure 4(*c*) shows the evaluation of the Re_{cr} for $\beta=1/6$ and $\beta=1/3$. For all blockages, predictions of Re_{cr} from the velocity signals at $y=0$ and $y=0.5$ are within 1%. Figure 4(*d*) shows the effect of blockage on the critical Reynolds number. A monotonically increasing linear relationship has been found between β and Re_{cr}.

4.2 Unsteady Vortex Shedding and Heat Transfer. At all blockage ratios, unsteady time-periodic flow has been found above the corresponding critical Reynolds number (Re_{cr}). Unsteady vortex shedding and heat transfer is described here, as shown in Figs. 5–10, using instantaneous stream lines (*a*)-(*d*), vorticity contours (*e*)-(*h*) and isotherms (*i*)-(*l*) at four equispaced

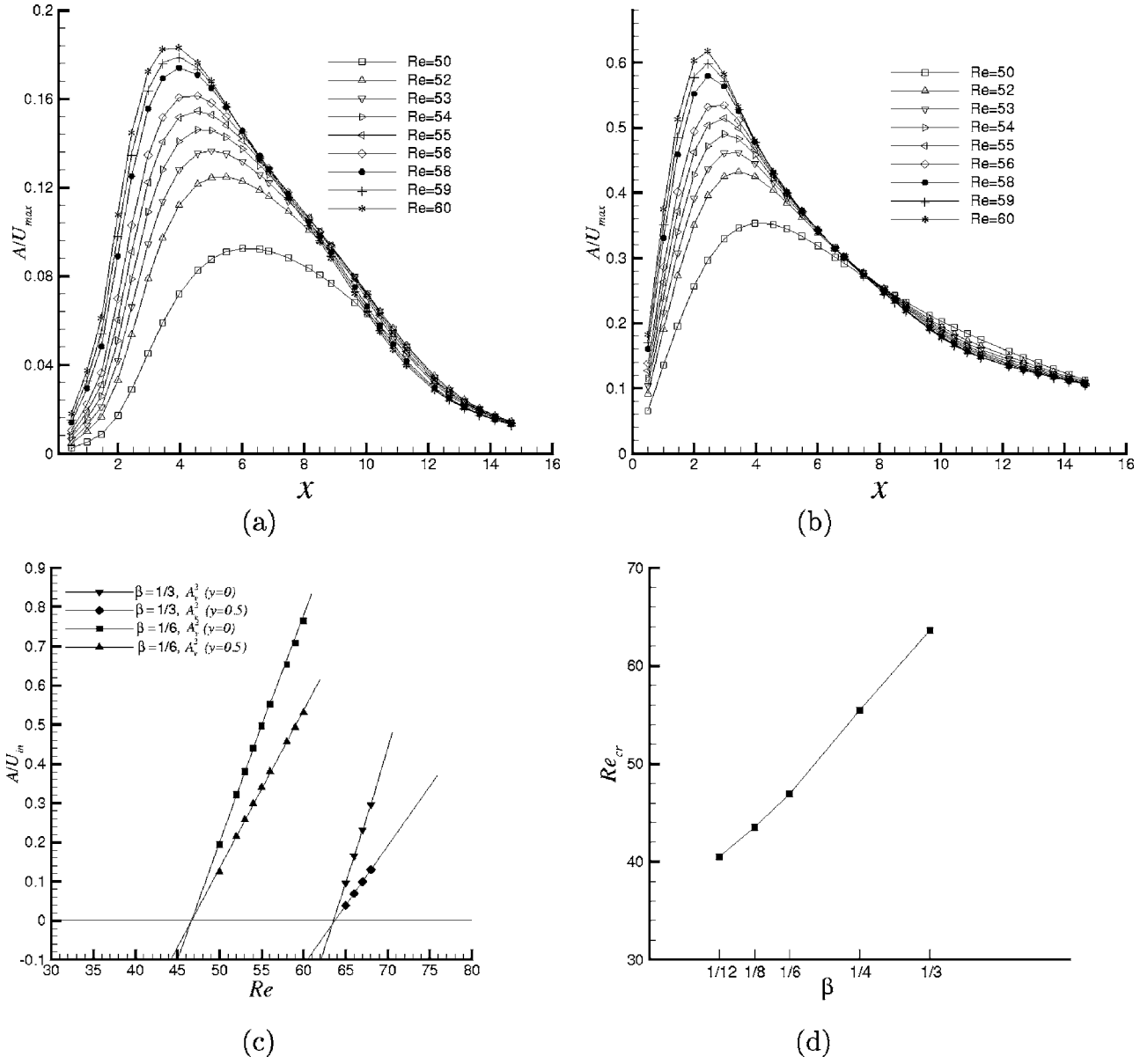

Fig. 4 Onset of vortex shedding; maximum peak-to-peak oscillation of v at (*a*) $y=0$, (*b*) $y=0.5$, (*c*) linear extrapolation of $A_v^2(y=0)$, and (*d*) variation of Re_{cr} with β

instants ($\tau/3$) within a period for $\beta=1/3, 1/6, 1/12$ and Re $=100,200$.

4.2.1 Fluid Flow. Because of its streamlined shape, flow always separates from the two rear-end vertices for a triangular cylinder. The vortices are shed alternately from the two vertices and are convected in the downstream direction. According to Perry et al. [19] and Eaton [20], two inviscid critical points, namely, "center," which is a point of indefinite stream-line slope with zero velocity, and "saddle," which is a point where two stream lines intersect. In the present study, a pair of inviscid critical points have been found for all cases except for $\beta=1/12$, Re $=200$, as evident from Figs. 5–9 and 10(*a*)–10(*d*)). A similar observation was made by Perry et al. [19] in his wake-visualization study for flow past a circular cylinder. For $\beta=1/12$, Re$=200$, coexistence of multiple pairs of critical points suggests the flow to be near its second bifurcation point. Wavering motion of the downstream wake increases at smaller β owing to lesser constraints imposed by the channel walls. At Re$=200$ and $\beta=1/3$, shown in Fig. 8, greater cross-stream motion of the wake and proximity of the channel walls to it lead to flow separation at the channel walls where small bubbles appear to form and convect in the downstream direction with the main flow. This fact has not been found for other cases and needs to be studied in greater detail because it can reveal the interaction between unsteady wake flow and separation from the walls at increasingly higher blockage ratios. The iso-vorticity lines, Figs. 5–9 and 10(*e*)–10(*h*), drawn by firm and dashed lines corresponding to positive (counterclockwise vortices) and negative (clockwise vortices) vorticity, respectively, show the alternate shedding and the von Kármán vortex street. The shear layers that separate from the vertices of the cylinder, stretch, bend, and finally disconnect into the wake. At higher β, owing to lesser extent in the cross-stream direction, the sizes of the shedding and the shed vortices are smaller with vorticity created at the channel walls almost reaches the wake. For all cases, positive and negative vorticity have been found in the upper and lower walls, respectively. In a shedding cycle, positive and negative vorticity engulf the rear end of the cylinder. Greater flapping motion of the separated shear layers at the cylinder vertices causes

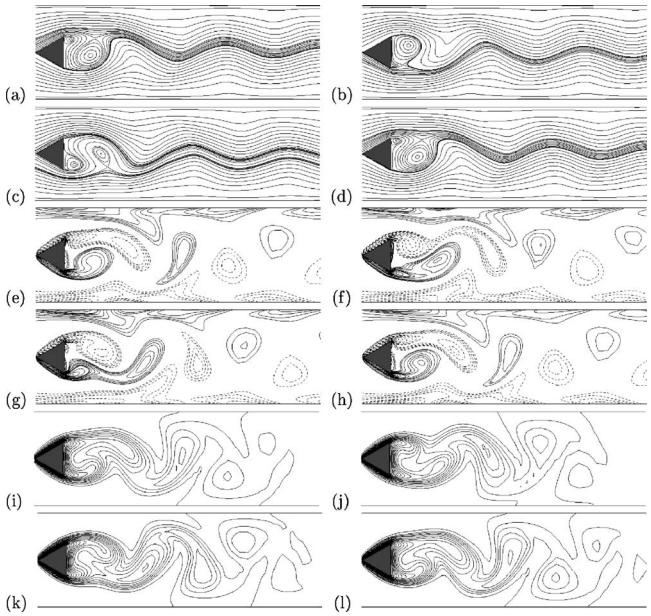

Fig. 5 Snapshots in a shedding cycle: (*a*)–(*d*) stream lines, (*e*)–(*h*) vorticity contours, and (*i*)–(*l*) isotherms for β=1/3, Re =100

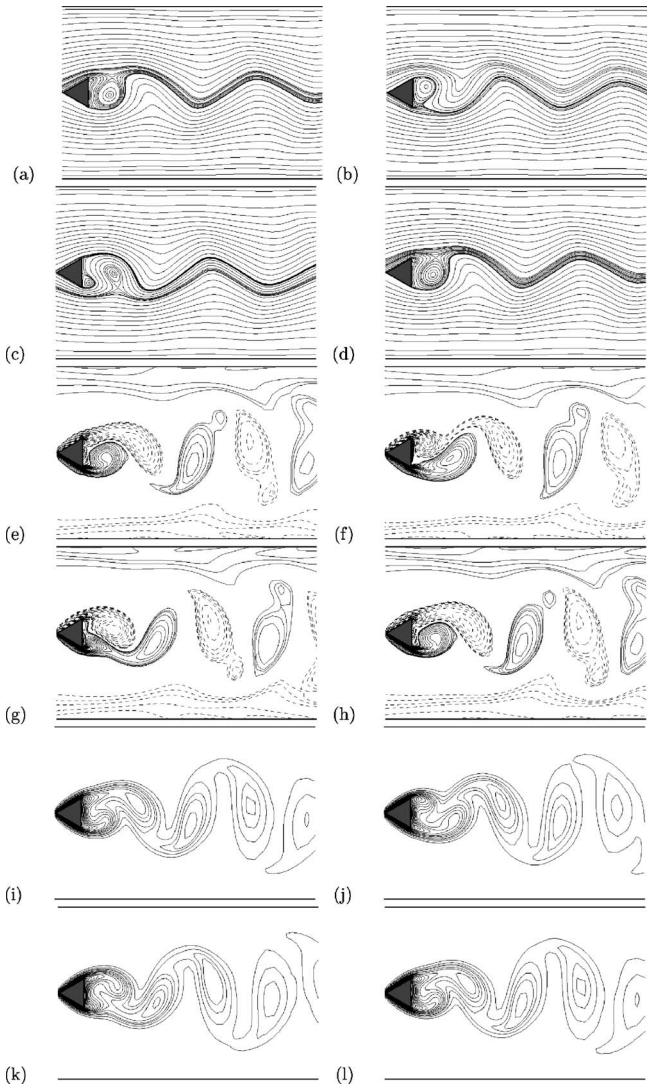

Fig. 6 Snapshots in a shedding cycle: (*a*)–(*d*) stream lines, (*e*)–(*h*) vorticity contours, and (*i*)–(*l*) isotherms for β=1/6, Re =100

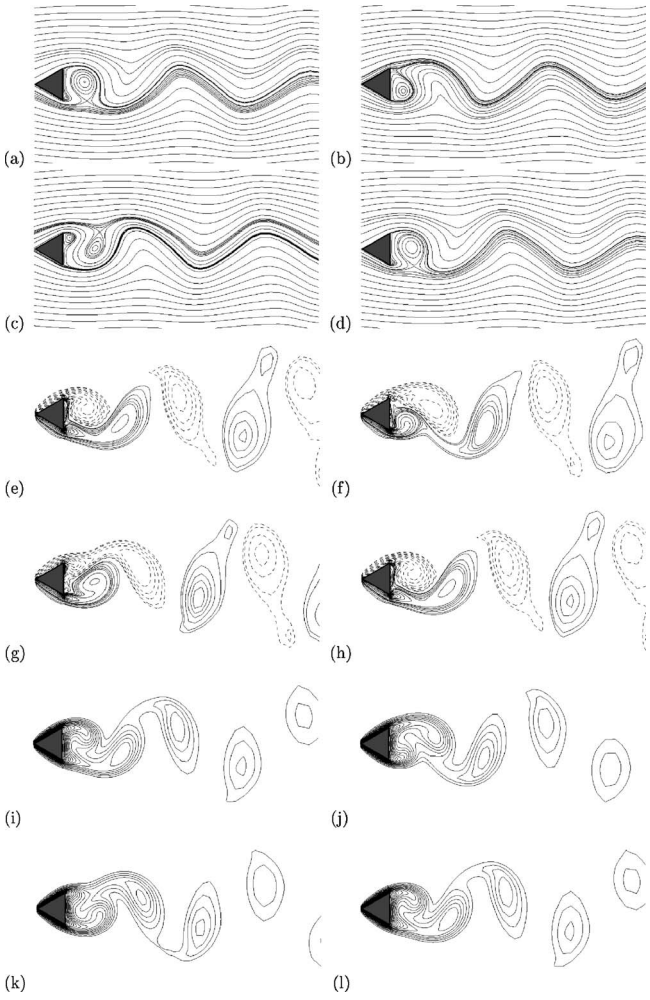

Fig. 7 Snapshots in a shedding cycle: (*a*)–(*d*) stream lines, (*e*)–(*h*) vorticity contours, and (*i*)–(*l*) isotherms for β=1/12, Re=100

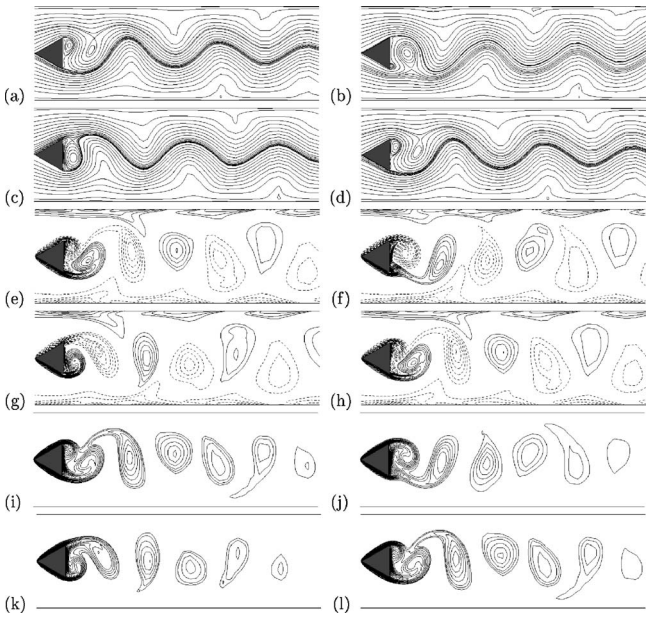

Fig. 8 Snapshots in a shedding cycle: (*a*)–(*d*) stream lines, (*e*)–(*h*) vorticity contours, and (*i*)–(*l*) isotherms for β=1/3, Re =200

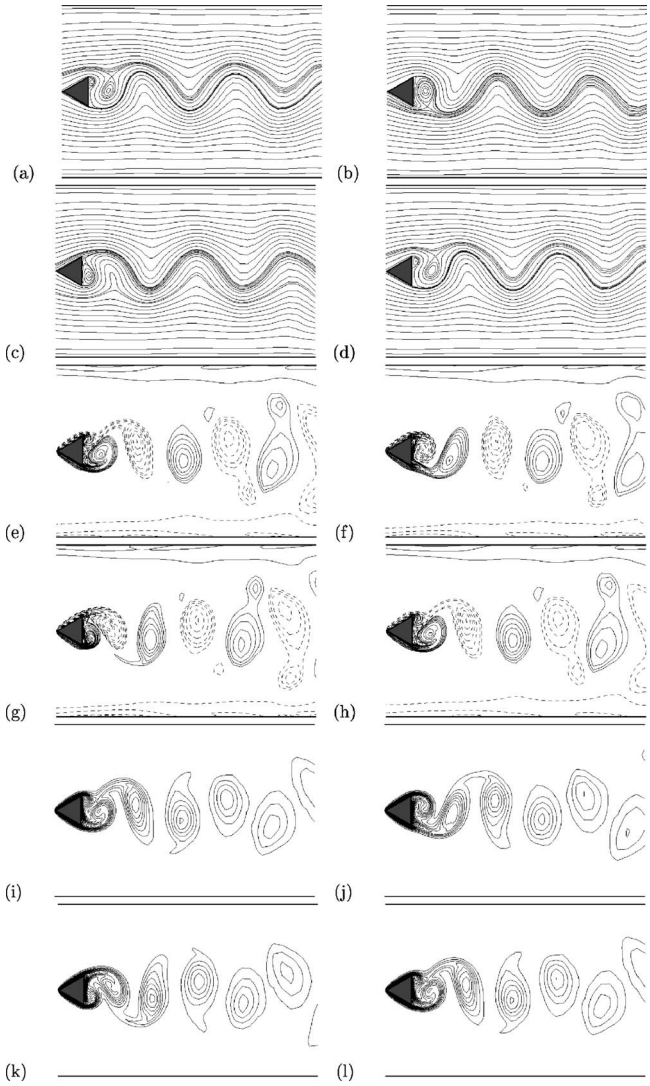

Fig. 9 Snapshots in a shedding cycle: (*a*)–(*d*) stream lines, (*e*)–(*h*) vorticity contours, and (*i*)–(*l*) isotherms for $\beta=1/6$, Re =200

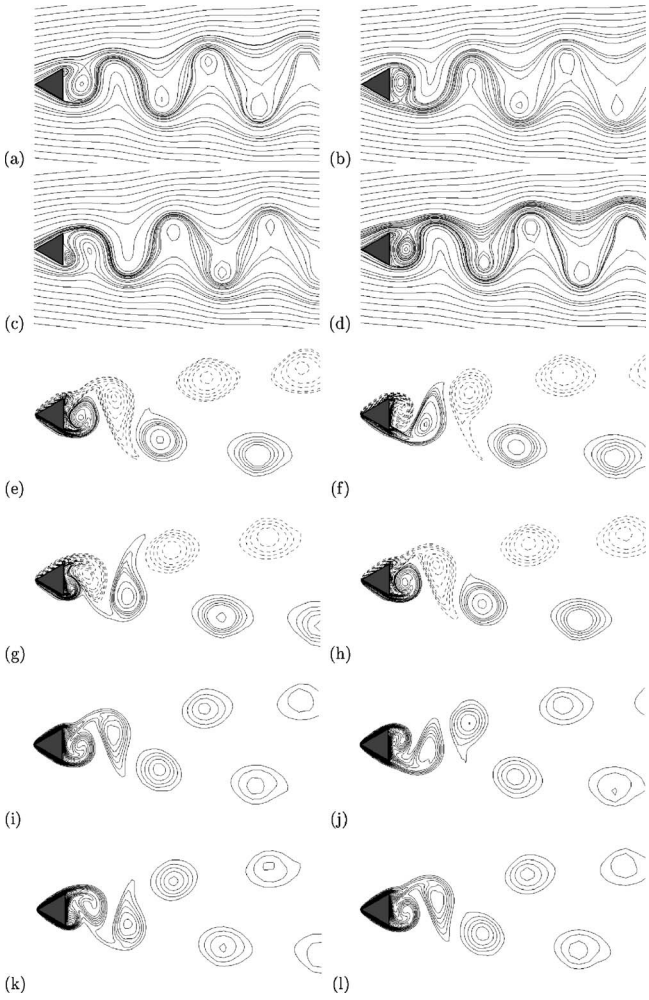

Fig. 10 Snapshots in a shedding cycle: (*a*)–(*d*) stream lines, (*e*)–(*h*) vorticity contours, (*i*)–(*l*) isotherms for $\beta=1/12$, Re =200

the narrower neck that joins the tip with the main body of a shedding vortex to bend more vigorously, leading to lesser stretching of the vortices at Re=200. Localized smaller vortex regions have been found both in the downstream wake as well as in the vicinity of the channel walls at Re=200 for all blockage ratios. For blockage ratio $\beta<1/3$, center of the positive and negative vorticity layers created at the vertices of the cylinder remain in the same half of the flow space after deattachment. Contrary to this fact, a criss-cross motion of these vorticity layers has been found for $\beta=1/3$ in which vorticity layers cross the centerline ($y=0$) moving to regions of vorticity with same sign leading to strengthening of vorticity field there. This observation is consistent with greater cross-stream motion of the wake at $\beta=1/3$. The boundary layers that form on the channel walls are disturbed for larger β and exhibit mild unsteadiness, whereas, for smaller β, wavering motion of the wake hardly affects their downstream development.

4.2.2 Heat Transfer. Instantaneous isotherms, shown in Figs. 5–9 and 10(*i*)–10(*l*), similar to vorticity, exhibit wavering motion along with streamwise stretching and bending leading to separated patches of fluid with different temperatures in the wake. Occurrence of crowded isotherms on the top and bottom sides of the cylinder indicates higher Nusselt number and development of thermal boundary layers that finally separates from the rear-end vertices. At Re=100, isotherms spread in the wake while they are crowded near the rear end of the cylinder, implying localized heat transfer. Isotherms bend sharply backward in the vicinity of the cylinder, emphasizing a shorter recirculation region at Re=200 compared to a greater spread of isotherms at Re=100.

4.3 Force Coefficients, Strouhal Number, and Nusselt Number. The effect of Reynolds number on time-averaged drag coefficient (C_D), pressure drag coefficient (C_{Dp}), and root mean square of lift coefficient (C_{Lrms}) for different blockage ratios are shown in Fig. 11. Total drag coefficient increases with Re, as can be seen from Fig. 11(*a*), for all blockage ratios with C_D reaching a flat maximum for $\beta=1/8$ and 1/12, and it is significantly higher ($\sim$12–28%) for $\beta=1/3$. Although C_D varies between the lowest blockage ($\beta=1/12$) and the unconfined case, Strouhal number remains almost same (Fig. 12(*a*)). This shows with diminishing blockage, effect of channel walls are only felt through the velocity gradient on the cylinder with frequency of vortex shedding remaining same. The pressure drag coefficient follows the same trend that of C_D with small numerical difference between them indicates pressure drag dominates or in other words friction drag hardly contributes to C_D at the supercritical range ($\mathrm{Re}>\mathrm{Re}_{cr}$), where size of the wake increases with increase in Re. At lower Re, $80\leq\mathrm{Re}\leq100$, an odd behavior in the $C_D-\mathrm{Re}$ relationship has been found for the highest blockage ratio. This range is close to

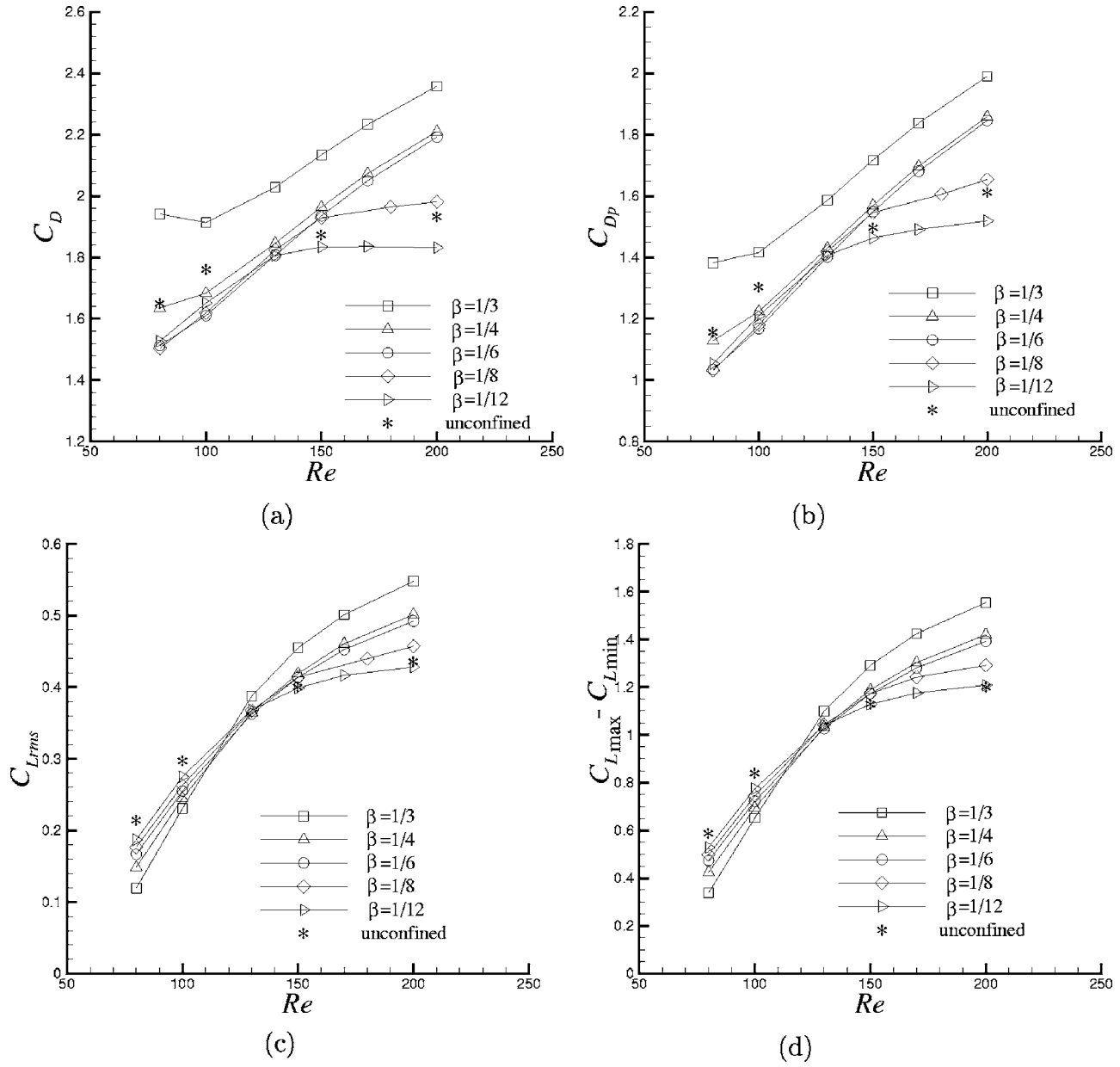

Fig. 11 Variation of integral parameters with Re: (*a*) C_D, (*b*) C_{Dp}, (*c*) C_{Lrms}, and (*d*) $C_{L\,max} - C_{L\,min}$

the Re_{cr} (at a particular β) as blockage ratio increases. In the near supercritical range (as is the case for higher and higher β) due to a developing wake (not attained fully developed vortex shedding mode), pressure drag is not enough to compensate for the reduction in friction drag that occurs with increase in Re. Thus, as β increases the slope of C_D–Re curve flattens, and at $\beta=1/3$, it shows a slight downfall, as evident from Fig. 11(*a*). At all blockage ratios, C_{Lrms}, which is a measure of unsteady wake oscillations, increases monotonically with Re (Fig. 11(*c*)). Wake oscillations are suppressed for increasingly larger β and smaller Re($<$130) owing to viscous effects while they are triggered at higher Re($>$130) due to strong convective flow. The same trend has been observed for $C_{L\,max} - C_{L\,min}$, evident from Fig. 11(*d*), suggesting the triangular cylinder has a stable transversal posture for increasingly larger β at Re$\leq$130 and vice versa.

Figure 12(*a*) shows the variation of Strouhal number with Reynolds number. As shown in Fig. 12(*a*), at smaller blockage ratios ($\beta<1/6$), St increases until it attains a flat maximum beyond which it falls, whereas St increases monotonically with Re in the range studied for higher blockage ratios ($\beta>1/6$). However, St increases monotonically for $\beta\geq 1/6$ with Re. As mentioned by Davis et al. [1], Sohankar et al. [6], and Suzuki et al. [3], an increase in the blockage ratio leads to an increase in Strouhal number for flow over a square cylinder placed in a channel. At the smallest blockage ratio, $\beta=1/12$, although the difference with the unconfined case is as small as ±4% indicating the diminishing influence of the channel walls for $\beta\leq 1/12$ it is 31% with the largest blockage ratio case ($\beta=1/3$), showing an increase in the unsteadiness in the flow leading to higher vortex shedding frequency. Discrete Fourier transform (DFT) of the drag and lift signals show that the dominating frequency for C_D is twice that of C_L for all the cases studied. Here, only spectra of C_D and C_L is shown for $\beta=1/3$ and Re=200 in Fig. 12(*b*).

Figure 13(*a*) illustrates the variation of the instantaneous local Nusselt number on the rear end of the cylinder at five equispaced instants within a cycle of vortex shedding for $\beta=1/6$ and Re =200. Nusselt number distribution changes only in the rear face of the cylinder with time due to unsteady vortex shedding and its

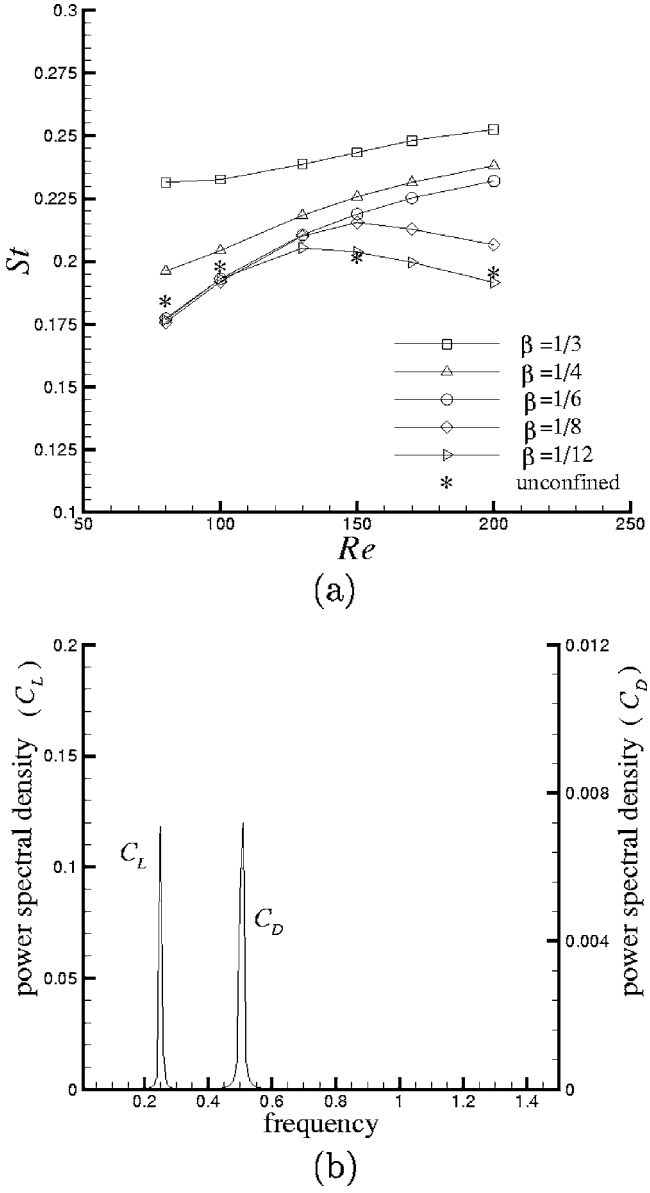

Fig. 12 Variation of Strouhal number (*a*) with Re for different β, (*b*) spectra of C_D and C_L for $\beta=1/3$, Re=200

effects on the flow field in the near wake. Profile of Nu_l contains two minima, corresponding to the locations of the shedding vortices, oscillating symmetrically due to the symmetric shedding of vortices from the two rear-end vertices. Alternate change in values and locations of these local minima further indicates symmetric vortex shedding, thus mixing of the fluid in the near wake. Moreover, the peak of the Nu_l changes both in value as well as its position during a cycle, emphasizing the effect of vortex shedding on the heat transfer from the cylinder. The time-averaged overall Nusselt number, shown in Fig. 13(*b*) increases almost linearly with Re for all blockage ratios, indicating better heat transfer at higher Re. However, the time-averaged overall Nusselt number remains almost unchanged at different blockage ratios with a maximum difference of 5.7% between $\beta=1/12$ and 1/3 at Re =200, suggesting a negligible effect of blockage ratio on the overall heat transfer.

4.4 Visualization of the Wake. Instantaneous streak lines are an excellent means of visualizing the wake that form behind the cylinder as a result of periodic vortex shedding. In the present study, particles, injected from 16 different locations just above and below the symmetry line $y=0$ ahead of the cylinder ($x<-0.866h$), have been tracked by the Lagrangian description

$$\frac{d\mathbf{x}(t)}{dt}=\mathbf{u}(\mathbf{x},t) \tag{12}$$

A second-order accurate formula has been used for the time integration while the velocities of the tracked particles have been computed by interpolating values of neighboring cells. Figures 14 and 15 show the instantaneous streak lines for three different blockage ratios, $\beta=1/3$, 1/6, and 1/12 and at two different Reynolds numbers, Re=100 and 200. The von Kármán vortex street that forms behind the cylinder has subtle differences for different blockage ratios and different Reynolds numbers. At lower blockage ratios, the wake widens in the cross-stream direction as one moves away from the cylinder with shed vortices remaining in their own half compared to higher β. However, at $\beta=1/3$, vortices that have already been shed cross the centerline through a criss-cross motion leading to a two-row arrangement of vortices separated by the symmetry line $y=0$. At all blockage ratios, flow becomes disorganized at Re=200, as shown by Figs. 14(*b*), 14(*d*), and 15(*b*), with increasingly higher wake instability at smaller β. Thus, viscous effects of the channel walls delays both the occurrence of first Hopf bifurcation and the wake transition. The disorganization at Re=200 is visualized by increase in the local intensity of the vortices, reduction in their sizes, and less prominent spiral connectors between two consecutive shed vortices. For $\beta=1/12$ at which channel wall effects are considerably small, two rows of localized spots with high vorticity intensity (Fig. 15(*b*)) have been found at Re=200, which suggests the flow is in the vicinity of wake transition.

5 Concluding Remarks

The present paper reports a numerical study of two-dimensional laminar flow and heat transfer past a triangular cylinder placed in a channel for $80\leq Re\leq 200$ and blockage ratio $1/12\leq\beta\leq 1/3$. The finite volume method with nonstaggered arrangement of the variables employing momentum interpolation for the pressure-velocity coupling is used. Signals of cross-stream velocity oscillations in the wake are used to predict the onset of vortex shedding (Re_{cr}), which increases linearly with β. A single pair of critical points are obtained for all the cases, with multiple pairs occurring for Re=200 and $\beta=1/12$. Sizes of the vortices reduce with lesser streamwise stretching occurring at increasingly higher blockage ratios. A criss-cross motion of the vorticity layers is observed at $\beta=1/3$, whereas they remain in their own half for other cases. St-Re relationship has a flat maxima around Re =130 for $\beta<1/6$, whereas it increases monotonically for $\beta\geq 1/6$ with Re and for Re>130 with β. Unsteady oscillations in the wake are suppressed at lower Re due to the viscous effects of the channel walls and triggered at higher Re owing to greater convection for larger β. Local Nusselt number changes with time only in the rear end of the cylinder due to the vortex shedding, whereas in other two faces it remain unchanged. Blockage ratio has negligible effects on the time-averaged overall Nusselt number. Instantaneous streak lines provide an excellent means to visualize the von Kármán vortex street. With an increase in β, flow becomes disorganized in the far wake while at smaller β localized vorticity zones are noted for higher Re.

Acknowledgment

Computations were carried out at the computational fluid dynamics laboratory of the Mechanical Engineering Department at the Indian Institute of Technology Kanpur. The authors are grateful to Prof. V. Eswaran for his timely advice and comments during the development of the numerical code.

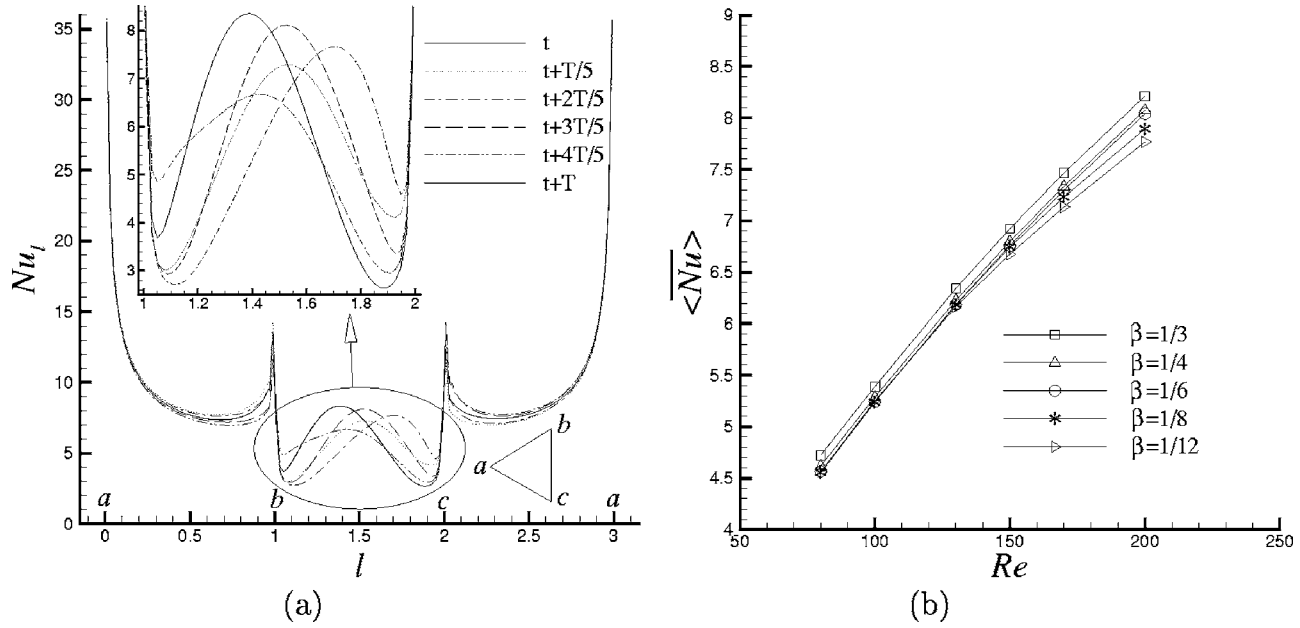

Fig. 13 Heat transfer parameters: (*a*) local Nu variation on the cylinder in a cycle for β=1/6 and Re=200, (*b*) time averaged overall Nu on the cylinder

Nomenclature

C_D = time-averaged drag coefficient
C_{Dp} = time-averaged pressure drag coefficient
C_{Lrms} = rms of lift coefficient
F = mass flux
h = side of the cylinder
H = height of the channel
Nu = Nusselt number
p = dimensionless pressure
Pr = Prandtl number
Re = Reynolds number
$\mathbf{S}$ = surface vector
U_{max} = maximum velocity at inlet
$\mathbf{u}$ = velocity vector
u,v = dimensionless Cartesian velocity components
V = volume of a cell
x,y = dimensionless Cartesian coordinates
X_d = downstream length
X_u = upstream length

Greek Symbols

β = blockage ratio (h/H)
Δt = time step

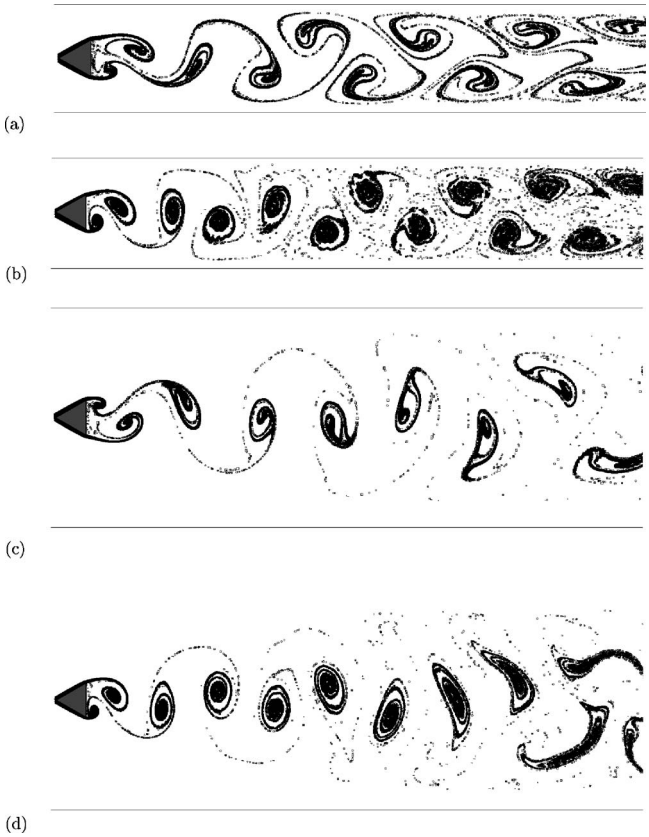

Fig. 14 Instantaneous streak lines for β=1/3 at (*a*) Re=100, (*b*) Re=200 and β=1/6 at (*c*) Re=100, and (*d*) Re=200

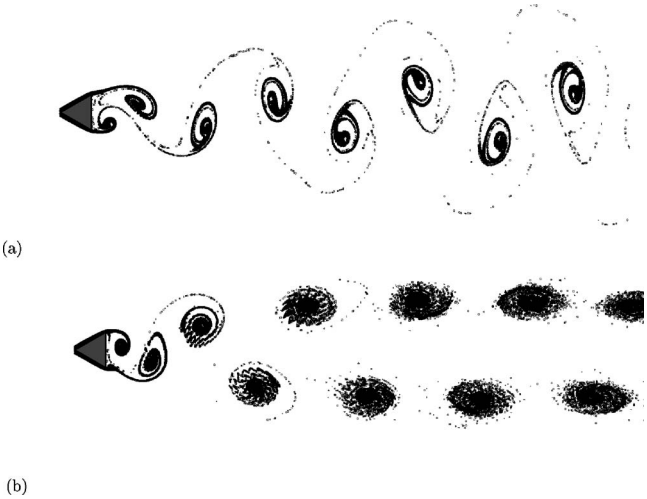

Fig. 15 Instantaneous streak lines for β=1/12 at (*a*) Re=100 and (*b*) Re=200

θ = nondimensional temperature
τ = time period of vortex shedding
ν = kinematic viscosity
ϕ = general variable representing u, v, and θ

Subscripts

$\langle\ \rangle$ = overall
b, r, t = bottom, rear, top
c = cylinder
f = face of a control volume
in = inlet
l = local
P = cell center

Superscripts

$*$ = provisional quantities
n = previous time step

References

[1] Davis, R. W., Moore, E. F., and Purtell, L. P., 1984, "A Numerical and Experimental Study of Confined Flow Around Rectangular Cylinders," Phys. Fluids, **27**, pp. 46–59.

[2] Mukhopadhyay, A., Biswas, G., and Sundararajan, T., 1992, "Numerical Investigation of Confined Wakes Behind a Square Cylinder in a Channel," Int. J. Numer. Methods Fluids, **14**, pp. 1473–1484.

[3] Suzuki, H., Inoue, Y., Nishimura, T., Fukutani, F., and Suzuki, K., 1993, "Unsteady Flow in a Channel Obstructed by a Square Rod (Cris-Cross Motion of Vortex)," Int. J. Heat Fluid Flow, **14**(1), pp. 2–9.

[4] Suzuki, K., and Suzuki, H., 1994, "Unsteady Heat Transfer in a Channel Obstructed by an Immersed Body," Annu. Rev. Heat Transfer, **5**, pp. 177–206.

[5] Hwang, R. R., and Yao, C., 1997, "A Numerical Study of Vortex Shedding From a Square Cylinder With Ground Effect," ASME J. Fluids Eng., **119**, pp. 512–518.

[6] Sohankar, A., Norberg, C., and Davidson, L., 1998, "Low-Reynolds Number Flow Around a Square Cylinder at Incidence: Study of Blockage, Onset of Vortex Shedding and Outlet Boundary Conditions," Int. J. Numer. Methods Fluids, **26**, pp. 39–56.

[7] Breuer, M., Bernsdorf, J., Zeiser, T., and Durst, F., 2000, "Accurate Computations of the Laminar Flow Past a Square Cylinder Based on Two Different Methods: Lattice-Boltzmann and Finite-Volume," Int. J. Heat Fluid Flow, **21**, pp. 186–196.

[8] Turki, S., Abbassi, H., and Nasrallah, S. B., 2003, "Effect of Blockage Ratio on the Flow in a Channel With a Built-in Square Cylinder," Comput. Mech., **33**, pp. 22–29.

[9] Sharma, A., and Eswaran, V., 2005, "Effect of Channel-Confinement on the Two-Dimensional Laminar Flow and Heat Transfer Across a Square Cylinder," Numer. Heat Transfer, Part A, **47**(1), pp. 79–107.

[10] Jackson, C. P., 1987, "A Finite-Element Study of the Onset of Vortex Shedding in Flow Past Variously Shaped Bodies," J. Fluid Mech., **182**, pp. 23–45.

[11] Zielinska, B. J., and Wesfreid, J. E., 1995, "On the Spatial Structure of Global Modes in Wake Flow," Phys. Fluids, **7**, pp. 1418–1424.

[12] Wesfreid, J. E., Goujon-Durand, S., and Zielinska, B. J., 1996, "Global Mode Behavior of the Stream-Wise Velocity in Wakes," J. Phys. II, **6**, pp. 1343–1357.

[13] Abbassi, H., Turki, S., and Nasrallah, S. B., 2001, "Numerical Investigation of Forced Convection in a Plane Channel With a Built-in Triangular Prism," Int. J. Therm. Sci., **40**, pp. 649–658.

[14] Johansson, S. H., Davidson, L., and Olsson, E., 2005, "Numerical Simulation of Vortex Shedding Past Triangular Cylinders at High Reynolds Number Using a k-ε Turbulence Model," Int. J. Numer. Methods Fluids, **16**(10), pp. 859–878.

[15] Orlanski, I., 1976, "A Simple Boundary Condition for Unbounded Hyperbolic Flows," J. Comput. Phys., **21**, pp. 251–269.

[16] Rhie, C. M., and Chow, W. L., 1983, "Numerical Study of the Turbulent Flow Past an Airfoil With Trailing Edge Separation," AIAA J., **21**(11), pp. 1525–1532.

[17] Leonard, B. P., 1979, "A Stable and Accurate Convective Modeling Procedure Based on Quadratic Upstream Interpolation," Comput. Methods Appl. Mech. Eng., **19**, pp. 59–98.

[18] Patankar, S. V., 1980, *Numerical Heat Transfer and Fluid Flow*, McGraw-Hill, New York.

[19] Perry, A. E., Chong, M. S., and Lim, T. T., 1982, "The Vortex Shedding Process Behind Two-dimensional Bluff Bodies," J. Fluid Mech., **116**, pp. 77–90.

[20] Eaton, B. E., 1987, "Analysis of Laminar Vortex Shedding Behind a Circular Cylinder by Computer-Aided Flow Visualization," J. Fluid Mech., **180**, pp. 117–145.

Effect of Hydraulic Jump on Hydrodynamics and Heat Transfer in a Thin Liquid Film Flowing Over a Rotating Disk Analyzed by Integral Method

S. Basu

B. M. Cetegen
Fellow ASME
e-mail: cetegen@engr.uconn.edu

Mechanical Engineering Department,
University of Connecticut,
Storrs, CT 06269-3139

Flow and heat transfer in a liquid film flowing over the surface of a rotating disk was analyzed by integral technique. The integral analysis includes the prediction of the hydraulic jump and its effects on heat transfer. The results of this analysis are compared to the earlier results that did not include this effect. At low inlet Reynolds numbers and high Rossby numbers, corresponding to low film inertia and low rotation rates, respectively, a hydraulic jump appears on the disk surface. The location of the jump and the liquid film height at this location are predicted. A scaling analysis of the equations governing the film thickness provided a semi-empirical expression for these quantities that was found to be in very good agreement with numerical results. Heat transfer analysis shows that the Nusselt numbers for both constant disk surface temperature and constant disk surface heat flux boundary conditions are lowered in the vicinity of the hydraulic jump due to the thickened liquid film. This effect can be more pronounced for the constant heat flux case depending on the location of the hydraulic jump. The Nusselt number exhibits a turning point at the jump location and can have higher values downstream of the hydraulic jump compared to those obtained from the analysis that does not include the gravitational effects. [DOI: 10.1115/1.2712854]

Keywords: heat transfer, thin liquid films, hydraulic jump, rotating disk, integral analysis

Introduction

Fluid flow and heat transfer in thin liquid films over a rotating disk surface have been studied extensively due to their many engineering applications. They include applications in gas turbines, micro-electronics fabrication, food processing, and spacecraft applications. Aside from its practicality, transport phenomena in thin liquid films over a rotating disk have rich physics, including transition from supercritical to subcritical flow (i.e., hydraulic jump phenomenon), wavy film phenomena, transition to turbulence, and the attendant changes in heat transfer rates.

Literature contains a number of analytical, numerical, and experimental studies concerning this flow configuration. Watson [1] was the first to analyze the flow field of a free-falling jet impinging on a horizontal stationary surface. Watson divided the flow field into four regions that included the stagnation zone immediately beneath the impinging jet, a region of growing momentum boundary layer, and transition to the fully developed film flow. The flow field was assumed to be self-similar in the fully developed film region containing the hydraulic jump. Watson's analysis was extended by Chadhury [2] and Ma et al. [3] to include heat transfer analysis. These analyses considered stationary disk and neglected inertial effects in the film flow.

Thomas et al. [4] proposed a one-dimensional analytical solution for the prediction of the liquid film thickness as well as the heat transfer coefficients. This analysis captured the phenomenon of hydraulic jump and its effect on heat transfer. The effect of turbulence and hydraulic jump on heat transfer were analyzed by Rahman et al. [5] for a controlled impingement jet. Their numerical model used k-ε model with body-fitted moving mesh. The problem was also studied numerically by Faghri et al. [6] for the controlled impingement jet heat transfer. They predicted the liquid film thickness in the vicinity of the hydraulic jump reasonably well and also evaluated the edge effects around the disk. Rahman and Faghri [7,8] reported numerical results for controlled liquid impingement on a rotating disk for constant disk surface heat flux condition. They also reported closed form solutions for heat transfer rates. However, they neglected the effect of fluid inertia and hydraulic jump phenomenon in this analysis. Rice et al. [9] investigated numerically both the hydrodynamics and heat transfer of a liquid film over a rotating disk using a 2D-axisymmetric simulation. The hydraulic jump phenomenon was not studied in detail in their computations. Their results matched reasonably well the experimental results of Ozar et al. [10] and the integral analysis of the same problem [11].

A number of experimental studies have also been reported. Carper and co-workers [12,13] studied the heat transfer for the impingement of cooling oil over a rotating isothermal disk for a range of Reynolds numbers. Their correlations did not include effects of rotation or Rossby number. Webb and Ma [14] studied the same problem for a water jet over an isothermal stationary disk. They presented correlations, which included the effect of gravity in the heat transfer analysis. Ozar et al. [10,15] presented an experimental study of liquid film flow and heat transfer over the surface of a heated rotating disk. They reported the variation of liquid thickness and Nusselt numbers for a range of liquid film flow rates and disk rotation speeds. A hydraulic jump existed on the disk surface for some of the experimental conditions (low flow rates and rotation rates). Avedesian and Zhao [16] investigated the phenomenon of circular hydraulic jump experimentally for normal

Contributed by the Heat Transfer Division of ASME for publication in the JOURNAL OF HEAT TRANSFER. Manuscript received April 11, 2006; final manuscript received June 26, 2006. Review conducted by Louis C. Burmeister.

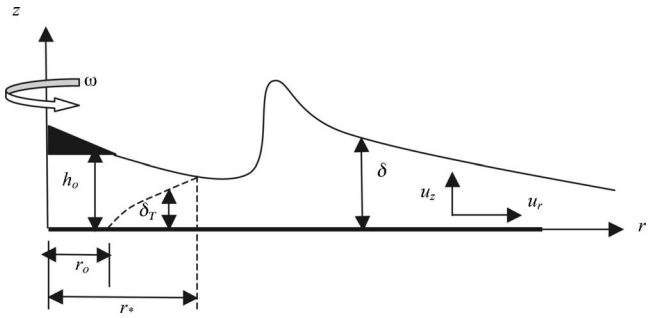

Fig. 1 Schematics of liquid film flow over a rotating disk

and reduced gravity conditions. They measured the circular hydraulic jump diameter and shape of the free liquid surface for an impinging jet on a stationary disk. They reported that the steady state diameter of the hydraulic jump under reduced gravity is larger than the diameter of the same jump under normal gravity conditions. It was predicted that the hydraulic jump would disappear in the absence of gravity.

A semi-analytical study was conducted by Rao and Arakeri [17] for a thin liquid film development from an impinging jet. Their analysis included an assumed velocity profile in the direction of the boundary layer growth and they predicted the variation of film thickness in the radial direction as a function of Reynolds and Froude numbers. However, they only considered flow over a stationary disk surface and did not extend their analysis for heat transfer. We recently presented a complete integral analysis for liquid film flow and heat transfer over a rotating disk in Ref. [11]. In this analysis, results were presented for liquid film thickness and Nusselt number variation over the disk surface for both constant temperature and constant heat flux boundary conditions. They were presented as functions of inlet film Reynolds and Rossby numbers. These results were found to be in reasonably good agreement with the detailed numerical computations [9] as well as the experiments [10]. However, that analysis did not consider the effect of radial and axial pressure gradients in the film that lead to the hydraulic jump phenomenon. This study is an extension of our earlier analysis with the inclusion of the hydraulic jump phenomenon affecting the film thickness and consequently the heat transfer in the liquid film. In the following, the integral analysis is first described followed by the presentation and discussion of the results. The article is concluded by a summary of the key findings.

Problem Formulation

In this analysis, the solution is based on the method adopted by the authors in Ref. [11], utilizing the Karman-Pohlhausen integral approach. In the previous study, only flow conditions that result in a thin supercritical liquid film flow on the disk surface were explored. Since a hydraulic jump exists on the disk surface for some flow conditions, this study focuses on the modified analysis and the range of conditions that include the hydraulic jump phenomenon.

The rotating disk configuration is schematically shown in Fig. 1, which is the same as utilized in our earlier study [11] as well as in the studies of Thomas et al. [4] and Ozar et al. [10,15]. As in the experiments, the flow is introduced from a central collar that directs the liquid radially outward over a gap height of h_o. The liquid flows over the rotating disk while being heated from underneath by an electric resistance heater. In these experimental studies, the liquid film thickness and heat transfer coefficients were measured.

The problem is considered in the radial (r) and axial (z) coordinates assuming azimuthal symmetry and including the hydrostatic pressure variation. The governing equations in cylindrical coordinates over a rotating circular disk can be written as

Continuity:

$$\frac{1}{r}\frac{\partial}{\partial r}(ru_r)+\frac{\partial u_z}{\partial z}=0 \tag{1}$$

r-momentum:

$$\frac{1}{r}\frac{\partial}{\partial r}(ru_ru_r)+\frac{\partial}{\partial z}(u_ru_z)=-\frac{1}{\rho}\frac{\partial p}{\partial r}+r\omega^2+\nu\left[\frac{\partial^2 u_r}{\partial z^2}-\frac{u_r}{r^2}+\frac{1}{r}\frac{\partial}{\partial r}\left(r\frac{\partial u_r}{\partial r}\right)\right] \tag{2}$$

Energy:

$$\frac{1}{r}\frac{\partial}{\partial r}(ru_rT)+\frac{\partial}{\partial z}(u_zT)=\alpha\left[\frac{1}{r}\frac{\partial}{\partial r}\left(r\frac{\partial T}{\partial r}\right)+\frac{\partial^2 T}{\partial z^2}\right] \tag{3}$$

The z-momentum equation reduces to the hydrostatic variation of pressure as $p=\rho g(\delta-z)+p_{\text{atm}}$, which is incorporated into the r-momentum equation. Defining nondimensional parameters as

$$\tilde{r}\equiv\frac{r}{r_0}\quad \tilde{u}_r\equiv\frac{u_r}{u_o}\quad \tilde{z}\equiv\frac{z}{h_o}\quad \tilde{u}_z\equiv\frac{u_z}{u_o}$$

$$\theta_T\equiv\frac{T-T_o}{T_o-T_i}\quad \theta_q\equiv\left(\frac{k}{q_oh_o}\right)(T-T_i)$$

where r_0 is the inlet radius of the disk, u_0 is the inlet velocity of the liquid jet at $r=r_o$, h_0 is the collar height, θ_T is the nondimensional temperature for the constant wall temperature case and θ_q is its counterpart for constant wall heat flux case. T_0 is the temperature of the disk surface for constant wall temperature case, T_i is the inlet temperature of the liquid jet, and q_0 is the heat flux supplied to the disk for the constant wall heat flux case. Nondimensionalizing the governing equations, we obtain

$$\frac{1}{\tilde{r}}\frac{\partial}{\partial\tilde{r}}(\tilde{r}\,\tilde{u}_r)+l_o\frac{\partial\tilde{u}_z}{\partial\tilde{z}}=0 \tag{4}$$

$$\frac{1}{\tilde{r}}\frac{\partial}{\partial\tilde{r}}(\tilde{r}\,\tilde{u}_r^2)+l_o\frac{\partial}{\partial\tilde{z}}(\tilde{u}_r\tilde{u}_z)=-\frac{1}{\mathrm{Fr}^2}\frac{\partial(\tilde{\delta}-\tilde{z})}{\partial\tilde{r}}+\frac{\tilde{r}}{\mathrm{Ro}}+\frac{1}{\mathrm{Re}}\left[\frac{1}{\tilde{r}}\frac{\partial}{\partial\tilde{r}}\left(\tilde{r}\frac{\partial\tilde{u}_r}{\partial\tilde{r}}\right)+l_o^2\frac{\partial^2\tilde{u}_r}{\partial\tilde{z}^2}-\frac{\tilde{u}_r}{\tilde{r}^2}\right] \tag{5}$$

$$\frac{1}{\tilde{r}}\frac{\partial}{\partial\tilde{r}}(\tilde{r}\,\tilde{u}_r\theta)+l_o\frac{\partial}{\partial\tilde{z}}(\tilde{u}_z\theta)=\frac{1}{\mathrm{Pe}}\left[\frac{1}{\tilde{r}}\frac{\partial}{\partial\tilde{r}}\left(\tilde{r}\frac{\partial\theta}{\partial\tilde{r}}\right)+l_o^2\frac{\partial^2\theta}{\partial\tilde{z}^2}\right] \tag{6}$$

where $l_o\equiv r_o/h_o$, and the Froude, Reynolds, Rossby, and Peclet numbers are defined as

$$\mathrm{Fr}\equiv\frac{u_0}{\sqrt{gh_0}}\quad \mathrm{Re}\equiv\frac{u_or_o}{\nu}\quad \mathrm{Ro}\equiv\frac{u_o^2}{\omega^2r_o^2}\quad \mathrm{Pe}\equiv\frac{u_or_o}{\alpha}$$

ν is the kinematic viscosity and α is the thermal diffusivity, both of which are assumed to be constant in the context of this analysis. Since $r_o>h_o$, $l_o>1$, $l_o^2\gg1$, terms with l_o^2 dominate within brackets on the right-hand sides of Eqs. (5) and (6). The resulting equations take on the form

$$\frac{1}{\tilde{r}}\frac{\partial}{\partial\tilde{r}}(\tilde{r}\,\tilde{u}_r^2)+l_o\frac{\partial}{\partial\tilde{z}}(\tilde{u}_r\tilde{u}_z)=-\frac{1}{\mathrm{Fr}^2}\frac{\partial(\tilde{\delta}-\tilde{z})}{\partial\tilde{r}}+\frac{\tilde{r}}{\mathrm{Ro}}+\frac{l_o^2}{\mathrm{Re}}\frac{\partial^2\tilde{u}_r}{\partial\tilde{z}^2} \tag{7}$$

$$\frac{1}{\tilde{r}}\frac{\partial}{\partial\tilde{r}}(\tilde{r}\,\tilde{u}_r\theta)+l_o\frac{\partial}{\partial\tilde{z}}(\tilde{u}_z\theta)=\frac{l_o^2}{\mathrm{Pe}}\frac{\partial^2\theta}{\partial\tilde{z}^2} \tag{8}$$

Liquid Film Hydrodynamics

The liquid film thickness is obtained from solution of the integral momentum equation, which is cast into

$$\frac{1}{\tilde{r}}\frac{\partial}{\partial \tilde{r}}\int_0^{\tilde{\delta}}(\tilde{r}\,\tilde{u}_r^2)d\tilde{z}-(\tilde{u}_r)_{\tilde{\delta}}\left[\frac{1}{\tilde{r}}\frac{\partial}{\partial \tilde{r}}\int_0^{\tilde{\delta}}\tilde{r}\,\tilde{u}_r d\tilde{z}\right]=-\frac{\tilde{\delta}}{\mathrm{Fr}^2}\frac{d\tilde{\delta}}{d\tilde{r}}+\frac{\tilde{r}\tilde{\delta}}{\mathrm{Ro}}-\frac{l_o^2}{\mathrm{Re}}\left.\frac{\partial \tilde{u}_r}{\partial \tilde{z}}\right|_{\tilde{\delta}} \tag{9}$$

by combining continuity and r-momentum equations and integrating the resulting equation from $\tilde{z}=0$ to $\tilde{\delta}=\delta/h_0$. The suitable radial velocity profile satisfying the boundary conditions of no slip at the wall $\tilde{u}_r(\tilde{z}=0)=0$ and no shear at the free surface $(\partial\tilde{u}_r/\partial\tilde{z})(\tilde{z}=\tilde{\delta})=0$ along with the total mass flow rate condition of $2\pi r_o u_o h_o=\int_0^{\delta}2\pi r u_r dz$ can be expressed as

$$\tilde{u}_r=3\left(\frac{\tilde{z}}{\tilde{r}\tilde{\delta}^2}\right)-\frac{3}{2}\left(\frac{\tilde{z}^2}{\tilde{r}\tilde{\delta}^3}\right) \tag{10}$$

Utilizing this velocity profile in Eq. (9) and integrating it yields

$$\frac{d\tilde{\delta}}{d\tilde{r}}=\frac{\frac{5l_o^2\tilde{r}}{2\mathrm{Re}}-\frac{\tilde{\delta}}{\tilde{r}}-\frac{5\tilde{r}^3\tilde{\delta}^3}{6\mathrm{Ro}}}{1-\frac{5\tilde{r}^2\tilde{\delta}^3}{6\mathrm{Fr}^2}} \tag{11}$$

This equation for the film thickness as a function of Re, Ro, and Fr contains a singularity in the denominator. For very large values of Fr (i.e., high values of u_o and/or small values of g and h_o), the denominator approaches unity and the resulting equation is the same as that obtained in our earlier analysis [11] for $\mathrm{Fr}\to\infty$. In this case, the film thickness for negligible film inertia takes the form

$$\tilde{\delta}=\left[\frac{3l_o^2\,\mathrm{Ro}}{\mathrm{Re}}\right]^{1/3}\frac{1}{\tilde{r}^{2/3}} \tag{12}$$

This result is identical to that obtained based on the falling film analysis with gravity being replaced by the centrifugal force [18]. Equation (11) was integrated numerically by fourth-order Runge-Kutta method. In the case of finite Fr, the hydraulic jump location, $\tilde{r}_{hj}$ can be obtained by equating the denominator of the right-hand side of Eq. (11) to zero, yielding

$$\tilde{r}_{hj}=\left(\frac{6}{5}\right)^{1/2}\delta_{hj}^{-3/2}\,\mathrm{Fr} \tag{13}$$

indicating that hydraulic jump location moves to larger radii with increasing Froude number.

Heat Transfer in the Liquid Film

The heat transfer in the liquid film is analyzed by considering the two cases of constant disk surface temperature and constant disk surface heat flux. Following the analysis presented in Ref. [11], the Nusselt number relations for the constant wall temperature and constant heat flux boundary conditions take the following forms Constant temperature:

$$\mathrm{Nu}_T=2\frac{l_o}{\tilde{\delta}}\exp\left[-\frac{5l_o^2}{2}\frac{1}{Pe}\int_1^{\tilde{r}}\frac{\tilde{r}d\tilde{r}}{\tilde{\delta}}+\frac{5}{4}(\tilde{\delta}-1)\right] \tag{14}$$

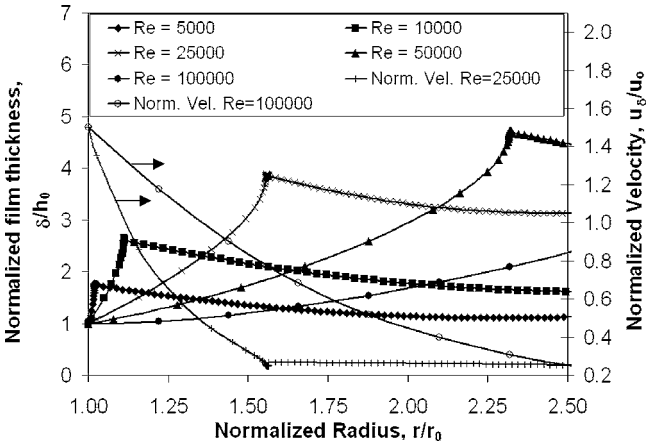

Fig. 2 Normalized film thickness for various values of Reynolds number at a Rossby number of 5000

Constant heat flux:

$$\mathrm{Nu}_q=\frac{l_o}{a_o}\ \text{where}\ \frac{da_0}{d\tilde{r}}+a_0\frac{d\tilde{\delta}}{d\tilde{r}}=\frac{\tilde{r}l_o^2}{\mathrm{Pe}}+\frac{2}{5}\frac{d\tilde{\delta}}{d\tilde{r}}+\frac{\tilde{\delta}}{2}\frac{d\tilde{\delta}}{d\tilde{r}} \tag{15}$$

subject to $a_o(\tilde{r}=1)=1/3$. The area-averaged Nusselt number can be defined as

$$\mathrm{Nu}_{\mathrm{avg}}=\frac{1}{\pi(\tilde{r}^2-1)}\int_1^{\tilde{r}}\mathrm{Nu}\,2\pi\tilde{r}d\tilde{r} \tag{16}$$

Results and Discussion

The calculation of the liquid film thickness and Nusselt numbers for constant wall temperature and constant heat flux cases were performed for a range of inlet velocities u_o and rotation speeds ω corresponding to inlet Reynolds number, $\mathrm{Re}\equiv u_o r_o/\nu$, range of $5\times10^3-10^5$ and Rossby number, $\mathrm{Ro}\equiv u_o^2/(\omega^2 r_o^2)$, range of $10^{-1}-10^3$. The value of the geometric parameter $l_o=r_o/h_o$ was taken to be 200, which corresponds to the value in our earlier analysis [11] and the experimental study of Ozar et al. [10,15]. It is assumed in this analysis that the fluid properties such as viscosity, density, and thermal conductivity remain constant in the temperature range of experiments [10,15]. Based on this temperature range, the maximum variation of these thermo-physical properties is in the range of 10 to 13%.

Figure 2 shows the variation of film thickness for different values of Reynolds number for a Rossby number of 5000, which corresponds to a low rotational speed of the disk. Hydraulic jump is present on the disk surface in the Reynolds number range $5\times10^3-10^5$. Hydraulic jump exhibits itself as a steep rise in liquid film thickness in the supercritical flow region followed by a gradual decay of film thickness in subcritical flow region behind the jump. As the Reynolds number is increased (for example, by increasing the liquid flow rate) the hydraulic jump moves progressively to larger radii with the peak film thickness also increasing. At a Reynolds number of 10^5, the hydraulic jump occurs at $\tilde{r}>3$, which is beyond the outer edge of the disk in the experimental configuration of Ozar et al. [10], suggesting that the flow remains supercritical throughout the disk surface for these conditions. The normalized liquid film surface velocity is also shown in this figure for two cases of $\mathrm{Re}=2.5\times10^4$ and 10^5. The film surface velocity decreases rapidly in the supercritical region due to the growth of the film thickness, but it levels off in the subcritical region. In fact, the film surface velocity can be obtained from the velocity profile in Eq. (10) as $\tilde{u}_r(\tilde{z}=\tilde{\delta})=3/(2\tilde{r}\tilde{\delta})$ showing a hyperbolic decrease of velocity with radial distance and film thickness. It should also be pointed out that the value of this velocity at the

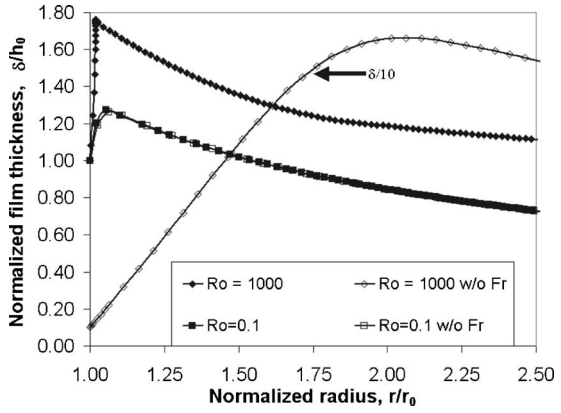

Fig. 3 Normalized film thickness for various values of Rossby numbers at a Reynolds number of 5000 for the cases with and without Froude number effect

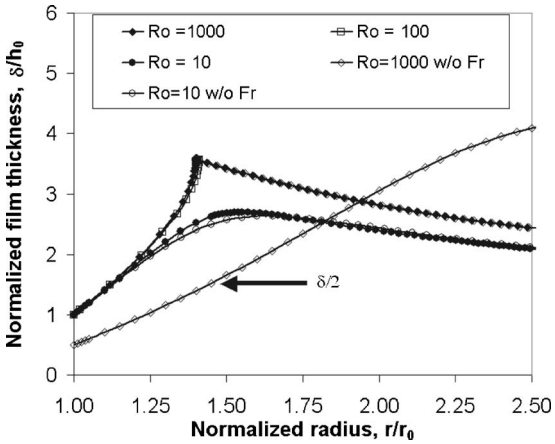

Fig. 4 Normalized film thickness for various values of Rossby numbers for a Reynolds number of 20,000

entrance is $1.5u_o$, due to the adjustment of the top-hat inlet velocity profile to the profile given by Eq. (10) at the inlet ($r=r_o$).

Figure 3 illustrates the influence of including the gravitational effect on the liquid film thickness. At $\mathrm{Re}=5\times10^3$, the gravitational effect is apparent for large Ro (i.e., low rotation speed) for which the computed film thicknesses are drastically different. Note that film thickness for the case without the hydraulic jump is much higher than that with the hydraulic jump. With inclusion of the Froude number effect, the liquid film exhibits a hydraulic jump that is not present in the absence of gravity. This is in agreement with the earlier predictions of Rahman and Faghri [7] and Avedisian and Zhao [16]. The Froude number effect is small at high disk rotation speeds (Ro=0.1). The film thickness variation is shown in Fig. 4 for $\mathrm{Re}=2\times10^4$ and different Rossby numbers Ro=10, 10^2, and 10^3. It is found that the hydraulic jump only occurs for high values of Ro or low rotational speeds, and disappears altogether at low Ro or high rotational speeds. The film thicknesses are very similar for $\mathrm{Ro}=10^2$ to 10^3. This additionally suggests that the effect of flow rate on the location and height of the hydraulic jump is more pronounced than the effect of the rotation speeds in that range.

The hydraulic jump location predicted from Eq. (13) suggests that it is pushed radially outward with increasing Froude number (i.e., high values of u_o and/or small values of g and h_o) in accordance with the results shown earlier. It is found that Eq. (13) gives a very good estimate of the location of the hydraulic jump if the hydraulic jump height is known, which is most likely not the case. However, it can be argued from scaling that

$$\tilde{\delta} \approx \frac{5l_o^2\tilde{r}^2}{2\mathrm{Re}} - \frac{5\tilde{r}^4\tilde{\delta}^3}{6\mathrm{Ro}} \tag{17}$$

Combining Eqs. (13) and (17), the dependence of hydraulic jump location can be expressed as

$$\tilde{r}_{hj} = \frac{C\,\mathrm{Fr}^{1/4}}{\left[\dfrac{5l_o^2}{2\mathrm{Re}} - \dfrac{\mathrm{Fr}^2}{\mathrm{Ro}}\right]^{3/8}} \tag{18}$$

This equation provides a means of determining the hydraulic jump location in terms of Re, Ro, and Fr. It should be realized, that this expression is a result of a scaling analysis and thus is good within a constant of proportionality that can in turn be a function of these parameters. Realizing that the hydraulic jump location is most sensitive to Re and not affected by Ro to the same extent, empirical determination of the proportionality constant yields $C \cong 1.3055\mathrm{Re}/(\mathrm{Re}-2504)$. Table 1 shows the comparison of the results from numerical integration of Eq. (11) and this scaling analysis. It is seen that the results from this approximate scaling analysis are in good agreement with the computed results. Hence, the expression in Eq. (18) can be used to estimate the hydraulic jump location and the film thickness at that location can be found from the rearranged version of Eq. (13) as

Table 1 Comparison of hydraulic jump location and film thickness

			$\tilde{r}_{hj}$		$\tilde{\delta}_{hj}$	
$\mathrm{Re}=\frac{u_o r_o}{\nu}$	$\mathrm{Fr}=\frac{u_o}{\sqrt{gh_o}}$	$\mathrm{Ro}=\frac{u_o^2}{\omega^2 r_o^2}$	Computed	Eq. (18)	Computed	Eq. (19)
5000	2.16	5000	1.027	1.031	1.750	1.734
5000	2.16	1000	1.030	1.031	1.754	1.734
10,000	4.32	5000	1.113	1.059	2.626	2.713
20,000	8.64	1000	1.404	1.407	3.570	3.563
20,000	8.64	100	1.405	1.487	3.550	3.435
25,000	10.8	5000	1.570	1.567	3.850	3.848
50,000	21.6	5000	2.326	2.326	4.700	4.695

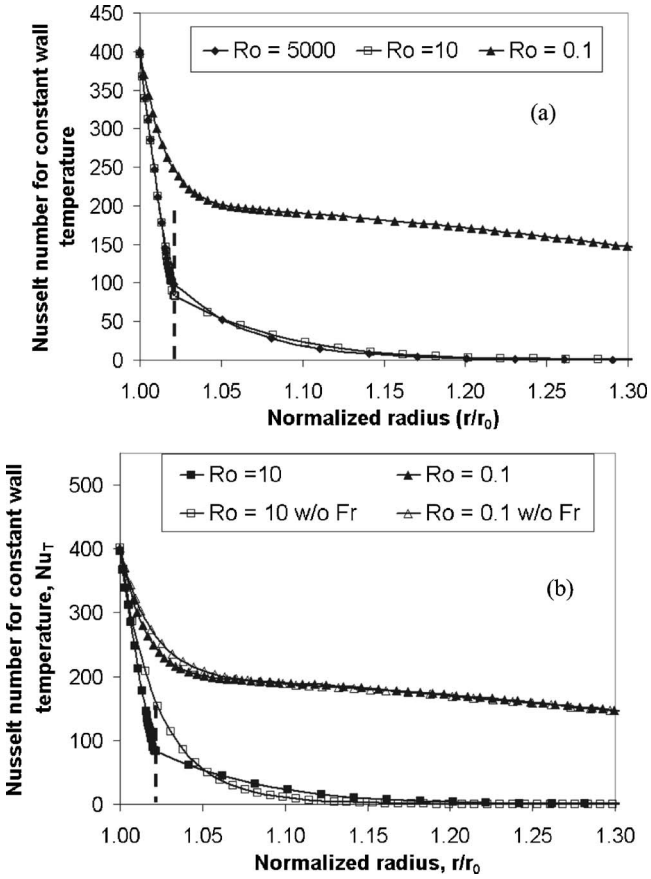

Fig. 5 Nusselt number variation for constant wall temperature case for different Rossby numbers at a Reynolds number of 5000. (*a*) Ro=0.1,10, 5×10^3, (*b*) Ro=0.1,10. Location of the hydraulic jump is delineated by a vertical dashed line.

$$\tilde{\delta}_{hj}=\left(\frac{6}{5}\right)^{1/3}\left(\frac{\mathrm{Fr}}{\tilde{r}_{hj}}\right)^{2/3} \tag{19}$$

It is found that the semi-empirical expressions predict the location and the film thickness of the hydraulic jump within 6% and 3%, respectively.

The hydraulic jump location determined experimentally by Ozar et al. [10] compares reasonably well with the jump locations from the analysis presented here. For a nonrotating disk, Ozar et al. [10] report the hydraulic jump location to be between $\tilde{r}_{hj}=1.67$ and 2.5 for $\mathrm{Re}=10^5$ and Fr=11.78, and at around $\tilde{r}_{hj}=4.0$ for $\mathrm{Re}=2.38\times10^5$ and Fr=42. For these two conditions, the present analysis predicts the hydraulic jump locations to be at $\tilde{r}_{hj}=2.6$ and $\tilde{r}_{hj}=4.4$, respectively.

Figure 5 shows the constant wall temperature Nusselt number variation at an inlet Reynolds number of 5×10^3 for different values of Rossby number between 0.1 and 5000. As shown in Fig. 5(*a*), Nusselt number profiles are very similar for Rossby numbers between 10 and 5×10^3. A hydraulic jump exists for these cases corresponding to low to moderate rotation speeds as indicated by the vertical dashed line in this figure. For Ro=0.1, the hydraulic jump is not present and the supercritical flow exists over the disk surface. The thin liquid film flowing over the disk surface results in higher Nusselt numbers as compared to the cases with hydraulic jump and thicker film thicknesses. Figure 5(*b*) shows the influence of including the Froude number effects (i.e., gravity) at low values of Ro between 0.1 and 10. It is found that the Froude number effect lowers the Nusselt number in the vicinity of the hydraulic jump; this effect becomes more pronounced with decreasing rotation speed or increasing Rossby number.

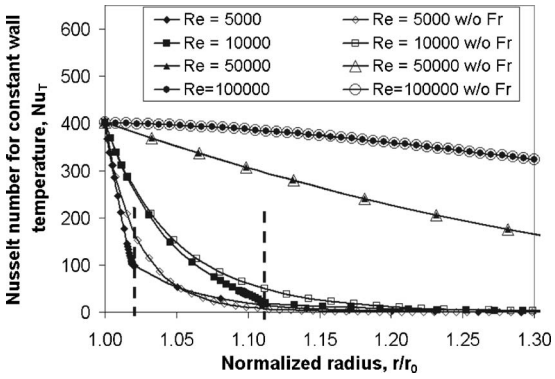

Fig. 6 Variation of Nusselt number for different Reynolds numbers for a Rossby number of 5000. Locations of the hydraulic jump are delineated by vertical dashed lines.

Figure 6 shows the effect of inlet Reynolds number on the constant wall temperature Nusselt number for a Rossby number of Ro=5000 (slow rotation). Also shown in this figure are the predictions that do not include the gravitational effects. At high Reynolds numbers ($\mathrm{Re}=5\times10^4$ and 10^5), the hydraulic jump is washed off the disk surface and the two sets of predictions become identical. At lower Reynolds numbers ($\mathrm{Re}=5\times10^3$ and 10^4), consideration of the Froude number effect results in lower local Nusselt numbers since the film thickness becomes significantly greater there. For the cases with hydraulic jump, there is also a discontinuity in the Nusselt number variation attributed to the discontinuity in the film thickness.

Computed Nusselt number variations are shown in Fig. 7 for

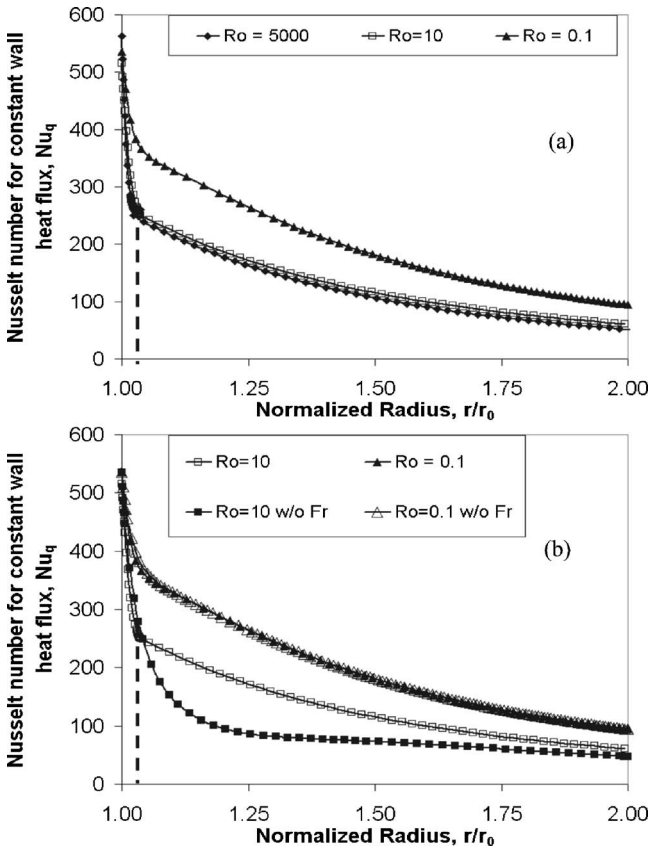

Fig. 7 Variation of Nusselt number for constant wall heat flux case for different Rossby numbers for a Reynolds number of 5000. (*a*) Ro=0.1,10, 5×10^3, (*b*) Ro=0.1,10.

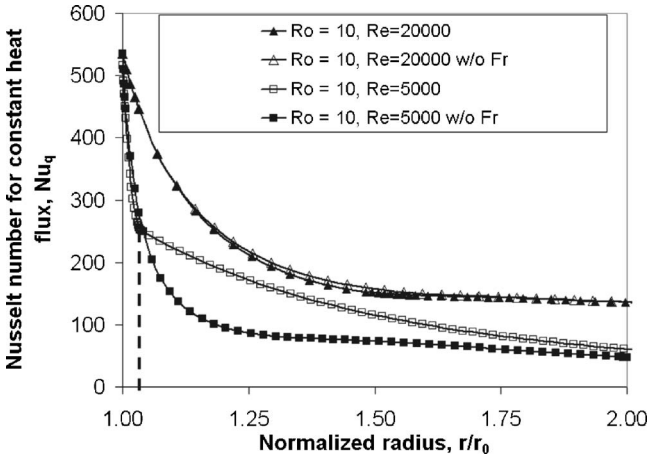

Fig. 8 Variation of Nusselt number for constant wall heat flux for Reynolds numbers of 5×10^3 and 2×10^4 at a Rossby number of 10

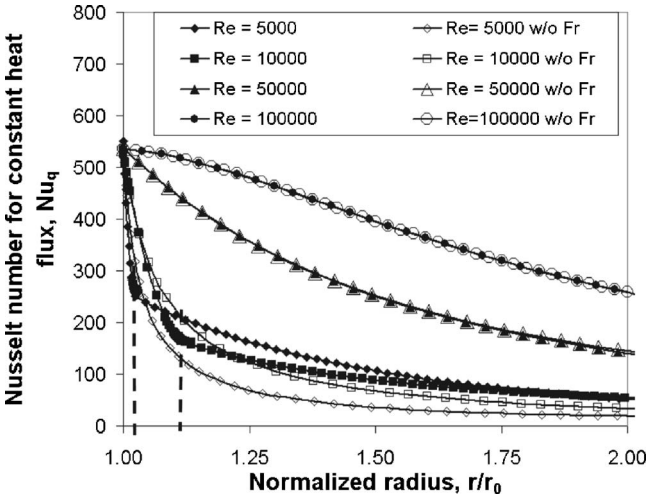

Fig. 9 Variation of Nusselt number for constant wall heat flux for different Reynolds numbers for a Rossby number of 5000

the constant wall heat flux condition for several values of Rossby number for an inlet Reynolds number of 5×10^3. Similar to the constant wall temperature case, the Nusselt number variations are very similar in the range of Ro between 10 and 5×10^3, corresponding to slow to moderate rotation speeds, as shown in Fig. 7(*a*). In these cases, a hydraulic jump exists near the inlet region. At high rotation speeds (Ro=0.1), the hydraulic jump is not present and the Nusselt number is higher than the high Rossby number cases. This is due primarily to thinning of the liquid film as a result of rotation. In Fig. 7(*b*), the effect of the Froude number on the Nusselt number distribution is shown for low Ro=0.1 and 10. While the effect is not present for high rotation speeds (Ro=0.1), there is a significant difference in Nusselt numbers downstream of the hydraulic jump for Ro=10.

Figure 8 compares the current results with the predictions from our earlier analysis [11] neglecting the gravitational effect. As it is seen, for the same Rossby number value of 10, the flow with a higher Reynolds number of 2×10^4 does not encounter a hydraulic jump on the disk surface, while the flow with a Reynolds number of 5×10^3 experiences the jump. As a result of this difference, the Nusselt number excluding the gravity effect [11] shows significant difference compared to this analysis for lower Reynolds numbers. However, there is virtually no difference in the predictions between the two predictions for the higher Reynolds numbers for which the hydraulic jump does not exist on the disk surface. This emphasizes the fact that as long as there is no hydraulic jump on the disk surface, the analysis neglecting gravitational effects is adequate.

Figure 9 illustrates the variation of constant wall heat flux Nusselt number profiles for different values of Reynolds number for low rotation rate; i.e., Rossby number of 5000. For $\mathrm{Re}=5\times10^4$ and 10^5, the hydraulic jump is not present and the Nusselt numbers decrease with increasing radial distance with no effect of the Froude number. For lower Reynolds numbers ($\mathrm{Re}=5\times10^3$ and 10^4), the Nusselt number decreases rapidly towards the hydraulic jump location due to thickening film thickness. It then varies gradually in the post-hydraulic jump region. Since the location of hydraulic jump determines the turning point in the Nusselt number profile, it appears that the overall heat transfer on the disk surface can be altered more significantly for the constant heat flux case. The overall magnitudes of the Nusselt number for constant heat flux condition are higher than the corresponding values for constant disk surface temperature case. Additionally, sensitivity of heat transfer to hydraulic jump location appears to be larger for the constant heat flux case.

Finally, the area-averaged Nusselt numbers are shown in Fig. 10 for both constant disk surface temperature and constant heat flux cases as a function of Reynolds number for a Rossby number of 5000. It is seen that average Nusselt numbers are higher for the constant heat flux by a significant amount. The Froude number effect is present for the constant heat flux case, particularly for low values of the Reynolds number, whereas it does not seem to influence the overall heat transfer for the constant disk surface temperature case.

Conclusions

The model presented here extends the previously presented integral analysis [11] to include the effect of hydraulic jump phenomenon in both hydrodynamics and heat transfer in a thin liquid film over a rotating disk. The analysis utilizes an integral method that reduces the dimensionality of the problem and allows simplified solutions of the governing equations. Inclusion of gravitational effects through a Froude number allowed prediction of the hydraulic jump phenomenon and its effects on local heat transfer. At low inlet Reynolds numbers and high Rossby numbers corresponding to low film inertia and low rotation rates, respectively, a hydraulic jump appears on the disk surface. The location of the jump and the liquid film height at this location are predicted by the analysis. The hydraulic jump location moves outward on the disk surface with increasing inlet Reynolds number and decreasing Rossby number (high rotation rates). A scaling analysis of the equations governing the film thickness provided a semi-empirical

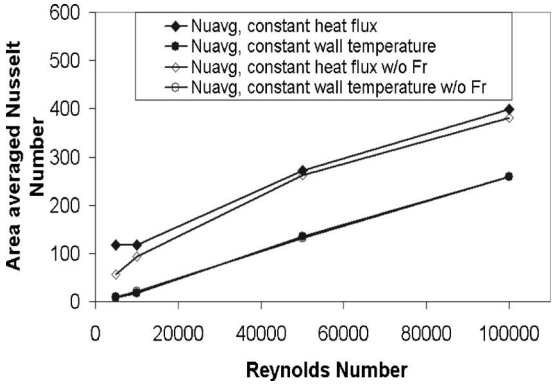

Fig. 10 Variation of area averaged Nusselt number for constant heat flux and constant wall temperature cases for Ro =5000

expression for these quantities that was found to be in very good agreement with the numerical results and in reasonable agreement with some experimental results. Heat transfer analysis shows that the Nusselt numbers for both constant disk surface temperature and constant disk surface heat flux boundary conditions are lowered in the vicinity of the hydraulic jump due to the larger liquid film thickness. The differences can be more pronounced for the constant heat flux case depending on the location of the hydraulic jump. The Nusselt number exhibits a turning point at the jump location and can have higher values downstream of the hydraulic jump compared to those obtained from the analysis that does not include the gravitational effects.

Acknowledgment

The work presented in this article was partially funded by NASA Microgravity Fluid Physics Program under Grant No. NCC3-789 with Dr. S. Sankaran as the grant monitor. We also would like to acknowledge the discussions of this problem with Professor A. Faghri, who stimulated our interest in this subject.

Nomenclature

a_o = coefficient in the temperature profile, $\theta = a_o + \tilde{\delta}(\hat{z}^2/2 - \hat{z})$ [11] and Eq. (14)
C = heat capacity, J/kg K
Fr = Froude number, $u_o/\sqrt{gh_o}$
h_o = collar height, m
h = convective heat transfer coefficient, W/m^2 K
k = thermal conductivity, W/m K
Nu = Nusselt number, hr_o/k
Pe = Peclet number, $u_o r_o/\alpha$
q_o = Constant wall heat flux, W/m^2
r = radial coordinate, m
$\tilde{r}$ = normalized radial coordinate, r/r_o
$\tilde{r}_{hj}$ = location of hydraulic jump
r_o = collar radius, m.
Re = Reynolds number, $u_o r_o/\nu$
Ro = Rossby number, $u_o^2/\omega^2 r_o^2$
l_o = Ratio of collar radius to collar height, r_o/h_o
T = temperature, K
T_o = temperature of the disk surface, K
T_i = inlet temperature of the liquid, K
u_o = liquid inlet velocity at the collar exit, m/s
u_r = velocity component in the radial direction, m/s
u_z = velocity component in the direction normal to disk surface, m/s
$\tilde{u}$ = nondimensional velocity, u/u_o
z = coordinate normal to disk surface
$\tilde{z}$ = normalized coordinate, z/h_o
$\hat{z}$ = normalized coordinate with respect to thermal boundary thickness

Greek

α = thermal diffusivity, $k/\rho C$, m^2/s
β = ratio of thermal to hydrodynamic boundary layer thickness, δ/δ_T
δ = hydrodynamic boundary layer or film thickness, m
δ_T = thermal boundary layer thickness, m
$\tilde{\delta}$ = normalized film thickness, δ/h_o
$\tilde{\delta}_{hj}$ = normalized film thickness at hydraulic jump location
$\tilde{\delta}_T$ = normalized film thickness, δ_l/h_o
θ_T = Nondimensional temperature for constant wall temperature, $(T-T_o)/(T_o-T_i)$
θ_q = Nondimensional temperature for constant wall heat flux, $k(T_o-T_i)/(q_o h_o)$
ω = rotational speed, rev/s

References

[1] Watson, E. J., 1964, "The Radial Spread of a Liquid Jet Over a Horizontal Plane," J. Fluid Mech., **20**, pp. 481–499.
[2] Chadhury, Z. H., 1964, "Heat Transfer in a Radial Liquid Jet," J. Fluid Mech., **20**, pp. 501–511.
[3] Ma, C. F., Zhao, Y. H., Masuoka, T., and Gomi, T., 1996 "Analytical Study on Impingement Heat Transfer With Single-Phase Free-Surface Circular Liquid Jets," J. Therm. Sci., **5**(4), pp. 271–277.
[4] Thomas, S., Hankey, W., Faghri, A., and Swanson, T., 1990, "One-Dimensional Analysis of the Hydrodynamic and Thermal Characteristics of Thin Film Flows Including Hydraulic Jump and Rotation," ASME J. Heat Transfer, **112**, pp. 728–735.
[5] Rahman, M. M., Faghri, A., and Hankey, W., 1991, "Computation of Turbulent Flow in a Thin Liquid Layer of Fluid Involving a Hydraulic Jump," ASME J. Fluids Eng., **113**, pp. 411–418.
[6] Faghri, A., Thomas, S., and Rahman, M. M., 1993, "Conjugate Heat Transfer From a Heated Disk to a Thin Liquid Film Formed by a Controlled Impinging Jet," ASME J. Heat Transfer, **115**, pp. 116–123.
[7] Rahman, M. M., and Faghri, A., 1992, "Numerical Simulation of Fluid Flow and Heat Transfer in a Thin Liquid Film Over a Rotating Disk," Int. J. Heat Mass Transfer, **35**, pp. 1441–1453.
[8] Rahman, M. M., and Faghri, A., 1992, "Analysis of Heating and Evaporation From a Liquid Film Adjacent to a Horizontal Rotating Disk," Int. J. Heat Mass Transfer, **35**, pp. 2655–2664.
[9] Rice, J., Faghri, A., and Cetegen, B. M., 2005, "Analysis of a Free Surface Film From a Controlled Liquid Impingement Jet Over a Rotating Disk Including Conjugate Effects With and Without Evaporation," Int. J. Heat Mass Transfer, **48**, pp. 5192–5204.
[10] Ozar, B., Cetegen, B. M., and Faghri, A., 2004, "Experiments on Heat Transfer in a Thin Liquid Film Flowing Over a Rotating Disk," ASME J. Heat Transfer, **126**, pp. 184–192.
[11] Basu, S., and Cetegen, B. M., 2006, "Analysis of Hydrodynamics and Heat Transfer in a Thin Liquid Film Flowing Over a Rotating Disk by Integral Method," ASME J. Heat Transfer, **128**, pp. 1–9.
[12] Carper, H. J., and Defenbaugh, D. M., 1978, "Heat Transfer From a Rotating Disk With Liquid Jet Impingement," Proceedings of 6th Int. Heat Transfer Conference, Toronto, pp. 113–118.
[13] Carper, Jr., H. J., Saavedra, J. J., and Suwanprateep, T., 1986, "Liquid Jet Impingement Cooling of a Rotating Disk," ASME J. Heat Transfer, **108**, pp. 540–546.
[14] Webb, B. W., and Ma, C. F., 1995, "Single Phase Liquid Impingement Heat Transfer," Adv. Heat Transfer, **26**, pp. 105–217.
[15] Ozar, B., Cetegen, B. M., and Faghri, A., 2003, "Experiments on the Flow of a Thin Liquid Film Over a Horizontal Stationary and Rotating Disk Surface," Exp. Fluids, **34**, pp. 556–565.
[16] Avedisian, C. T., and Zhao, Z., 2000, "The Circular Hydraulic Jump in Low Gravity," Proc. R. Soc. London, Ser. A, **456**, pp. 2127–2151.
[17] Rao, A., and Arakeri, J. H., 1998, "Integral Analysis Applied to Radial Film Flows," Int. J. Heat Mass Transfer, **41**, pp. 2757–2767.
[18] Nusselt, W. Z., 1916, "Die Oberflachenkondensation des Wasserdampfes," Z. Ver Deut. Ing., **60**, pp. 541–546.

Transfer From a Droplet at High Peclet Numbers With Heat Generation: Interior Problem

Adham Souccar

Douglas L. Oliver

Mechanical Engineering,
University of Toledo,
Toledo, OH 43606

Transient heat transfer from a droplet with heat generation is investigated. It is assumed that the bulk of the thermal resistance resides in the droplet. Two cases were investigated: low Peclet flows and very high Peclet flows. As expected, it was found that the temperature rise due to the heat generation was less for high Peclet flows. In addition, the temperature profile responds more quickly for high Peclet flows. This analysis is also applicable for mass transfer with a zero-order reaction. [DOI: 10.1115/1.2712849]

Keywords: spherical droplet, interior problem, high Peclet number, creeping flow

Introduction

There have been many investigations of heat or mass transfer from bubbles and droplets over the past half century. Many of these investigations are reviewed in Sadhal et al. [1]. However, little of this research has investigated the effects of distributed heat (or mass) sources or sinks.

The intent of this technical note is to investigate the heat or mass transfer from a droplet with a uniform heat source $\dot{q}$. A heat source may be created by an exothermic chemical or nuclear reaction or by an electromagnetic field. A heat sink may be created by an endothermic reaction.

Recently, several investigations have been made to characterize mass transfer near a bubble or droplet with chemical reactions. For example, Klienman and Reed [2] investigated conjugate mass transfer between a droplet and an ambient fluid with a first-order chemical reaction in the ambient flow. Similarly, Juncu [3] investigated conjugate mass transfer to a droplet with a second-order chemical reaction in the droplet.

Problem Statement

For simplicity, further discussion of this problem will emphasize the heat transfer problem. The applicability to mass transfer is discussed in the Appendix. Consider a droplet in an ambient fluid. The droplet is experiencing a uniformly distributed rate of heat generation $\dot{q}$. The ambient fluid has no corresponding heat generation.

This investigation is limited to the so-called interior problem. For interior problems, all resistance to heat transfer is assumed to reside in the droplet. As such, the temperature at the surface of the droplet T_s is assumed to be the free-stream temperature

$$T_s = T_{\text{ext}} \tag{1}$$

With this assumption, only the heat transfer in the droplet phase needs to be considered.

Assuming symmetry about the azimuth, the temperature profile in the droplet will be a function of two spatial coordinates, r and θ, as well as time t or $T(r,\theta,t)$. An energy balance on a differential volume of the sphere yields the following partial differential equation:

$$\frac{1}{r^2}\frac{\partial}{\partial r}\left(r^2\frac{\partial T}{\partial r}\right) + \frac{1}{r^2\sin\theta}\frac{\partial}{\partial\theta}\left(\sin\theta\frac{\partial T}{\partial\theta}\right) + \frac{\dot{q}a^2}{k} = \frac{\text{Pe}}{2}\left(u\frac{\partial T}{\partial r} + \frac{v}{r}\frac{\partial T}{\partial\theta}\right) + \frac{\partial T}{\partial\tau} \tag{2}$$

where r is the radial coordinate scaled by the droplet radius, a; u and v are radial and tangential velocities, scaled by the droplet velocity U. Pe is the Peclet number and τ is the dimensionless time with $\text{Pe}=2Ua/\alpha$ and $\tau=t\alpha/a^2$, where α is the thermal diffusivity.

Finally, the temperature may be made dimensionless with

$$\Theta(r,\theta,\tau) = \frac{k[T(r,\theta,\tau) - T_s]}{\dot{q}a^2} \tag{3}$$

With this substitution, Eq. (2) becomes

$$\frac{1}{r^2}\frac{\partial}{\partial r}\left(r^2\frac{\partial\Theta}{\partial r}\right) + \frac{1}{r^2\sin\theta}\frac{\partial}{\partial\theta}\left(\sin\theta\frac{\partial\Theta}{\partial\theta}\right) + 1 = \frac{\text{Pe}}{2}\left(u\frac{\partial\Theta}{\partial r} + \frac{v}{r}\frac{\partial\Theta}{\partial\theta}\right) + \frac{\partial\Theta}{\partial\tau} \tag{4}$$

The initial and boundary conditions imposed on Eq. (4) are

$$\Theta(r,\theta,\tau=0) = 0 \text{ (initial condition)} \tag{5}$$

$$\Theta(r=1,\theta,\tau) = 0 \text{ (outer edge of the droplet)} \tag{6}$$

and

$$\left.\frac{\partial\Theta}{\partial\theta}\right|_{\theta=0} = \left.\frac{\partial\Theta}{\partial\theta}\right|_{\theta=\pi} = 0 \text{ (azimuthally symmetric)} \tag{7}$$

For a spherical droplet, at low Reynolds number and without surface agents, the interior steady-stream function is given using dimensionless coordinates by [4]

$$\psi(r,\theta) = \frac{\bar{\psi}(r,\theta)}{Ua^2} = \frac{(r^2 - r^4)\sin^2\theta}{4(1+\kappa)} \tag{8}$$

where κ is the ratio of dynamic viscosities, $\mu_{\text{ext}}/\mu_{\text{drop}}$. The scaled velocities are then

$$u(r,\theta) = \frac{1}{r^2\sin\theta}\frac{\partial\psi}{\partial\theta} = \frac{(1-r^2)\cos\theta}{2(1+\kappa)} \tag{9}$$

and

$$v(r,\theta) = \frac{-1}{r\sin\theta}\frac{\partial\psi}{\partial r} = \frac{(-1+2r^2)\sin\theta}{2(1+\kappa)} \tag{10}$$

Contributed by the Heat Transfer Division of ASME for publication in the JOURNAL OF HEAT TRANSFER. Manuscript received December 5, 2005; final manuscript received June 27, 2006. Review conducted by Jose L. Lage.

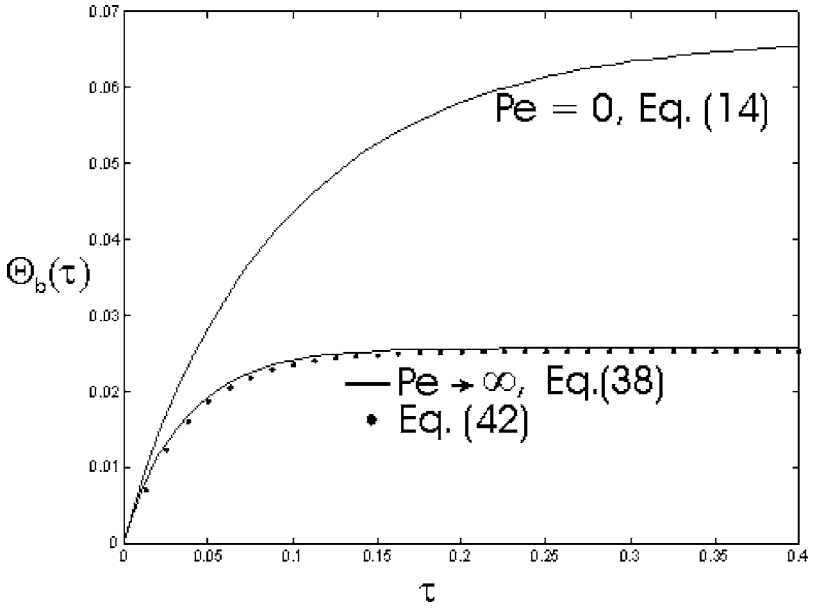

Fig. 1 Θ_b as a function of time

Solution Procedure

The solution to Eq. (4) has been obtained for two limiting cases: first, an analytic solution was obtained for pure diffusion with Pe=0, and second, a semianalytic solution was obtained for limiting case of very high Peclet numbers.

Special Case 1: Pe=0. As the Peclet number approaches zero, the problem loses its dependence on the tangential coordinate. Thus, the dimensionless temperature is a function of r and τ only. In this case, Eq. (4) becomes

$$\frac{1}{r^2}\frac{\partial}{\partial r}\left(r^2\frac{\partial\Theta}{\partial r}\right)+1=\frac{\partial\Theta}{\partial\tau} \tag{11}$$

Using standard separation-of-variable techniques, the solution to Eq. (11) may be shown to be

$$\Theta(r,\tau)=\frac{1-r^2}{6}+\sum_{n=1}^{\infty}\frac{2(-1)^n}{n^3\pi^3}\frac{\sin(n\pi r)}{r}e^{-n^2\pi^2\tau} \tag{12}$$

A parameter of interest is the bulk or average temperature of the droplet, Θ_b,

$$\Theta_b(\tau)=\frac{\int_{\mathrm{Vol}}\Theta(r,\theta,\tau)d\mathrm{Vol}}{\int_{\mathrm{Vol}}d\mathrm{Vol}}=\frac{3}{2}\int_0^1\left[\int_0^{\pi}\Theta(r,\theta,\tau)\sin\theta d\theta\right]r^2dr \tag{13}$$

Application of Eq. (13) yields the following for the bulk temperature:

$$\Theta_b(\tau)=\frac{1}{15}-\sum_{n=1}^{\infty}\frac{6}{n^4\pi^4}e^{-n^2\pi^2\tau} \tag{14}$$

Equation (14) is graphically shown in Fig. 1.

Special Case 2: Pe→∞. As the Peclet number becomes very large, the temperature contours are assumed to be parallel to the stream function contours [5]. With this assumption, Eq. (4) may be solved using the procedure described in Oliver and Souccar [6]. Specifically, the dimensionless temperature is assumed to be a function of the stream function, ψ, and τ

$$\lim_{\mathrm{Pe}\to\infty}\Theta(r,\theta,\tau)=\Theta(\psi,\tau) \tag{15}$$

Following the example of Ref. [6], Eq. (15) may be restated in terms of the dimensionless spatial variable ξ and the dimensionless time τ

$$\lim_{\mathrm{Pe}\to\infty}\Theta(r,\theta,\tau)=\Theta(\xi,\tau) \tag{16}$$

where

$$\xi=16(1+\kappa)\psi=4r^2(1-r^2)\sin^2\theta \tag{17}$$

Note that the exterior of the droplet is at $\xi=0$, and at the vortex center is at $\xi=1$.

With these assumptions, Eq. (4) may be restated as

$$\frac{\partial}{\partial\xi}\left[p(\xi)\frac{\partial\Theta}{\partial\xi}\right]=\frac{q(\xi)}{16}\left(\frac{\partial\Theta}{\partial\tau}-1\right) \tag{18}$$

The functions $p(\xi)$ and $q(\xi)$ are

$$p(\xi)=\frac{2\sqrt{1+\sqrt{\xi}}}{3}\left[(4-3\xi)E\left(\frac{1-\sqrt{\xi}}{1+\sqrt{\xi}}\right)-(4\sqrt{\xi}-3\xi)K\left(\frac{1-\sqrt{\xi}}{1+\sqrt{\xi}}\right)\right] \tag{19}$$

and

$$q(\xi)=\frac{2}{\sqrt{1+\sqrt{\xi}}}K\left(\frac{1-\sqrt{\xi}}{1+\sqrt{\xi}}\right) \tag{20}$$

where $E(x)$ and $K(x)$ are the complete elliptic integrals [7].

The boundary conditions imposed on Eq. (18) are

$$\Theta(\xi=0,\tau)=0 \text{ (along the exterior of the droplet)} \tag{21}$$

and

$$\Theta(\xi=1,\tau) \text{ is finite (at the vortex center)} \tag{22}$$

Equation (21) states that the dimensionless temperature along the exterior of the droplet is zero. This boundary condition, coupled with the assumption implicit in Eq. (16) requires that the dimensionless temperature at the droplet center also be zero. (Note that the streamline associated with the droplet exterior is the same as the streamline through the droplet center.) This will generally not be the case for a real droplet with a finite Peclet number. Rather, Eq. (16) is a limiting case as the Peclet number ap-

proaches infinity.

For brevity, a plot of the streamlines has not been included. A plot of these streamlines may be found in both Refs. [5,6]. With the assumption implicit in Eq. (16) the direction of flow of the streamlines is not material.

Unlike the previous analysis of Ref. [6], the initial condition imposed on Θ is based on Eq. (5)

$$\Theta(\xi, \tau = 0) = 0 \tag{23}$$

Equation (18) is solved using separation-of-variables techniques, where $\Theta(\xi, \tau)$ is assumed to be of the form

$$\Theta(\xi, \tau) = F(\xi) + \sum_{n=1}^{\infty} A_n \Xi_n(\xi) e^{-16\lambda_n^2 \tau} \tag{24}$$

Note that the function, $F(\xi)$, is the steady-state function and the terms in the summation become very small as time increases, especially for large values of n. As such, except for very small times, the summation in Eq. (24) may be truncated without a significant loss of accuracy.

The differential equation for the steady-state component of Eq. (24), $F(\xi)$, is

$$\frac{d}{d\xi}\left[p(\xi) \frac{dF}{d\xi} \right] = -\frac{q(\xi)}{16} \tag{25}$$

The boundary conditions imposed on $F(\xi)$ are then

$$\left. \frac{dF}{d\xi} \right|_{\xi=0} = \frac{1}{16} \text{ (energy balance at the outer stream function)} \tag{26}$$

$$F(\xi = 0) = 0 \text{ (along the exterior of the droplet)} \tag{27}$$

and

$$F(\xi = 1) \text{ (at the vortex center) is finite} \tag{28}$$

Equation (25) was solved iteratively using second-order finite difference techniques.

The transient component of Eq. (24) was solved in a manner similar to the solution procedure used by Ref. [6] for heat transfer without heat generation. Using standard separation-of-variables techniques and substitution Eq. (24) into Eq. (18), the corresponding ordinary differential equation for the eigenfunction Ξ_n is

$$\frac{d}{d\xi}\left[p(\xi) \frac{d\Xi_n}{d\xi} \right] + \lambda_n^2 q(\xi) \Xi_n(\xi) = 0 \tag{29}$$

The boundary conditions imposed on $\Xi_n(\xi)$ are

$$\Xi_n(\xi = 0) = 0 \text{ (at the outer stream function of the droplet)}$$

and

$$\Xi_n(\xi = 1) \text{ is finite(at the droplet vortex center)}$$

Equation (29) is solved using second-order finite difference techniques. With this solution procedure, Eq. (29) is transformed into a matrix system of equations.

Both of the functions $p(\xi)$ and $q(\xi)$ are positive on the interval (0,1). In addition, $\lim_{\xi \to 0} p(\xi) = 0$. Under these circumstances, Eq. (29) is a proper Sturm-Liouville-type problem, where the corresponding eigenfunctions Ξ_n are orthogonal on the interval (0,1) with respect to the weighting function $q(\xi)$ [8]. That is,

$$\int_0^1 \Xi_m(\xi) \Xi_n(\xi) q(\xi) d\xi = \delta_{mn} \int_0^1 [\Xi_n(\xi)]^2 q(\xi) d\xi \tag{30}$$

where δ_{mn} is the Kronecker δ function.

The eigenvalues λ_n may be evaluated using an energy balance analysis, which requires that

$$\lambda_n^2 \int_0^1 \Xi_n(\xi) q(\xi) d\xi = \frac{8}{3} \left. \frac{d\Xi_n}{d\xi} \right|_{\xi=0} \tag{31}$$

Once the eigenvalues and corresponding eigenfunctions are ascertained, the eigenfunctions are *normalized* so that

$$1 = \int_0^1 [\Xi_n(\xi)]^2 q(\xi) d\xi \tag{32}$$

The coefficients A_n may be obtained using the orthogonality of the eigenfunctions Ξ_n coupled with the initial condition, Eq. (5),

$$0 = F(\xi) + \sum_{n=1}^{\infty} A_n \Xi_n(\xi) \tag{33}$$

The inner products of both sides of Eq. (33) are taken with $\Xi_m(\xi)$. Since the eigenfunctions Ξ_n are orthonormal with respect to the weighting function $q(\xi)$:

$$A_n = -\int_0^1 F(\xi) \Xi_n(\xi) q(\xi) d\xi \tag{34}$$

The solution procedure used to find the eigenfunctions Ξ_n and the eigenvalues λ_n was similar to the procedure reported in Ref. [6]. As such, these eigenfunctions and eigenvalues will be the same as those cited in that work. However, the coefficients A_n will be different.

The bulk or average temperature, $\Theta_b(\tau)$, may be calculated by taking the weighted average of $\Theta(\xi, \tau)$, with

$$\Theta_b(\tau) = \frac{3}{8}\left[\int_0^1 F(\xi) q(\xi) d\xi + \sum_{n=1}^{\infty} A_n \int_0^1 \Xi_n(\xi) q(\xi) d\xi e^{-16\lambda_n^2 \tau} \right] \tag{35}$$

Defining, $B_n = \int_0^1 \Xi_n(\xi) q(\xi) d\xi$, the bulk temperature is then

$$\Theta_b(\tau) = \frac{3}{8}\left[\int_0^1 F(\xi) q(\xi) d\xi + \sum_{n=1}^{\infty} A_n B_n e^{-16\lambda_n^2 \tau} \right] \tag{36}$$

All integrations were performed using the trapezoidal rule using the same node points as were used for the finite difference scheme. As a practical matter, the summations used in Eq. (24) and subsequent equations are truncated such that

$$\Theta(\xi, \tau) = F(\xi) + \sum_{n=1}^{n_{\max}} A_n \Xi_n(\xi) e^{-16\lambda_n^2 \tau} \tag{37}$$

and

$$\Theta_b(\tau) = \frac{3}{8}\left[\int_0^1 F(\xi) q(\xi) d\xi + \sum_{n=1}^{n_{\max}} A_n B_n e^{-16\lambda_n^2 \tau} \right] \tag{38}$$

The rate of convergence with respect to $n_{\max}$ and the grid spacing are investigated below.

Results

When using numerical integration and finite-difference techniques, it is important to know if the numerical grid is small enough to insure convergence. To illustrate the convergence of the solution with $\Delta\xi$, the values of A_n and λ_n^2 are given in Table 1.

As may be seen in Table 1, the convergence with respect to $n_{\max}$ and $\Delta\xi$ is rapid for the first few modes. However, the convergence for higher-order modes is slower. However, the coefficients A_n become very small as n increases. Inspection of Eq. (37) demonstrates that, except at very small times, the higher-order terms are irrelevant due to the exponential operator.

Table 1 Convergence with Respect to $\Delta\xi$ and n_{max}

$\Delta\xi=0.01$ $n_{max}=5$	$\Delta\xi=0.005$ $n_{max}=10$	$\Delta\xi=0.0010$ $n_{max}=30$	$\Delta\xi=0.0005$ $n_{max}=30$
$A_1=-0.04956$	$A_1=-0.04946$	$A_1=-0.04938$	$A_1=-0.04937$
$\lambda_1^2=1.6778$	$\lambda_1^2=1.6777$	$\lambda_1^2=1.6777$	$\lambda_1^2=1.6777$
$A_2=0.00436$	$A_2=0.00437$	$A_2=0.00439$	$A_2=0.00439$
$\lambda_2^2=8.5874$	$\lambda_2^2=8.5959$	$\lambda_2^2=8.5987$	$\lambda_2^2=8.5988$
$A_3=-0.00124$	$A_3=-0.00120$	$A_3=-0.00118$	$A_3=-0.00118$
$\lambda_3^2=20.9458$	$\lambda_3^2=20.9605$	$\lambda_3^2=20.9645$	$\lambda_3^2=20.9646$
	$A_{10}=0.000062$	$A_{10}=0.0000293$	$A_{10}=0.0000282$
	$\lambda_{10}^2=251.7077$	$\lambda_{10}^2=259.8718$	$\lambda_{10}^2=260.1168$
		$A_{20}=0.00000678$	$A_{20}=0.00000431$
		$\lambda_{20}^2=1054.2324$	$\lambda_{20}^2=1062.91$
		$A_{30}=0.000006288$	$A_{30}=0.00000239$
		$\lambda_{30}^2=2354.63$	$\lambda_{30}^2=2394.52$

For practicing engineers, it is often valuable that simple, yet reasonably accurate, approximations be reported for important parameters. The steady-state temperature profile value may be approximated well by the relation

$$\lim_{r\to\infty}\Theta(\xi,\tau)=F(\xi)\cong\tfrac{1}{18}\xi \tag{39}$$

Substitution of Eq. (17) into Eq. (39) yields

$$\lim_{r\to\infty}\Theta(r,\theta,\tau)\cong\tfrac{1}{18}\xi=\tfrac{2}{9}(r^2-r^4)\sin^2\theta \tag{40}$$

Equation (40) may be extended to finite times by including an approximation of Eq. (24) that is truncated at the first mode while insuring that the initial condition, Eq. (5) is satisfied

$$\Theta(r,\theta,\tau)\cong\tfrac{2}{9}(r^2-r^4)\sin^2\theta(1-e^{-16\lambda_1^2\tau})$$

From Table 1, the value of λ_1^2 is 1.6777. Hence,

$$\Theta(r,\theta,\tau)\cong\tfrac{2}{9}(r^2-r^4)\sin^2\theta(1-e^{-26.8\tau}) \tag{41}$$

Inspection of Fig. 2 indicates that Eq. (41) is reasonably accurate for $\tau>0.05$.

An approximation for the bulk temperature may be obtained from Eq. (41) by applying Eq. (13)

$$\Theta_b(\tau)\cong\tfrac{8}{315}(1-e^{-26.8\tau}) \tag{42}$$

This approximation is compared with the predictions of Eq. (38) in Fig. 1. As may be seen, Eq. (42) predicts the bulk temperature well, except at very low times.

Conclusion

The heat transfer from a droplet with a distributed heat generation has been predicted for two special cases: at very low Peclet numbers, and at very high Peclet numbers. In both cases, all of the resistance to heat transfer was assumed to be in the droplet (interior problem). As may be expected, the droplet temperature rises less for high Peclet numbers than it does for low Peclet numbers. Similarly, the droplet temperature profile responds more rapidly at high Peclet numbers than it does at low Peclet numbers.

Nomenclature

a = droplet radius
A_n = coefficient; see Eq. (24)
B_n = coefficient; see Eq. (36)
n_{max} = truncation limit
$p(\xi)$ and $q(\xi)$ = functions defined by Eqs. (19) and (20)
Pe = Peclet number, $\mathrm{Pe}=2Ua/\alpha$
r = radial coordinate made dimensionless with the radius a
T = temperature
U = droplet velocity

Greek Symbols

α = diffusivity
θ = tangential coordinate
Θ = dimensionless temperature $\Theta=[(T-T_S)k]/\dot{q}a^2$
λ_n = eigenvalue; see Eq. (24)
μ = dynamic viscosity
ξ = spatial coordinate; see Eq. (17)
$\Xi_n(\xi)$ = eigenfunction; see Eq. (24)
τ = dimensionless time, $\tau=\alpha t/a^2$
ψ = dimensionless stream function

Subscripts

drop = droplet or dispersed phase

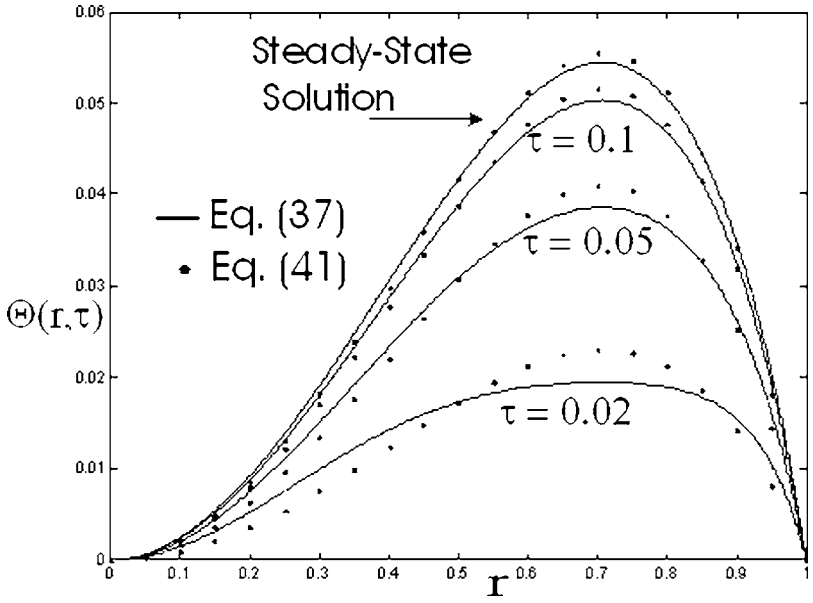

Fig. 2 $\Theta(r)$ along $\theta=\pi/2$ at several times

ext = continuous phase
s = droplet surface

Appendix: Application to Mass Transfer

This analysis may be applied to mass transfer. For an explanation of the analogy between heat transfer and mass transfer, see Ref. [4] (pp. 10–14).

Consider a parent species A that produces the daughter species, through a chemical or nuclear reaction, at a constant volumetric rate $\dot{R}$. Furthermore, assume that the daughter species is stable without further reaction or decay.

A differential mass balance of the daughter species with a corresponding generation term yields the following differential equation:

$$\frac{1}{r^2}\frac{\partial}{\partial r}\left(r^2\frac{\partial c}{\partial r}\right)+\frac{1}{r^2\sin\theta}\frac{\partial}{\partial\theta}\left(\sin\theta\frac{\partial c}{\partial\theta}\right)+\frac{\dot{R}a^2}{D}=\frac{\mathrm{PeLe}}{2}\left(u\frac{\partial c}{\partial r}+\frac{v}{r}\frac{\partial c}{\partial\theta}\right)+\frac{\partial c}{\partial\tau} \tag{A1}$$

where c is the daughter species concentration level, D is the mass diffusivity, $\dot{R}$ is the volumetric rate of production of the daughter species, Le is the Lewis number, and τ is the dimensionless time

$$\mathrm{Le}=\left(\frac{\mu}{\rho D}\right)_{\mathrm{drop}} \quad \text{and} \quad \tau=\frac{Dt}{a^2} \tag{A2}$$

For mass transfer, Θ represents the dimensionless species concentration with

$$\Theta=\frac{(c-c_s)D}{\dot{R}a^2} \tag{A3}$$

With these substitutions, and the associated implied assumptions, the above analysis is applicable to mass transfer.

References

[1] Sadhal, S. S., Ayyaswamy, P. S., and Chung, J. N., 1997, *Transport Phenomena With Drops and Bubbles*, Springer, New York.

[2] Kleinman, L. S., and Reed, X. B., 1996, "Unsteady Conjugate Mass Transfer between a Single Droplet and an Ambient Flow With External Chemical Reaction, Ind. Eng. Chem. Res., **35**, pp. 2875–2888.

[3] Juncu, Gh., 2002, "Conjugate Mass Transfer to a Spherical Drop Accompanied by a Second Order Chemical Reaction Inside the Drop," Int. J. Heat Mass Transfer, **45**, pp. 3817–3819.

[4] Clift, R., Grace, J. R., and Weber, M. E., 1978, *Bubbles, Drops, and Particles*, Academic Press, New York, Eqs. (3) and (8).

[5] Kronig, R., and Brink, J. C., 1950, "On the Theory of Extraction from Falling Droplets, Appl. Sci. Res., Sect. A, **2**, pp. 142–154.

[6] Oliver, D. L., and Souccar, A. W., 2006, "Heat Transfer From a Translating Droplet at High Peclet Numbers: Revisiting the Classic Solution of Kronig & Brink," ASME J. Heat Transfer, **128**, pp. 648–652.

[7] Abramowitz, M., and Stegun, I., 1964, *Handbook of Mathematical Functions*, National Bureau of Standards, Eqs. (17.3.6) and (17.3.4).

[8] Hildebrand, F. B. 1976, *Advanced Calculus for Applications*, 2nd ed., Prentice-Hall, Englewood Cliffs, NJ, Chap. 5.6.

Journal of Heat Transfer

Technical Briefs

Least-Squares Radial Point Interpolation Collocation Meshless Method for Radiative Heat Transfer

J. Y. Tan

L. H. Liu
e-mail: lhliu@hit.edu.cn

B. X. Li

School of Energy Science and Engineering,
Harbin Institute of Technology,
92 West Dazhi Street,
Harbin 150001, People's Republic of China

A least-squares radial point interpolation collocation meshless method based on the discrete ordinates equation is developed for solving the radiative transfer in absorbing, emitting, and scattering media, in which compact support radial basis functions augmented with polynomial basis are employed to construct the trial functions. In addition to the collocation nodes, a number of auxiliary points are also adopted to form the total residuals of the problem. The least-squares technique is used to obtain the solution of the problem by minimizing the summation of residuals of all collocation and auxiliary points. Three typical examples of radiative transfer in semitransparent media are examined to verify this new solution method. The numerical results are compared with other benchmark approximate solutions in references. By comparison, the results show that the least-squares radial point interpolation collocation meshless method has good accuracy in solving radiative transfer problems within absorbing, emitting, and scattering media. [DOI: 10.1115/1.2712861]

Keywords: radiative heat transfer, meshless method, radial basis function

1 Introduction

Numerical solutions of radiative transfer equation (RTE) in participating medium require considerable effort for most practical systems composed of semitransparent media. Many numerical methods have been developed to solve this problem in past decades, such as the zonal method [1–3], the Monte Carlo method [4,5], the discrete ordinates method (DOM) [6,7], the finite volume method (FVM) [8–14], and the finite element method [15,16]. Because the problem domain needs to be discretized into meshes, these traditional methods suffer from drawbacks such as tedious meshing and re-meshing, especially for the design and inverse problems of geometry shape.

Meshless methods [17–20] have been proposed for the problem of computational mechanics to avoid the tedious meshing and re-meshing. Meshless methods use a set of nodes scattered within the problem domain and its boundaries to establish a system of algebraic equations for whole problem domain without the use of a predefined mesh. These scattered nodes do not form a mesh, which means that no information on the relationship among the nodes is required. Various methods belonging to this family are the element free Galerkin method, the meshless local Petrov-Galerkin (MLPG) method, the point interpolation method, the smoothed particle hydrodynamics method, and so on [17–20]. Recently, the meshless methods were introduced into the community of radiative heat transfer. Liu [21,22] solved the multi-dimensional radiative transfer equation using a MLPG method. One of the major difficulties in the implementation of MPLG is the numerical integration. In addition, radiative transfer equation can be considered as a special case of the general convection-diffusion [14]. The standard MLPG solution of convection-diffusion equation sometimes exhibits oscillation to some extent [17]. Sadat [23] observed this type of solution oscillation for a one-dimensional radiative transfer problem. In order to overcome the drawback of MLPG method, Tan et al. [24] extended the least-squares collocation meshless approach proposed by Zhang et al. [25] to solve a coupled radiative and conductive heat transfer in semitransparent media.

The meshless method includes two important parts. One is the construction of trial functions (shape functions), and the other is the discretization of differential equation. Several techniques have been developed to construct trial functions, such as the moving least-squares (MLS) approximation, the local radial point interpolation (LRPI) approximation, and so on [18,19]. In the LRPI approximation, radial basis functions [18,19] are used to construct the shape functions. The important difference between the LRPI and the MLS approximations is that the LRPI shape functions possess the Kronecker delta function property, while the MLS shape functions do not possess the Kronecker delta function property. The Kronecker delta function property allows essential boundary conditions to be treated easily and accurately.

In this paper, the least-squares radial point interpolation collocation meshless (LSRPICM) method based on the discrete ordinate equations is developed for solving radiative transfer problems in semitransparent media, in which compact support radial basis functions augmented with polynomial basis are employed to construct shape functions. Except for the collocation nodes, a number of auxiliary points are also adopted to form the total residuals of the problem. Three typical examples of radiative transfer are examined to verify the LSRPICM method.

2 Mathematical Formulation

2.1 Discrete-Ordinates Equation of Radiative Transfer. Consider a radiative transfer problem in gray semitransparent me-

Contributed by the Heat Transfer Division of ASME for publication in the JOURNAL OF HEAT TRANSFER. Manuscript received March 3, 2006; final manuscript received June 30, 2006. Review conducted by Walter W. Yuen.

dia enclosed by diffusely emitting and reflecting boundaries. By dividing the 4π solid angle into M discrete directions, the discrete-ordinates equation of radiative transfer can be written as [26,27]

$$\mu^m \frac{\partial I^m}{\partial x} + \eta^m \frac{\partial I^m}{\partial y} + \xi^m \frac{\partial I^m}{\partial z} + \left(\kappa_a + \kappa_s - \frac{\kappa_s}{4\pi} \Phi^{m,m} \right) I^m = \kappa_a I_b + \frac{\kappa_s}{4\pi} \sum_{m'=1, m' \neq m}^{M} I^{m'} \Phi^{m',m} w^{m'}, \quad m = 1,2, \ldots, M \quad (1)$$

with boundary conditions

$$I_w^m = \varepsilon_w I_{bw} + \frac{1-\varepsilon_w}{\pi} \sum_{\mathbf{n}_w \cdot \mathbf{s}^{m'} < 0} I_w^{m'} |\mathbf{n}_w \cdot \mathbf{s}^{m'}| w^{m'}, \quad \mathbf{n}_w \cdot \mathbf{s}^m > 0 \quad (2)$$

2.2 Local Radial Point Interpolation Approximation. In the LSRPICM implementation, first N_{col} collocation nodes are scattered within the problem domain and its boundaries, and then compact support radial basis functions (CSRBFs) augmented with polynomial basis are employed to construct shape functions. A typical CSRBF is given as follows [19,20]

$$R_i(\mathbf{x}) = \begin{cases} (1-r)^4 (4 + 16r + 12r^2 + 3r^3), & r \leqslant 1 \\ 0, & r > 1 \end{cases} \quad (3)$$

where $r = \|\mathbf{x} - \mathbf{x}_i\| / d_i$ is the dimensionless distance between points $\mathbf{x}$ and $\mathbf{x}_i$, and $d_i = \alpha_{\text{RBF}} r_a$ is the radius of support domain of collocation node $\mathbf{x}_i$, r_a is the averaged nodal distance between two neighboring collocation nodes, and α_{RBF} is the dimensionless size parameter.

In this paper, the unknown radiative intensities $I^m(\mathbf{x})$ are only stored in the collocation nodes, which are used to construct the shape functions by the LRPI approximation. Consider a spatial sub-domain $V_{\mathbf{x}}$ in the neighborhood of a point $\mathbf{x}$ and denoted as the domain of definition of the LRPI approximation for the trial function at $\mathbf{x}$, which is located within the problem domain. To approximate the radiative intensity I^m in $V_{\mathbf{x}}$, over a number of local collocation points $\{\mathbf{x}_i\}$, $i = 1,2,\ldots,n$, the LRPI approximant $\tilde{I}^m(\mathbf{x})$ of I^m can be defined as a linear combination of n radial basis functions and k polynomial basis functions as follows

$$\tilde{I}^m(\mathbf{x}) = \sum_{i=1}^{n} R_i(\mathbf{x}) a_i + \sum_{j=1}^{k} p_j(\mathbf{x}) b_j \quad (4)$$

where a_i is the coefficient for the CSRBF $R_i(\mathbf{x})$, and b_j is the coefficient for the polynomial basis function $p_j(\mathbf{x})$. The coefficients a_i and b_j are determined by enforcing that the interpolation passes through all n collocation nodes within the support domain

$$\sum_{i=1}^{n} R_i(\mathbf{x}_l) a_i + \sum_{j=1}^{k} p_j(\mathbf{x}_l) b_j = \hat{I}_l^m, \quad l = 1,2,\ldots n \quad (5)$$

Here, $\hat{I}_i^m$ in Eq. (6) is a fictitious nodal value, and not the nodal value of the unknown trial function $\tilde{I}_i^m$ in general. The polynomial function has to satisfy the extra requirement as follows [18,20]

$$\sum_{i=1}^{n} a_i p_j(\mathbf{x}_i) = 0, \quad j = 1,2,\ldots,k \quad (6)$$

By solving Eqs. (5) and (6), Eq. (13) can be rewritten as

$$\tilde{I}^m(\mathbf{x}) = \sum_{i=1}^{n} \phi_i(\mathbf{x}) \hat{I}_i^m \quad (7)$$

where $\phi_i(\mathbf{x})$ is usually called as the shape function corresponding to collocation node $\mathbf{x}_i$.

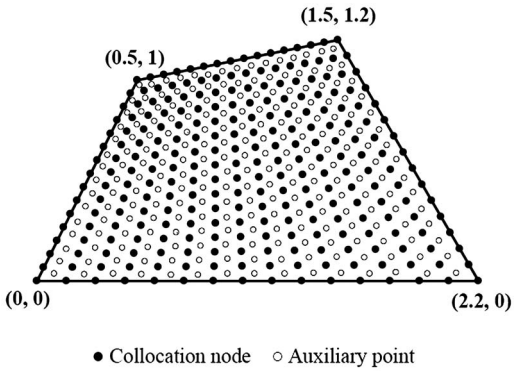

Fig. 1 Schematic and node system of the irregular quadrilateral enclosure (dimension in meters)

2.3 Discretization of Discrete-Ordinates Equation and Numerical Implementation. Except for the collocation nodes, $N_{\max}$ auxiliary points are also adopted to form the total residuals of the problem. Substituting Eq. (7) into Eq. (1), we can obtain the following residual E_Q^m at $\mathbf{x}_Q$ for discrete ordinates equation defined in the problem domain

$$E_Q^m = \sum_{j=1}^{n} D^m[\phi_j(\mathbf{x}_Q)] I_j^m - C^m(\mathbf{x}_Q), \quad Q = 1,2,\ldots,N_{\text{col}} + N_{\text{aux}} \quad (8)$$

where

$$D^m[\phi_j(\mathbf{x}_Q)] = \mu^m \phi_{j,x}(\mathbf{x}_Q) + \eta^m \phi_{j,y}(\mathbf{x}_Q) + \xi^m \phi_{j,z}(\mathbf{x}_Q) + \left(\kappa_a + \kappa_s - \frac{\kappa_s}{4\pi} \Phi^{m,m} \right) \phi_j(\mathbf{x}_Q) \quad (9)$$

$$C^m(\mathbf{x}_Q) = \sum_{j=1}^{n} \phi_j(\mathbf{x}_Q) \left(\kappa_a I_b(\mathbf{x}_j) + \frac{\kappa_s}{4\pi} \sum_{m'=1, m' \neq m}^{M} I^{m'}(\mathbf{x}_j) \Phi^{m',m} w^{m'} \right) \quad (10)$$

Here, $(\,)_{,l} = \partial(\,)/\partial l$ represents the derivative with respect to spatial coordinate l, $l = x, y, z$. We then obtain the following functional of all residuals for all collocation and auxiliary points

$$\Gamma^m = \sum_{Q=1}^{N_{\text{col}}+N_{\text{aux}}} \left\{ \sum_{j=1}^{n} D^m[\phi_j(\mathbf{x}_Q)] I_j^m - C^m(\mathbf{x}_Q) \right\}^2 \quad (11)$$

By minimizing the function Γ^m with respect to the radiative intensity I_i^m, we have

$$\frac{\partial \Gamma^m}{\partial I_i^m} = 2 \sum_{Q=1}^{N_{\text{col}}+N_{\text{aux}}} \left\{ \left[\sum_{j=1}^{n} D^m[\phi_j(\mathbf{x}_Q)] I_j^m - C^m(\mathbf{x}_Q) \right] D^m[\phi_j(\mathbf{x}_Q)] \right\} = 0, \quad i = 1,2,\ldots,N_{\text{col}} \quad (12)$$

This leads to the following discretized system of linear equations

$$\sum_{j=1}^{N_{\text{col}}} K_{ij}^m I_j^m = f_i^m, \quad i = 1,2,\ldots,N_{\text{col}} \quad (13)$$

where

$$K_{ij}^m = \sum_{Q=1}^{N_{\text{col}}+N_{\text{aux}}} D^m[\phi_j(\mathbf{x}_Q)] D^m[\phi_i(\mathbf{x}_Q)] \quad (14)$$

$$f_i^m = \sum_{Q=1}^{N_{\text{col}}+N_{\text{aux}}} C^m(\mathbf{x}_Q) D^m[\phi_i(\mathbf{x}_Q)] \quad (15)$$

For each node i on the inflow boundary, the radiative intensity I_i^m is given by Eq. (2), and the boundary condition can be directly imposed as follows

$$K_{ij}^m = \delta_{ij}, \quad f_i^m = I_i^m \tag{16}$$

where δ_{ij} is Kronecker's delta. Because the in-scattering term in the discrete ordinates equation at the direction m contains the radiative intensities of the other direction, global iterations similar to those used in the discrete ordinates method are necessary to include the source and boundary conditions.

3 Results and Discussion

To verify the accuracy of the LSRPICM approach for solving the radiative heat transfer problems in absorbing, emitting, and scattering media, three typical examples are examined. A computer code based on the preceding calculation procedure was written. Node densification studies were also performed for solutions to ensure that the solutions are independent of node number. For the following numerical study, the equal-weight even quadrature S_8 is selected. In this paper, the maximum relative error (10^{-4}) of the radiative intensity is taken as the stopping criterion for iteration. For the sake of comparison, the relative error based on the data in references is defined as

$$\text{relative error} = 100 \times \frac{\left[\int_0^L [\text{data obtained by LSRPICM} - \text{data in references}]^2 \mathrm{d}x\right]^{1/2}}{\int_0^L \text{data in references } \mathrm{d}x} \tag{17}$$

3.1 Case 1: Nonscattering Gray Medium in Irregular Quadrilateral Enclosure. As shown in Fig. 1, we consider the radiative heat transfer problem in a two-dimensional irregular enclosure filled with uniform absorbing and emitting media. The walls are cold blackbodies (0 K). The medium is gray and isothermal, The absorption coefficient of media is $\kappa_a = 1\ \mathrm{m}^{-1}$, and the medium temperature is denoted as T_g. The LSRPICM approach is applied to solve the net radiant heat flux along the bottom surface. $N_{\mathrm{col}} = 256$ collocation nodes are distributed in the problem domain and on its boundaries. In addition, $N_{\mathrm{aux}} = 225$ auxiliary points are also used in the problem domain. The dimensionless size parameter is taken as $\alpha_{\mathrm{RBF}} = 6$. The dimensionless net radiative heat fluxes $q_w/\sigma T_g^4$ on the bottom wall are shown in Fig. 2, and compared with the results obtained by Chai et al. [12] using the FVM. The results of the LSRPICM approach agree with those obtained using the FVM very well. The relative error is 1.01%.

3.2 Case 2: Anisotropically Scattering in a Black Enclosure. In this case, we consider the radiative heat transfer problem in two-dimensional rectangular gray semitransparent medium bounded with black boundaries. The optical thickness based on the side length L of the rectangular is $\tau_L = 1.0$. The medium is kept hot at temperature T_g, but the temperatures of all boundary walls are maintained at 0 K. The medium scatters radiation aniso-

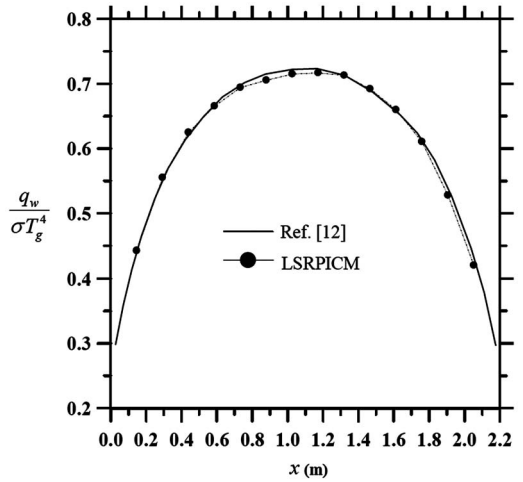

Fig. 2 Dimensionless net radiative heat fluxes on the bottom wall of irregular quadrilateral enclosure

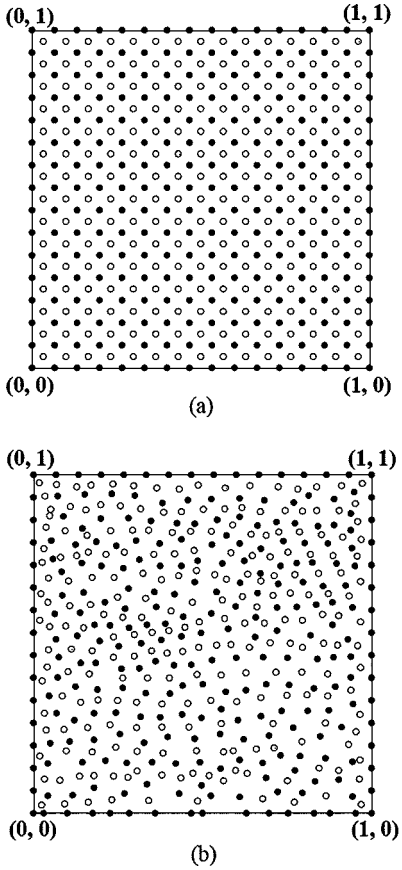

Fig. 3 Schematic and node system of the rectangular black enclosure (dimension in meters): (*a*) Uniform node distribution and (*b*) Nonuniform node distribution

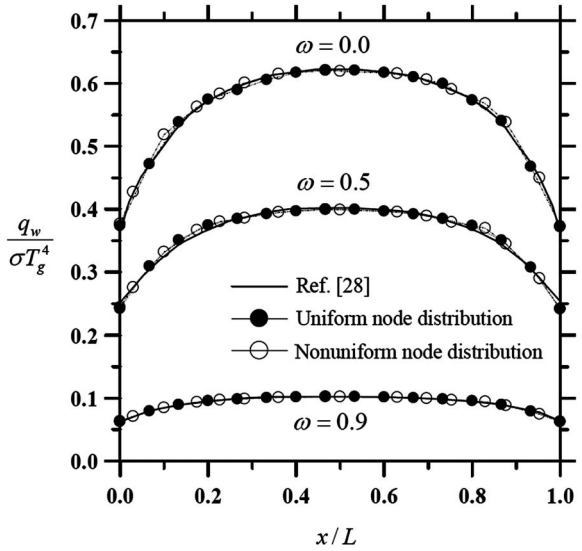

Fig. 4 Dimensionless net radiative heat fluxes on the bottom wall of rectangular black enclosure

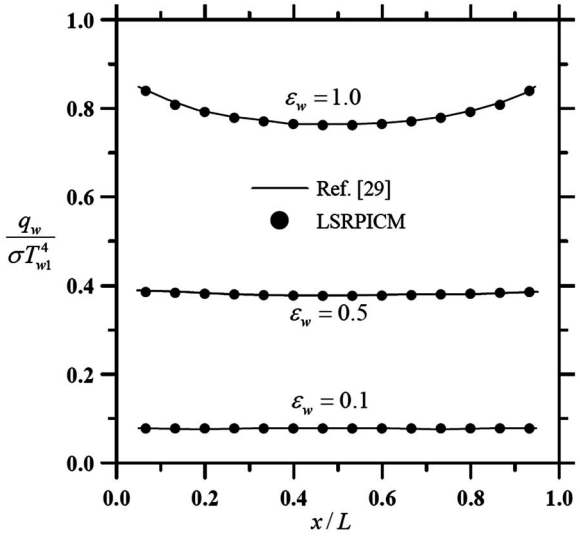

Fig. 5 Dimensionless net radiative heat fluxes on the bottom wall of rectangular gray enclosure

tropically according to the F2 phase function reported in Ref. [28].

$N_{\text{col}}=256$ collocation points and $N_{\text{aux}}=225$ auxiliary points are used to discretize the problem domain. As shown in Fig. 3, two different types of node distribution are considered. One is uniform, and the other is random distribution. The dimensionless net radiative heat fluxes $q_w/\sigma T_g^4$ on the bottom wall are shown in Fig. 4 for three values of single scattering albedo ω, namely, 0.0, 0.5, and 0.9, and are compared with the results obtained by Kim and Lee [28] using the DOM. The results of the LSRPICM approach are very close to those obtained using the DOM. The relative errors based on the data in Ref. [28] are less than 1.1%. No obvious differences between the results obtained using the uniform and the nonuniform node distributions are observed.

3.3 Case 3: Isotropically Scattering in a Gray Enclosure. In this case, a square enclosure filled by isotropically scattering medium with single albedo $\omega=1.0$ is considered. The bottom wall of the enclosure is kept hot, but all other walls and the medium enclosed by the enclosure are kept cold. $N_{\text{col}}=256$ collocation points and $N_{\text{aux}}=225$ auxiliary points are used to discretized the problem domain. The LSRPICM approach is applied to solve the net radiative heat fluxes on the bottom wall. The dimensionless net radiative heat fluxes $q_w/\sigma T_{w1}^4$ along the hot wall are presented in Fig. 5 for three values of wall emissivities, namely, $\varepsilon_w=0.1$, 0.5, and 1.0. By comparison with the results obtained from zone method in Ref. [29], it can be seen that the solutions of LSRPICM agree with those obtained from zone method very well. The relative errors are less than 1.5%.

4 Conclusions

A least-squares radial point interpolation collocation meshless method based on the discrete ordinates equation is developed for solving the radiative transfer in absorbing, emitting, and scattering media. Three typical examples of radiative transfer in semitransparent media are examined to verify this new solution method. The numerical results are compared with other benchmark approximate solutions in references. By comparison, the results show that the least-squares radial point interpolation collocation meshless method has good accuracy in solving radiative transfer problems within absorbing, emitting, and scattering media.

Acknowledgment

The support of this work by the National Science Foundation of China (50425619, 50336010) is gratefully acknowledged.

Nomenclature

a = coefficients for CSRBF in Eq. (4)
b = coefficients for polynomial basis function in Eq. (4)
d_i = radius of support domain of collocation node $\mathbf{x}_i$
E_Q^m = residual of the discrete-ordinates equation at the point $\mathbf{x}_Q$
f = coefficients defined in Eq. (13)
I = radiative intensity, W/m^2 sr
$\tilde{I}$ = LRPI approximant of radiative intensity, W/m^2 sr
$\hat{I}$ = fictitious radiative intensity, W/m^2 sr
k = order of polynomial basis function
K = coefficients in linear equations
M = number of discrete ordinates for radiative transfer equation
n = number of the nodes used for LRPI approximation
n_w = outward unit normal vector of boundary surface
N_{aux} = number of auxiliary point
N_{col} = number of collocation node
q_w = net radiative heat flux on the wall, W/m^2
r = dimensionless distance between two points
r_a = averaged nodal distance between two neighboring collocation nodes, m
R = radial basis function
$\mathbf{s}^m$ = unit vector of the direction m
T = temperature, K
$V_{\mathbf{x}}$ = domain of definition of PRI approximation at $\mathbf{x}$
w^m = weight corresponding to the direction m
x, y, z = Cartesian coordinates
$\mathbf{x}$ = Vector of spatial position

Greek Symbols

α_{RBF} = dimensionless size parameter

Γ = residual sum of discrete-ordinates equation in all collocation and auxiliary points
δ_{ij} = Kronecker's delta
ε_w = wall emissivity
κ_a = absorption coefficient, m^{-1}
κ_s = scattering coefficient, m^{-1}
μ, η, ξ = direction cosines
σ = Stefen-Boltzmann constant
τ_L = optical thickness
ϕ = shape function
Φ = scattering phase function
ω = single scattering albedo
Ω = solid angle, sr

Superscripts

m, m' = discrete direction

References

[1] Hottel, H. C., and Cohen, E. S., 1958, "Radiant Heat Exchange in a Gas-Filled Enclosure: Allowance for Nonuniformity of Gas Temperature," AIChE J., **4**, pp. 3–14.
[2] Yuen, W. W., and Takara, E. E., 1997, "The Zonal Method, a Practical Solution Method for Radiative Transfer in Non-Isothermal Inhomogeneous Media," Annu. Rev. Heat Transfer, **8**, pp. 153–215.
[3] Yuen, W. W., 2006, "The Multiple Absorption Coefficient Zonal Method (MACZM), an Efficient Computational Approach for the Analysis of Radiative Heat Transfer in Multidimensional Inhomogeneous Nongray Media," Numer. Heat Transfer, Part B, **49**, pp. 89–103.
[4] Yang, W. J., Taniguchi, H., and Kudo, K., 1995, "Radiative Heat Transfer by Monte Carlo Method," in *Advances in Heat Transfer*, Vol. 27, Academic Press, New York.
[5] Farmer, J. T., and Howell, J. R., 1998, "Comparison of Monte Carlo Strategies for Radiative Transfer in Participating Media," in *Advances in Heat Transfer*, Vol. 31, Academic Press, New York.
[6] Fiveland, W. A., 1984, "Discrete-Ordinates Solution of the Radiative Transport Equation for Rectangular Enclosures," ASME J. Heat Transfer, **106**, pp. 699–706.
[7] Truelove, J. S., 1987, "Discrete-Ordinate Solutions of the Radiation Transport Equation," ASME J. Heat Transfer, **109**, pp. 1048–1051.
[8] Raithby, G. D., and Chui, E. H., 1990, "A Finite-Volume Method for Predicting a Radiant Heat Transfer Enclosures With Participating Media," ASME J. Heat Transfer, **112**(2), pp. 415–423.
[9] Chui, E. H., Raithby, G. D., and Hughes, P. M. J., 1992, "Prediction of Radiative Transfer in Cylindrical Enclosures With the Finite Volume Method," J. Thermophys. Heat Transfer, **6**, pp. 605–611.
[10] Chui, E. H., and Raithby, G. D., 1993, "Computation of Radiation Heat Transfer on a Nonorthogonal Mesh Using the Finite-Volume Method," Numer. Heat Transfer, Part B, **23**, pp. 269–288.
[11] Chai, J. C., Lee, H. S., and Patankar, S. V., 1994, "Finite Volume Method for Radiation Heat Transfer," J. Thermophys. Heat Transfer, **8**, pp. 419–425.
[12] Chai, J. C., Parthasarathy, H. S., Lee, H. S., and Patankar, S. V., 1995, "Finite Volume Method Radiative Heat Transfer Procedure for Irregular Geometries," J. Thermophys. Heat Transfer, **9**, pp. 410–415.
[13] Chai, J. C., Lee, H. S., and Patankar, S. V., 1994, "Treatment of Irregular Geometries Using a Cartesian Coordinates Finite-Volume Radiation Heat Transfer Procedure," Numer. Heat Transfer, Part B, **26**, pp. 225–235.
[14] Chai, J. C., and Patankar, S. V., 2000, "Finite-Volume Method for Radiation Heat Transfer," in *Advances in Numerical Heat Transfer*, Vol. 2, Taylor & Francis, New York, pp. 109–141.
[15] Fiveland, W. A., and Jessee, J. P., 1994, "Finite Element Formulation of the Discrete-Ordinates Method For Multidimensional Geometries," *Journal of Thermophsics and Heat Transfer*, Vol. 7, pp. 426–433.
[16] Liu, L. H., 2004, "Finite Element Simulation of Radiative Heat Transfer in Absorbing and Scattering Media," J. Thermophys. Heat Transfer, **18**, pp. 555–557.
[17] Atluri, S. N., and Shen, S. P., 2002, *The Meshless Local Petrov-Galerkin (MLPG) Method*, Tech Science Press, Encino, CA.
[18] Liu, G. R., 2003, *Mesh Free Methods*, CRC Press, Boca Raton, FL.
[19] Liu, G. R., and Gu, Y. T., 2005, *An Introduction to Meshfree Methods and Their Programming*, Springer, New York.
[20] Zhang, X., and Liu, Y., 2004, *Meshless Methods*, Tsinghua University Press, Beijing.
[21] Liu, L. H., 2006, "Meshless Local Petrov-Galerkin Method for Solving Radiative Transfer Equation," J. Thermophys. Heat Transfer, **20**, pp. 150–154.
[22] Liu, L. H., 2006, "Meshless Method for Radiative Heat Transfer in Graded Index Medium," Int. J. Heat Mass Transfer, **49**, pp. 219–229.
[23] Sadat, H., 2006, "On the Use of a Meshless Method for Solving Radiative Transfer With the Discrete Ordinates Formulations," J. Quant. Spectrosc. Radiat. Transf., **101**, pp. 263–268.
[24] Tan, J. Y., Liu, L. H., and Li, B. X., 2006, "Least-Squares Collocation Meshless Approach for Coupled Radiative and Conductive Heat Transfer," Numer. Heat Transfer, Part B, **49**, pp. 179–195.
[25] Zhang, X., Liu, X. H., Song, K. Z., and Lu, M. W., 2001, "Least-Squares Collocation Meshless Method," Int. J. Numer. Methods Eng., **51**, pp. 1089–1100.
[26] Modest, M. F., 2003, *Radiative Heat Transfer*, 2nd ed., Academic Press, San Diego.
[27] Chai, J. C., Lee, H. S., and Patankar, S. V., 1994, "Improved Treatment of Scattering Using the Discrete Ordinates Method," ASME J. Heat Transfer, **116**, pp. 260–263.
[28] Kim, T. K., and Lee, H., 1988, "Effect of Anisotropic Scattering on Radiative Heat Transfer in Two-Dimensional Rectangular Enclosures," Int. J. Heat Mass Transfer, **31**, pp. 1711–1721.
[29] Ratzel, A. C., and Howell, J. R., 1983, "Two-Dimensional Radiation in Absorbing-Emitting Media Using the P-N Approximation," ASME J. Heat Transfer, **105**(2), pp. 333–340.

Optimally Staggered Finned Circular and Elliptic Tubes in Turbulent Forced Convection

R. L. S. Mainardes

R. S. Matos

J. V. C. Vargas[1]
e-mail: jvargas@demec.ufpr.br

Departamento de Engenharia Mecânica,
Centro Politécnico,
Universidade Federal do Paraná,
Caixa Postal 19011,
Curitiba, PR, 81531-990, Brazil

J. C. Ordonez
Department of Mechanical Engineering and Center for Advanced Power Systems,
Florida State University,
Tallahassee, FL, 32310-6046

This work presents an experimental geometric optimization study to maximize the total heat transfer rate between a bundle of finned tubes in a given volume and a given external flow both for circular and elliptic arrangements, for general staggered configurations. The results are reported for air as the external fluid, in the range $2650 \leq Re_{2b} \leq 10{,}600$, *where 2b is the smaller ellipse axis. Experimental optimization results for finned circular and elliptic tubes arrangements are presented. A relative heat transfer gain of up to 80%* ($Re_{2b} = 10{,}600$) *is observed in the elliptic arrangement optimized with respect to tube-to-tube spacings, as compared to the optimal circular one. A relative heat transfer gain of 80% is observed in the three-way optimized elliptic arrangement in comparison with the two-way optimized circular one; i.e., with respect to tube-to-tube and fin-to-fin spacings. An empirical correlation for the three-way optimized configuration was obtained to evaluate the resulting maximized dimensionless heat transfer rate.* [DOI: 10.1115/1.2712860]

Keywords: heat transfer enhancement, constructal theory, internal geometry

1 Introduction

Finned cross-flow heat exchangers are part of numerous engineering processes in industry and are unquestionably responsible for a large share of the total energy consumption wherever they are present [1–12].

In this work, the geometric optimization of design parameters for maximum heat transfer is pursued experimentally. The basic idea is to analyze the heat transfer gain using elliptic tubes heat exchangers as compared to the traditional circular ones when varying the following design parameters: δ=fin-to-fin spacing; e=ellipses' eccentricity, and S=spacing between rows of tubes. Hence, the problem consists of identifying a configuration (internal architecture, shape) that provides maximum heat transfer for a given space [13].

The paper describes a series of experiments conducted in the laboratory in the search for optimal geometric parameters in general staggered finned circular and elliptic configurations for maximum heat transfer in turbulent flow. Circular and elliptic arrangements, with the same flow obstruction cross-sectional area, are then compared on the basis of maximum total heat transfer and total mass of manufacturing material.

2 Theory

Dimensionless variables have been defined based on appropriate physical scales as follows

$$\theta = \frac{T - T_\infty}{T_w - T_\infty} \quad \mathrm{Re}_{2b} = \frac{u_\infty (2b)}{\nu} \tag{1}$$

The dimensionless overall thermal conductance $\tilde{q}$, or volumetric heat transfer density, is defined as follows [14–16]

$$\tilde{q} = \frac{Q/(T_w - T_\infty)}{kLHW/(2b)^2} \tag{2}$$

where the overall heat transfer rate between the finned tubes and the free stream, i.e., Q, has been divided by the constrained volume, LHW; k is the fluid thermal conductivity [$\mathrm{W\,m^{-1}\,K^{-1}}$], and $2b=D$ the ellipse smaller axis or tube diameter.

A balance of energy in one elemental channel states that

$$Q = N_{\mathrm{ec}} Q_{\mathrm{ec}} = N_{\mathrm{ec}} \dot{m}_{\mathrm{ec}} c_p (\bar{T}_{\mathrm{out}} - T_\infty) \tag{3}$$

where N_{ec} is the number of elemental channels. The elemental channel is defined as the sum of all unit cells in direction z. Therefore, the mass flow rate [$\mathrm{kg\,s^{-1}}$] entering one elemental channel is

$$\dot{m}_{\mathrm{ec}} = \rho u_\infty [(S + 2b)/2](W - n_f t_f) \tag{4}$$

The number of fins in the arrangement is given by

$$n_f = \frac{W}{t_f + \delta} \tag{5}$$

The dimensionless overall thermal conductance is rewritten utilizing Eqs. (2)–(5) as follows

$$\tilde{q} = \frac{N_{\mathrm{ec}}}{2} \mathrm{Pr}\, \mathrm{Re}_{2b} \left[\frac{2b}{L}\right]^2 \frac{2b}{H} \left(\frac{S}{2b} + 1\right) (1 - \phi_f) \bar{\theta}_{\mathrm{out}} \tag{6}$$

where $\phi_f = n_f t_f / W = t_f / t_f + \delta$, is the dimensionless linear fin density ($0 \leq n_f t_f \leq W$), and Pr the fluid Prandtl number; i.e., ν/α.

For the sake of generalizing the results for all configurations of the type studied in this work, the dimensionless overall thermal conductance is alternatively defined as follows

$$\tilde{q}_* = \frac{2}{N_{\mathrm{ec}}} \left[\frac{L}{2b}\right]^2 \frac{H}{2b} \tilde{q} = \mathrm{Pr}\, \mathrm{Re}_{2b} \left(\frac{S}{2b} + 1\right) (1 - \phi_f) \bar{\theta}_{\mathrm{out}} \tag{7}$$

The volume fraction occupied by solid material in the arrangement is given by

$$\tilde{V} = \frac{W}{L^3} \{n_t \pi [ab - (a - t_t)(b - t_t)] + \phi_f (LH - n_t \pi ab)\} \tag{8}$$

where t_t is the thickness of the tube wall (m) and n_t is the total number tubes of the arrangement.

3 Experiments

The same experimental rig that was utilized in previous studies for the laminar regime [14–16] was re-utilized in the laboratory to produce the necessary experimental data to perform the experimental optimization of finned arrangements. The forced air flow

[1]Corresponding author.

Contributed by the Heat Transfer Division of ASME for publication in the JOURNAL OF HEAT TRANSFER. Manuscript received April 10, 2006; final manuscript received December 15, 2006. Review conducted by Anthony M. Jacobi.

was induced by suction with an axial electric fan, with a nominal power of 1 HP, and was capable of providing air free-stream velocities (u_∞) up to 20 m s^{-1}.

The objective of the experimental work was to evaluate the volumetric heat transfer density (or overall thermal conductance) of each tested arrangement by computing $\tilde{q}_*$ with Eq. (7) through direct measurements of $u_\infty(\mathrm{Re}_{2b})$, and $\bar{T}_{\mathrm{out}}$, $\bar{T}_w$, and $T_\infty(\bar{\theta}_{\mathrm{out}})$. The volume fraction occupied by solid material in the arrangement, i.e., $\tilde{V}$, was also evaluated according to Eq. (8), in order to compare the resulting total volume of solid material of the elliptic and circular arrangements.

Five runs were conducted for each experiment. Steady-state conditions were reached after 3 h in all the experiments. The precision limit for each temperature point was computed as two times the standard deviation of the five runs [17]. It was verified that the precision limits of all variables involved in the calculation of $\tilde{q}_*$ were negligible in comparison to the precision limit of $\bar{\theta}_{\mathrm{out}}$, therefore $P_{\tilde{q}_*}=P_{\bar{\theta}_{\mathrm{out}}}$. The thermistors, anemometer, properties, and lengths bias limits were found negligible in comparison with the precision limit of $\tilde{q}_*$. As a result, the uncertainty of $\tilde{q}_*$ was calculated by

$$\frac{U_{\tilde{q}_*}}{\tilde{q}_*}=\left[\left(\frac{P_{\tilde{q}_*}}{\tilde{q}_*}\right)^2+\left(\frac{B_{\tilde{q}_*}}{\tilde{q}_*}\right)^2\right]^{1/2}\cong\frac{P_{\bar{\theta}_{\mathrm{out}}}}{\bar{\theta}_{\mathrm{out}}} \tag{9}$$

Several free-stream velocities; set points were tested, such that u_∞=2.5, 5.0, 7.5, and 10.0 m s^{-1}, corresponding to Re_{2b}=2650, 5300, 7950, and 10,600, respectively, which covered a significant portion of the air velocity range of interest for typical air conditioning applications; i.e., 1.8 m s$^{-1}\leqslant u_\infty\leqslant$18.2 m s^{-1} [2]. For those values of Re_{2b}, the turbulent flow regime is observed. The largest uncertainty calculated according to Eq. (10) in all tests was $U_{\tilde{q}_*}/\tilde{q}_*$=0.075.

4 Results and Discussion

For each tested Reynolds number (Re_{2b}), the three-way optimization procedure was performed according to the following steps: (i) for a given eccentricity, the dimensionless overall thermal conductance $\tilde{q}_*$ was computed with Eq. (7), for the range of tube-to-tube spacings $0.1\leqslant S/2b\leqslant 1.5$; (ii) the same procedure was repeated for several eccentricities, i.e., e=0.4, 0.5, 0.6, and 1; and (iii) steps (i) and (ii) were repeated for different fin-to-fin spacings configurations; i.e., ϕ_f=0.006, 0.094, and 0.26.

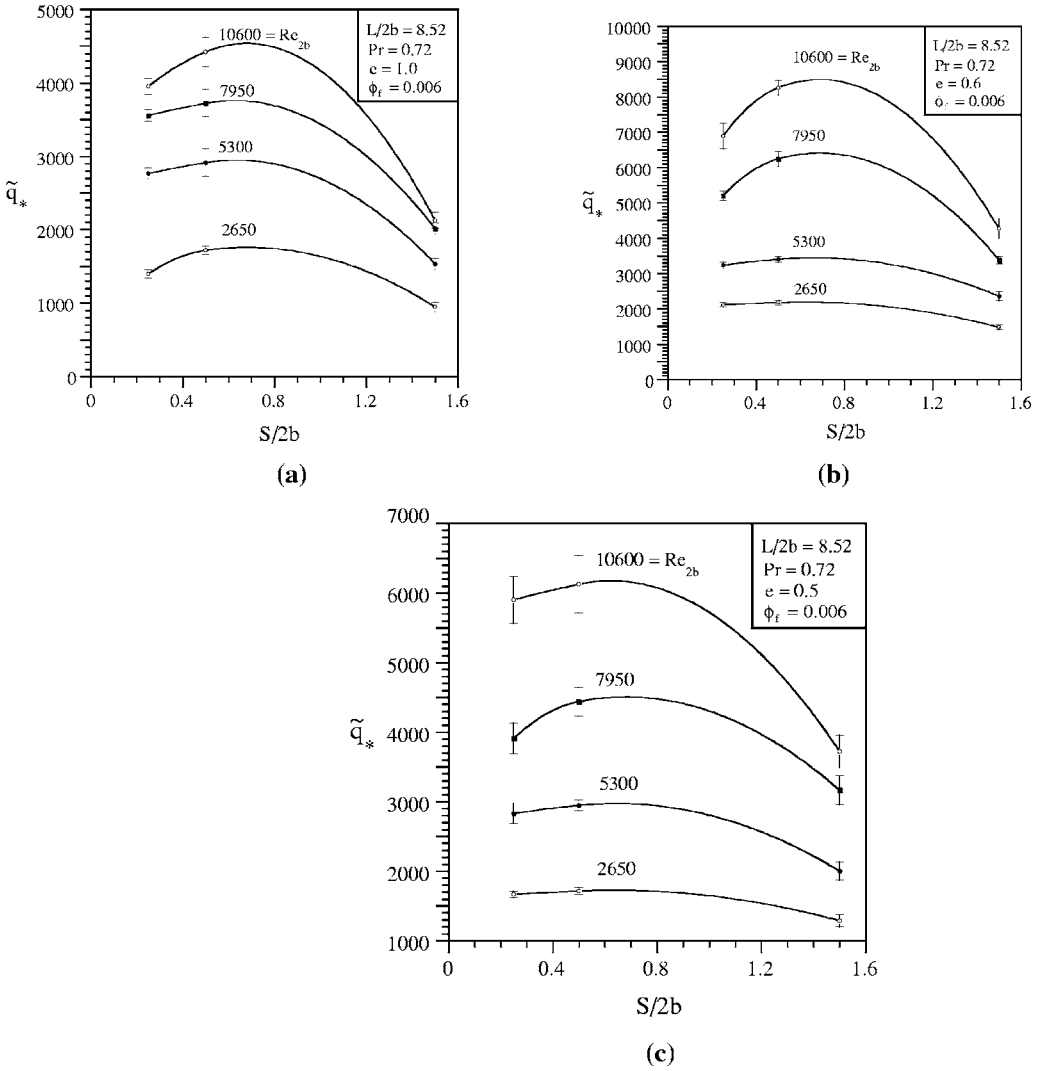

Fig. 1 (***a***) **One-way experimental optimization results (*e*=1 and Re_{2b}=2650, 5300, 7950, and 10,600); (*b*) one-way experimental optimization results (*e*=0.6 and Re_{2b}=2650, 5300, 7950, and 10,600), and (c) one-way experimental optimization results (*e*=0.5 and Re_{2b}=2650, 5300, 7950, and 10,600)**

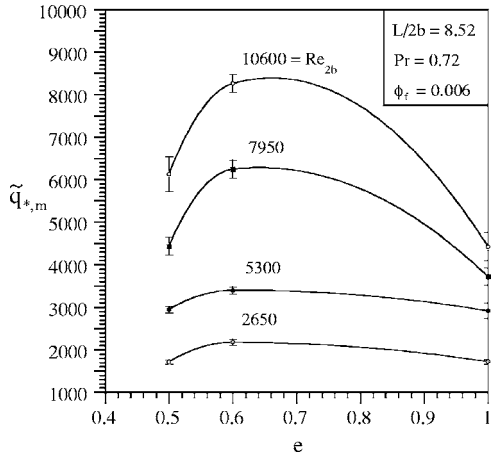

Fig. 2 Two-way optimization of finned arrangements with respect to tube-to-tube spacing and eccentricity

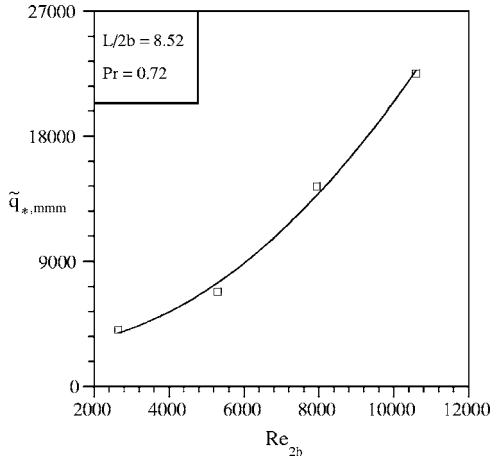

Fig. 4 The three-way maximized dimensionless heat transfer rate with respect to Re_{2b}

This study presents experimental optimization results for a higher range of Reynolds numbers than in previous optimization studies for finned elliptic tubes arrays [15,16], i.e., for Re_{2b} =2650, 5300, 7950, and 10,600, therefore investigating the turbulent flow regime.

The first step of the three-way optimization procedure is documented by Figs. 1(*a*)–1(*c*), which show the experimental optimization of the same tube-to-tube spacing, $S/2b$, for e=1, 0.6, and 0.5, respectively, for a fixed fin-to-fin spacing ϕ_f=0.006. It is observed that the maximum is less pronounced for lower values of Re_{2b}. This phenomenon is physically expected based on the fact that heat transfer increases as mass flow rate increases.

The experiments have shown that $(S/2b,e)_{\text{opt}} \cong (0.5,0.6)$ for ϕ_f=0.006. Indeed, Fig. 2 depicts the one-way maximized $\tilde{q}_{*,m}$ values obtained experimentally for $0.5 \leqslant e \leqslant 1$, for a fixed fin-to-fin spacing ϕ_f=0.006. As Re_{2b} increases, the importance of optimal design is noticeable as turbulence takes place.

Figure 3(*a*) illustrates the existence of a local optimal fin-to-fin spacing, (ϕ_f) for $(S/2b)_{\text{opt}}$=0.5 and e=1 (circular tubes). Figure 3(*b*) reports the results of the three-way global optimization with respect to the three degrees of freedom, $S/2b$, e, and ϕ_f, obtained after performing the three steps of the optimization procedure. The geometric parameters were determined experimentally such that $\tilde{q}_*$ was maximized three times; i.e., $(S/2b,e,\phi_f)_{\text{opt}} \cong (0.5,0.6,0.094)$. The three-way optimized internal configuration is "robust" with respect to the variation of the Reynolds number. A correlation for $2650 \leqslant Re_{2b} \leqslant 10{,}600$ is given by

$$\tilde{q}_{*,mmm} = 2943.8 - 0.16778\,Re_{2b} + 0.00019174\,Re_{2b}^2 \quad R = 0.9978 \tag{10}$$

Figure 4 shows the experimentally determined points for $\tilde{q}_{*,mmm}$, and a curve plotted with Eq. (10). The $\tilde{q}_{*,mmm}$ trend with respect to the variation of Re_{2b} is well approximated.

In sum, a heat transfer gain of up to 80% was observed in the three-way optimized elliptic arrangement of Fig. 3(*b*), as compared to the two-way optimized circular one.

Figure 5 shows the volume fraction of solid material computed with Eq. (9). When the dimensionless fin density is small, the volume fraction of solid material $(\tilde{V})$ increases as eccentricity decreases (from 0.033 at e=1 to 0.053 at e=0.4, for ϕ_f=0.006). Such trend is inverted as the number of fins increases. For example, the volume fraction $\tilde{V} \cong 0.104$ for e=0.5, 0.6, and 1, for ϕ_f=0.094, and $\tilde{V}$=0.215, 0.222, and 0.238 for e=0.5, 0.6, and 1, respectively, for ϕ_f=0.26, as is shown by Fig. 5. Thus, for the

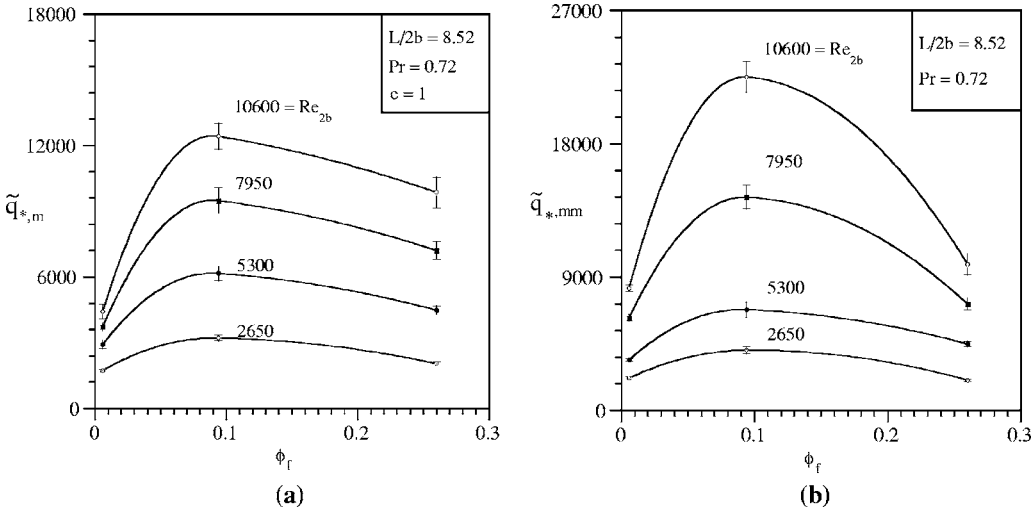

Fig. 3 (*a*) Two-way optimization of finned circular arrangements with respect to tube-to-tube and fin-to-fin spacing, and (*b*) three-way optimization of finned arrangements with respect to tube-to-tube spacing, eccentricity and fin-to-fin spacing.

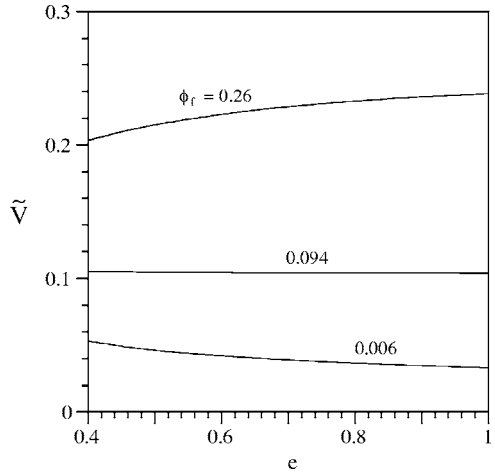

Fig. 5 The total solid volume fraction of the arrangements with respect to eccentricity and fin-to-fin spacing

three-way optimized elliptic configuration, with $\phi_{f,\mathrm{opt}}$=0.094, the volume fraction of solid material of the elliptic arrangement is the same as the circular one. Therefore, the same amount of material is required for manufacturing both the three-way optimized elliptic arrangement and the circular one with the same dimensionless fin density.

5 Conclusions

Several experimental arrangements were built in the laboratory and many test runs were conducted in a wind tunnel in turbulent forced convection. The internal geometric structure of the arrangements was optimized for maximum heat transfer. Better global performance is achieved when flow and heat transfer resistances are minimized together. Optimal distribution of imperfection represents flow architecture, or constructal design [13].

A comparison criterion was adopted as in previous studies [1–3,14–16], i.e., establishing the same air input velocity and flow obstruction cross-sectional for the circular and elliptic arrangements, to compare the arrangements on the basis of maximum heat transfer in the most isolated way possible. An optimal set of geometric parameters was determined experimentally such that $\widetilde{q}_*$ was maximized three times, i.e., $(S/2b, e, \phi_f)_{\mathrm{opt}} \cong (0.5, 0.6, 0.094)$, where the three-way maximized dimensionless heat transfer rate is achieved. The three-way optimized elliptic arrangement exhibits a heat transfer gain up to 90% relative to the optimal circular tube arrangement. A compact analytical correlation was proposed to estimate the actual three-way maximized heat transfer rate in the design of elliptic tubes heat exchangers of the type studied in this paper. For the three-way optimized elliptic configuration, with $\phi_{f,\mathrm{opt}}$=0.094, the volume fraction of solid material of the elliptic arrangement is the same as the circular one. The heat transfer gain, and a similar amount of material to manufacture both arrangements show that the elliptic tubes optimized arrangement has the potential to deliver significantly higher global performance than the circular arrangement, with a similar investment cost.

Nomenclature

a = larger ellipse semi-axis, m
b = smaller ellipse semi-axis, m
B_a = bias limit of quantity a
c_p = fluid specific heat at constant pressure, J kg^{-1} K^{-1}
D = tube diameter, m
e = ellipses eccentricity: b/a
H = array height, m
k = fluid thermal conductivity, W m^{-1} K^{-1}
L = array length, m
$L/2b$ = array length to smaller ellipses axis aspect ratio
$\dot{m}_{\mathrm{ec}}$ = fluid mass flow rate entering one elemental channel, kg s^{-1}
n_f = number of fins
n_t = total number of tubes in the arrangement
N = number of tubes in one unit cell
N_{ec} = number of elemental channels
t_f = fin thickness, m
t_t = tube thickness, m
T = temperature, K
$\bar{T}$ = average fluid temperature, K
Pr = fluid Prandtl number: ν/α
P_a = precision limit of quantity a
$\widetilde{q}$ = dimensionless overall thermal conductance, Eq. (2)
$\widetilde{q}_*$ = dimensionless overall thermal conductance, Eq. (7)
Q = overall heat transfer rate, W
Q_{ec} = heat transfer rate of one elemental channel, W
R = statistics correlation coefficient
Re_{2b} = Reynolds number based on smaller ellipse semi-axis length: $u_\infty(2b)/\nu$
S = spacing between rows of tubes, m
S/D = dimensionless spacing between rows of tubes (circular arrangement)
$S/2b$ = dimensionless spacing between rows of tubes (elliptic arrangement)
U_a = uncertainty of quantity a
$\widetilde{V}$ = volume fraction, Eq. (8)
W = array width, m

Greek Symbols

α = thermal diffusivity, m^2/s
δ = fin-to-fin spacing, m
θ = dimensionless temperature
$\bar{\theta}$ = dimensionless average fluid temperature
ν = fluid kinematic viscosity, m^2 s^{-1}
ρ = density, kg m^{-3}
ϕ_f = dimensionless fin density in direction z

Subscripts

m = 1-way maximum
mm = 2-way maximum
mmm = 3-way maximum
opt = optimal
out = unit cell outlet
w = tube surface
∞ = free-stream

References

[1] Bordalo, S. N., and Saboya, F. E. M., 1999, "Pressure Drop Coefficients for Elliptic and Circular Sections in One, Two and Three-Row Arrangements of Plate Fin and Tube Heat Exchangers," J. Braz. Soc. Mech. Sci., **21**(4) pp. 600–610.
[2] Saboya, S. M., and Saboya, F. E. M., 2001, "Experiments on Elliptic Sections in One and Two-Row Arrangements of Plate Fin and Tube Heat Exchangers," Exp. Therm. Fluid Sci., **24**(1–2), pp. 67–75.
[3] Rosman, E. C., Carajilescov, P., and Saboya, F. E. M., 1984, "Performance of One and Two-Row Tube and Plate Fin Heat Exchangers," ASME J. Heat Transfer, **106**(3), pp. 627–632.
[4] Khan, M. G., Fartaj, A., and Ting, D. S. K., 2004, "An Experimental Characterization of Cross-Flow Cooling of Air via an In-Line Elliptical Tube Array," Int. J. Heat Fluid Flow, **25**(4), pp. 636–648.
[5] Elshazly, K., Moawed, M., Ibrahim, E., and Emara, M., 2005, "Heat Transfer by Free Convection from the Inside Surface of the Vertical and Inclined Elliptic Tube," Energy Convers. Manage., **46**(9–10), pp. 1443–1463.
[6] Elsayed, A. O., Ibrahim, E. Z., and Elsayed, S. A., 2003, "Free Convection from a Constant Heat Flux Elliptic Tube," Energy Convers. Manage., **44**(15), pp. 2445–2453.

[7] Min, J. C., and Webb, R. L., 2004, "Numerical Analyses of Effects of Tube Shape on Performance of a Finned Tube Heat Exchanger," J. Enhanced Heat Transfer, **11**(1), pp. 61–73.
[8] Kundu, B., Maiti, B., and Das, P. K., 2006, "Performance Analysis of Plate Fins Circumscribing Elliptic Tubes," Heat Transfer Eng., **27**(3), pp. 86–94.
[9] O'Brien, J. E., and Sohal, M. S., 2005, "Heat Transfer Enhancement for Finned-Tube Heat Exchangers With Winglets," ASME J. Heat Transfer, **127**(2), pp. 171–178.
[10] O'Brien, J. E., Sohal, M. S., and Wallstedt, P. C., 2004, "Local Heat Transfer and Pressure Drop for Finned-Tube Heat Exchangers Using Oval Tubes and Vortex Generators," ASME J. Heat Transfer, **126**(5), pp. 826–835.
[11] Gao, S. D., Wang, L. B., Zhang, Y. H., and Ke, F., 2003, "The Optimum Height of Winglet Vortex Generators Mounted on Three-row Flat Tube Bank Fin," ASME J. Heat Transfer, **125**(6), pp. 1007–1016.
[12] Kim, N. H., Youn, B., and Webb, R. L., 1999, "Air-Side Float Transfer and Friction Correlations for Plain Fin-and-Tube Heat Exchangers With Staggered Tube Arrangements," ASME J. Heat Transfer, **121**(3), pp. 662–667.
[13] Bejan, A., 2000, *Shape and Structure, From Engineering to Nature*, Cambridge University Press, Cambridge, UK.
[14] Matos, R. S., Vargas, J. V. C., Laursen, T. A., and Saboya, F. E. M., 2001, "Optimization Study and Heat Transfer Comparison of Staggered Circular and Elliptic Tubes in Forced Convection," Int. J. Heat Mass Transfer, **44**(20), pp. 3953–3961.
[15] Matos, R. S., Vargas, J. V. C., Laursen, T. A., and Bejan, A., 2004, "Optimally Staggered Finned Circular and Elliptic Tubes in Forced Convection," Int. J. Heat Mass Transfer, **47**(6–7), pp. 1347–1359.
[16] Matos, R. S., Laursen, T. A., Vargas, J. V. C., and Bejan, A., 2004, "Three-Dimensional Optimization of Staggered Finned Circular and Elliptic Tubes in Forced Convection," Int. J. Therm. Sci., **43**(5), pp. 477–487.
[17] Editorial, 1993, "Journal of Heat Transfer Policy on Reporting Uncertainties in Experimental Measurements and Results," ASME J. Heat Transfer, **115**, pp. 5–6.

Boundary Condition Dependent Natural Convection in a Rectangular Pool With Internal Heat Sources

Seung Dong Lee

Jong Kuk Lee

Kune Y. Suh[1]
e-mail: kysuh@snu.ac.kr

Department of Nuclear Engineering,
Seoul National University,
San 56-1 Sillim-dong,
Gwanak-gu, Seoul 151-742,
Korea

This paper presents results of steady-state experiments concerned with natural convection heat transfer of air in a rectangular pool in terms of the Nusselt number (Nu) versus the modified Rayleigh number (Ra′) varying from 10^9 to 10^{12}. Cartridge heaters were immersed in the working fluid to simulate uniform volumetric heat generation. Two types of boundary conditions were adopted in the test: (I) top cooled, and (II) top and bottom cooled. The other sides were kept insulated. In the case of boundary condition II, the upward heat transfer ratio, $Nu_{up}/(Nu_{up}+Nu_{dn})$, turned out to be 0.7–0.8 in the range of Ra′ between 1.05×10^{10} and 3.68×10^{11}. [DOI: 10.1115/1.2424238]

1 Introduction

Natural convection flow is caused by buoyancy force which results from the difference in density field under the gravitational field. A number of theoretical and experimental programs were conducted to study the heat transfer in the molten pool such as plane layer, rectangular pool, circular pool, and hemispherical pool. This paper is concerned with a fluid layer or a rectangular pool. In general, the natural convection heat transfer phenomena involving internal heat generation are represented by the modified Rayleigh number (Ra′) which quantifies the internal heat source and hence the strength of the buoyancy force.

The first case represented the upper wall being cooled isothermally, while the lower as well as side walls were maintained adiabatically. Work on natural convection with internal heat sources with this type of boundary condition dates back to Woodrow [1] and Hamilton et al. [2]. In the 1950s, particular attention was paid to the molten fuel phenomena, where several numerical and experimental programs were conducted to study the heat transfer in the molten pool. One of the earliest experimental works was due to Globe and Dropkin [3] in the fluid layer. In the 1960s, Tritton and Zarraga [4] conducted experiments with electrically conducting fluid layers. They observed a more or less regular hexagonal plan form in the convection flow. A theoretical study on Tritton and Zarraga [4] was conducted by Roberts [5]. A theoretical investigation was also made of steady laminar convection in an infinite horizontal layer of fluid by Thirlby [6]. In the 1970s, fundamental theoretical (Tveitereid and Palm [7], Cheung [8], and Emara and Kulacki [9]) and experimental (Fiedler and Wille [10], Schwiderski and Schwab [11], Kulacki and Nagle [12], and Kulacki and Emara [13]) studies on the flow structure and the Nusselt number (Nu) versus the Rayleigh number (Ra) relation were conducted.

The second case had to do with both the upper and the lower walls being cooled isothermally, while the side walls were insulated. This case typified the severe accident condition under which the molten core material in the lower head was cooled both at the top and at the bottom. The earliest experimental studies (Kulacki and Goldstein [14], Jahn and Reineke [15], and Mayinger et al. [16]) showed the Nu versus Ra relation and horizontally averaged temperature profiles, wherein the aspect ratio had little effect on the heat transfer results. As a result of the experiment, convective motion began above the center of the layer and the isothermal core region expanded both upward and downward as Ra increased. In addition, theoretical studies (Emara and Kulacki [9], Mayinger et al. [16], Cheung [17], Bergholz et al. [18], and Grotzbach [19]) were conducted to quantify the downward versus the upward natural convection heat transfer.

Natural convection phenomena can be scaled in terms of the Grashof number (Gr), Pr, and additionally, the Dammköhler number (Da) in the presence of volumetric heat sources. The dimensionless numbers are defined as

$$\mathrm{Gr}=\frac{g\beta\Delta TL^3}{\nu^2};\quad \mathrm{Pr}=\frac{\nu}{\alpha};\quad \mathrm{Da}=\frac{QL^2}{k\Delta T} \tag{1}$$

Ra can be used to characterize the heat transfer in natural or free convection problems, including those involving external heat sources or external heating such as heating from below. This dimensionless number is defined as

$$\mathrm{Ra}=\mathrm{Gr}\,\mathrm{Pr}=\frac{g\beta\delta TL^3}{\alpha\nu};\quad \alpha=\frac{k}{\rho c_p};\quad \nu=\frac{\mu}{\rho} \tag{2}$$

The spatial and temporal variation of heat flux on the pool wall boundaries and the pool superheat characteristics depend strongly on the natural convection flow pattern inside the molten pool. The natural convection heat transfer phenomena involving internal heat generation are represented by Ra′ which quantifies the internal heat source and hence the strength of the buoyancy. The preceding equation relates the buoyancy and viscous forces. Ra′ with internal heat source and the isothermal upper and lower wall boundary condition is expressed as

$$\mathrm{Ra}'=\mathrm{Ra}\,\mathrm{Da}=\mathrm{Gr}\,\mathrm{PrDa}=\frac{g\beta qL^5}{\alpha\nu k} \tag{3}$$

However, Ra′ with the internal heat source and the upper wall as a heat sink and the lower wall at the adiabatic boundary condition is expressed as

$$\mathrm{Ra}'=\frac{g\beta qL^5}{2\alpha\nu k} \tag{4}$$

The other side, the Nusselt number (Nu), is proportional to total heat transfer divided by conductive heat transfer. It is defined in the following form

$$\mathrm{Nu}=\frac{hL}{k} \tag{5}$$

Also, a relation between Nu and Ra′ is expressed as

$$\mathrm{Nu}=C\cdot\mathrm{Ra}'^{m} \tag{6}$$

2 Experimental Apparatus and Procedure

In previous studies, the rectangular pool was distinguished from the plane layer. The plane layer means an enclosure for which the aspect ratio (X/L) is much less than unity. The aspect ratio represents an appropriate horizontal length to a pool height. In contrast to a plane layer, the aspect ratio of a rectangular pool is on the order of unity or greater. Compared to studies on the plane layer,

[1]Corresponding author

Contributed by the Heat Transfer Division of ASME for publication in the JOURNAL OF HEAT TRANSFER. Manuscript received July 26, 2005; final manuscript received May 21, 2006. Review conducted by Suresh V. Garimella.

numerical and experimental investigations on a rectangular pool were lacking according to Kulacki and Richards [20].

The (simulant internal gravitated material apparatus rectangular pool) SIGMA RP test apparatus was made from a rectangular cavity 500 mm long, 160 mm wide, and 500 mm high. The walls of the test apparatus were acrylic. The heat loss rate ranged from 3% to 6% through the side walls. The upper and lower plates of the test section were made of copper in order to enhance the heat transfer. The pool height corresponding to the distance between the upper and lower plates had a tolerance of ±1.0 mm. The width-to-height ratio (W/L) of the rectangular pool was greater than 0.25 to avoid the wall effect according to Dinh et al. [21].

A variety of heating methods had been utilized such as external heating, direct current heating (Joule heating), microwave heating, and internal heater heating. Out of numerous experiments, SIMECO was the only one that had adopted the internal heater heating method for two-dimensional circular slice geometry [22]. The current study turns out to be the first experiment employing the internal heater heating method in a rectangular pool. The results demonstrated the practicality of the internal heater heating method to simulate uniform volumetric heat generation in SIGMA RP. Forty thin cartridge heaters, 4.2 mm in diameter and 500 mm in length, were installed to simulate internal heating in the pool. The heater average resistance was 210 Ω within ±5%. The heaters were uniformly distributed to supply a maximum power of 2 kW to the rectangular pool. The distance between centers of the heaters was 40 mm horizontally and 50 mm vertically.

A total of 49 T-type thermocouples were installed in the test apparatus. Four T-type thermocouples were used to measure the upper and lower boundary temperatures. Eleven thermocouples were installed at midplane 3 mm, 50 mm, 100 mm, 150 mm, 200 mm, 250 mm, 300 mm, 350 mm, 400 mm, 450 mm, and 497 mm, respectively, from the bottom plate. 22 thermocouples were installed at the line of symmetry, which was 150 mm off the centerline. Twelve thermocouples were installed to obtain the upper and lower heat fluxes. In order to obtain Nu, the local heat flux can be calculated using a pair of thermocouples. The local heat flux substantiates calculation of the heat transfer coefficient via the relationship $\mathrm{Nu}=hL/k$. The working fluid was air and the Prandtl number (Pr) ranged from 0.71 to 0.74. All data were recorded once a steady state had been established. The steady state was defined such that the temperature fluctuation stayed within ±0.2 K over a period of 11 h.

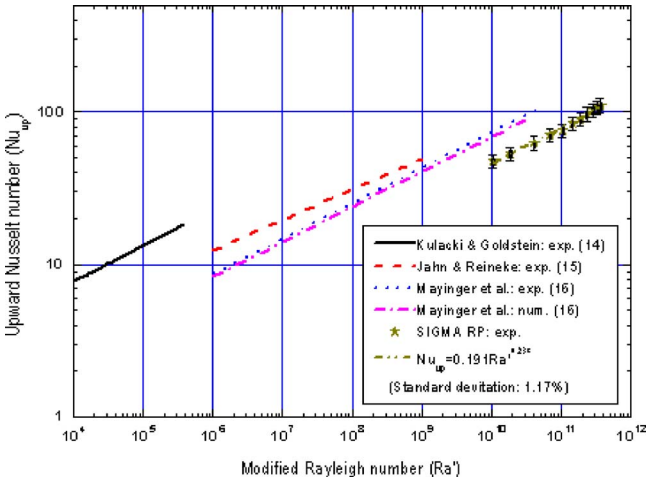

Fig. 2 Upward natural convection heat transfer with isothermal upper and lower walls

3 Results and Discussion

This experiment covered a range of $10^9<\mathrm{Ra}'<10^{12}$ so that the thermal convection flow was fully turbulent. In natural convection experiments, the uniform heat generation rate was one of the prerequisites. The thermophysical properties of the fluids needed to compute the dimensionless numbers were evaluated at the mean value of the maximum and boundary temperatures, viz. $T_m=(T_{\max}+T_b)/2$.

3.1 Condition I. Upper Wall Cooled Isothermally. The test yielded two distinct regions: the upper boundary layer and the turbulent mixing core. In contrast, Cheung [17] had theoretically found an additional lower stagnant boundary layer. Within the upper boundary layer conduction dominated. Away from the upper conduction region, the fluid was in the state of turbulent mixing for high Ra′. Nearly all of the heat generated in the rectangular pool was transported from the core to the upper surface because the lower wall was insulated. Thus, the local heat flux near the lower wall was minor. Figure 1 presents the upward heat transfer data. A correlation has been developed as

$$\mathrm{Nu}_{up}=0.176\mathrm{Ra}'^{0.247} \tag{7}$$

in the range $9.93\times10^9<\mathrm{Ra}'<3.32\times10^{11}$.

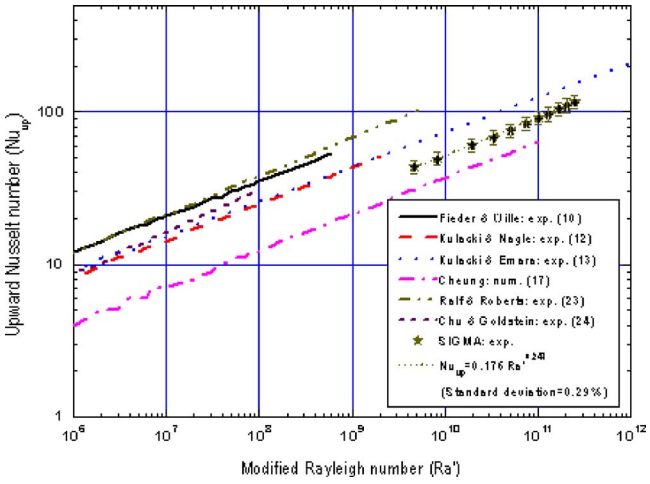

Fig. 1 Upward natural convection heat transfer with isothermal upper wall and insulated lower wall [10,12,13,17,23,24]

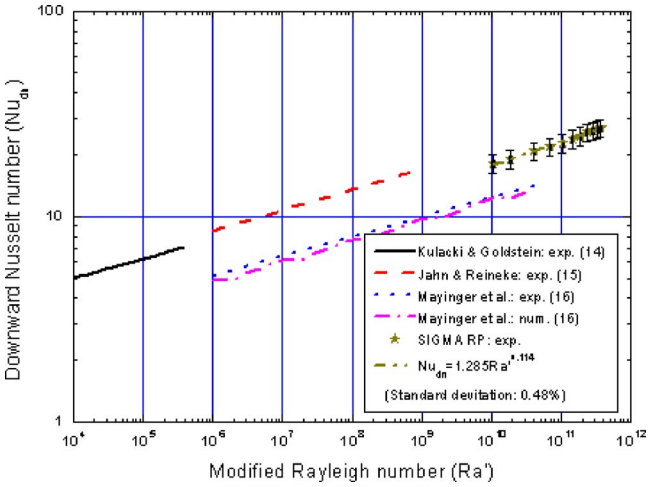

Fig. 3 Downward natural convection heat transfer with isothermal upper and lower walls

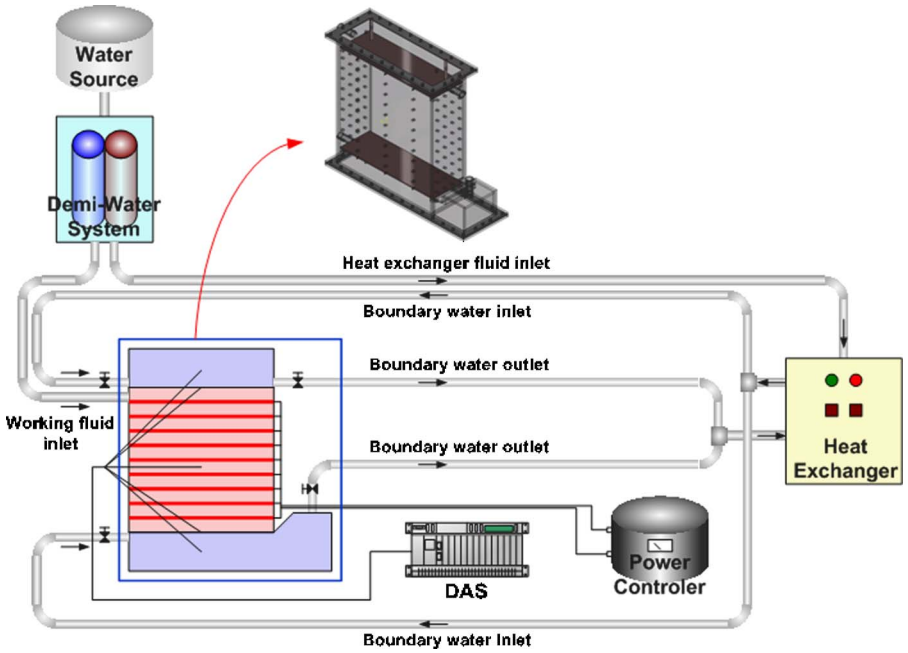

Fig. 4 Schematic diagram of SIGMA RP test loop

3.2 Condition II. Upper and Lower Walls Cooled Isothermally. A steady state was reached after 7 h. Buoyancy affected the central isothermal core of the layer to displace this region upward, thus the upper boundary layer became thin. This signifies that the heat transfer coefficient at the upper surface was relatively large. During the process of heat transfer, the turbulent thermal energy, which was produced in the upper wall region, was being diffused gradually into the turbulent mixing core. Simultaneously, a portion of the turbulent energy was being dissipated by the mixing process until the steady state was reached. The overall balance was such that the turbulent energy distribution was maintained constant in the mixing core.

Figure 2 presents the upward heat transfer data. The data were less than previous correlations in the range of $Ra' = 10^{12}$. A correlation has been developed as

$$Nu_{up} = 0.191 Ra'^{0.238} \tag{8}$$

given $1.05 \times 10^{10} < Ra' < 3.68 \times 10^{11}$. Equation (2) shows that Eq. (1) of Case I enhanced the upward heat transfer, Nu_{up}, through the upper wall from 11% to 14%.

Figure 3 shows the downward heat transfer data. The data lay between Jahn and Reineke [15] and Mayinger et al. [16] in the range $10^{10} < Ra' < 10^{12}$. A correlation has been developed as

$$Nu_{dn} = 1.285 Ra'^{0.114} \tag{9}$$

for $1.05 \times 10^{10} < Ra' < 3.68 \times 10^{11}$.

When the upper and lower walls of the rectangular pool were isothermally cooled, the upward heat transfer ratio, $Nu_{up}/(Nu_{up} + Nu_{dn})$, approached 0.7–0.8 in the range $1.05 \times 10^{10} < Ra' < 3.68 \times 10^{11}$.

4 Error Estimates

The power input per unit volume by the voltmeter readings produced an experimental uncertainty of 6%. The uncertainty in measurement of temperature related to the material properties of the working fluid produced an experimental uncertainty of 3%. The uncertainty in the geometrical factor L^5 was 2%. A reasonable uncertainty in Ra' would be approximately 11%. For the duration of 12 h, the variation of boundary water temperature was neglected since the temperature differences stayed within ±0.4 K. The uncertainty in measurement of heat flux was 4% and that of heat transfer coefficient was 6%. The total experimental uncertainty from the computed values of Nu was found to be 10%. The uncertainty in the geometrical factor L was 0.4%. The uncertainty in the thermal conductivity was 1%. The maximum uncertainty in Nu was 12%.

5 Conclusions

Natural convection tests were conducted in a rectangular pool heated by a discrete cartridge heater used to simulate uniform volumetric heating at high Ra'. The results demonstrated the feasibility of simulating the volumetric heat source. Cartridge heaters may interfere with heat transfer. So as to minimize interruption of heaters, smaller diameter cartridge heaters are being used in the follow-on tests. The present work extends the available data to a higher Ra range.

Nomenclature

- C = constant in Eq. (6)
- Da = Dammköhler number
- g = gravitational acceleration (m/s^2)
- Gr = Grashof number
- h = heat transfer coefficient ($W/(m^2K)$)
- k = thermal conductivity (W/m K)
- L = pool height (m)
- m = an exponent in Eq. (6)
- Nu = Nusselt number
- Pr = Prandtl number
- Q = volumetric heat generation rate (W/m^3)
- Ra = Rayleigh number
- Ra′ = modified Rayleigh number
- T = temperature (K)
- W = pool width (m)
- X = pool length (m)

Greek Letters

- α = thermal diffusivity (m^2/s)
- β = thermal expansion coefficient (K^{-1})
- μ = dynamic viscosity (kg/(m s))

ν = kinematic viscosity (m^2/s)

Subscripts

b = boundary
dn = downward
m = arithmetic mean
max = maximum
up = upward

References

[1] Woodrow, J, 1953, "Free Convection in Heat Generating Fluids (Laminar Flow)," UKAEA, AERE, U.K., Rep. No. E/R-1267.

[2] Hamilton, D. C., Poppendiek, H. F., Redmond, R. F., and Paler, L. D., 1954, "Free Convection in Fluids Having a Volume Heat Source," Oak Ridge National Laboratory, Oak Ridge, TN, Rep. No. ORNL-1769.

[3] Globe, S., and Dropkin, D., 1959, "Natural-Convection Heat Transfer in Liquids Confined by Two Horizontal Plates and Heated from Below," J. Heat Transfer, **81**, pp. 24–28.

[4] Tritton, D. J., and Zarraga, M. N., 1967, "Convection in an Internally Heated Layer," J. Fluid Mech., **30**, pp. 21–31.

[5] Roberts, P. H., 1967, "Convection in Horizontal Layers with Internal Heat Generation. Theory," J. Fluid Mech., **30**, pp. 33–47.

[6] Thirlby, R., 1970, "Convection in an Internally Heated Layer," J. Fluid Mech., **44**, pp. 673–693.

[7] Tveitereid, M., and Palm, E., 1976, "Convection due to Internal Heat Sources," J. Fluid Mech., **76**, pp. 481–499.

[8] Cheung, F. B., 1977, "Natural Convection in a Volumetrically Heated Fluid Layer at High Rayleigh Numbers," Int. J. Heat Mass Transfer, **20**, pp. 499–506.

[9] Emara, A. A., and Kulacki, F. A., 1980, "A Numerical Investigation of Thermal Convection in a Heat-Generating Fluid Layer," J. Heat Transfer, **102**, pp. 531–537.

[10] Fiedler, H. E., and Wille, R., 1970, "Turbulente Freie Konvektion in Einer Horizontalen Flussigkeitsschicht mit Volumen-Warmequelle," Proceedings 4th International Heat Transfer Conference, Paris, France, NC 4.5.

[11] Schwiderski, E. W., and Schwab, H. J. A., 1971, "Convection Experiments with Electrolytically Heated Fluid Layers," J. Fluid Mech., **48**, pp. 703–719.

[12] Kulacki, F. A., and Nagle, M. E., 1975, "Natural Convection in a Horizontal Fluid Layer with Volumetric Energy Sources," J. Heat Transfer, **97**, pp. 204–211.

[13] Kulacki, F. A., and Emara, A. A., 1977, "Steady and Transient Thermal Convection in a Fluid Layer with Uniform Volumetric Energy Sources," J. Fluid Mech., **83**, pp. 375–395.

[14] Kulacki, F. A., and Goldstein, R. J., 1972, "Thermal Convection in a Horizontal Fluid Layer with Uniform Volumetric Energy Sources," J. Fluid Mech., **55**, pp. 271–287.

[15] Jahn, M., and Reineke, H. H., 1974, "Free Convection Heat Transfer with Internal Heat Sources Calculations and Measurements," Proceedings 5th International Heat Transfer Conference, Tokyo, Japan, Vol. 13, NC2.8 pp. 74–78.

[16] Mayinger, F., Jahn, M., Reineke, H., and Steibnberner, V., 1976, "Examination of Thermohydraulic Processes and Heat Transfer in a Core Melt," BMFT RS 48/1, Institut für Verfahrenstechnik der TU, Hanover Germany.

[17] Cheung, F. B., 1978, "Correlation Equations for Turbulent Thermal Convection in a Horizontal Fluid Layer Heated Internally and from Below," J. Heat Transfer, **100**, pp. 416–422.

[18] Bergholz, R. F., Chen, M. M., and Cheung, F. B., 1979, "Generalization of Heat Transfer Results for Turbulent Free Convection Adjacent to Horizontal Surfaces," Int. J. Heat Mass Transfer, **22**, pp. 763–769.

[19] Grotzbach, G., 1981, "Numerical Simulation of Turbulent Temperature Fluctuations in Liquid Metals," Int. J. Heat Mass Transfer, **24**, pp. 475–490.

[20] Kulacki, F. A., and Richards, D. E., 1985, "Natural Convection in Layers and Cavities With Volumetric Energy Sources," *Natural Convection, Fundamentals and Applications*, S. Kakac, W. Aung, and R. Viskanta, eds., Hemisphere Washington, D.C, pp. 179–258.

[21] Dinh, T. N., Nourgaliev, R. R., and Sehgal, B. R., 1997, "On Heat Transfer Characteristics of Real and Simulant Melt Pool Experiments," Nucl. Eng. Des., **169**, pp. 151–164.

[22] Kolb, G., Theerthan, S. A., and Sehgal, B. R., 2000, "Experiments on In-vessel Melt Pool Formation and Convection with $NaNO_3$–KNO_3 Salt Mixture as Melt Simulant," ICONE-8639, Proceedings 8th International Conference on Nuclear Engineering, Baltimore, MD.

[23] Ralf, J. C., and Roberts, D. N., 1974, "Free Convection Heat Transfer Measurements in Horizontal Liquid Layers with Internal Heat Generation," Research Group, Harwell, UK, Rep. No. AERE-R784 UKAEA.

[24] Chu, T. Y., and Goldstein, R. J., 1973, "Turbulent Convection in a Horizontal Layer of Water," J. Fluid Mech., **60**, pp. 141–159.

Journal of Heat Transfer

Erratum

Publisher's Note: "Phase-Change Heat Transfer in Microsystems" [Journal of Heat Transfer, 2007, 129(2), pp. 101–107]

Ping Cheng, Hui-Ying Wu, and Fang-Jun Hong

This article was originally published online and in print with typographical errors. All online versions of the article have been corrected.

For the print readership of ASME, the revised online version will be available through Open Access (no online subscription required) until March 2008.

